Tunable resilience to charge noise of a hole spin

Marion Bassi

THÈSE

Pour obtenir le grade de

DOCTEUR DE L'UNIVERSITÉ GRENOBLE ALPES

École doctorale : PHYS - Physique
Spécialité : Nanophysique
Unité de recherche : PHotonique, ELectronique et Ingéniérie QuantiqueS

Résilience ajustable d'un spin de trou au bruit de charge

Tunable resilience to charge noise of a hole spin

Présentée par :

Marion BASSI

Direction de thèse :

Xavier JEHL DIRECTEUR DE RECHERCHE, CEA CENTRE DE GRENOBLE	Directeur de thèse
Étienne DUMUR INGENIEUR CHERCHEUR, CEA	Co-encadrant de thèse

Rapporteurs :

ALEXANDER HAMILTON
FULL PROFESSOR, UNIVERSITY OF NEW SOUTH WALES
GEORGIOS KATSAROS
FULL PROFESSOR, IST AUSTRIA

Thèse soutenue publiquement le **27 juin 2024**, devant le jury composé de :

ALEXANDER HAMILTON, FULL PROFESSOR, UNIVERSITY OF NEW SOUTH WALES	Rapporteur
GEORGIOS KATSAROS, FULL PROFESSOR, IST AUSTRIA	Rapporteur
ARNE LAUCHT, ASSOCIATE PROFESSOR, UNIVERSITY OF NEW SOUTH WALES	Examinateur
DAVID FERRAND, PROFESSEUR DES UNIVERSITES, UNIVERSITE GRENOBLE ALPES	Président
MAXIMILIAN RIMBACH-RUSS, DOCTEUR EN SCIENCES, DELFT UNIVERSITY OF TECHNOLOGY	Examinateur
HELENE BEA, MAITRESSE DE CONFERENCES HDR, UNIVERSITE GRENOBLE ALPES	Examinatrice

Abstract - English version

Spin quantum bits (qubits) established in group-IV semiconductor quantum dots structures (QD) embody a promising platform for large-scale quantum processors leveraging on small footprint and compatible fabrication processes with mainstream semiconductor industry. In particular, hole particles recently gained attention as spin qubit platform as they enable fast and all-electrical manipulation due to their intrinsically large spin-orbit coupling. The latter coupling however stands as a two-edged sword as it also exposes the hole spin to undesired interactions with the surrounding environment, which in turn degrade the qubit coherence time. Over the past years, many efforts have been conducted to mitigate electrical noise influence stemming from the environment thus revealing the existence of preferential points of enhanced coherence time, named "sweetspots", depending on magnetic field orientation.

In this manuscript, the emphasis is laid on the characterization of electrical noise contributions impacting a single hole spin qubit with respect to magnetic field orientation on a P-doped natural silicon-MOS architecture. The hole particle is spatially confined in a QD defined electrostatically within the device. The spin orientation is readout by radio-frequency reflectometry based on energy-selective readout method. We experimentally demonstrate that the reported "sweetspots" belong in fact to continuous "sweetlines" wrapped around the sphere of magnetic-field polar-angle components, in agreement with theoretical predictions. We also show that, in addition to extended coherence time, sweetline operation is compatible with efficient electric-dipole spin resonance with Rabi frequencies, f_R, comfortably exceeding 10 MHz, and a qubit quality factor $Q = 2f_R T_2^R$ as high as 690, competing with reported values for electrons. Our study evidences ample gate-voltage control of the sweetlines position in magnetic field, an aspect particularly relevant in the purview of scalability. Finally, the experimental investigation of such optimal operation points is extended to a two qubit system as a proof of concept underscoring the importance of sweetlines tuning for spin qubit systems.

Abstract - Version française

Les bits quantiques de spin (qubits) établis dans des boîtes quantiques au sein de semiconducteurs du groupe IV constituent une plateforme prometteuse en vue de futurs processeurs quantiques à grande échelle, du fait de leur faible encombrement et de leur processus de fabrication compatibles avec l'industrie des semiconducteurs traditionnelle. En particulier, les particules de trous ont gagné en attention ces dernières années en vue de leur potentiel en tant que qubit de spin car elles permettent une manipulation rapide de l'orientation du spin, entièrement induites par des champs électriques grâce à leur couplage spin-orbite intrinsèquement important. Ce dernier est toutefois à double tranchant car il expose aussi le spin de trou à des fluctuations électriques indésirables provenant du milieu environnant, ce qui en somme, dégrade le temps de cohérence du qubit. Au cours des dernières années, de nombreux efforts ont été déployés pour réduire l'influence du bruit électrique provenant de l'environnement sur les qubits de spins, révélant ainsi l'existence de points préférentiels, appelés « sweetspots », où le temps de cohérence est grandement étendu dépendamment de l'orientation du champ magnétique.

Dans ce manuscrit, l'accent est mis sur la caractérisation des contributions de bruit électrique ayant un impact sur un qubit de spin à trou unique en fonction de l'orientation du champ magnétique dans un échantillon de silicium naturel dopé P ayant une structure MOS. La particule de trou est confinée spatialement dans une boîte quantique définie électrostatiquement à l'intérieur du dispositif. L'orientation de son spin est lue par réflectométrie radio-fréquence basée sur une méthode de discrimination en énergie des états de spin. Nous démontrons expérimentalement que les « sweetspots »précédemment mentionnés appartiennent en fait à des lignes continues, dites « sweetlines »autour de la sphère angulaire du champ magnétique, en accord avec les prédictions théoriques. Nous montrons également qu'en plus d'un temps de cohérence étendu, le fonctionnement des sweetlines est compatible avec une manipulation efficace avec des fréquences de Rabi, f_R, dépassant confortablement 10 MHz, et un facteur de qualité defini comme $Q = 2f_R T_2^R$ s'élevant jusqu'à environ 690, rivalisant avec les estimations rapportées pour les électrons. En outre, cette étude met en évidence un contrôle accru de la position angulaire

des sweetlines en fonction de la tension de grille. Ceci constitue un aspect particulièrement important dans le contexte d'une future implémentation à plus grande échelle. Enfin, l'étude expérimentale de ces points de fonctionnement optimaux est reproduite pour un système à deux qubits soulignant l'importance des sweetlines pour les systèmes de qubits de spin.

Acknowledgments

Completing a PhD can be likened to a wild ride with its ups and downs. Fortunately, this journey has been made much smoother thanks to the light-hearted atmosphere of the LATEQS team, which I had the privilege to join. In the few lines below, I would like to mention and thank all the individuals who played a significiant role in this thesis and who became friends with time.

First of all, this work would have never been possible without the unwavering support of my supervisor, XAVIER. I would like to express my deepest gratitude for your invaluable guidance over the years. Your constant presence, attention to my progress, and willingness to listen during difficult times have been crucial to the accomplishment of this project. A good example is how you meticulously organized everything for my defense, dealing with the well-known issues with the university (and finally we made it with no delay)!

VIVIEN, I can safely say that none of these results could have been realized without your help and expertise. Thank you for patiently addressing all my (sometimes stupid) questions and for guiding me on managing such a complex experiment calmly, as well as for always being up for a break to play (and lose) at darts. I wish that in a few years, I will possess at least 10% of your knowledge and strive to be as an excellent post-doc as you were for me! Collaborating with you has been a true pleasure and I have no doubt about your success in the future.

Another significant factor that greatly contributed to this project is the close collaboration with talented theoreticians from L-SIM lab. I was extremely lucky to team up with you, ESTEBAN. All the discussions with LORENZO and YANN-MICHEL were truly fruitful in helping me deeply understand the intricated physics of holes. I would also like to mention your coding skills, which continue to impress me. Let me also acknowledge MICHELE (we are still waiting for the famous Bolognese!), ALESSANDRO, MAURICIO, JOSÉ, and BIEL, with whom it is always a pleasure to interact and a great opportunity to learn a lot.

ROMAIN and SILVANO, thank you for being very approachable big bosses! You have an amazing ability to explain the spin qubit physics with simple hand-waving arguments and at the same time, it is possible to play darts with you or meet at

the Loco Mosquito. Thank you for giving me the opportunity to explore physics at the CEA and to join the lab, I truly appreciated learning physics by your side!

During my PhD, I had the opportunity to work with two brilliant post-docs: Simon and Boris, now permanent members of staff. First of all, congratulations again, you are going to be amazing! Simon, you are an excellent physicist, always prone to help. I am absolutely thankful for all the time you spent explaining me whatever physics concepts, when Triton got blocked but also for the time spent outside from the lab! Boris, thank you for taking the time to listen and help (almost all) the students. I am impressed by your ability to adapt and learn quickly, as for instance when you measured momentarily on Triton. Do not hesitate to call again for a jackhammer-pizza party.

I would like to convey my gratitude also to the head of the lab, François, who puts loads of efforts -and succeeds- to orchestrate a collaborative and friendly mood by organizing the "Lateqs days" or barbecues at his place; to Étienne for the valuable help you provided me, especially when it comes to writing my manuscript or coding. Additionnally, it was always a true pleasure to interact with the STM team: Clemens and Vincent.

Un grand merci à Marielle et Vinciane qui m'ont aidé tout au long de ma thèse à faire face à la déroutante administration du CEA; à Jean-Luc toujours présent pour faire des blagues et aider au besoin; et finalement à Michel sans qui aucune amélioration technique sur les expériences ne serait possible.

To a greater extent, I would like to thank the CEA-LETI team, more specifically Heimanu, Emmanuel and Benoit, who made this project possible by providing the samples. It was also a great experience to get to know you better at the karaoke in Japan!

Undoubtedly, times at the lab wouldn't have been the same without the other PhD students, starting with my favourite trio: Axel, Diego and Victor C. Besides the lab, you were always ready to go to bars (at the opening or sometimes even before...), do obscur experiments by freezing fruits with Nitrogen, play board games, bivouac in the mountains and do sports together. Now, I am definitely sure that I am no good at tennis. Victor C., thank you also for joining the morning "pédibus", I will probably miss it in Delft. I wish you the best of luck for the end of PhD journey, you are all getting close to the finish line! Remember, you're always welcome if you ever happen to come to the Netherlands.

A special word goes to Victor M., aka the most willing person to bring his help ! I really enjoyed our endless discussions on any topic over a cup of tea or learning new board games. I wish you the best for the rest of your PhD !

I would like also to mention Léo for being always cheerful and also my experimental neighbor, competing for the qubit totem (my qubit remains the best for sure, sorry!); Elyjah, who I regret not spending more time with; Nesrine, to whom

I wish good luck for being the only female representative, I have absolutely no doubt you'll rock your PhD! Oliver, Hamza and Matteo, I really appreciated sharing the office and having the opportunity to chat with you, even if it was only for a short time... Good luck to Sébastien, Johannes and Jean-Maxime, I hope we'll have the chance to meet again. I would like also to wish the best to the newcomers: Buvan, Julius, Thanh and Mathis.

I definitely cannot forget all the moments spent with the generation of students who already left. Thank you Cécile & Batiste for the Chinese fondues and the evenings at your place. We'll probably see each other again very soon I guess...! Estelle & Dorian, I was always thrilled to go bivouac or discuss with you. Good luck Estelle for your new adventures, hopefully full of catching pinguins in the Antarctic! Florie you are a very inspiring person, I was lucky to meet you. Thank you Thomas J. for the Coinche or Catan times, but also for being always motivated to do barbecues! Nathan, despite that we did not see each other much during our PhDs, let me mention all the fruitful discussions we had concerning writing a manuscript, and the "after". Hopefully we'll keep in touch in the future. Thank you Rami, for being patient and teaching me your knowledge about the fridge and spectroscopy measurements towards the end of your PhD. Also a great thank to Gonzalo, Agostino, Chotivut, Thomas H.

Nico, what a sweet story in the end. We've both finished our PhDs and now we're about to start a brand new chapter in the Netherlands. I rarely tell you how grateful I am for your support, your help over the past years. You have been a true cornerstone to me and I can't wait to face new adventures by your side.

J'aimerai remercier aussi toutes les personnes qui m'ont soutenu pendant ma thèse, de près ou de loin. Un immense merci à Marie, Julie, Adé et Mathilde d'avoir essayé de comprendre ce que je mesurai ces dernières années (parfois même quand je n'en avais aucune idée), mais aussi d'être présentes en toutes occasions, me permettant de m'évader de ma thèse quand il le fallait. Merci à mes copains de prépa, avec qui tout à commencé à Grenoble: Ludo, Marion, Sarah, Jon, Benji, Emma, Lison, Bastien. Aussi, j'aimerai mentionner les personnes du meilleur club de badminton: Elisa, Chris, Margaux, Antoine, Thomas M., Julien, Pauline, Benjamin et j'en passe... J'ai été ravie de passer la plupart de mes weekends à vos côtés, que ce soit sur les terrains, en camping ou autour d'une bière.

Thank you for making nine years in Grenoble such a pleasant time.

Papa, Maman et Loan, il m'est difficile de trouver les mots pour vous remercier de tout ce que vous m'avez apporté, mais surtout de votre indéfectible soutient. Merci d'être toujours présents pour moi et de m'aider à garder confiance en moi. Plus généralement, merci à ma famille pour leur soutient et leur présence depuis toujours.

Finally, I would like to express my deepest gratitude to my committee members, starting with the referees A. Hamilton and G. Katsaros, who took the time

to read this manuscript and provide me with valuable comments. Thanks to H. Béa, D. Ferrand, A. Laucht and M. Rimbach-Russ for their participation in the defence and for the interesting discussions during the question and answer session.

Contents

List of Figures

List of Tables

Introduction

0.1 English version

Logical operations performed within a classical processor nowadays heavily rely upon the operation of billions of silicon transistors simultaneously encoding binary information depending on their conducting ("ON") or insulating ("OFF") behaviour. Processor calculation time is intrinsically limited by the number of on-chip transistors to perform logical algorithm. In this scope, an everlasting race of miniaturizing the transistor dimensions to ever increase their number embedded on chip pushes forward microelectronics industry with a state-of-the-art footprint of about 3 nm.

Early theorized in the eighties, quantum computer has since emerged as an alternative to classical computer by exploiting the quantum properties of two-level systems to encode binary information [1, 2]. Unlike its classical counterpart, a quantum bit (qubit) standing as the building block for quantum processor, can be in a superposition of $|0\rangle$ and $|1\rangle$ quantum states simultaneously before being projected to one of these states upon experimental measurement. This quantum superposition property is expected to confer the ability to quantum processor to perform previously too complex classical algorithms at the short end [3]. So far, the technology to build a quantum processor is not universally accepted and many potential platforms are emerging, namely cold atoms [4], photons [5], trapped ions [6], NV centres [7], superconducting systems [8] and dopants [9] or quantum dots [10] in semiconductor materials.

Common to any platform coming to light, quantum properties are fragile and any interaction with the physical environment results in a noise contribution that limits the timescale during which the qubit can reliably store a quantum information. Up to this point, it is relevant to distinguish between an error-free logical qubit [1] and an imperfect physical qubit with limited coherence and relaxation

1. i.e. a qubit defined with infinite relaxation and coherence timescales.

times. An error-correction algorithm using multiple imperfect physical qubits aims at compensating for noise-induced errors and thus forming an error-free logical qubit. In this sense, the implementation of a quantum processor would require the integration of millions of physical qubits [11]. Following such reasoning, the crux of the matter in realizing quantum computers nowadays resides in (i) mitigating sources of noise that impair with qubits coherence and relaxation timescales while maintaining fast operation speed and (ii) on the large-scale implementation and addressability of physical qubits.

In 1998, a pioneering proposal [10] theoretically suggested the use of confined electron spins in semiconductor materials as a two-level system for quantum computation. Semiconductor structures benefit from well-established manufacturing processes inherited from microelectronic foundries and offer the potential for future high-density and large-scale integration. Since then, many milestones have been witnessed, mostly in AlGaAs/GaAs heterostructures demonstrating single-shot readout of spin orientation [12] and coherent control of one and two qubits [13]. Owing to the presence of nuclear spins, which cause unwanted magnetic noise and in turn hinder long coherence times [14, 15, 16], the attention has grown towards Silicon [17] and Germanium [18, 19] materials chosen for their naturally abundant spin-free isotope. Isotopic purification allows the remaining non-zero isotope of Si or Ge to be eliminated and the magnetic noise contribution to be mitigated, extending the electron spin coherence by an order of magnitude up to $T_2^{\mathrm{CPMG}} \simeq 28\,\mathrm{ms}$ [20, 21].

While many breakthroughs have been reported with electron spin qubits [17, 22, 23], hole counterpart has quickly shown clear asset in terms of large-scale integration. In fact, hole spins in low-dimensional nanostructures leverage on a strong spin-orbit coupling that allows for fast manipulation using only electrical signals [24, 25, 26], therefore reducing the device overhead by dispensing the need for local micro-magnets [27] or ESR lines. Maurand *et al.* [28] experimentally demonstrated the coherent control of the first hole spin qubit spatially confined within a semiconductor quantum dot in 2016, introducing a new branch for spin-based qubits. This Electrically Driven Spin Resonance (EDSR) property, often achieved by high-frequency gate voltage excitation, permits the evolution from one [28, 26, 29, 30, 20], two [31, 32] up to large qubits arrays [33, 34] in both Silicon and Germanium platforms.

The major downside coming along with large spin-orbit interactions is the unwanted interaction of hole spins with electrical noise stemming from the nearby environment, which consequently hampers with the qubit performance [22, 26, 35, 36]. The electrical noise encapsulates the contribution of both phonons and charge noise. The latter originates from the presence of localized defects in the semiconductor due to fabrication imperfections or from the quantum dot potential fluctuations and is recognized as the primary cause of hole spin decoherence to overcome

[22]. Recent investigations have predicted [37, 38, 39, 40] and demonstrated [41, 42, 43] the existence of "dephasing sweetspots" with respect to hole wavefunction confinement and magnetic field orientation that minimize the charge noise contribution, resulting in an improved qubit coherence time approaching 100 µs [41]. However, a clear understanding of the nature of such sweetspots and their ability to maintain a fast operation speed remains to be experimentally underpinned.

This manuscript focuses on the operation and charge noise behaviour of a single hole spin qubit within a quantum dot accumulated in a natural silicon nanowire, similar to refs. [28, 44, 45]. **Chapter 1** provides theoretical background to understand peculiarities of hole spin physics and the formalism adopted. **Chapter 2** details the experimental setup and the device layout. In **Chapter 3**, the attention is laid on the realization of single hole spin manipulation and readout, then on the primary characterization of charge noise experienced by the qubit, evidencing the presence of sweetspots. The angular dependence of sweetspots with respect to the magnetic field orientation and the hole wavefunction confinement is clarified in **Chapter 4** before evaluating the qubit performance (coherence, and operation speed). In the scope of large-scale integration of hole spin qubits, **Chapter 5** provides an introduction to sweetspots tunability to enhance simultaneous two-qubits performances. Besides the charge noise characterization affecting the hole spins coherence times, **Chapter 6** elaborates experimental methods to operate hole Singlet-Triplet qubit within a double quantum dot structure with reduced overhead readout lines. Finally, before drawing conclusions, **Chapter 7** elucidates an alternative measurement method using Landau-Zener adiabatic transitions to probe the qubit operation speed (i.e. Rabi frequency) when subjected to low-frequency fluctuations.

0.2 French Version

Les opérations logiques effectuées dans un processeur classique reposent aujourd'hui fortement sur le fonctionnement de milliards de transistors en silicium qui encodent une information binaire en fonction de leur comportement conducteur ("ON") ou isolant ("OFF"). Le temps de calcul du processeur est intrinsèquement lié au nombre de transistors au sien du processeur utilisé pour effectuer l'algorithme logique. Dans cette optique, une course perpétuelle à la miniaturisation de la taille des transistors est lancée afin d'augmenter sans cesse leur nombre par puce. Ces avancées font progresser l'industrie microélectronique qui peut aujourd'hui atteindre, pour les technologies de pointe, une taille de transistor d'environ 3 nm.

Théorisé dès les années 80, l'ordinateur quantique est apparu comme une al-

ternative à l'ordinateur classique en exploitant les propriétés quantiques des systèmes à deux niveaux pour encoder l'information binaire [1, 2]. Contrairement à son homologue classique, un bit quantique (qubit), qui constitue l'élément de base du processeur quantique, peut se trouver simultanément dans une superposition d'états quantiques $|0\rangle$ et $|1\rangle$ avant d'être projeté dans l'un de ces états lors d'une mesure expérimentale. Cette propriété de superposition permettrait au processeur quantique d'exécuter des algorithmes classiques jusqu'ici trop complexes en des temps réduits. Jusqu'à présent, la technologie permettant de construire un processeur quantique n'est pas universellement adoptée et de nombreuses plateformes potentielles apparaissent, dont les plus avancées sont notamment les atomes froids [4], les photons [5], les ions piégés [6], les centres NV [7], les systèmes supraconducteurs [8] et les dopants [9] ou les boîtes quantiques [10] dans les matériaux semiconducteurs.

Les propriétés quantiques sont fragiles et toute interaction avec l'environnement physique proche du qubit entraîne une contribution de bruit qui limite le laps de temps pendant lequel l'information quantique est fiablement stockée. Il convient de faire la distinction entre un qubit logique considéré sans erreur [2] et un qubit physique imparfait dont les temps de cohérence et de relaxation sont limités. Afin de compenser les erreurs inhérentes aux qubits physiques, des algorithmes « de correction d'erreur »ont vu le jour, de sorte que plusieurs qubits imparfaits forment finalement un qubit logique sans erreur. En suivant ce raisonnement, la mise en œuvre d'un processeur quantique (sans erreur) nécessiterait l'intégration de millions de qubits physiques. Aujourd'hui, le nœud du problème dans la réalisation d'ordinateurs quantiques réside dans (i) la réduction des sources de bruits qui nuisent à la cohérence et relaxation des qubits tout en maintenant une vitesse d'opération rapide et (ii) dans la réalisation à grande échelle d'un grand nombre de qubits physiques et leur adressabilité.

En 1998, une publication théorique [10] suggère l'utilisation de spins d'électrons confinés dans des matériaux semiconducteurs comme système à deux niveaux pour former un qubit. Les structures semiconductrices bénéficient de processus de fabrication bien établis hérités des fonderies microélectroniques et offrent donc un fort potentiel en vue d'une future intégration à grande échelle. Depuis lors, de nombreuses étapes ont été franchies, principalement dans les hétérostructures AlGaAs/GaAs qui ont démontré la lecture en temps réel de l'orientation du spin [12] et le contrôle cohérent d'un et de deux qubits [13]. Cependant, en raison de la présence de spins nucléaires, qui provoquent un bruit magnétique indésirable et réduisent les temps de cohérence [14, 15, 16], l'attention s'est peu à peu tournée vers des matériaux tels que le silicium [17] et le germanium [18]. Ces derniers sont notamment choisis pour leur abondance naturelle contenant peu d'isotope avec des spins nucléaires non nuls et leur proximité avec les procédés de microélectroniques

2. c'est-à-dire avec des temps de cohérence et de relaxation infinis.

déjà existants. La purification isotopique permet d'éliminer le restant d'isotope dont les spins nucléaires sont non nuls, et donc d'amoindrir artificiellement la contribution du bruit magnétique, de sorte que le temps de cohérence d'un spin d'électron peut être étendu d'un ordre de grandeur jusqu'à $T_2^{\mathrm{CPMG}} \simeq 28\,\mathrm{ms}$ [20, 21].

Alors que de nombreuses avancées concernant les qubit de spins d'électrons ont été publiées [17, 22], les spins de trou ont rapidement montré des atouts évidents en termes d'intégration à grande échelle. En effet, les spins des trous dans les nanostructures fortement confinées bénéficient d'un fort couplage spin-orbite qui permet une manipulation rapide uniquement à l'aide de signaux électriques [24, 25, 26]. N'ayant besoin que de signaux électriques, et non plus de champ magnétique oscillant (comme les électrons), l'encombrement du dispositif est réduit du fait de la suppression du besoin de micro-aimants à proximité [27] ou de lignes ESR. En 2016, Maurand *et al.* [28] a démontré expérimentalement le contrôle cohérent du premier qubit de spin à trou spatialement confiné dans une boîte quantique semiconducteur, introduisant une nouvelle branche pour les qubits basés sur le spin. Cette propriété de résonance de spin induite électriquement (EDSR), souvent obtenue par une excitation de tension de grille à haute fréquence, a permis l'évolution d'un [26, 28, 29, 30, 20], à deux [31, 32] jusqu'à un grand nombre de qubits [33, 34] à la fois dans des échantillons de silicium et/ou de germanium.

Le principal inconvénient provenant de cet important couplage spin-orbit est l'intéraction des spins de trou avec le bruit électrique provenant de l'environnement proche, qui entrave par conséquent les performances du qubit [22, 26, 35, 36]. Le bruit électrique englobe entre autre la contribution des phonons et du bruit de charge. Ce dernier provient de la présence de défauts localisés dans le semiconducteur en raison d'imperfections de fabrication ou de fluctuations du potentiel de la boîte quantique et est reconnu comme la principale source de décohérence à surmonter dans le cas d'un spin de trou [22]. De récentes recherches ont prédit [37, 38, 39, 40] et démontré expérimentalement [41, 42, 43] l'existence de « sweetspots »qui minimisent la contribution du bruit de charge en fonction du confinement de la fonction d'onde du trou et de l'orientation du champ magnétique. Dans ce cas précis, le temps de cohérence du qubit est amélioré et avoisine $100\,\mu\mathrm{s}$ [41]. Cependant, une compréhension claire de la nature de ces sweetspots et de leur capacité à maintenir une vitesse de fonctionnement rapide reste à étudier expérimentalement et constitue les principaux axes de recherche de ce manuscrit.

Cette étude se concentre sur le fonctionnement d'un qubit de spin de trou et de son comportement vis-à-vis du bruit de charge au sein d'une boîte quantique accumulée dans un nanofil de silicium naturel, similairement aux refs. [28, 44, 45]. Le **Chapitre 1** fournit les rudiments théoriques pour comprendre les particularités de la physique du spin des trous et le formalisme adopté par la suite. Le **Chapitre 2** détaille le dispositif expérimental. Dans le **Chapitre 3**, l'attention est portée sur la réalisation de la manipulation et de la lecture du spin d'un trou unique,

puis sur les premières caractérisations du bruit de charge, mettant en évidence la présence de sweetspots. La dépendance angulaire de ces sweetspots par rapport à l'orientation du champ magnétique et au confinement de la fonction d'onde du trou est clarifiée dans le **Chapitre 4** avant d'étudier les performances du qubit (cohérence et vitesse de fonctionnement). Dans le cadre de l'intégration à grande échelle des qubits de spin à trous, le **Chapitre 5** fournit une introduction à l'alignement simultané de sweetspots de deux qubits afin d'en améliorer les performances. Outre la caractérisation du bruit de charge affectant les temps de cohérence des spins de trou, le **Chapitre 6** présente des méthodes expérimentales afin de mieux comprendre les propriétés d'un qubit singlet-triplet de trou dans une structure à double boîte quantique. Enfin, avant de conclure, le **Chapitre 7** explicite comment sonder la vitesse de fonctionnement (c'est-à-dire la fréquence de Rabi) d'un qubit soumis à un bruit basse fréquence en étudiant les transitions adiabatiques de Landau-Zener.

References

[1] Richard P. Feynman. « Simulating physics with computers ». In: *International Journal of Theoretical Physics* 21.6 (June 1982), pp. 467–488. DOI: 10.1007/BF02650179.

[2] M. A. Nielsen and I. L. Chuang. *Quantum Computation and Quantum Information*. Ed. by Cambridge. Cambridge University Press, 2010.

[3] P.W. Shor. « Algorithms for quantum computation: discrete logarithms and factoring ». In: *Proceedings 35th Annual Symposium on Foundations of Computer Science*. 1994, pp. 124–134. DOI: 10.1109/SFCS.1994.365700.

[4] K. Wintersperger et al. « Neutral atom quantum computing hardware: performance and end-user perspective ». In: *EPJ Quantum Technology* 10.1 (Aug. 2023), p. 32. DOI: 10.1140/epjqt/s40507-023-00190-1.

[5] S. Slussarenko and G. J. Pryde. « Photonic quantum information processing: A concise review ». In: *Applied Physics Reviews* 6.4 (Oct. 2019), p. 041303. DOI: 10.1063/1.5115814.

[6] J. I. Cirac and P. Zoller. « Quantum Computations with Cold Trapped Ions ». In: *Phys. Rev. Lett.* 74 (20 May 1995), pp. 4091–4094. DOI: 10.1103/PhysRevLett.74.4091.

[7] R. Hanson, O. Gywat, and D. D. Awschalom. « Room-temperature manipulation and decoherence of a single spin in diamond ». In: *Phys. Rev. B* 74 (16 Oct. 2006), p. 161203. DOI: 10.1103/PhysRevB.74.161203.

[8] M. H. Devoret and J. M. Martinis. « Implementing Qubits with Superconducting Integrated Circuits ». In: *Quantum Information Processing* 3.1 (Oct. 2004), pp. 163–203. DOI: 10.1007/s11128-004-3101-5.

[9] B. E. Kane. « A silicon-based nuclear spin quantum computer ». In: *Nature* 393.6681 (May 1998), pp. 133–137. DOI: 10.1038/30156.

[10] D. Loss and David P. DiVincenzo. « Quantum computation with quantum dots ». In: *Physical Review A* 57 (1 Jan. 1998), pp. 120–126. DOI: 10.1103/PhysRevA.57.120.

[11] Austin G. Fowler et al. « Surface codes: Towards practical large-scale quantum computation ». In: *Phys. Rev. A* 86 (3 Sept. 2012), p. 032324. DOI: 10.1103/PhysRevA.86.032324.

[12] J. M. Elzerman et al. « Single-shot read-out of an individual electron spin in a quantum dot ». In: *Nature* 430.6998 (July 2004), pp. 431–435. DOI: 10.1038/nature02693.

[13] J. R. Petta et al. « Coherent Manipulation of Coupled Electron Spins in Semiconductor Quantum Dots ». In: *Science* 309.5744 (2005), pp. 2180–2184. DOI: 10.1126/science.1116955.

[14] H. Bluhm et al. « Enhancing the Coherence of a Spin Qubit by Operating it as a Feedback Loop That Controls its Nuclear Spin Bath ». In: *Phys. Rev. Lett.* 105 (21 Nov. 2010), p. 216803. DOI: 10.1103/PhysRevLett.105.216803.

[15] H. Bluhm et al. « Dephasing time of GaAs electron-spin qubits coupled to a nuclear bath exceeding 200 μs ». In: *Nature Physics* 7.2 (Feb. 2011), pp. 109–113. DOI: 10.1038/nphys1856.

[16] Cywinski L., W. M. Witzel, and S. Das Sarma. « Electron Spin Dephasing due to Hyperfine Interactions with a Nuclear Spin Bath ». In: *Phys. Rev. Lett.* 102 (5 Feb. 2009), p. 057601. DOI: 10.1103/PhysRevLett.102.057601.

[17] B. M. Maune et al. « Coherent singlet-triplet oscillations in a silicon-based double quantum dot ». In: *Nature* 481.7381 (2012), pp. 344–347. DOI: 10.1038/nature10707.

[18] E. Kawakami et al. « Electrical control of a long-lived spin qubit in a Si/SiGe quantum dot ». In: *Nature Nanotechnology* 9.9 (Sept. 2014), pp. 666–670. DOI: 10.1038/nnano.2014.153.

[19] G. Scappucci et al. « The germanium quantum information route ». In: *Nature Reviews Materials* 6.10 (Oct. 2021), pp. 926–943. DOI: 10.1038/s41578-020-00262-z.

[20] M. Veldhorst et al. « An addressable quantum dot qubit with fault-tolerant control-fidelity ». In: *Nature Nanotechnology* 9.12 (Dec. 2014), pp. 981–985. DOI: 10.1038/nnano.2014.216.

[21] A. M. Tyryshkin et al. « Electron spin coherence exceeding seconds in high-purity silicon ». In: *Nature Materials* 11.2 (Feb. 2012), pp. 143–147. DOI: 10.1038/nmat3182.

[22] J. Yoneda et al. « A quantum-dot spin qubit with coherence limited by charge noise and fidelity higher than 99.9% ». In: *Nature Nanotechnology* 13.2 (2018), pp. 102–106. DOI: 10.1038/s41565-017-0014-x.

[23] K. Takeda et al. « Quantum tomography of an entangled three-qubit state in silicon ». In: *Nature Nanotechnology* 16.9 (Sept. 2021), pp. 965–969. DOI: 10.1038/s41565-021-00925-0.

[24] Y. Fang et al. « Recent advances in hole-spin qubits ». In: *Materials for Quantum Technology* 3.1 (Mar. 2023), p. 012003. DOI: 10.1088/2633-4356/acb87e.

[25] G. Burkard et al. « Semiconductor spin qubits ». In: *Rev. Mod. Phys.* 95 (2 June 2023), p. 025003. DOI: 10.1103/RevModPhys.95.025003.

[26] F. N. M. Froning et al. « Ultrafast hole spin qubit with gate-tunable spin–orbit switch functionality ». In: *Nature Nanotechnology* 16.3 (Mar. 2021), pp. 308–312. DOI: 10.1038/s41565-020-00828-6.

[27] M. Pioro-Ladrière et al. « Electrically driven single-electron spin resonance in a slanting Zeeman field ». In: *Nature Physics* 4.10 (Oct. 2008), pp. 776–779. DOI: 10.1038/nphys1053.

[28] R. Maurand et al. « A CMOS silicon spin qubit ». In: *Nature Communications* (May 2016). DOI: 10.1038/ncomms13575.

[29] H. Watzinger et al. « A germanium hole spin qubit ». In: *Nature Communications* 9.1 (2018), p. 3902. DOI: 10.1038/s41467-018-06418-4.

[30] N. W. Hendrickx et al. « A single-hole spin qubit ». In: *Nature Communications* 11.1 (July 2020), p. 3478. DOI: 10.1038/s41467-020-17211-7.

[31] N. W. Hendrickx et al. « Fast two-qubit logic with holes in germanium ». In: *Nature* 577.7791 (2020), pp. 487–491. DOI: 10.1038/s41586-019-1919-3.

[32] M. Veldhorst et al. « A two-qubit logic gate in silicon ». In: *Nature* 526.7573 (Oct. 2015), pp. 410–414. DOI: 10.1038/nature15263.

[33] N. W. Hendrickx et al. « A four-qubit germanium quantum processor ». In: *Nature* 591.7851 (Mar. 2021), pp. 580–585. DOI: 10.1038/s41586-021-03332-6.

[34] S. G. J. Philips et al. « Universal control of a six-qubit quantum processor in silicon ». In: *Nature* 609.7929 (Sept. 2022), pp. 919–924. DOI: 10.1038/s41586-022-05117-x.

[35] O. Malkoc, P. Stano, and D. Loss. « Charge-Noise-Induced Dephasing in Silicon Hole-Spin Qubits ». In: *Phys. Rev. Lett.* 129 (24 Dec. 2022), p. 247701. DOI: 10.1103/PhysRevLett.129.247701.

[36] Lorenzo Mauro et al. « Geometry of the dephasing sweet spots of spin-orbit qubits ». In: *Phys. Rev. B* 109 (15 Apr. 2024), p. 155406. DOI: 10.1103/PhysRevB.109.155406.

[37] V. P. Michal et al. « Tunable hole spin-photon interaction based on g-matrix modulation ». In: *Phys. Rev. B* 107 (4 Jan. 2023), p. L041303. DOI: 10.1103/PhysRevB.107.L041303.

[38] Y. Choi and R. Joynt. « Anisotropy with respect to the applied magnetic field of spin qubit decoherence times ». In: *npj Quantum Information* 8.1 (June 2022), p. 70. DOI: 10.1038/s41534-022-00576-6.

[39] S. Bosco, Bence Hetényi, and Daniel Loss. « Hole Spin Qubits in Si FinFETs With Fully Tunable Spin-Orbit Coupling and Sweet Spots for Charge Noise ». In: *PRX Quantum* 2 (1 Mar. 2021), p. 010348. DOI: 10.1103/PRXQuantum.2.010348.

[40] Z. Wang et al. « Optimal operation points for ultrafast, highly coherent Ge hole spin-orbit qubits ». In: *npj Quantum Information* 7.1 (Apr. 2021), p. 54. DOI: 10.1038/s41534-021-00386-2.

[41] N. Piot et al. « A single hole spin with enhanced coherence in natural silicon ». In: *Nature Nanotechnology* 17.10 (Sept. 2022), pp. 1072–1077. DOI: 10.1038/s41565-022-01196-z.

[42] M. J. Carballido et al. *A Qubit with Simultaneously Maximized Speed and Coherence*. arXiv. 2024. DOI: 10.48550/arXiv.2402.07313.

[43] N. W. Hendrickx et al. *Sweet-spot operation of a germanium hole spin qubit with highly anisotropic noise sensitivity*. arXiv. 2023. DOI: 10.48550/arXiv.2305.13150.

[44] A. Crippa et al. « Gate-reflectometry dispersive readout and coherent control of a spin qubit in silicon ». In: *Nature Communications* 10.1 (2019), p. 2776. DOI: 10.1038/s41467-019-10848-z.

[45] A. Crippa et al. « Electrical Spin Driving by g-Matrix Modulation in Spin-Orbit Qubits ». In: *Physical Review Letters* 120.13 (Mar. 2018), p. 137702. DOI: 10.1103/physrevlett.120.137702.

CHAPTER 1

Theory and basics of spin qubits

Qubits are two-level systems constituting basic building blocks for quantum computing that can be encoded in various platforms, such as superconducting, semiconductor materials, or photons, ions, cold atoms. In the scope of this manuscript, the emphasis is laid onto the realization of a hole spin qubit enclosed within a Quantum Dot (QD) in a natural Si-MOS device architecture. Before going any further into experimental considerations, it is relevant to theoretically understand the implications of such platform choice. This chapter provides an introduction to fundamental mathematical concepts necessary for understanding hole spin physics within quantum dots. The primary section acquaints the concept of quantum dots, aiming to host the further defined spin qubit [1]. Subsequently, we detail the principal characteristics of fermionic spin-1/2 particles and explore the relevant energy scales when experiencing magnetic fields and spatial confinement. The focus then shifts to hole spin qubit systems adapted to silicon devices, outlining the key criteria to improve qubit performance. This naturally leads to a discussion about the physical phenomena impairing these performances, i.e. decoherence and relaxation processes, therefore defining hyperfine and spin-orbit interactions. Finally, we present a theoretical description of the latter noise contributions using the g-matrix formalism.

Contents

1.1 Quantum dots

1.1.1 Single quantum dot

A quantum dot (QD) is an artificial box confined in 3 dimensions about few nanometers size. Due to spatial confinement, particles enclosed within the QD exhibit interesting quantum properties among which the discretization of energy levels as explained in the following. Over the last decades, planar QDs gained a growing interest in the scope of qubit platforms [1] and have been widely studied in various semiconductor structures such as GaAs/AlGaAs, Si/SiGe, Ge/SiGe and Si-MOS heterostructures [2, 3, 4, 5].

When connected to charge reservoirs, a quantum dot can exchange particle (hole or electron) by tunnelling process, as depicted in figure 1.1(a). The latter charge reservoirs are hereafter denoted "S" for Source and "D" for Drain. So as the QD confines a definite amount of charges N, the dot charging energy, denoted E_c, must be (i) greater than the thermal energy : $E_c \gg k_B T$ and (ii) the energy to add an extra particle must remain below the tunnel barrier resistance. These two conditions prevent charges that do not fulfil both conditions from entering the dot. Such regime is commonly referred to as "Coulomb blockade". By capacitively coupling a controllable gate (labelled V_G), the electrostatic potential of the QD can be tuned, such that charge may flow again, provided certain conditions detailed below.

Transport through QD can be understood using the so-called constant interaction model [7, 8]. In that model, all capacitances connected of the QD -coming from the reservoirs or from the gate- are assumed to be constant. The total capacitance of the QD can thus be written as $C = C_G + C_S + C_D$, with C_i the capacitance between the dot and the i contact.

The electrochemical potential of the dot is defined as the difference between two distinct energy levels : $\mu(N) = U(N) - U(N-1)$. A slight bias between the two reservoirs is applied ($\mu_S \neq \mu_D$), creating a difference in the electrochemical potentials, thus forming a so-called "bias window". Whenever the dot potential $\mu(N)$

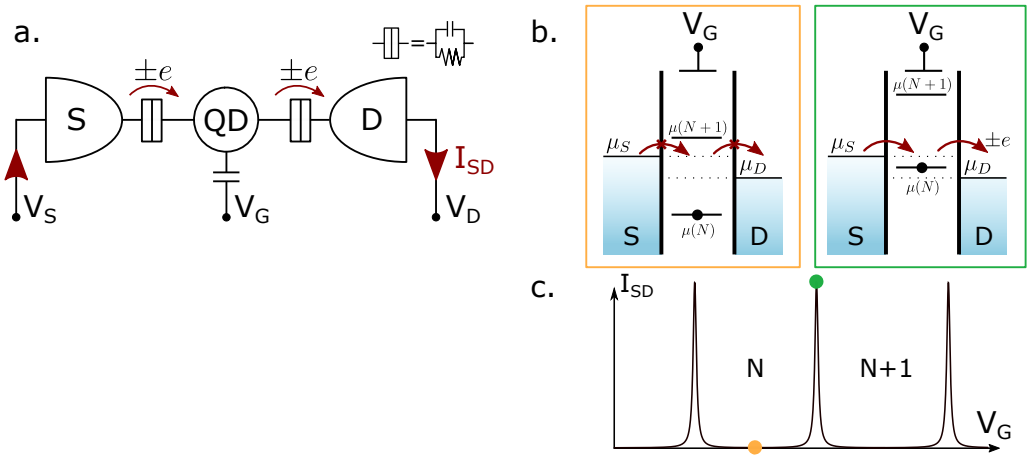

Figure 1.1 – **Schematic of single QD and Coulomb blockade regime:** (a) Equivalent electronic circuit of a quantum dot capacitively connected to reservoirs Source (S) and Drain (D) and a gate electrode G. Charges can flow from one reservoir to the other by going through the QD if the electrochemical conditions are satisfied (see main text). (b) Considering a low bias applied between the two reservoirs, thus creating a so-called "bias window", the transport of charges is allowed whenever the electrochemical potential of the dot filled with N particles, denoted $\mu(N)$, enters within the bias window (right panel). Otherwise, the system remains in Coulomb blockade regime, no charges can transfer as depicted in the left panel. (c) Corresponding current while alternating between Coulomb blockade (yellow) and charge flow (green). Two peaks are distant by the adding energy E_{add} rescaled by the lever-arm of gate V_G to the dot electrochemical potential μ. Figure adapted from [6].

enters within this bias window ($\mu_S \geq \mu(N) \geq \mu_D$), as shown in 1.1(b), charges can flow through the device: there is current from source to drain contacts. Conversely if $\mu(N) \notin [\mu_S; \mu_D]$, charges are blocked due to Coulomb repulsion and no charge transport is observed. Figure 1.1(c) illustrates the corresponding current measured when charge transport is permitted/forbidden. The impact of gate voltage V_G to the dot electrochemical potential is defined as the gate lever-arm, often denoted α. This factor can be experimentally measured. Consequently, two consecutive Coulomb peaks (which translate the addition of one particle), are distant in gate voltage by $\Delta V_G = {}^{E_{add}}/_{\alpha}$.

Adding a N^{th} charge within the dot requires an energy which corresponds to the charging energy E_C and an additional energy spacing ΔE: $E_{add}(N) = E_C + \Delta E = \mu(N+1) - \mu(N)$. One can distinguish the two terms arising from :

- The charging energy E_C defined as ${}^{e^2}/_{C}$ is pure electrostatic contribution from already present charges within the dot repelling the extra charge by Coulomb interactions.
- The additional energy spacing ΔE stems from the discrete orbital energy spectrum of the QD due to strong confinement [4, 8].

In the following of this manuscript, quantum dot will be the elementary block to host a hole spin qubit. Nevertheless, manipulation and readout of these spin qubits may necessitate the presence of additional QDs to provide for instance charge sensor [2] [1]. The question is extended in the next section to the case of two QDs in series coupled to charge reservoirs.

1.1.2 Double quantum dot

The attention is now drawn onto a chain of two quantum dots between unbiased reservoirs, which forms a so-called Double Quantum Dot (DQD) system, see figure 1.2(a). The two dots are mutually and tunnel coupled by a capacitance labelled C_m, which mainly depends on physical distance between the dots. In addition to this mutual capacitance, the dot i exhibits a weak capacitive coupling -known as cross-talk- to the gate voltage of dot j, symbolized by the capacitance C_{ij}.

Charge transport is governed by the same electrochemical conditions than in the case of a single QD, although it now depends on two distinct gate voltages V_{G_1} (V_{G_2}) related to dot 1 (2), see figure 1.2(b). Current relation to both gate voltages is often referred as a stability diagram, as depicted in figure 1.2(c). Depending on the strength of mutual and cross-talk capacitances of the system, the stability diagram exhibit different features, hereafter discussed.

In the case of uncoupled dots and no cross-talk ($C_m = C_{12} = C_{21} = 0$), charges can only go from one reservoir to its neighbouring dot and a charging event of dot i keeps the potential of dot j unchanged. As a result, the stability diagram only exhibits dot-lead transition (no charge exchange between the two dots) as vertical and horizontal lines.

Considering a non-zero mutual capacitance, charges can now be exchanged from one dot to the other, a new kind of transition appears called “interdot”, depicted in red in 1.2(c). The length of such interdot transition is directly related to the mutual and the tunnel coupling, which translate the ability of one particle to hop to the neighbouring QD. Black triple points illustrate the alignment of all dot and reservoir potentials (right panel of (b)). In a vast majority, cross-talk and mutual capacitances coexist and $0 \geq C_m \geq C_{ij}$ so that the stability diagram manifests a well-known honeycomb-pattern [4]. Finally, in the particular instance of a large mutual capacitance C_m, the latter will cause the dots to merge and behave as a single dot equally affected by gate voltages V_{G_1} and V_{G_2}. Dot-lead transition lines are now equally tailored by both gates (lower panel of fig.1.2(c)).

1. The role of such charge sensor will be discussed in the following chapters.

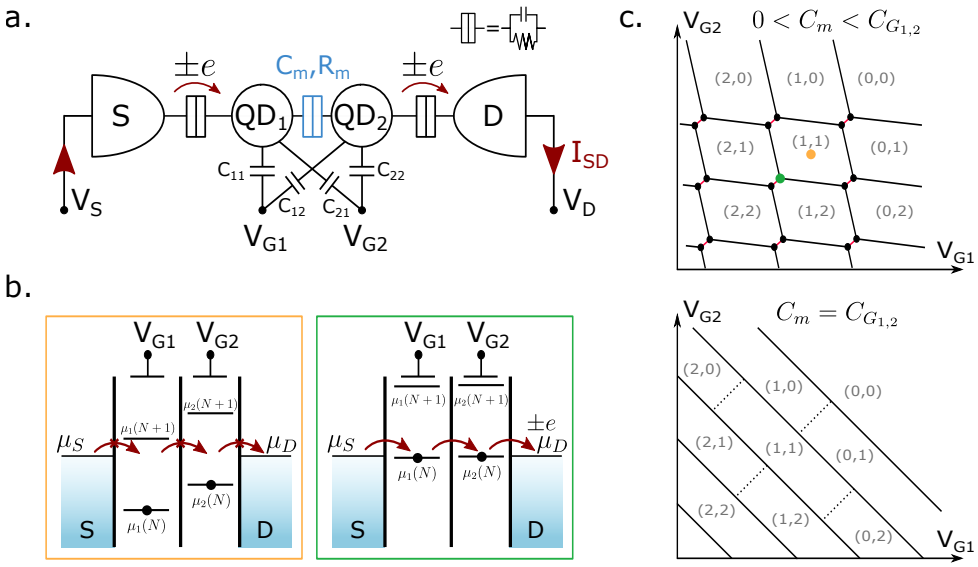

Figure 1.2 – **Schematic of Double QD and stability diagram according to mutual capacitances:** (a) Schematic of the equivalent circuit of DQD system. The two dots are mutually and tunnel coupled to allow for charge exchange. An intrinsic coupling between the gate voltage and the corresponding dot is denoted C_{ii} and the cross-talk capacitance of gate i onto dot j is labelled C_{ij}. (b) Coulomb blockade regime and transport through DQD picture. In this case, no bias is applied between reservoirs. (c) Stability diagrams showing the dot QD_1 (QD_2) charge occupancy as a function of V_{G1} and V_{G2}, depending on the mutual capacitance. A weak mutual coupling (compared to respective gate capacitance), is depicted in upper panel. Herein, remarkable points appear when all electrochemical potentials are aligned. The lower panel describes a strong mutual coupling between the two dots. In this situation, the quantum dots merge and form a unique dot whose potential is equally governed by both gate voltages.

1.2 Spin-1/2 specificities

A quantum bit (qubit) can be encoded in several manners in quantum dots, as far as it is a two-level system. For instance, the qubit can rely upon the presence either left or right inside a double quantum dot of a charge, forming a "charge qubit" or into the spin orientation of a fermion particle (electron or hole) with spin values of $\pm 1/2$. This has been first theoretically proposed by Loss and DiVincenzo in 1998 [1]. Such quantum system can be described by the Schrödinger equation :

$$i\hbar \frac{\partial}{\partial t} |\psi(t)\rangle = \mathcal{H} |\psi(t)\rangle \tag{1.1}$$

with

$\mathcal{H}$ *the system Hamiltonian whose eigenvalues are the total energy,*

$|\psi(t)\rangle$ *the time-dependent particle wavefunction,*

$\hbar$ the reduced Planck constant.

In the spin basis, that we denote $\mathcal{B} = \{|\downarrow\rangle, |\uparrow\rangle\}$ respectively representing $-1/2$ and $+1/2$ spins, the solutions of the above equation are :

$$|\psi(t)\rangle = \cos\left(\frac{\theta}{2}\right)|\downarrow\rangle + \sin\left(\frac{\theta}{2}\right)e^{i\phi}|\uparrow\rangle \tag{1.2}$$

with

(θ, ϕ) the polar and azimutal angles in spherical coordinates.

This equation reveals that any spin orientation of the system can be mapped onto a Bloch sphere, with the eigenvectors $|\downarrow\rangle$ and $|\uparrow\rangle$ defining the poles.

1.2.1 Zeeman splitting

Magnetic field is of crucial importance when working with spin qubit. Indeed, thanks to the Zeeman effect, which lifts the spin degeneracy, magnetic field provides a natural two-level system for quantum operation. The following sections aim at detailing the effect of static (section 1.2.1) and slanting (section 1.2.2) fields. Then, sources of magnetic noise are reviewed and related to their influence on spin coherence and relaxation times.

Zeeman Hamiltonian

When immersed in a static magnetic field, the spin is subject to the Zeeman effect, modelled as:

$$\mathcal{H}_Z(t) = \mu_B \, \mathbf{S}_i \, \tilde{g} \, \mathbf{B}_{\text{eff}} \tag{1.3}$$

with

μ_B the Bohr magneton ($= 58\,\mu eV/T$),

$\boldsymbol{S}_i = \frac{\hbar}{2}\hat{\sigma}_i$ the spin operator and $\hat{\sigma}_{i=(\boldsymbol{x},\boldsymbol{y},\boldsymbol{z})}$ the corresponding Pauli matrices,

$\tilde{g}$ the particle Landé factor also hereafter referred as the g-matrix,

$\boldsymbol{B}_{eff}$ the magnetic field experienced by the spin particle, including an applied magnetic field $\boldsymbol{B}_0$ and internal ones (e.g. hyperfine coupling and spin-orbit effects).

When the effective magnetic field boils down to a static external field along the **z**-axis denoted B_0, the hamiltonian $\mathcal{H}_Z = \mu_B \, \mathbf{S}_z \, \tilde{g} \, \mathbf{B}_0$ is thus time-independent. The corresponding eigenvalues in the spin basis $\mathcal{B}$ are the Zeeman energies : $E_Z = \pm\hbar\omega_L/2$, with ω_L the Larmor angular frequency.

Larmor precession

We consider the spin to be initially in an arbitrary state: $|\psi(t=0)\rangle$ as defined in equation 1.2. The solutions of time-independent Zeeman hamiltonian 1.3 can

be written as:

$$|\psi(t)\rangle = \cos\left(\frac{\theta}{2}\right) e^{-i\frac{E_\downarrow}{\hbar}t} |\downarrow\rangle + \sin\left(\frac{\theta}{2}\right) e^{i\phi} e^{-i\frac{E_\uparrow}{\hbar}t} |\uparrow\rangle \tag{1.4}$$

A static magnetic field B_0 introduces a phase term $e^{-i\frac{E_{\uparrow,\downarrow}}{\hbar}t}$ to the spin wavefunction, but does not change its initial admixture of states $|\downarrow\rangle$ and $|\uparrow\rangle$. This additional phase is linearly dependent to time and represents a precession around field axis at Larmor frequency, also called Larmor precession [9].

1.2.2 Coherent Spin Resonance

The spin degeneracy is lifted when immersed in a static magnetic field by the aforementioned Zeeman effect. Yet, a permanent field is not sufficient to induce rotations between up and down-spin states. First coherent control of single spin in QD was evidenced by Koppens et al. [10] taking advantage of an additional oscillating magnetic field to promote spin transition. As a matter of facts, such oscillating magnetic field may be generated by multiple manners. First, spin-orbit interaction (particularly strong in the case of holes) couples the particle motion to an effective magnetic field B_{SO}. By controlling the particle movement with AC signals, the resulting magnetic field $B_{\mathrm{SO}}(t)$ will induce spin rotation [11, 12]. These specifications will be further discussed in section 1.2.3. By using on-chip micromagnets to create a synthetic spin-orbit coupling, similar results can be obtained with electron spins [13]. As an alternative approach, Electron Spin Resonance (ESR) line nearby the QDs aims at creating an oscillating magnetic field, directly responsible for spin manipulation.

Spin affected by an oscillating magnetic field

We now consider an extra slanting magnetic field with the expression $\mathbf{B}_1(t) = \mathbf{B}_\parallel(t) + \mathbf{B}_\perp(t)$. The perpendicular contribution of $\mathbf{B}_1$ is supposed to oscillate over time so that:

$$\mathbf{B}_\perp(t) = B_\perp \cos(\omega\, t + \varphi)\, \mathbf{x} \tag{1.5}$$

with

- ω *the angular frequency of the driving field,*
- φ *a phase factor induced by the slanting field,*
- $\boldsymbol{x}, \boldsymbol{y}, \boldsymbol{z}$ *the coordinate system defining magnetic field orientation.*

Given that the amplitude of the oscillating field remains significantly smaller than the static one $||\mathbf{B}_0|| \gg ||\mathbf{B}_1||$, the total Hamiltonian can be derived as the bare Hamiltonian (as per equation 1.3) in combination with a first-order perturbation.

$$\mathcal{H}(t) \simeq \mathcal{H}_{Z_0} + \mathcal{H}_{Z_1}(t) = \frac{\mu_B \tilde{g}}{\hbar} \mathbf{S} \cdot [\mathbf{B}_0 + \mathbf{B}_1(t)] \tag{1.6}$$

The perpendicular contribution of oscillating field can be written as a rotating system whose frequency is denoted ω_{R0} such that $\mu_B\,\tilde{g}\,|\mathbf{B}_\perp| = \hbar\,\boldsymbol{\omega}_{R0}$. In the following derivation, the longitudinal contribution of the slanting field $\mathbf{B}_\parallel(t)$ is neglected compared to the static field, but in practice accounts for small perturbations of the amplitude of the angular Larmor frequency. The effect of static and slanting magnetic fields onto the spin orientation is depicted in figure 1.3. We can consider the following Hamiltonian:

$$\begin{aligned}\mathcal{H}(t) &= \frac{\mu_B\tilde{g}}{\hbar}\mathbf{S}_Z\cdot\left(\mathbf{B}_0+\mathbf{B}_\parallel\right)+\mathbf{S}_X\cdot\mathbf{B}_\perp\cos(\omega t+\varphi)\\ &= \mathbf{S}_Z\cdot\boldsymbol{\omega}_L+\mathbf{S}_X\cdot\boldsymbol{\omega}_{R0}\cos(\omega t+\varphi)\end{aligned} \tag{1.7}$$

The phase φ induced by the time-dependent field translates the rotation of $\mathbf{B}_1$ in the $(\mathbf{xy})$ plane. As a consequence, the oscillating field can be expressed as a function of $\mathbf{S}_X$ and $\mathbf{S}_Y$ operators : $\mathbf{S}_X\cos(\omega t+\varphi) = \mathbf{S}_X\cos(\omega t)+\mathbf{S}_Y\sin(\omega t)$. Finally, the hamiltonian reads:

$$\boxed{\mathcal{H}(t) = \mathbf{S}_Z\cdot\boldsymbol{\omega}_L+\mathbf{S}_X\cdot\boldsymbol{\omega}_{R0}\cos(\omega t)+\mathbf{S}_Y\cdot\boldsymbol{\omega}_{R0}\sin(\omega t)} \tag{1.8}$$

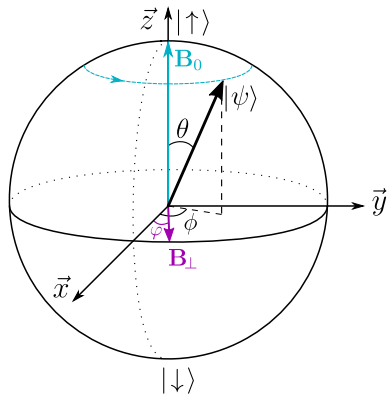

Figure 1.3 – **Bloch sphere representation and impact of slanting magnetic field on spin precession:** Bloch sphere representation of the spin state $|\psi\rangle$. The two poles correspond to the basis eigenstates $|\uparrow\rangle$ and $|\downarrow\rangle$. When immersed in a static magnetic field $\mathbf{B}_0$, the spin state will precess at its Larmor frequency, highlighted by the blue dashed line. In combination with a slanting field $\mathbf{B}_\perp$, displayed in purple, coherent oscillations of spin state can be performed. For sake of clarity, only the perpendicular component of slanting field is shown.

Rotating Wave Approximation

A two-level system dynamics can be approximate with the Rotating Wave Approximation (RWA) by discarding the fast rotating terms.

$$\mathcal{H}(t) = \frac{\hbar}{2}\begin{bmatrix}\omega_L & \omega_{R0}\,e^{-i\omega t}\\ \omega_{R0}\,e^{i\omega t} & -\omega_L\end{bmatrix}\overset{RWA}{\simeq}\frac{\hbar}{2}\begin{bmatrix}\delta\omega & \omega_{R0}\\ \omega_{R0} & -\delta\omega\end{bmatrix} \tag{1.9}$$

with

$\delta\omega = \omega_L - \omega$ *the detuning between Larmor and the driving angular frequencies.*

Solving such approximate Hamiltonian therefore boils down to a time-invariant system with a solution similar to equation 1.4. The probability for the spin to be in the up-state is given by $P_\uparrow(t) = |\langle\uparrow|\psi\rangle|^2$ which finally ends up as:

$$\boxed{P_\uparrow(t) = \frac{\omega_{R0}^2}{\omega_{R0}^2 + \delta\omega^2}\sin^2\left(\sqrt{\omega_{R0}^2 + \delta\omega^2}\,\frac{t}{2}\right)} \tag{1.10}$$

At resonance, i.e. $\delta\omega = 0$, the probability to flip the spin from its ground ($|\downarrow\rangle$) to excited ($|\uparrow\rangle$) state reaches a maximum with a so-called Rabi frequency $f_R = {}^{\omega_{R0}}/_{(2\pi)}$. The spin transition probability is therefore proportional to the excitation ω_{R0} stemming from the oscillating field $\mathbf{B}_1$. Beyond resonance condition, the spin rotation probability is damped by a factor ${}^{\omega_{R0}^2}/_{(\omega_{R0}^2+\delta\omega^2)}$ with modified Rabi frequency, commonly referred as the generalized Rabi frequency $\omega_R = \sqrt{\omega_{R0}^2 + \delta\omega^2}$.

1.2.3 Qubit metrics: relaxation and decoherence timescales

Over the years, important metrics to assess qubit performances as for quantum computation have emerged, mosty inherited from NMR research. First, the coherence time, often denoted T_2, which translates the ability of a system to maintain a superposition of quantum state over time. Second, the spin lifetime T_1 illustrates the characteristic time of the qubit energy relaxation. Such metrics relate to the interactions between the qubit and its surrounding environment and provide a direct indication on the effects of these interactions. Spin qubits offer the advantage of a natural two-level system and can exhibit much longer coherence times compared to the charge ones. Nevertheless, the particle still interacts with the surrounding environment that negatively reverberates on coherence and relaxation times.

Theoretical definitions of T_1 and T_2

The density operator ρ used to describe a two-level system, can be expressed as a function of the Pauli matrices as follow [14, 15]:

$$\rho = \frac{1}{2}(1 + \mathbf{p}\cdot\boldsymbol{\sigma}) = \begin{bmatrix}\rho_{\uparrow\uparrow} & \rho_{\uparrow\downarrow}\\ \rho_{\downarrow\uparrow} & \rho_{\downarrow\downarrow}\end{bmatrix} \tag{1.11}$$

with

$\boldsymbol{\sigma}$ *the Pauli matrices,*

$\boldsymbol{p}$ *the Bloch vector, representing the expectation values of spin components :* $\boldsymbol{p}/2 \equiv \langle \boldsymbol{S}\rangle = Tr(\boldsymbol{S}\rho)$.

Bloch equations formalism [16] is used to describe the exponential decay of the density-matrix components. Using both the Born-Markov approximation and Redfield equation, see reference [14](section 1.4), the first-order decay of spin expectation value reads as:

$$\frac{\partial}{\partial t}\langle \mathbf{S} \rangle = \boldsymbol{\omega} \times \langle \mathbf{S} \rangle - R\langle \mathbf{S} \rangle \tag{1.12}$$

with

$\langle \boldsymbol{S} \rangle$ *the expectation values of the spin component* $\langle \boldsymbol{S} \rangle = (\langle \boldsymbol{S}_x \rangle, \langle \boldsymbol{S}_y \rangle, \langle \boldsymbol{S}_z \rangle)$,

$\boldsymbol{\omega} = (0, 0, \omega_Z)$ *represents the Zeeman splitting in the case of a static field along* $\vec{z}$,

R *the relaxation matrix, also called Redfield tensor.*

Considering that the Zeeman splitting remains much larger than the relaxation processes, the Redfield tensor can be approximated by only diagonal elements:

$$R = \begin{bmatrix} T_2^{-1} & 0 & 0 \\ 0 & T_2^{-1} & 0 \\ 0 & 0 & T_1^{-1} \end{bmatrix} \tag{1.13}$$

The Redfield tensor describes the damping of spin expectation values over time (sources of quantum errors). Relaxation term T_1 occurs as a longitudinal contribution and illustrates the undesired spin flip, whereas T_2 coherence time describes a transverse component which accounts for a phase randomization of quantum state. When $R = 0$, the scenario reverts to the classical depiction of a spin particle within a static magnetic field merely experiencing its Larmor precession. Timescale metrics can be formally defined a follow:

$$\begin{cases} T_1^{-1} = \Gamma_\uparrow + \Gamma_\downarrow \\ \dfrac{1}{T_2} = \dfrac{1}{2T_1} + \dfrac{1}{T_\phi} \end{cases} \tag{1.14}$$

with

$\Gamma_\uparrow(\Gamma_\downarrow)$ *the transition rate from ground to excited (excited to ground) state,*

T_ϕ *pure dephasing term.*

For spins in semiconductor QD, two major interactions with the environment contribute to decoherence and relaxation times : the hyperfine interaction (HF) [17, 18] and the spin-orbit coupling (SOC)[19]. Importantly enough, these interaction terms now strongly depend on the nature of the particle, e.g. hole or electron.

Besides, virtual exchange processes with nearby reservoir can also constitute a non-negligible source of relaxation and decoherence [4]. Though, it can be strongly reduced by removing (partially or totally) the coupling to charges reservoir. From now on, this latter process will be neglected as it is highly experiment-dependent.

Hyperfine interactions

Even if strongly spatially confined [2], the particle wavefunction overlaps with about 10^4 to 10^6 nuclear spins present within the host material [4, 20], see a simplified schematic in figure 1.4(a). In the case of confined electrons (mostly s-like orbitals) in semiconductor materials, the Fermi contact interaction is the outweighing term. The ensemble of nuclear spins can thus be described as a time-varying magnetic field B_N, also referred as Overhauser field. The confined particle experiences the latter field in combination with the external static one, which in turn causes a subsequent evolution into a statistical mixture of states. In other words, the hyperfine interactions directly induce decoherence [21, 22, 23, 24, 25]. Groups III-V and IV semiconductor are especially prone to such hyperfine interactions, which can be circumvented by the use of purified materials (i.e. by removing the surrounding nuclear spins).

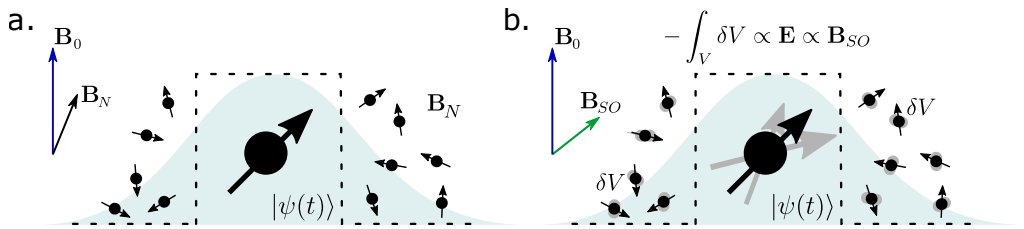

Figure 1.4 – **Illustration of hyperfine and spin-orbit interaction mechanisms:** (a) Hyperfine interaction representation. The spin qubit with wavefunction $|\psi(t)\rangle$ is enclosed within a quantum dot whose potential is depicted by the dashed line. As the wavefunction spreads beyond the QD dimension, the spin qubit encounters nuclear spins from the host material. As an ensemble, such nuclear spins create an Overhauser magnetic field B_N, added to the external field B_0, causing undesired relaxation and decoherence processes. (b) Spin-orbit interaction illustration. Charge movements ∇V and potential fluctuations induce an electrical field $\mathbf{E}$ which can also be seen as an analogous magnetic field B_{SO} acting on the spin qubit.

In the particular case of hole, the Fermi contact term vanishes in the valence band (due to the predominance of p-like states). The hyperfine interactions are therefore mainly governed by dipole-dipole and orbital couplings [20, 26]. This renders the global hyperfine interaction strongly anisotropic with respect to external magnetic field orientation [27]. The exact derivation of such hamiltonians stands beyond the scope of this manuscript, yet it is important to notice that the resulting coupling is strongly affected by the Light-Hole (LH), Heavy-Hole (HH) mixing, further described in section 1.3.2. For heavy holes, HF interactions can be casted into an Ising term ($\propto S_z I_l^z$) whereas for light holes, it will take the form of an in-plane component ($\propto S_x I_l^x, S_y I_l^y$), with $I(S)$ the nuclear (spin) degree of

2. In the device presented later on, in chapter 2, the maximum expected dimensions of the QD are about $40\,\mathrm{nm}^3$.

freedom. LH-HH mixing causes the hyperfine interactions to be significantly more complex than in the case of electrons. Surprisingly enough, similar hyperfine coupling magnitude is found for holes and electrons in silicon [20].

Some particular confinement geometry and magnetic field orientations are predicted to render the spin qubit comparatively insensitive to nuclear-field fluctuations [28]. As many efforts have recently been made to cope with charge noise [24, 29], establishing a deep understanding of hyperfine couplings will presumably be relevant to enhance qubit coherence times [27]. Alternative approaches also take advantage of such hyperfine coupling to act on the nuclear degree of freedom [23].

Spin-orbit coupling

A particle moving through a solid, i.e. immersed in an electrical field $\mathbf{E}$, experiences a magnetic field $\mathbf{B}_{\mathrm{SO}}$ proportional to $\mathbf{E} \times \mathbf{p}$ with $\mathbf{p}$ the particle momentum [4, 20]. This artificial magnetic field strongly depends on the orbital occupied by the particle and acts on its spin; hence, this interaction is named Spin-Orbit Coupling (SOC). Usually, SOC is described as:

$$\mathcal{H}_{SO} = \frac{\hbar}{4m_0^2c^2}(\boldsymbol{\sigma} \times \nabla V) \cdot \mathbf{p} \tag{1.15}$$

with

m_0 *the bare electron mass,*

c *speed of light in vacuum,*

∇V *potential energy gradient created by nearby moving charges.*

Holes in the valence band are mainly p-type orbitals, rendering them particularly sensitive to SOC in comparison to electrons, which are mainly s-like orbitals. Spin-orbit interaction can be expressed as two main contributions which arise from inversion-symmetry breaking mechanisms: a bulk-inversion symmetry (BIA), known as Dresselhaus term [30], and a structural inversion symmetry (SIA), referred as Rashba component. A third contribution may contribute as an interface ivnersion asymmetry close by the interfaces, hereafter referred as Surface Dresselhaus [31]. Both contributions are highly dependent on the chosen material, the nature of the particle, and the confinement dimension. Figure 1.4(b) depicts the spin-orbit interaction between the qubit and its surrounding environment. Capturing the SOC anisotropy and the weighting mechanisms is very challenging, especially in the case of holes. In the following chapters, this anisotropy, which is linearly dependent on the magnetic field, is cast into a defined G-tensor using the g-matrix formalism, which will be discussed in more details in section 1.4. As a result, no a priori assumption on the SOC terms is needed and all mechanisms are thus treated as a unique contribution.

Dresselhaus coupling term stems from bulk inversion asymmetry, present in particular in crystals with a zinc-blende structure such as GaAs. In the case of Silicon or Germanium materials, which exhibit a diamond structure, there is no bulk inversion asymmetry, thus the Dresselhaus term cancels out. However, such materials often manifest the presence of finite strain (especially in the case of SiGe quantum wells or core-shell nanowires) which can be modelled using the Bir-Pikus correction Hamiltonian [20, 32].

Owing to the anisotropy of chemical bonds at the interface, a Dresselhaus-like term can additionally influence the particle SOC response. The latter is particularly scrutinized in the case of diamond-diamond structure interface (e.g. Si/Ge) [31, 33, 34]. It is directly related to the steepness profile and the roughness at the interface and can be captured by a four-band $\mathbf{k}\cdot\mathbf{p}$ model with proper corrections to the Luttinger-Kohn Hamiltonian [35]. Considering a silicon-oxide interface like in Si-MOS structure, the Surface Dresselhaus contribution is expected to be far less prominent because the interface is disordered (diamond-amorphous interface). Nevertheless, an experimental investigation [34] in Si-MOS architecture highlighted a particularly strong Surface Dresselhaus term for electron particles.

Besides, Rashba spin-orbit contribution arises from the asymmetry of confining potentials, namely structural confinement (heterostructure (2D) or nanowire (1D)), strain or gate potential. As previously mentioned, Dresselhaus contribution vanishes for diamond structure materials, thus the Rashba interaction is expected to outweigh. In the case of a particle confined in a 2D potential, or for holes in both 1D or 2D confinement structures, the Rashba SOC term is cubic in momentum ($\propto \mathbf{p}^3$), whilst it remains linear ($\propto \mathbf{p}$) for electrons in a 1D confinement potential[3]. Moreover for holes, Rashba interaction couples the HH to LH states and involves non-linearity unlike Dresselhaus term, permitting the existence of optimal coherence point [24]. For Si and Ge nanowires, the spin-orbit coupling can reach up to meV value.

The following table 7.1 summarizes the different contributions -Rashba and Dresselhaus- correspondingly to device dependent parameters:

Because of spin-orbit interaction, the spin qubit becomes sensitive to surrounding electric field fluctuations stemming from phonons bath or electrical potential variations, also known as charge noise. The latter is particularly ubiquitous in semiconductor structures in the vicinity of gate oxides [36]. As such, spin-orbit interaction definitely plays a role in decoherence and relaxation processes.

About the consequences on relaxation and decoherence:
On the one hand, fluctuating electric fields lead to spin relaxation in an indirect manner via the coupling to phonons. This mechanism is less efficient than induced

3. This phenomenon is also known as the Direct-Rashba interaction.

		Rashba	Dresselhaus
Material	diamond (Si,Ge) zinc-blende (GaAs)	mostly	∅ (Bir-Pikus for strain) $\propto \mathbf{p}$
Confinement	1D (nanowire) 2D (heterostructure)	$\propto \mathbf{p}$ $\propto \mathbf{p}^3$	
Particle	holes electrons	$\propto \mathbf{p}^3$ $\propto \mathbf{p}$	

Table 1.1 – **Different contributions of SOC:** Rashba and Dresselhaus scaling as a function of material type, confinement dimension and nature of the particle. $\mathbf{p}$ is the particle momentum. This table is a summary of reference [20].

phase randomization, and for this reason, experimental spin-relaxation times remain long compared to different qubit platforms [2, 21, 37, 38]. The minimum electric field fluctuation boils down to the phonon bath contribution, which can produce electric fields in two distinct ways:

- *deformation potential phonons*: inhomogeneously distort the crystal lattice, thus inducing electric fields. This phenomenon is present in all semiconductors,
- *piezoelectric phonons*: create homogeneous strain in polar crystals (e.g. GaAs). Piezoelectric phonons have much weaker impact in Si and Ge-based spin qubit [24, 36].

The phonon-induced transition rate can be determined by the Fermi's Golden rule and directly relates to the phonon density at the Larmor energy and the spin-phonon coupling strength. It has been theoretically predicted that hole spin relaxation induced by phonons is anisotropic with respect to magnetic field orientation [39]. When phonons are involved, relaxation time T_1 is expected to scale as either B^{-5} (piezoelectric phonons, at low energy) or B^{-7} (deformation potential phonons at higher energy). [4]

On the other hand, and more especially in the case of holes exhibiting larger SOC (see section 1.3), the coherence time T_2 is greatly affected by charge noise. Indeed, such electrostatic fluctuations induce a modification of the g-factor (and thus the Zeeman energy), creating direct phase randomization.

Against a backdrop of a constant qubit performance enhancement, relaxation and decoherence processes remain intrinsically limited by device dependent parameters, such as hyperfine and spin-orbit coupling. Nonetheless, preceding section surveyed that the choice of material, experimental conditions (e.g. magnetic

4. In the case of weak contribution of piezoelectric phonons (Si and Ge), relaxation time T_1 can scale down to B^{-9}.

field orientation) and device type (e.g. material, nature of particle), may help to circumvent such limitations or at least reduce their impact on the qubit. For instance electron spin qubits in GaAs, early acknowledged as a promising platform for spin qubit operation [2, 10, 37], suffer from decoherence due to hyperfine coupling, piezoelectric phonons and Dresselhaus terms, interactions that cannot be mitigated. Consequently, hole spin qubits in diamond based structures (Si or Ge namely) recently gained a growing interest as for quantum operation [5, 12, 40, 41]. Spin-orbit coupling can also be beneficial, as it allows for all-electrical manipulation of spin referred as Electric Dipole Spin Resonance (EDSR) [19].

1.3 Focus on hole particles in Silicon quantum dots

1.3.1 Experimental specificities

This manuscript aims at documenting the experimental realization of hole spin qubit operation based on Silicon-Metal-Oxide-Semiconductor (Si-MOS). As aforementioned, the choice of material, confinement and doping is of crucial importance as it will impact the physical mechanisms at stake as sources of decoherence and relaxation (namely HF and SOC).

First, Si-MOS technology benefits from well-established industrial fabrication processes, that offers better scalability prospects and integration through nanofabrication [12, 42, 43].

Second, silicon material crystallizes in a diamond structure. This renders the qubit almost indifferent to piezoelectric phonons and Dresselhaus interaction, which are partly responsible for relaxation and decoherence processes. Silicon also takes advantage of a weakly abundant isotope ^{29}Si ($\sim 4.7\%$) that carries non-zero nuclear spins[5]. Silicon spin qubit systems already demonstrated long coherence times and quantum operations [44, 45, 46].

Finally, holes do not exhibit valley degree of freedom, lessening experimental complications (absence of nearby quantum levels that could be excited) and causing Fermi contact interactions (part of HF) to vanish. In addition, they offer an intrinsically strong spin-orbit coupling (stronger than electrons), which appears as an ambivalent property. On the one hand, spin manipulation is possible by using only electrical fields, giving rise to EDSR control, that reduces the on-chip complexity by removing micro-magnets or ESR-line [10, 12, 13, 44, 47]. On the other hand, the particle couples to any electric field fluctuations nearby (charge noise and phonons), which is detrimental to its spin coherence [48]. Charge noise is known to be the main source of decoherence for hole spin qubit in silicon and

5. Note that the second most abundant (about $\sim 3\%$) and stable isotope of silicon is ^{30}Si, that carries a zero nuclear spin.

germanium devices. As the sources of hole spin decoherence (e.g. phonons, hyperfine and Rashba), and g-matrix, are strongly anisotropic regarding to the external magnetic field, this suggests that T_2 timescale may be enhanced by proper field alignment. This has been recently investigated both theoretically [49, 50] and experimentally [27, 29], highlighting the existence of dephasing sweetspot. At such sweetspot, hole spin coherence time is drastically enhanced [29].

1.3.2 HH-LH mixing

In group IV semiconductors, the conduction band is mainly formed by s-like orbitals, having an angular momentum $L = 0$, whilst the valence band is associated with p-like orbitals ($L = 1$) [20]. In combination with the spin-$1/2$ of holes, the total angular momentum J = L + S can either take the values $\pm 3/2$ or $\pm 1/2$. This sets the proper basis to describe particle properties within silicon valence band structure: $\mathcal{B} = \{|+3/2\rangle, |-3/2\rangle, |+1/2\rangle |-1/2\rangle\}$.

Bulk silicon band structure exhibits an indirect band-gap about 1.17 eV as shown in figure 1.5. The conduction band is 6-fold degenerate at the k_0 point. In contrary, the valence band exhibits a fourfold degeneracy at $\mathbf{k} = 0$ -henceforth denoted Γ point- and a split-off band due to the presence of an intrinsically strong spin-orbit coupling. Left panel of figure 1.5 highlights the unrealistic silicon band structure in absence of SOC whereas the right panel zooms nearby the Γ point and highlights the lifted degeneracy and the emergence of a split-off band in addition to HH and LH bands. The energy splitting at the Γ point between the split-off and HH-LH bands is $\Delta_0 \simeq 44$ meV. In the limit of $k \to 0$, the higher (lower) valence band states are labelled heavy (light) holes with respective angular momentum $J = \pm 3/2$ ($\pm 1/2$) at an energy $\Delta_0/3$. The split-off band lies at $-2\Delta_0/3$ below the topmost of valence band with angular momentum $J = \pm 1/2$. Holes physics is captured by the Luttinger-Kohn (LK) Hamiltonian [51] which is well-approximated by the $\mathbf{k} \cdot \mathbf{p}$ model around the Γ point for theoretical simulation purposes.

Strong confinement along one axis is known to lift the fourfold degeneracy of the valence band and pulls away the LH band from the HH one (e.g. Ge heterostructure) [40, 41]. In this case, the HH states will naturally dominate as the ground state of the system [39]. Symmetry reduction due to confinement geometry in two equivalent axis (as for nanowires) causes hole mixing, arising from the off-diagonal terms of the Luttinger-Kohn hamiltonian [26, 51]. This constitutes the so-called HH-LH mixing. As heavy and light holes behave differently in magnetic field (Zeeman response), their mixing confers peculiar physic properties on the spin qubit.

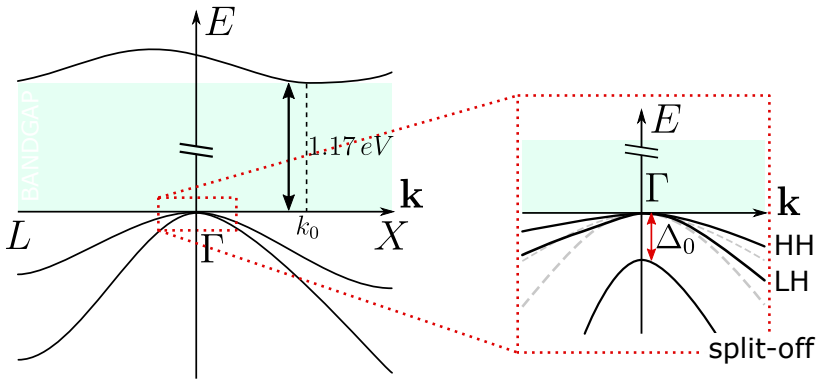

Figure 1.5 – **Bulk silicon band structure schematic:** Left panel shows the band structure of bulk silicon in absence of spin-orbit coupling. Valence and conduction bands are 6-fold degenerate respectively at Γ and k_0 points. Silicon crystal manifests an indirect bandgap of 1.17 eV. Right panel is a focus on the valence band nearby the Γ point, where the $\mathbf{k}\cdot\mathbf{p}$ model is valid. Gray dashed lines depict the case in absence of spin-orbit coupling. SOC lifts the valence band degeneracy : leaving spin states $j = 1/2$ as the lowest band (called split-off), and fourfold degenerate band, made of (i) $j = 1/2$ states at corresponding energy $-2\Delta_0/3$ and (ii) $j = 3/2$ at $\Delta_0/3$. The energy splitting is about 44 meV. Figure adapted from ref.[39].

1.4 *g*-matrix formalism

Nowadays, and despite the growing interest towards such technology, hole spin qubit physics remain challenging to apprehend. Having an estimation of the particle *g*-factor would help to deeply understand the relevant mechanisms and would constitute a useful asset for modelling. Unfortunately, the *g*-matrix is experimentally hard to reconstruct as the working two level basis is hardly explicit [39, 52]. In this scope, *g*-matrix formalism aims at bridging the gap between theoretical models and experimental measurements by introducing a *G*-tensor quantity. In the linear response regime, this formalism relates to measurable quantities (such as Larmor or Rabi frequencies) and provides a way to indirectly estimate the system *g*-matrix. The following discussion focuses on the theoretical derivations to capture the charge noise variations studied later on in chapter 3.

1.4.1 Landé factor for holes

Holes exhibit strong spin-orbit coupling leading to anisotropic response in magnetic field orientation [53, 54, 55, 34, 56]. This comes along with a particular Landé factor (or *g*-factor), which -unlike electrons- is a real 3×3 matrix that depends on the particle confinement and strain. As a consequence, the hole spin does not necessarily align with the external magnetic field. Its behaviour can be expressed by the following Hamiltonian:

$$\mathcal{H} = \mathcal{H}_{LK} + \mathcal{H}_Z + \mathcal{H}_{SO} + \mathcal{H}_{HF} + V_{\text{conf}} \tag{1.16}$$

with

$\mathcal{H}_{LK}$ *the Luttinger-Kohn Hamiltonian (see section 1.3.2),*

$\mathcal{H}_{Z}$ *The Zeeman Hamiltonian (see section 1.2.1),*

$\mathcal{H}_{SO}$ *the spin-orbit Hamiltonian, created by nearby moving charges (see section 1.2.3),*

$\mathcal{H}_{HF}$ *the hyperfine interactions Hamiltonian (section 1.2.3),*

V_{conf} *the confinement potential.*

Such Hamiltonian $\mathcal{H}$ can be approximated using the g-matrix formalism, which assumes a linear-response from spin qubit to magnetic and electric fields [39]. Considering the two lowest eigenstates of the Hamiltonian as the pseudo-spin basis $\mathcal{B} = \{|\uparrow\rangle, |\downarrow\rangle\}$, the system is described as:

$$\mathcal{H} \simeq \frac{1}{2}\mu_B \boldsymbol{\sigma} \cdot g\,\mathbf{B} \tag{1.17}$$

Importantly enough, the g-matrix depends on the eigenbasis and on the axes for the magnetic field X, Y, Z. When taking into account the possible basis change between the magnetic axes and the principal spin axes, g can be decomposed into singular values as:

$$g = U\tilde{g}W^{\mathrm{T}}, \tag{1.18}$$

with

$\tilde{g} = \mathrm{diag}(g_1, g_2, g_3)$ *is a diagonal matrix with* g_1, g_2, *and* g_3 *elements being the "principal" g-factors,*

W *a unitary matrix whose columns denoted* $(\boldsymbol{w}_X, \boldsymbol{w}_Y, \boldsymbol{w}_Z)$ *define the principal magnetic axes,*

U *a unitary matrix acting on the spin Hilbert space. As the spin does not align with magnetic field,* U *can be associated with a rotation* $R(U)$ *in the two-level subspace* $|\downarrow\rangle$ *(resp.* $|\uparrow\rangle$*)* $\xrightarrow{R}$ $|\tilde{\downarrow}\rangle$ *(resp.* $|\tilde{\uparrow}\rangle$*).*

In order to describe the spin behaviour in magnetic field orientation without the loss of generality, we define the Zeeman tensor G as follow:

$$(E_Z)^2 = \mu_B^2\, \mathbf{B}^{\mathrm{T}} \cdot G \cdot \mathbf{B} \quad \text{such that} \quad G = g^{\mathrm{T}} g \tag{1.19}$$

with

G *a symmetrical positive tensor, having eigenvalues* (g_1^2, g_2^2, g_3^2).

Inserting equation 1.18 into the G-tensor definition gives : $G = W\tilde{g}^2 W^{\mathrm{T}}$. This G tensor description allows the g matrix variations (squared) to be conveyed while being independent of the choice of magnetic field axes. Indeed, a unitary transformation applied to g-matrix would let the G-tensor invariant. By construction,

the Zeeman tensor eigenvalues are therefore the squares of the principal g-factors so that $\text{eigvals}(G_i) = \text{eigvals}(g_i)^2$, and its eigenvectors are the magnetic axes. Experimentally, G is an observable that can be reconstructed by at least six measurements of the Zeeman splitting in magnetic field orientations [39, 50, 52]. Using this formalism, the Larmor vector $\boldsymbol{\omega}_L$ reads as : $\hbar\boldsymbol{\omega}_L = \mu_B\sqrt{\mathbf{B}^{\mathrm{T}}\cdot G\cdot\mathbf{B}}$.

1.4.2 Derivation of charge noise contributions

Hole wavefunction confinement is mainly governed by the system electrostatics (gate potentials), thus defining the g-matrix. Fluctuations of this electric potential inherently affects this g-matrix. Such modifications can be derived at first order around a reference voltage V_0 as: $g(V) = g(V_0) + g'(V_0)\delta V$. Note that the prime notation stands for the first derivative of a quantity with respect to electric potential. The Hamiltonian in equation 1.17 becomes:

$$\mathcal{H}(V_0+\delta V) = \frac{1}{2}\mu_B\left(g(V_0)+g'(V_0)\delta V\right)\cdot\mathbf{B}\cdot\boldsymbol{\sigma} \tag{1.20}$$

To have a deeper understanding of the charge noise contribution on the spin dynamics, it is relevant to separate it as a longitudinal ($\beta_\parallel$) and a transverse ($\beta_\perp$) term leading to [39]:

$$\boxed{\mathcal{H}(V_0+\delta V) = \omega_L\cdot\boldsymbol{\sigma}_\parallel + \delta V\frac{\mu_B}{2\hbar}B\left(\beta_\parallel\cdot\boldsymbol{\sigma}_\parallel+\beta_\perp\cdot\boldsymbol{\sigma}_\perp\right)} \tag{1.21}$$

with the corresponding definitions,

$$\begin{cases}\beta_\parallel = \left(g'(V_0)\cdot\mathbf{b}\right)\cdot\mathbf{n}\\ \beta_\perp = \left|\left(g'(V_0)\cdot\mathbf{b}\right)\times\mathbf{n}\right|\end{cases} \tag{1.22}$$

with

$\boldsymbol{b} = \boldsymbol{B}/||B||$ *the magnetic field orientation,*

$\boldsymbol{n} = g\cdot\boldsymbol{B}/||g\cdot\boldsymbol{B}||$ *the normalized Larmor vector.*

The longitudinal component $\beta_\parallel$ represents the Larmor frequency modulation. In other words, the longitudinal fluctuations induced by charge noise can be seen as a slight change in the Zeeman energy needed to promote spin transition. Besides, the transverse component $\beta_\perp$ acts as a modulation of the precession axis [49, 53, 57]. The Rabi frequency can be derived from perpendicular contribution as further discussed in section 1.4.2. Figure 1.6 illustrates the participating terms from voltage fluctuations induced by charge noise.

As a result, the voltage fluctuations δV can change the norm of the Larmor vector and/or its orientation (causing spin-flip events, thus modifying the qubit Rabi frequency). The following sections aim at relating both longitudinal and transverse contributions to experimentally measurable quantities (e.g. Larmor and Rabi frequencies) using the g-matrix formalism.

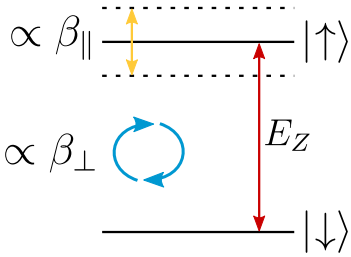

Figure 1.6 – **Longitudinal and Transverse contributions of charge noise:** The Zeeman energy, denoted E_Z, being the needed energy to promote spin transition from ground ($|\downarrow\rangle$) to excited ($|\uparrow\rangle$) state, is embodied by the red arrow. The longitudinal contribution (yellow arrow) of charge noise acts as a modulation of the Zeeman energy, whereas the transverse one (blue arrow) modifies the precession axis. Figure adapted from reference [49].

Longitudinal Spin Electric Susceptibility (LSES)

Longitudinal spin susceptibility to charge perturbation results in a modulation of the Zeeman tensor G (for electrically coupled fluctuators) and a magnetic field modulation (for magnetically coupled fluctuators such as nuclear spins). Hole spin qubits primarily couple electrically to fluctuators due to their strong SOC [50]. Therefore, as a first assumption, we discard the hyperfine contribution and only consider charge noise. Spin response to nearby charge movements thus boils down to a Longitudinal Spin Electric Susceptibility (LSES). From equation 1.4.1, the first derivative of Larmor vector compared to voltage is:

$$\boxed{f'_L = \frac{\mu_B B}{h}\beta_{\parallel} = \frac{\mu_B B}{h}\frac{\mathbf{b}^{\mathrm{T}}\cdot G'\cdot\mathbf{b}}{2\sqrt{\mathbf{b}^{\mathrm{T}}\cdot G\cdot\mathbf{b}}}} \tag{1.23}$$

From the definition of G, the derivative G' can be expressed as the sum of two modulations:

$$\begin{aligned} G' &= \frac{\partial}{\partial V}\left(W\tilde{g}^2 W^{\mathrm{T}}\right) \\ &= W\frac{\partial\tilde{g}^2}{\partial V}W^{\mathrm{T}} + \frac{\partial W}{\partial V}\tilde{g}^2 W^{\mathrm{T}} + \text{transpose} \end{aligned} \tag{1.24}$$

First term accounts for the modifications of the principal g-factors, whereas the rest of equation results in the modulation of the principal magnetic axes $(\mathbf{w}_X, \mathbf{w}_Y, \mathbf{w}_Z)$ [6]. The G' tensor can be fully reconstructed by measuring the Larmor displacement with respect to voltage at least in 9 different orientations of magnetic field and provides valuable information on the spin-orbit coupling mechanisms at stake in the system.

About the relation to coherence time:
As shown in previous sections, fluctuations induced by nearby charges undoubtedly

6. Complete calculations can be found in ref.[50].

affects the Larmor frequency. The system therefore accumulates an additional phase term over a time t which is directly proportional to the variation of f_L with respect to a perturbation quantity V, hereafter denoted f'_L as:

$$\Delta\Phi(t) = 2\pi f'_L(0) \times \int_0^t dt' V(t') \tag{1.25}$$

with

$\Delta\Phi(t)$ *the phase shift compared to free precession over a time* t,

$f'_L(0)$ *the variation of Larmor vector when considering no perturbation.*

Such phase deviation may be directly linked to spin decoherence. Considering the simple model of voltage fluctuation having a power spectrum $\propto 1/f$, the resulting pure dephasing time is [58]:

$$\frac{1}{T_2^*} = \sqrt{2}\pi V^{\mathrm{rms}} |f'_L(0)| \tag{1.26}$$

with

V^{rms} *the Root Mean Square (RMS) fluctuations of voltage* V.

Gate voltages shape the electrostatic potential experienced by the hole and thus affect its wavefunction, the aforementioned G-tensor. In practice, slight variations of nearby electric fields alter the latter G-tensor, that can be experimentally probed by measurements of the Larmor vector with respect to gate voltage fluctuations. We can define the LSES quantity so as to capture the influence of electric field modifications onto the hole spin as:

$$\mathrm{LSES}(G_n) = \frac{\partial f_L}{\partial V_{G_n}} \tag{1.27}$$

with

V_{G_n} *being the voltage setting of gate* n.

The decoherence induced by gate voltages is therefore the sum of all contributions from the N nearby gates, similarly to equation 1.26:

$$\boxed{\frac{1}{T_2^*} = \sqrt{2}\pi \sqrt{\sum_{n=1}^{N} \left(\delta V_{G_n}^{\mathrm{rms}} \, \mathrm{LSES}(G_n)\right)^2}} \tag{1.28}$$

Electric field fluctuations, causing anisotropic modulation of the Larmor vector with respect to magnetic field orientation, are responsible for qubit decoherence. This has been recently investigated experimentally, evidencing particular magnetic field orientations named sweetspots, at which the spin qubit is insensitive to first-order gate voltage fluctuations. Minimizing surrounding gate voltages fluctuations

(higher order terms of LSES) demonstrated a hole spin qubit with enhanced coherence time about 88 µs [29] in natural silicon nanowire.

Though, theory predictions indicate that the nature of sweetspots might also be extended into a continuous line of magnetic field orientations, also called sweetline [49, 50]. A particular focus will be held on the evidence of such dephasing sweetline in chapter 3. The existence of sweetlines can be figured out by computing the eigenvalues of the previously discussed G'-tensor. Different geometry of sweetspots with respect to G' eigenvalues is given is table 1.2.

Signs of the G'_i	Sweetspot nature
(0, 0, 0)	Unit sphere
(0, 0, +) (0, 0, −)	1 Sweet line
(0, +, +) (0, −, −)	2 Sweet points
(0, +, −)	2 Sweet lines
(+, +, −) (−, −, +)	2 Sweet lines
(+, +, +) (−, −, −)	None

Table 1.2 – **Possible geometrical nature of dephasing sweetspots:** The first column showcases the possible sign configuration of G' eigenvalues. Second column is the geometrical nature of sweetspot orientations. Table adapted from [50].

Transverse Spin Electric Susceptibility (TSES)

As briefly alluded, the transverse contribution of charge noise affects the qubit Rabi frequency. It can also be denoted Transverse Spin Electric Susceptibility (TSES). In this case, the Rabi frequency can be expressed as follow:

$$\boxed{f_R = \frac{\mu_B}{2h} B\, V_{ac}\, \beta_\perp = \frac{\mu_B}{2h|g|} B\, V_{ac}\, |(g\mathbf{b}) \times (g'\mathbf{b})|} \tag{1.29}$$

with

V_{ac} *the driving amplitude.*

Equation 3.9 highlights the dependency between the variations of G' and the modulations of the main g-factors and the magnetic axes. For sake of clarity, G' can also be written as:

$$G' = g^{\mathrm{T}} \cdot g' + (g')^{\mathrm{T}} \cdot g \tag{1.30}$$

From this equation, we understand that the G' variation does not fully capture the system response g' due to charge fluctuations. Indeed, $G' = 0$ does not necessarily

imply that $g' = 0$. For this reason, using the g-matrix formalism to apprehend the Rabi frequency variation appears more difficult than for the Larmor vector. To this aim, we distinguish two driving mechanisms to describe the g-matrix changes:

$$g' = g'_{\mathrm{TMR}} + g'_{\mathrm{IZR}} \tag{1.31}$$

with the corresponding definitions:

$$\begin{cases} g'_{\mathrm{TMR}} = (g^{\mathrm{T}})^{-1} \cdot S = (g^{\mathrm{T}})^{-1} \cdot \dfrac{G'}{2} \\ g'_{\mathrm{IZR}} = (g^{\mathrm{T}})^{-1} \cdot A \end{cases} \tag{1.32}$$

with

$$g^{\mathrm{T}} \cdot g' = A + S \text{ with } A(S) \text{ a } 3 \times 3 \text{ anti-symmetric (symmetric) matrices.}$$

When the magnetic axes remain unaltered upon volage modulations, only the g'_{TMR} subsists, and the g'-matrix can be reconstructed by the means of G and G' tensors. This particular case is named Tensor Modulation Resonance (TMR) and is illustrated in figure 1.7(a). In this case, the confinement potential is modulated by an electrical drive, changing the hole wavefunction shape while leaving the hole wavefunction position unchanged.

On the contrary, when the main magnetic axes are modified, a second driving mechanism -called Iso-Zeeman Resonance (IZR)- enters into play. Here, the electrical drive induces a shift of the confinement potential which, in turn, causes the hole wavefunction to move without changing its overall shape. Such driving mechanism is depicted in figure 1.7(b).

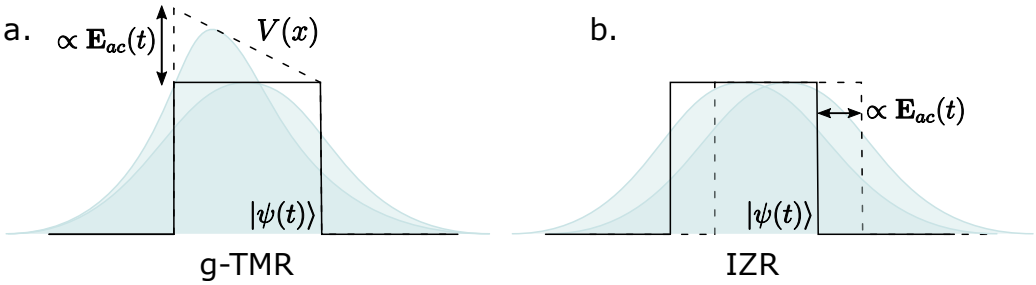

Figure 1.7 – **Driving mechanisms induced by an oscillating electric field:** (a) The hole wavefunction ($\psi(t)$) shape is modified due to slanting electric field $\mathbf{E}_{ac}$ causing the modulation of main g-factors. This is g-TMR effect. (b) The excitation field displaces the confinement potential $V(x)$, thus the hole wavefunction, without modifying its shape. This mechanism is known as iso-Zeeman resonance (IZR). Both driving mechanisms induce spin rotation and contribute to the Rabi frequency.

Both mechanisms coexist and contribute to the Rabi frequency as : $\mathbf{f}_R \propto (\mathbf{f}_{\mathrm{TMR}}, \mathbf{f}_{\mathrm{IZR}})$. Experimental characterizations of Rabi frequency anisotropy in magnetic field have already been successfully corroborated by theoretical predictions

relying on g-matrix formalism [52, 59]. Such confirmation enables a clear understanding of driving mechanisms at stake for spin rotation.

Reciprocal sweetness:
Longitudinal and transverse contributions respectively participate to hole spin decoherence and operation speed and their relative strength depend on the magnetic field orientation. From the literature, the presence in magnetic field of dephasing sweetspots evidenced a successful cancellation of the longitudinal spin susceptibility. Yet, the gain in coherence time may be irrelevant if it comes along with an overall reduction of the Rabi frequency (stemming from transverse contribution). This trade-off is described by the quality factor Q_2^* that embodies the number of operations before the qubit evolve into a statistical mixture of states:

$$Q_2^* = 2 f_{\mathrm{R}} T_2^* \tag{1.33}$$

Furthermore, theory [49] predicts that the transverse contribution is expected to vanish where the longitudinal one is maximum and vice-versa. This relation between $\beta_{\parallel}$ and $\beta_{\perp}$ is known as the reciprocal sweetness [49]. In essence, dephasing sweetspot are expected to coincide with maxima of Rabi frequency, therefore maximizing the quality factor Q_2^* for semiconductor spin qubit. Reciprocal sweetness opens the opportunity to a strong enhancement in hole spin quality factor.

1.5 Conclusions

This chapter aimed at detailing mathematical concepts used to describe physics of hole spin qubit hosted within silicon quantum dot. This system displays inherently robust spin-orbit coupling, making it highly responsive to its surrounding environment. Electrical noise contributions, mainly charge noise, have the potential to significantly impair qubit performances. Nevertheless, charge noise exhibits strong anisotropy with respect to magnetic field and can even be cancelled at specific orientations labelled sweetspots. These particular settings revealed enhanced coherence times and are expected to be also fast-operating points for qubit. This further motivates the charge noise characterization with respect to magnetic field and confinement.

References

[1] D. Loss and David P. DiVincenzo. « Quantum computation with quantum dots ». In: *Physical Review A* 57 (1 Jan. 1998), pp. 120–126. DOI: 10.1103/PhysRevA.57.120.

[2] J. M. Elzerman et al. « Single-shot read-out of an individual electron spin in a quantum dot ». In: *Nature* 430.6998 (July 2004), pp. 431–435. DOI: 10.1038/nature02693.

[3] M. Xiao et al. « Electrical detection of the spin resonance of a single electron in a silicon field-effect transistor ». In: *Nature* 430.6998 (July 2004), pp. 435–439. DOI: 10.1038/nature02727.

[4] R. Hanson et al. « Spins in few-electron quantum dots ». In: *Reviews of Modern Physics* 79 (4 Oct. 2007), pp. 1217–1265. DOI: 10.1103/RevModPhys.79.1217.

[5] B. M. Maune et al. « Coherent singlet-triplet oscillations in a silicon-based double quantum dot ». In: *Nature* 481.7381 (2012), pp. 344–347. DOI: 10.1038/nature10707.

[6] R. Ezzouch. « Gate reflectometry as readout and spectroscopy tool for silicon spin qubits ». PhD thesis. June 2021.

[7] L. P. Kouwenhoven et al. « Single electron charging effects in semiconductor quantum dots ». In: *Zeitschrift für Physik B Condensed Matter* 85.3 (Oct. 1991), pp. 367–373. DOI: 10.1007/BF01307632.

[8] L. P. Kouwenhoven, David Guy Austing, and Seigo Tarucha. « Few-electron quantum dots ». In: *Reports on Progress in Physics* 64 (2001), pp. 701–736.

[9] C. Cohen-Tannoudji, Bernard Diu, and Franck Laloë. *Mécanique Quantique - Tome 1*. Ed. by CNRS Editions. Vol. 1. p.415. Les Ulis: EDP Sciences, Dec. 2018. DOI: 10.1051/978-2-7598-2288-1.

[10] F. H. L. Koppens et al. « Driven coherent oscillations of a single electron spin in a quantum dot ». In: *Nature* 442.7104 (Aug. 2006), pp. 766–771. DOI: 10.1038/nature05065.

[11] K. C. Nowack et al. « Coherent Control of a Single Electron Spin with Electric Fields ». In: *Science* 318.5855 (2007), pp. 1430–1433. DOI: 10.1126/science.1148092.

[12] R. Maurand et al. « A CMOS silicon spin qubit ». In: *Nature Communications* (May 2016). DOI: 10.1038/ncomms13575.

[13] M. Pioro-Ladrière et al. « Electrically driven single-electron spin resonance in a slanting Zeeman field ». In: *Nature Physics* 4.10 (Oct. 2008), pp. 776–779. DOI: 10.1038/nphys1053.

[14] L. Chirolli and Guido Burkard. « Decoherence in solid-state qubits ». In: *Advances in Physics* 57.3 (2008), pp. 225–285. DOI: 10.1080/00018730802218067.

[15] P. Stano and Daniel Loss. « Review of performance metrics of spin qubits in gated semiconducting nanostructures ». In: *Nature Reviews Physics* 4.10 (Oct. 2022), pp. 672–688. DOI: 10.1038/s42254-022-00484-w.

[16] F. Bloch. « Nuclear Induction ». In: *Phys. Rev.* 70 (7-8 Oct. 1946), pp. 460–474. DOI: 10.1103/PhysRev.70.460.

[17] A. V. Khaetskii, Daniel Loss, and Leonid Glazman. « Electron Spin Decoherence in Quantum Dots due to Interaction with Nuclei ». In: *Phys. Rev. Lett.* 88 (18 Apr. 2002), p. 186802. DOI: 10.1103/PhysRevLett.88.186802.

[18] E. A. Chekhovich et al. « Nuclear spin effects in semiconductor quantum dots ». In: *Nature Materials* 12.6 (June 2013), pp. 494–504. DOI: 10.1038/nmat3652.

[19] A. V. Khaetskii and Yuli V. Nazarov. « Spin-flip transitions between Zeeman sublevels in semiconductor quantum dots ». In: *Phys. Rev. B* 64 (12 Sept. 2001), p. 125316. DOI: 10.1103/PhysRevB.64.125316.

[20] Y. Fang et al. « Recent advances in hole-spin qubits ». In: *Materials for Quantum Technology* 3.1 (Mar. 2023), p. 012003. DOI: 10.1088/2633-4356/acb87e.

[21] D. Pines, John Bardeen, and Charles P. Slichter. « Nuclear Polarization and Impurity-State Spin Relaxation Processes in Silicon ». In: *Phys. Rev.* 106 (3 May 1957), pp. 489–498. DOI: 10.1103/PhysRev.106.489.

[22] R. Zhao et al. « Single-spin qubits in isotopically enriched silicon at low magnetic field ». In: *Nature Communications* 10.1 (Dec. 2019), p. 5500. DOI: 10.1038/s41467-019-13416-7.

[23] B. Hensen et al. « A silicon quantum-dot-coupled nuclear spin qubit ». In: *Nature Nanotechnology* 15.1 (Jan. 2020), pp. 13–17. DOI: 10.1038/s41565-019-0587-7.

[24] Z. Wang et al. « Optimal operation points for ultrafast, highly coherent Ge hole spin-orbit qubits ». In: *npj Quantum Information* 7.1 (Apr. 2021), p. 54. DOI: 10.1038/s41534-021-00386-2.

[25] H. Bluhm et al. « Dephasing time of GaAs electron-spin qubits coupled to a nuclear bath exceeding 200 μs ». In: *Nature Physics* 7.2 (Feb. 2011), pp. 109–113. DOI: 10.1038/nphys1856.

[26] C. Testelin et al. « Hole–spin dephasing time associated with hyperfine interaction in quantum dots ». In: *Phys. Rev. B* 79 (19 May 2009), p. 195440. DOI: 10.1103/PhysRevB.79.195440.

[27] N. W. Hendrickx et al. *Sweet-spot operation of a germanium hole spin qubit with highly anisotropic noise sensitivity*. arXiv. 2023. DOI: 10.48550/arXiv.2305.13150.

[28] S. Bosco and Daniel Loss. « Fully Tunable Hyperfine Interactions of Hole Spin Qubits in Si and Ge Quantum Dots ». In: *Phys. Rev. Lett.* 127 (19 Nov. 2021), p. 190501. DOI: 10.1103/PhysRevLett.127.190501.

[29] N. Piot et al. « A single hole spin with enhanced coherence in natural silicon ». In: *Nature Nanotechnology* 17.10 (Sept. 2022), pp. 1072–1077. DOI: 10.1038/s41565-022-01196-z.

[30] G. Dresselhaus. « Spin-Orbit Coupling Effects in Zinc Blende Structures ». In: *Phys. Rev.* 100 (2 Oct. 1955), pp. 580–586. DOI: 10.1103/PhysRev.100.580.

[31] L. E. Golub and E. L. Ivchenko. « Spin splitting in symmetrical SiGe quantum wells ». In: *Phys. Rev. B* 69 (11 Mar. 2004), p. 115333. DOI: 10.1103/PhysRevB.69.115333.

[32] G. L. Bir et al. *Symmetry and strain-induced effects in semiconductors*. eng. New York: Wiley New York, 1974.

[33] R. Ferdous et al. « Valley dependent anisotropic spin splitting in silicon quantum dots ». In: *npj Quantum Information* 4.1 (June 2018), p. 26. DOI: 10.1038/s41534-018-0075-1.

[34] T. Tanttu et al. « Controlling Spin-Orbit Interactions in Silicon Quantum Dots Using Magnetic Field Direction ». In: *Physical Review X* 9 (2 May 2019), p. 021028. DOI: 10.1103/PhysRevX.9.021028.

[35] E. A. Rodriguez-Mena et al. « Linear-in-momentum spin orbit interactions in planar Ge/GeSi heterostructures and spin qubits ». In: *Physical Review B* 108.20 (Nov. 2023). DOI: 10.1103/physrevb.108.205416.

[36] L. A. Terrazos et al. « Theory of hole-spin qubits in strained germanium quantum dots ». In: *Phys. Rev. B* 103 (12 Mar. 2021), p. 125201. DOI: 10.1103/PhysRevB.103.125201.

[37] R. Hanson et al. « Zeeman Energy and Spin Relaxation in a One-Electron Quantum Dot ». In: *Phys. Rev. Lett.* 91 (19 Nov. 2003), p. 196802. DOI: 10.1103/PhysRevLett.91.196802.

[38] S. Amasha et al. *Measurements of the spin relaxation rate at low magnetic fields in a quantum dot*. 2006.

[39] B. Venitucci. « Modélisation de la manipulation électrique des qubits de trou dans le silicium ». Theses. Université Grenoble Alpes (2020), Nov. 2020.

[40] H. Watzinger et al. « A germanium hole spin qubit ». In: *Nature Communications* 9.1 (2018), p. 3902. DOI: 10.1038/s41467-018-06418-4.

[41] N. W. Hendrickx et al. « A single-hole spin qubit ». In: *Nature Communications* 11.1 (July 2020), p. 3478. DOI: 10.1038/s41467-020-17211-7.

[42] B. Voisin et al. « Electrical Control of g-Factor in a Few-Hole Silicon Nanowire MOSFET ». In: *Nano Letters* 16.1 (Jan. 2016), pp. 88–92. DOI: 10.1021/acs.nanolett.5b02920.

[43] M. F. Gonzalez-Zalba et al. « Scaling silicon-based quantum computing using CMOS technology ». In: *Nature Electronics* 4.12 (Dec. 2021), pp. 872–884. DOI: 10.1038/s41928-021-00681-y.

[44] E. Kawakami et al. « Electrical control of a long-lived spin qubit in a Si/SiGe quantum dot ». In: *Nature Nanotechnology* 9.9 (Sept. 2014), pp. 666–670. DOI: 10.1038/nnano.2014.153.

[45] M. Veldhorst et al. « An addressable quantum dot qubit with fault-tolerant control-fidelity ». In: *Nature Nanotechnology* 9.12 (Dec. 2014), pp. 981–985. DOI: 10.1038/nnano.2014.216.

[46] M. Veldhorst et al. « A two-qubit logic gate in silicon ». In: *Nature* 526.7573 (Oct. 2015), pp. 410–414. DOI: 10.1038/nature15263.

[47] A. Corna et al. « Electrically driven electron spin resonance mediated by spin–valley–orbit coupling in a silicon quantum dot ». In: *npj Quantum Information* 4.1 (Feb. 2018), p. 6. DOI: 10.1038/s41534-018-0059-1.

[48] J. Yoneda et al. « A quantum-dot spin qubit with coherence limited by charge noise and fidelity higher than 99.9% ». In: *Nature Nanotechnology* 13.2 (2018), pp. 102–106. DOI: 10.1038/s41565-017-0014-x.

[49] V. P. Michal et al. « Tunable hole spin-photon interaction based on g-matrix modulation ». In: *Phys. Rev. B* 107 (4 Jan. 2023), p. L041303. DOI: 10.1103/PhysRevB.107.L041303.

[50] Lorenzo Mauro et al. « Geometry of the dephasing sweet spots of spin-orbit qubits ». In: *Phys. Rev. B* 109 (15 Apr. 2024), p. 155406. DOI: 10.1103/PhysRevB.109.155406.

[51] J. M. Luttinger and W. Kohn. « Motion of Electrons and Holes in Perturbed Periodic Fields ». In: *Phys. Rev.* 97 (4 Feb. 1955), pp. 869–883. DOI: 10.1103/PhysRev.97.869.

[52] A. Crippa et al. « Electrical Spin Driving by g-Matrix Modulation in Spin-Orbit Qubits ». In: *Physical Review Letters* 120.13 (Mar. 2018), p. 137702. DOI: 10.1103/physrevlett.120.137702.

[53] Y. Kato et al. « Gigahertz Electron Spin Manipulation Using Voltage-Controlled g-Tensor Modulation ». In: *Science* 299.5610 (2003), pp. 1201–1204. DOI: 10.1126/science.1080880.

[54] N. Ares et al. « Nature of Tunable Hole g Factors in Quantum Dots ». In: *Physical Review Letters* 110 (4 Jan. 2013), p. 046602. DOI: 10.1103/PhysRevLett.110.046602.

[55] M. Brauns et al. « Electric-field dependent g-factor anisotropy in Ge-Si core-shell nanowire quantum dots ». In: *Phys. Rev. B* 93 (12 Mar. 2016), p. 121408. DOI: 10.1103/PhysRevB.93.121408.

[56] S. D. Liles et al. « Electrical control of the g tensor of the first hole in a silicon MOS quantum dot ». In: *Phys. Rev. B* 104 (23 Dec. 2021), p. 235303. DOI: 10.1103/PhysRevB.104.235303.

[57] B. Venitucci et al. « Electrical manipulation of semiconductor spin qubits within the g-matrix formalism ». In: *Phys. Rev. B* 98 (15 Oct. 2018), p. 155319. DOI: 10.1103/PhysRevB.98.155319.

[58] G. Ithier et al. « Decoherence in a superconducting quantum bit circuit ». In: *Phys. Rev. B* 72 (13 Oct. 2005), p. 134519. DOI: 10.1103/PhysRevB.72.134519.

[59] V. P. Michal, Benjamin Venitucci, and Yann-Michel Niquet. « Longitudinal and transverse electric field manipulation of hole spin-orbit qubits in one-dimensional channels ». In: *Phys. Rev. B* 103 (4 Jan. 2021), p. 045305. DOI: 10.1103/PhysRevB.103.045305.

CHAPTER 2

Experimental setup

The choice of spin qubit within silicon (Si) QDs platform is motivated by two reasons. First, the long spin coherence times (few µs in natural Si) [1] and second the potential scalability offered by well-known fabrications steps inherited from microelectronics industry. Maune *et al.* [2] primarily demonstrated the possible operation of an electron spin qubit in a Si transistor-like architecture, soon followed by the equivalent demonstration using holes in a nanowire [3]. This chapter stands as an introduction to experimental measurements and aims to pinpoint the specificities to operate a single hole spin qubit in a Si-nanowire architecture. Fabrication processes are the first focus before reaching up to preliminary room temperature characterization of the sample. As low temperatures are necessary for quantum measurements, we specify the wiring and connections inside the dilution cryostat. Finally, the emphasis is placed on the readout method consisting of dispersive probing of capacitive changes by radio-frequency reflectometry.

Contents

2

2.1 Si-MOS structure devices

Spin qubit in semiconductor QD can be implemented in various structures, the most acknowledged being layered heterostructures. Such devices early hit many quantum computing milestones such as high fidelity single- and multiple-qubit gate operations [4] in GaAs/AlGaAs. In the scope of large-scale quantum processor, adapted silicon structure has emerged as a promising candidate, because it leverages on well-established fabrication processes inherited from industry [5, 6, 7]. The principal candidate coming to light is silicon Metal-Oxide-Semiconductor (MOS), which can be separated in different categories: planar quantum dots [8], fin-field-effect transistors (Fin-FET) [9] and Si-MOS nanowire devices [3]. The latter technology will be the further focus of this manuscript.

Si-MOS nanowire structures are defined by a silicon channel, within which the electrostatic potential is shaped by an overlapping metallic gate, tailoring the current flow. At low temperatures, the gate is used to electrostatically induce the formation of quantum dot(s), whose charge filling is regulated by the means of Si_xN_y spacers acting as tunnel barriers [10]. The nanowire (NW) and the gate are capacitively coupled via an oxide insulator sandwiched in between the two. Numerous gate stack and nanowire geometry exist [3, 11, 12], both affecting the particle wavefunction [11, 13, 14]. The following section describes the standard fabrication steps to form Si-MOS nanowire devices, which are, in this manuscript, fabricated by the CEA-LETI.

2.1.1 Device fabrication steps

Device fabrication starts with a 300 mm wafer made of an intrinsic silicon film on top of an insulating layer (SOI technology from SOITEC) and natural silicon. This insulating layer is a 145 nm thick buried silicon dioxide (BOX), which strongly reduces current leakage to the substrate and constitutes a spatial boundary for carriers confinement. Top silicon layer, from 8 to 20 nm height, is shaped into narrow channels by deep UV lithography, optionally followed by trimming process to further reduce the nanowire dimensions down to few tens of nanometers [5, 15].

The gate stack consists of i) a thermally grown SiO_2 of about 5 nm [1], ii) 5 nm

1. This step slightly consumes the silicon nanowire by a ratio 1:3 nm.

of deposited TiN and iii) a 50 nm layer of heavily doped poly-silicon. Such metal gates are patterned using e-beam lithography to achieve a gate pitch below 100 nm. Importantly enough, the gate pitch must be minimum as it defines the spatial distance between quantum dots, and thus the wavefunction overlap, crucial requirement for multiple qubit operation using spin exchange interaction. Recent process improvements in Si-MOS fabrication facilities permit a second gate layer also referred as "trench gate", which intend to control the tunnelling rates between QDs [15]. The number of gates can easily be changed at convenience. The following figure 2.1(a) is a schematic view along the nanowire, revealing the aforementioned gate-stack and layers in the case of a three gates P-doped device. Panel (b) is a Transmission Electron Microscope (TEM) image of a real Si-MOS device with 3 gates in series, connected to charge reservoirs (source S and drain D).

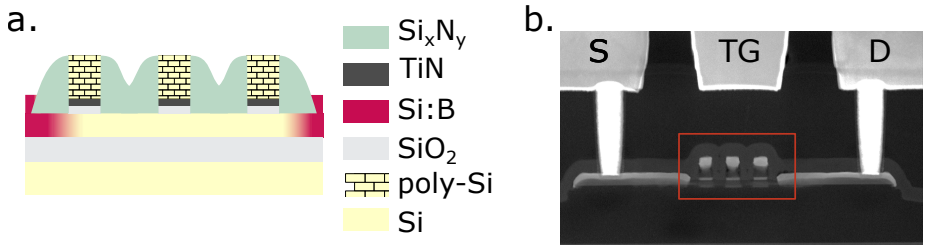

Figure 2.1 – **Schematics of the gate-stack of Si-MOS device and TEM image:** (a) Illustration of cut along the silicon nanowire for a three-gate, P-doped device. For sake of clarity, the NiPtSi alloy is not displayed on top of the device. Adapted from [16]. (b) TEM image of a 3-gates device provided by the LETI. S and D refers to the doped contacts, labelled Source and Drain. Central contact (TG) is a Top Gate (or metal line), aiming to modify the overall device electrostatics. Red frame represents the region sketched in panel (a).

On top of previously described gate-stack, it is important to deposit Si_xN_y spacers for two main purposes. First, to isolate the gates from neighbouring ones, in order to independently form and address a single quantum dot. Second, to cover the silicon nanowire before ion implantation step. Spacers thus create a modulation of doping along the nanowire, that act as fixed tunnel barrier for charges [10]. However, spacers are known to introduce a high density of charge traps and disorder, that can be detrimental to spin operation afterwards especially in the few particles regime [17].

In the device presented hereafter, Boron atoms are implanted and then thermally activated. This doping step therefore creates reservoirs of holes at the wire extremities, whose contacts are named Source and Drain. As the carriers are positively charged, the device is also labelled PMOS (P stands for Positive). Same doping using Phosphorus or Arsenic atoms can be done, resulting in a NMOS device used for electron accumulation.

Final stage is metallizing all contacts (gates and reservoirs) by deposition of NiPt. This forms a silicide alloy of NiPtSi that reduces the contact resistance [2]. Over the years, Si-MOS devices demonstrated abilities for hole spin manipulation using these aforementioned fabrication processes [3, 18, 19, 20, 21, 22]. Similar processes have also shown ambivalent doping, allowing to use both electron and hole sytems [23].

2.1.2 Description of split-gate device

The device studied in this manuscript slightly differs from the process flow described in the previous section. Indeed, as illustrated by figure 2.2(a) and the corresponding zoom in panel (b), gates are not wrapped around the nanowire, but are split on the top and can be independently controlled. Before spacers deposition, gates are thereupon split in two by etching a gap parallel to the silicon channel. Then, next fabrication steps remain unchanged. This architecture is supposed to allow for a stronger spatial confinement of hole, and will be hereafter also referred as a "split" geometry. On the contrary, when gates are overlapping entirely the nanowire, it is named "pump" structure as in references [3, 22]. Figure 2.2(c) illustrates the shallow gate overlap onto the nanowire by a TEM image after spacer deposition step.

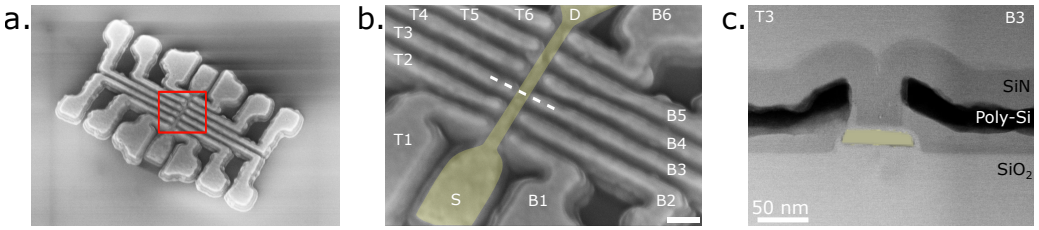

Figure 2.2 – **SEM and TEM images of the 6-split gate device:** (a) Tilted SEM image of a Si-MOS device taken after the spacer etching fabrication step. (b) Zoomed and false coloured SEM image of the area framed in red in panel (a). Silicon nanowire (yellow) is partly overlapped by 12 gates (in gray). Source (drain) contacts are labelled S (D). Scale bar is 100 nm. (c) TEM image taken across the nanowire, as illustrated by the white dashed line in panel (b). This reveals the weak overlap of the gates on the nanowire (yellow).

The device presented in chapters 3 and 4 is a 6 split-gate structure. The gate pitch is 80 nm, and the silicon channel width is 40 nm. The gap separating two gates on each side of the nanowire is 40 nm as well. As the NW width and the gap between facing gates are the same, a slight misalignment of the fabrication masks may consequently result in some gates that do not overlap the Si-channel. This possibility is not excluded in the device presented in the next chapters as images

2. Interested reader may find more details on fabrication steps in reference [16].

of 2.2 are made from another chip from the same batch.

From Source to Drain contacts, gates on Top side of the nanowire are labelled T_i with i their respective position, same for the Bottom gates which are named B_i. A metallic gate lying 180 nm above the whole device is designed to globally shape the electrostatic landscape, as presented in figure 2.1(b).

2.1.3 Room temperature characterization

At room temperature, there is no quantum effect, thus each gate of the system is expected to act as a normal transistor. Beyond a voltage threshold, the current can flow throughout the device, otherwise it is blocked. Before any further measurement at low temperatures, it is necessary to check whether each gate behave as such. To this aim, I-V characteristic is evaluated for each gate of the aforementioned 6-split device, as presented in figure 2.3. Gate voltages are controlled using a Digital to Analog Converter (DAC) connected with filtered DC lines[3].

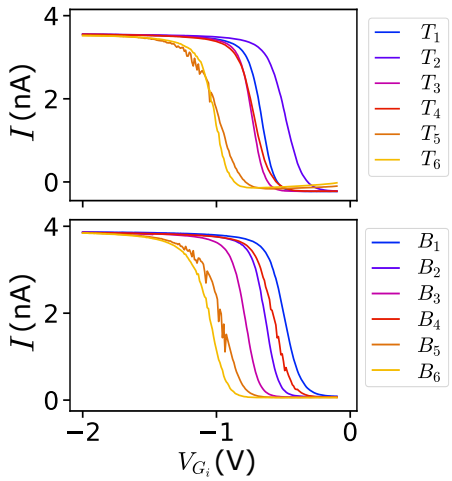

Figure 2.3 – **Room temperature characterization of 6 split gates device:** Top panel presents the I-V characteristic of top gates (labelled T_i with $i \in [1, 2, 3, 4, 5, 6]$). Upon sweeping voltage of gate j, other gates $T_{i\neq j}$ are set at -2 V. In the meantime, gates B_i remain at 0 voltage. A bias voltage is applied between S and D such that $V_{\mathrm{SD}} = 10$ mV. Bottom panel is the I-V characteristic when sweeping B_i gate voltages using the same procedure.

To probe the gate response $I = f(V_{T_i})$, all $T_{j\neq i}$ are kept opened at -2 V allowing for current flow, whilst all B-gates remain in the blocked regime at 0 V. In addition, a bias of 10 mV is applied between source and drain contacts. Gate voltage V_{T_i} is swept from 0 to -2 V so as to overreach the gate threshold (expected around -700 mV), in this particular case, the current flows. I-V response

3. This is further explained in section 2.2.1.

is measured by an Agilent DMM 34410A connected to the drain after being amplified by a Femto amplifier DLPCA-200 with a gain set to $10^7\,\mathrm{V/A}$. Measurement is performed for all gates, revealing a certain variability in gate threshold from about $-500\,\mathrm{mV}$ to $-1\,\mathrm{V}$. Such discrepancies may arise from fabrication processes imperfections such as a misalignment of the gates over the nanowire or dopant diffusion on the edge gates. This in turn causes the gates efficiency to set the surface potential to be highly inhomogeneous along the Si-channel. This non-uniformity may presumably remain at low temperatures as a voltage variability for the first hole to enter the QD.

Despite such threshold variability of the gate openings, the device consistently reveal transistor-like feature and can thus be used to perform quantum measurements.

2.2 Setup description for cryogenic measurements

In order to unveil quantum properties of such Si-MOS system, measurements must be performed at cryogenic temperatures, meaning that the temperature stands below the energy quantum $E_c \gg k_B T$, (E_c the dot charging energy). When operating spins, a second condition on the temperature range imposes to use cryogenics temperatures, namely that the temperature remains below the Zeeman splitting : $k_B T \ll \mu_B g B$ (see chapter 3 for details). Consequently, the device is bonded onto a Printed Circuit Board (PCB), named "daughter board" to be cooled down inside a dilution cryostat. The cryostat used in this manuscript is a Triton from Oxford company having a base temperature $T_{\mathrm{base}} \simeq 20\,\mathrm{mK}$ which rises over time (for long-term experiment) up to $T_{\mathrm{meas}} \simeq 85\,\mathrm{mK}$. The fridge is electrically isolated from the building, and is grounded by the Arbitrary Waveform Generator (AWG) instrument.

Quantum properties are fragile, thus a meticulous attenuation (RF) and filtering (DC) of the connections to the device is necessary to mitigate electrical noise stemming from room temperature. The complete setup wiring schematic is displayed in figure 2.5. Next sections aim at describing the different types of connections further used in chapters 4 to 5 and chapter 7.

As already mentioned, the sample is embedded on a PCB: the daughter board. The latter is mounted onto a second PCB, called "mother board". Electrical connections are routed between the two PCBs via an interposer, consisting of vias filled with randomly packed CuBe wires acting as springs. Mother board supports 24 DC and 8 RF lines (with dedicated bias-tees). In addition, the daughter board comprises 4 RF lines, which are both used for qubit manipulation and readout. For sake of clarity, the schematic in figure 2.5 omits the distinction between mother and daughter board. Detailed pictures of the two PCBs are shown in figure 2.4.

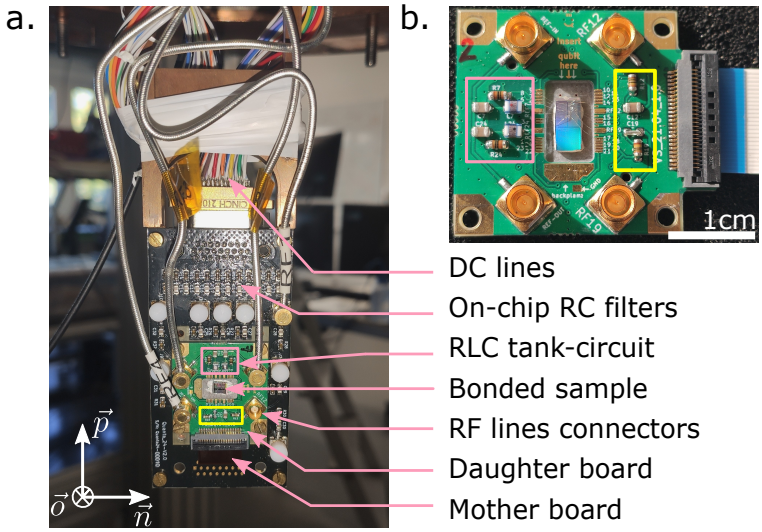

Figure 2.4 – **Photographs of the PCBs:** (a) Combination of mother and daughter boards screwed onto the cold finger of the dilution cryostat. The sample is micro-bonded to Au pads on the daughter board, itself connected to the mother board and the fridge wiring via the interposer (not visible herein). Copper semi-rigid cables are used to bring high-frequency signals onto the PCB. System coordinate is for magnetic field orientation. (b) Daughter board with a bonded sample on it. Pink framed region highlights two RLC embedded tank-circuits used for radio-frequency reflectometry readout (see section 2.3.1). Yellow rectangle points out on-chip bias tees (made of RC circuit).

2.2.1 DC lines

DC gate voltages shaping the electrostatic landscape of the device are biased between $\pm 2\,\mathrm{V}$ by a 16 bits DAC IVVI (from Delft). As the DAC resolution ($\sim 61\,\mu\mathrm{V}$) is not sufficiently high for qubit experiments, two lines have been internally modified and divided by a factor 100, acting as "fine gates" thus allowing for more precise voltage control. Inside the fridge, these DC lines correspond to the gates B_2 and T_3. In addition, the DC connection dedicated to the metal line on the device is internally amplified by a factor of 30 inside the DAC module, so the typical values achievable are around $-10\,\mathrm{V}$. In chapter 5, a DAC BE2142 instrument from Bilt is replacing the IVVI, chosen for its high resolution of 21 bits.

A twisted pair wiring loom with 24 lines connects the DAC (room temperature) to filters at the Mixing Chamber level (MXC$= 20\,\mathrm{mK}$). DC lines are thermalized at each fridge stage. Thereafter, each DC line passes through a silver-epoxy filter having a cut-off frequency $f_{co} \sim 100\,\mathrm{MHz}$. Such filtering both play the role of microwave filter and thermal anchoring [24]. A final stage of RC-filtering is embedded on-PCB and is made of surface mount resistors $R = 2\,\mathrm{k}\Omega$ and capacitors $C = 10\,\mathrm{nF}$ ($f_{co} \sim 220\,\mathrm{kHz}$) before reaching the sample.

2.2.2 RF lines

High-frequency signals are necessary for both Si-MOS spin qubit operation ($\sim$ a few tens of GHz) and readout ($\sim$ hundreds of MHz). The cryostat is equipped with four coaxial cables for Radio-Frequency signals (RF). Except the readout line comprising a superconducting cable, all lines are attenuated throughout the fridge plates and thermally anchored. We differentiate two types of high-frequency lines: two are used for qubit manipulation, and the rest to perform readout measurements.

On the one hand, qubit manipulation lines, both attenuated by 40 dB in total, are connected to gates T_3 and T_4 by 2.2 mm wide stainless steel cables. Gate voltage pulses in addition to microwave (MW) tone can be sent to the device. Sinusoidal MW signals are generated by a vector source SMW200A from Rohde&Schwarz, whose frequency can reach up to 20 GHz. Voltage pulses are produced by an AWG 5208 from Tektronix. Both signals are combined to the same physical line by room temperature diplexers ZDSS-3G4GS+ from Mini Circuits. At the mixing chamber level, on-chip bias-tees combine the RF and the DC signals. Such combiners wired to gate T_3 (resp. T_4) are made of a resistor $R_{T_3,T_4} = 1\,\mathrm{M\Omega}$ and a capacitor $C_{T_3} = 10\,\mathrm{nF}$ (resp. $C_{T_4} \simeq 0\,\mathrm{nF}$). In the particular case of gate T_4, the signal passes through a PicoSecond PulseLab DC block 5509-222-224 before the bias-tee, hence no additional capacitor is needed. This prevents spurious DC voltage leakages stemming from the DC lines.

On the other hand, RF lines are used for qubit readout performed by Radio-frequency Reflectometry in the few hundreds of MHz range. The signal is generated and demodulated by a lock-in UHF-Li from Zurich Instruments. Readout signal is first filtered by high-pass (HP whose cut-off frequency is 250 MHz) and low-pass (LP : cut-off frequency about 650 MHz) components from Mini Circuits before being attenuated by 96 dB along the cryostat plates for thermalization purposes. On the PCBs, the transmission line is multiplexed and serves two resonators for reflectometry readout (see section 2.3.1). In short, each resonator consists in a RLC tank-circuit, either connected to the Source or to the Drain contact. Once transmitted at the device level, the signal is carried back by a superconducting (NbTi) cable [4] to be amplified by +30 dB via a low-noise amplifier LNF-LNC0.2-3GHz (typical noise temperature 1.6 K). At room temperature, the signal is band-pass filtered (by the combination of low pass and high pass filters so that $f \in [300, 650]$MHz) and further amplified by about +42 dB by the means of two room temperature amplifiers. The reference of each electronic component can be found in appendix. Finally, the lock-in internally demodulates the signal by homodyne detection technique. In figure 2.5, the most attentive reader may notice the presence of a directional coupler, connected to a 50 Ω cap, (inherited from

4. Superconducting cables are often used to minimize the electrical losses and heat flow before amplification stage.

prior measurements) within the readout line. The latter is used only in chapter 6 but is no longer used in the rest of the manuscript. It does not affect the readout signal (almost no attenuation in the desired frequency range).

RF signals are of crucial importance for qubit operation and readout and necessitate a careful attenuation. Internal 10MHz-clocks of the electronics are synchronized at room temperature.

2.2.3 Magnet

A 3D vector magnet surrounding the device allows for spin manipulation by creating high magnetic fields. It is thermally anchored to the 4K plate of the cryostat and can deliver up to 6 T in the vertical axis and a maximum of 1 T along the horizontal axes. Apart from the principal axes, the magnet dispenses up to 1 T.

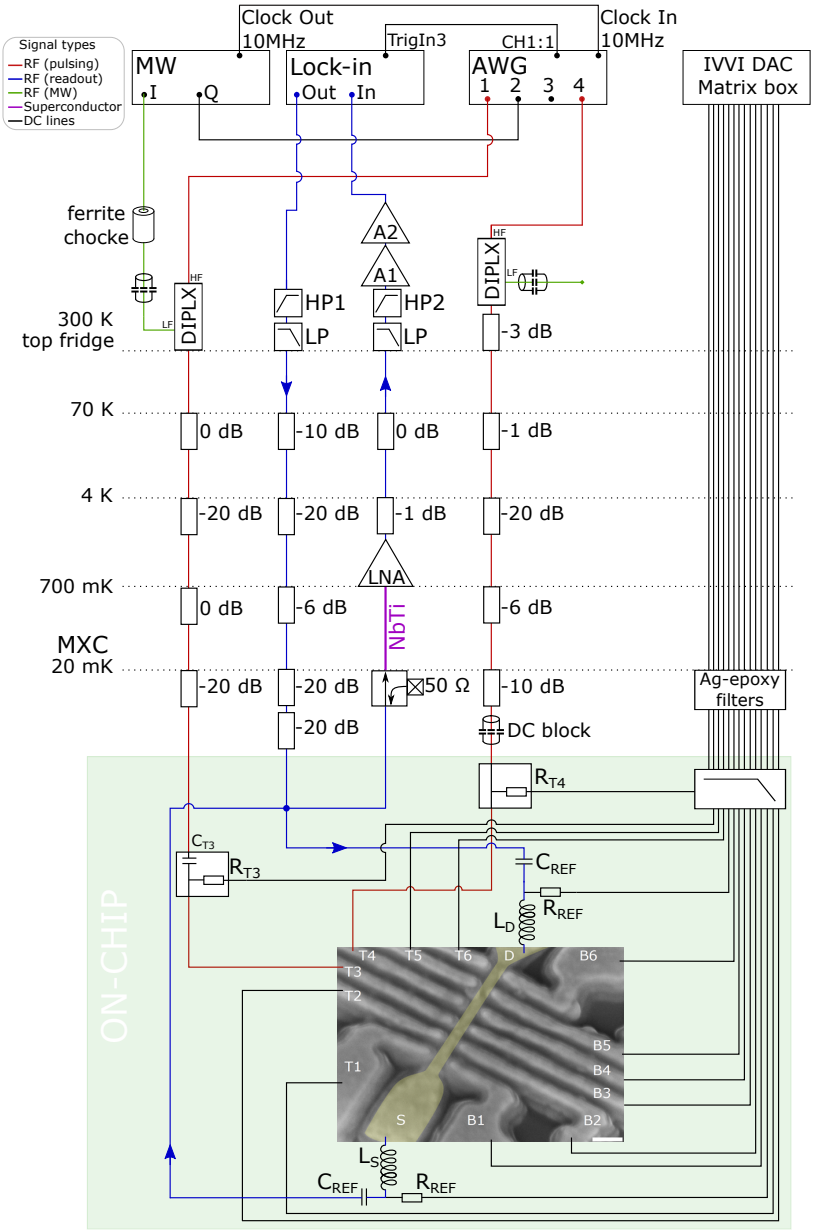

Figure 2.5 – **Experimental setup and wiring:** Connections from room temperature to device under test (DUT) through the dilution fridge. DC blocks at room temperature are home made. The SEM image is not representative of the device orientation in the cryostat. All references of electrical components can be found in appendix.

2.3 Radio-Frequency reflectometry for dispersive readout

Charge or spin state readout in semiconductor systems remain a hurdle to their scalability as it requires many electrodes for conductance measurements. Furthermore, time-averaged measurements may not be sufficient to fully describe quantum systems having rapid physical response. Radio-frequency reflectometry (RFR)[25] stands as an efficient readout method thanks to its fast response timescales down to microsecond events or even less [26] and a low footprint on the sample. This method has permitted many breakthroughs in the scope of qubit readout as: the determination of charge occupancy in QD system [27, 28, 29], time-domain measurements of tunnelling events and qubit single-shot readout [4, 30, 31, 32].

In practice, RFR is used in combination with an intermediate resonant circuit as a detector for quantum capacitance change of low dimensional quantum system. Sensing capacitive change is also referred in the literature as "dispersive readout". The key feature resides in impedance mismatch variations during measurements. A qubit's state evolution causes modifications of the quantum capacitance thus an abrupt change in amplitude and phase response at the resonance frequency [33], readily captured by RFR. Many experimental realizations of spin qubit readout, especially in silicon QDs, rely on such dispersive sensing technique with RFR [21, 23, 34, 35].

In this manuscript, RFR technique is used to perform dispersive readout, permitting to indirectly probe the qubit state. The attention of the reader is first drawn onto the principles and the possible experimental implementations of such reflectometry setup. Then, the emphasis is laid on the origins of the quantum capacitance in the case of low dimensional systems. As for QDs, dispersive readout can either leverage on the use of nearby sensors (dispersive charge sensing) or directly probe the quantum system response (in-situ dispersive readout). Finally, preliminary low-temperature characterization of the RFR setup and resonator is conducted.

2.3.1 Principles of Radio-Frequency Reflectometry

In its core, RFR relies upon the impedance mismatch between a transmission line, whose characteristic impedance is denoted Z_0 and a load capacitance Z_{load}. The load impedance relates to the device under test, therefore RFR provides a direct insight on any sample impedance change. This method can either be used in reflection as sketched in figure 2.6(b) (the impedance mismatch causes the signal to be partly reflected), or in transmission as in panel (a) of figure 2.6. The first technique is used in chapter 6 whereas the second is performed in chapters 3, 4 and 5.

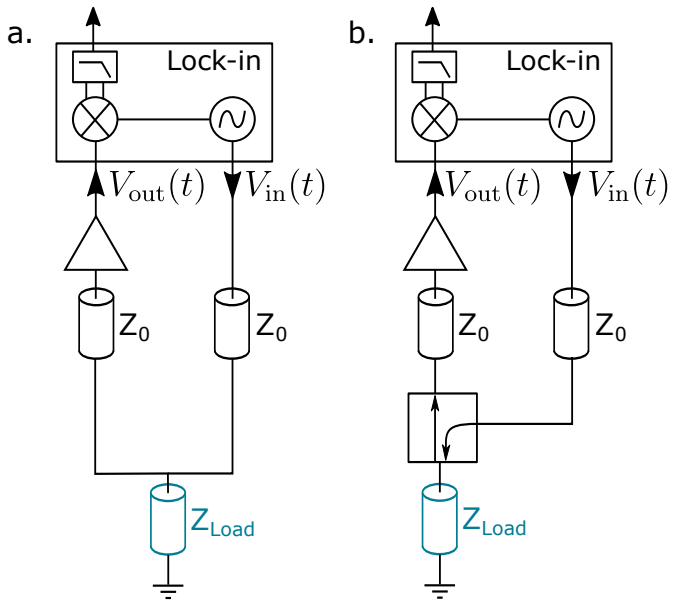

Figure 2.6 – **Circuit diagrams of radio-frequency reflectometry methods:** (a) Diagram for reflectometry in transmission. The signal $V_{\text{in}}(t)$ sent by the lock-in passes through the load. The outgoing signal $V_{\text{out}}(t)$ is amplified and then demodulated. (b) Diagram when measuring the reflected signal from the load impedance. In this case, a directional coupler separates the input and output signals. Schematic adapted from reference [26].

Scattering at impedance mismatch

Following figure 2.6(a), a high-frequency signal $V_{\text{in}}(t)$ is sent from the lock-in instrument to the load sample. Once transmitted or reflected by the load, the outgoing signal $V_{\text{out}}(t)$ differs from the initial one depending on the impedance value Z_{load}. We can define the transmission coefficient $T(\omega)$ in Fourier space as in supplementary of reference [26]:

$$\boxed{T(\omega) = \text{FFT}\left(\frac{V_{\text{out}}(t)}{V_{\text{in}}(t)}\right) = \frac{2Z_{\text{load}}(\omega)}{2Z_{\text{load}}(\omega) + Z_0}} \tag{2.1}$$

A similar equation holds for reflection circuit, see figure 2.6(b):

$$\Gamma(\omega) = \frac{Z_{\text{load}}(\omega) - Z_0}{Z_{\text{load}}(\omega) + Z_0} \tag{2.2}$$

Regardless of the reflectometry method, when $|Z_{\text{load}}| \gg Z_0$, the reflection/transmission coefficients barely depend on the load impedance value. In practice, this is common situation as the transmission line is often $50\,\Omega$-matched and the impedance of a quantum system is $Z_{\text{load}} \sim h/e^2 = 25.8\,\text{k}\Omega$. In order to circumvent such limitation, an impedance transformer (e.g. a tank-circuit) is interposed between the transmission line and the sample. As a consequence, the load impedance

hereafter refers to the sample impedance and that of the tank-circuit.

Impedance matched sample

As above mentioned, a tank-circuit consisting in an embedded RLC system, with $R_{REF} = 1\,\mathrm{M\Omega}$ and $C_{REF} = 10\,\mathrm{nF}$, plays the role of bias-tee to combine the readout ($\simeq$ hundreds of MHz) and DC signals prior to the resonator, see right panel of figure 2.7. On PCB, the "resonator" circuit boils down to a surface mount inductor, either denoted $L_S = 330\,\mathrm{nH}$ or $L_D = 470\,\mathrm{nH}$ relative to the connection to Source or Drain contacts. When micro-bonded to the sample, (i) a parasitic capacitance induced by the PCB dielectric and (ii) a variable capacitance stemming from the sample (C_{sample}) both connect to the inductor, thus forming a resonant LC_{res} circuit, whose frequency is:

$$f_{\mathrm{res}} = \frac{1}{2\pi\sqrt{LC_{\mathrm{res}}}} = \frac{1}{2\pi\sqrt{L(C_{\mathrm{sample}} + C_{\mathrm{para}})}} \tag{2.3}$$

The aforementioned load impedance Z_{load} can therefore be derived as:

$$Z_{\mathrm{load}}(\omega) = \frac{R\left(jL\omega + \frac{1}{jC_{\mathrm{res}}\omega}\right)}{R + jL\omega + \frac{1}{jC_{\mathrm{res}}\omega}} + jC_{\mathrm{REF}}\omega \tag{2.4}$$

In the case of a DQD system, figure 2.7 depicts an equivalent circuit of the load impedance and the blue region underlines the resonant circuit. The latter exhibits a resonance at f_{res}, which appears in the reflection/transmission coefficient frequency spectrum as a dip in amplitude and a steep change in phase. Importantly, the surface mount inductors are chosen so that the resulting resonance frequency falls within the lock-in detection bandwidth ($f_{\mathrm{res}} \in [50\,\mathrm{MHz}, 500\,\mathrm{MHz}]$), without knowing a priori the value of both sample and parasitic capacitances.

Subsequently, when probing at a fixed frequency equal to the resonance one, any change in circuit capacitances will lead to a strong variation of the outgoing signal amplitude and phase. As the parasitic capacitance is intrinsic to the chip, hence constant, this method opens the path to dispersive readout of low dimensional system exhibiting variable quantum capacitance C_{sample}. The latter originates from multiple factors as detailed in the following section.

2.3.2 Load impedance: quantum and tunnelling capacitance definitions

The load capacitance includes the parasitic and that of the sample itself when connected to the RLC circuit. Yet, AC response of low dimensional systems may differ from classical expectations and thus requires corrections to the electronic

model, namely an additional quantum capacitance C_Q [5]. The understanding of such quantum capacitance is of crucial importance for quantum-state dispersive readout [33, 36].

In the case of a DQD system, the low dimensional sample can be modelled as a variable quantum capacitance, acting in parallel of a geometric and tunnelling terms. It can be separated as:

$$C_{\text{sample}} = C_{\text{geom}} + C_{\text{tunnelling}} + C_{\text{Q}} \tag{2.5}$$

with,

- $C_{\text{geom}} = \sum_i \alpha_i C_i$ an intrinsic capacitance term related to the geometry of the device under study. It translates the coupling to nearby QDs and reservoirs C_i, rescaled by the corresponding lever-arms α_i.
- $C_{\text{Q}} \propto (\partial^2 E/\partial \epsilon^2)\,\chi$ is linked to changes in charge occupation ($\chi = P_\downarrow - P_\uparrow$) caused by time-dependent detuning variation. It originates from the curvature of the eigenenergies with respect to detuning [21, 37, 38, 39] and is a reversible process [26].
- $C_{\text{tunnelling}} \propto (\epsilon/\Delta E)\,(\partial \chi/\partial \epsilon)$ strongly depends on the system dynamics and explains irreversible thermal probability redistribution. It namely appears whenever non-elastic tunnelling processes occur.

Figure 2.7 illustrates the equivalent electronic circuit of the load impedance in the case of a DQD system galvanically coupled to an RLC tank-circuit [6]. All contributions to the sample capacitance act in parallel. The tunnelling and quantum terms depend on the physical phenomena in the device, while the geometrical contribution remains constant, given by the device layout.

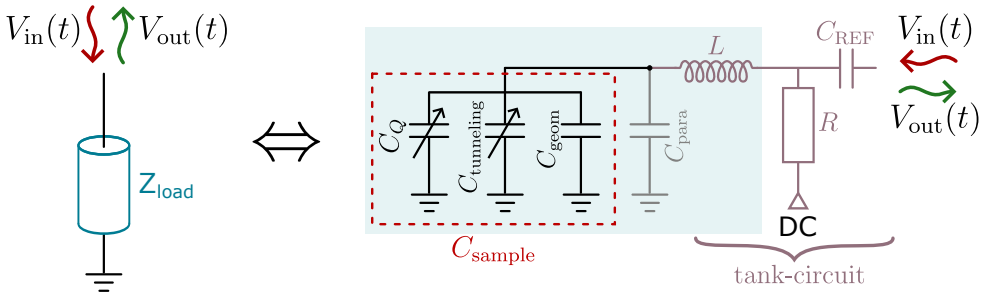

Figure 2.7 – **Equivalent circuit of the load impedance when considering DQD system:** Load impedance probed by RFR and its equivalent circuit in the case of a DQD coupled to an embedded tank-circuit made of RLC (values given in the main text). The blue shaded region embodies the resonant circuit used afterwards for qubit readout.

5. A Sisyphus resistance correction can also be taken into account but stands beyond the scope of this manuscript, see reference [26] for more details.

6. Estimation of the parasitic capacitance value is discussed in section 2.3.4.

2.3.3 Types of dispersive readout for QDs

In this manuscript, two methods of dispersive readout will be tackled. On the one hand, *dispersive charge sensing*, in chapters 3 to 5, necessitates the presence of a nearby charge sensor connected to the reflectometry setup in order to indirectly probe the qubit state. When the charge occupation of the QD of interest changes, the sensor potential shifts, which in turns produces a capacitance modification measured by reflectometry. This method can also perform single-shot spin readout when relying on spin-dependent tunnelling and spin-to-charge conversion [4, 30] (see details in chapter 3 section 3.1.3). However, a moot point arises regarding to scalability prospects as the presence of nearby charge sensor may be arduous for integration of large arrays of QDs.

On the other hand, *in-situ dispersive readout*, presented in chapter 6, allows for DQD probing by directly connecting the reflectometry to the gate defining the QD of interest. This is also referred as "gate-based" dispersive readout in literature [18, 21, 32]. In this case, the reflectometry setup directly senses any capacitive change experienced by the QD with the neighbouring environment. This method has been widely used for singlet-triplet (S-T) qubits.

2.3.4 Low temperature characterization of the tank-circuit

Low-T frequency spectrum

The on-PCB tank-circuit acts as a resonator to probe the sample capacitive changes. When bonding the device to the PCB, an unknown additional parasitic capacitance C_{para} to ground, stemming from the bonding wires, PCB routing and dielectric is connected to the tank-circuit. Accordingly to equation 2.3, measuring the resonance frequency of the tank-circuit allows to infer the parasitic coupling.

Figure 2.8 shows a measurement of the frequency response of the tank-circuit at low temperature (4K) when bonded to the sample. The latter remains grounded, hence no quantum capacitance enters into play. The upper (lower) panel is the amplitude (phase) response in frequency. Radio-frequency signal is measured by homodyne detection via a lock-in UHF-Li from Zurich Instruments. For clarity, the phase signal is unwrapped. Importantly, the frequency spectrum exhibits two distinct resonances as expected: $f_{\text{res},1} = 361.5\,\text{MHz}$ and $f_{\text{res},2} = 292.2\,\text{MHz}$, which are attributed to the resonators connected to the Source and Drain device contacts. Knowing the resonance frequency and the electronic component values ($L_{S,D}$), the parasitic capacitances are estimated about few hundreds of femto Farad as summarized in the following table 7.1.

Despite the relatively small value of the capacitances induced by PCB dielectric and routing, the latter are responsible for a degradation of the resonator sensitivity (characterized by the internal quality factor, defined hereafter). This comes along

Contact	L (nH)	f_{res} (MHz)	C_{para} (fF)
Source	330	361.5	587
Drain	470	292.2	632

Table 2.1 – **Estimation of parasitic capacitances:** Measured parasitic capacitances at low temperatures for two distinct resonances connected to Source and Drain contacts.

with added losses to ground through the dielectric.

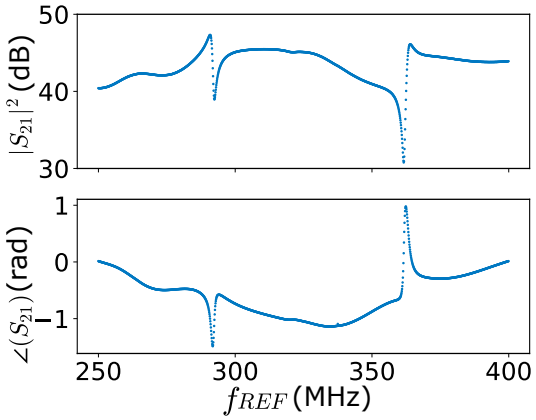

Figure 2.8 – **Low temperature load impedance characterization:** Amplitude (top) and phase (bottom) response of the RLC resonator read by radio-frequency reflectometry at low temperature (4 K), bonded to a grounded sample. A Lock-in detector from Zurich Instrument (UHF-Li) is used for homodyne demodulation. Two resonances are readily visible at $f_S = 361.5\,\text{MHz}$ ($f_D = 292.2\,\text{MHz}$) and are respectively attributed to the inductance $L_S = 330\,\text{nH}$ ($L_D = 470\,\text{nH}$) connected to the Source (Drain) contact. Phase signal has been unwrapped and the electronic delay removed.

Internal and coupling quality factors

One way to quantify how accurately the resonator captures the sample impedance change is the quality factor Q_{tot}. The latter is determined by the energy losses from the resonator, either internally Q_{int} (due to dissipation) or throughout coupling to the transmission line : externally Q_{c}. As a consequence, the Q-factor is defined as the combination of internal and coupling quality factors as:

$$Q_{\text{tot}}^{-1} = Q_{\text{int}}^{-1} + Q_{\text{c}}^{-1} \qquad \text{and} \qquad \begin{cases} Q_{\text{int}} = \dfrac{1}{R}\sqrt{\dfrac{L}{C}} \\ Q_{\text{c}} = \dfrac{1}{Z_0}\sqrt{\dfrac{L}{C}} \end{cases} \tag{2.6}$$

A large Q_{tot}-factor is suitable to maximise the resonance sharpness and thus

the resonator sensitivity to circuit changes[7]. We evaluate the tank-circuit quality factor for both resonances (fitting procedure for drain contact is not shown). Figure 4.17(a) displays a zoom on the Source resonance, with the background in amplitude and the electronic delay in phase being removed. The normalized transmission $\tilde{S}_{21}$ therefore reads:

$$\tilde{S}_{21} = A\, e^{i\phi} \times 10^{-B/20} e^{i(2\pi f \delta_e + \phi_0)} \tag{2.7}$$

with,

$A = |S_{21}|^2$ *the transmission amplitude,*

$\phi = \angle(S_{21})$ *the transmission phase,*

B *is the background in amplitude,*

δ_e *is the electronic delay,*

ϕ_0 *is the phase shift.*

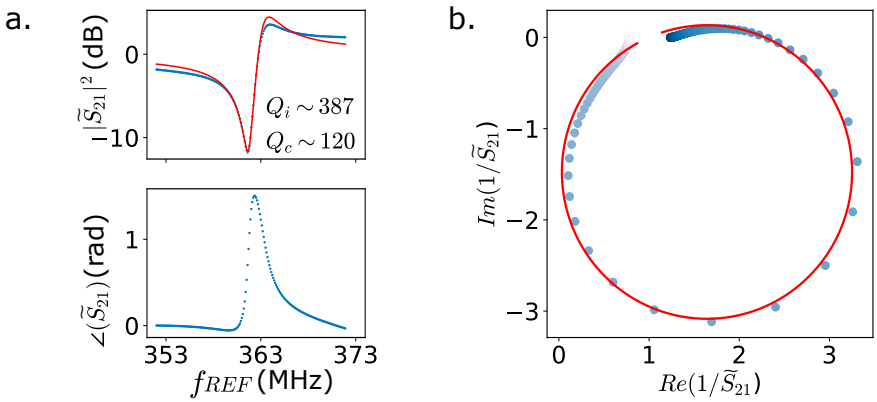

Figure 2.9 – **Estimation of quality factor for source contact resonance:** (a) Amplitude and phase signals zoomed close by the Source resonance. Red line is a fit using the formula in reference [40], giving the resonator internal and coupling quality factors: $Q_{\text{int}} \sim 387$, $Q_{\text{c}} \sim 120$. Code for the fitting procedure has been made by E. Dumur. (b) Source resonance plotted in complex plane for Q_{tot}-factor estimation.

Then, this transmission spectrum in frequency is fitted using the formula in reference [40], and allows for the extraction of the internal and coupling quality factors:

$$\tilde{S}_{21}^{-1} = 1 + \frac{Q_{\text{int}}}{Q_{\text{c}}} e^{i\phi} \frac{1}{1 + i\, 2Q_{\text{int}} \frac{f - f_{\text{res}}}{f_{\text{res}}}} \tag{2.8}$$

Panel (b) of figure 2.9 shows the normalized transmission in the inverse complex plane, with the red line being a fit (also shown in panel (a)). In the case of resonator connected to source contact of the sample (which is the readout line in

7. Remarkably, having a too large Q_{tot} factor, so that $Q_{\text{tot}} \to \infty$, can be an experimental ordeal as the resonance is in turn extremely sharp and the system has a very long response time.

chapters 3, 4 and 7), the evaluated quality factors are about $Q_{\text{int}} \sim 387$, $Q_{\text{c}} \sim 120$. All quality factors are gathered in the following table 2.2. In both cases, internal quality factor is larger than coupling one, suggesting that the main channel for losses is the dissipation. Experimentally, an internal quality factor much greater than coupling one is suitable as it minimizes the information losses.

Contact	Q_{int}	Q_{c}	$Q_{\text{int}}/Q_{\text{c}}$	Q_{tot}
Source	387	120	3.2	91
Drain	318	249	1.3	140

Table 2.2 – **Quality factors of resonators:** Summary of fitted quality factors for both contacts with their own readout tank-circuit. The slight discrepancy between the two contacts sensitivity is imputed to variability on the soldering of surface mount inductors, capacitors and the bondings.

The total resonator sensitivity is therefore about $Q \sim 91$ which is far from being state-of-the-art. Indeed, this readout line suffers from losses through the parasitic capacitance to ground (due to routing, dielectric...). Recent improvements of dispersive readout have been made possible thanks to the development of on-chip microwave resonators, having an internal quality factor reaching up to million when non-connected to a sample [40]. Their integration to spin qubit device, which still withstand losses within the semiconductor substrate, permits a strong enhancement of the total quality factor to 400 in similar structures [41] and even exceeding 2000 in GaAs [42] and in Ge devices [43].

2.4 Conclusions

Si-MOS device architecture stands as a promising platform to host spin qubit enclosed in quantum dots due to their foundry-compatible processes. First, we detailed the particular fabrication steps in order to realize a 6-split gates device which is further studied in following chapters. Preliminary I-V characterization is conducted prior to quantum measurements so as to check the transistor-like behaviour of the sample. When turning to low temperatures inside a dilution cryostat, a particular attention is drawn to filtering and attenuation of the lines. The complete setup wiring used to perform quantum measurements is then elaborated. Second, we motivated the choice of dispersive readout by radio-frequency reflectometry. In addition to its low on-chip footprint, dispersive readout allows to resolve fast and single-shot events, which remained so far impossible for time-averaged measurements. First and second chapters were an initial springboard to understand -theoretically and experimentally- the following quantum measurements at low temperatures and set the proper vocabulary to deal with hole spin qubit in Si-MOS device.

References

[1] P. Stano and Daniel Loss. « Review of performance metrics of spin qubits in gated semiconducting nanostructures ». In: *Nature Reviews Physics* 4.10 (Oct. 2022), pp. 672–688. DOI: 10.1038/s42254-022-00484-w.

[2] B. M. Maune et al. « Coherent singlet-triplet oscillations in a silicon-based double quantum dot ». In: *Nature* 481.7381 (2012), pp. 344–347. DOI: 10.1038/nature10707.

[3] R. Maurand et al. « A CMOS silicon spin qubit ». In: *Nature Communications* (May 2016). DOI: 10.1038/ncomms13575.

[4] J. R. Petta et al. « Coherent Manipulation of Coupled Electron Spins in Semiconductor Quantum Dots ». In: *Science* 309.5744 (2005), pp. 2180–2184. DOI: 10.1126/science.1116955.

[5] B. Bertrand et al. « Development of spin quantum bits in SOI CMOS technology ». In: *2018 IEEE 18th International Conference on Nanotechnology (IEEE-NANO)*. 2018, pp. 1–3. DOI: 10.1109/NANO.2018.8626273.

[6] M. F. Gonzalez-Zalba et al. « Scaling silicon-based quantum computing using CMOS technology ». In: *Nature Electronics* 4.12 (Dec. 2021), pp. 872–884. DOI: 10.1038/s41928-021-00681-y.

[7] A. M. J. Zwerver et al. « Qubits made by advanced semiconductor manufacturing ». In: *Nature Electronics* 5.3 (Mar. 2022), pp. 184–190. DOI: 10.1038/s41928-022-00727-9.

[8] S. D. Liles et al. « Electrical control of the g tensor of the first hole in a silicon MOS quantum dot ». In: *Phys. Rev. B* 104 (23 Dec. 2021), p. 235303. DOI: 10.1103/PhysRevB.104.235303.

[9] S. Geyer et al. « Self-aligned gates for scalable silicon quantum computing ». In: *Applied Physics Letters* 118.10 (Mar. 2021), p. 104004. DOI: 10.1063/5.0036520.

[10] M. Hofheinz et al. « Simple and controlled single electron transistor based on doping modulation in silicon nanowires ». In: *Applied Physics Letters* 89.14 (Oct. 2006), p. 143504. DOI: 10.1063/1.2358812.

[11] S. Barraud et al. « Performance of Omega-Shaped-Gate Silicon Nanowire MOSFET With Diameter Down to 8 nm ». In: *IEEE Electron Device Letters* 33.11 (2012), pp. 1526–1528. DOI: 10.1109/LED.2012.2212691.

[12] H. Liu et al. « Ultrafast and Electrically Tunable Rabi Frequency in a Germanium Hut Wire Hole Spin Qubit ». In: *Nano Letters* 23.9 (May 2023), pp. 3810–3817. DOI: 10.1021/acs.nanolett.3c00213.

[13] S. Bosco, Bence Hetényi, and Daniel Loss. « Hole Spin Qubits in Si FinFETs With Fully Tunable Spin-Orbit Coupling and Sweet Spots for Charge Noise ». In: *PRX Quantum* 2 (1 Mar. 2021), p. 010348. DOI: 10.1103/PRXQuantum.2.010348.

[14] S. Bosco and Daniel Loss. « Fully Tunable Hyperfine Interactions of Hole Spin Qubits in Si and Ge Quantum Dots ». In: *Phys. Rev. Lett.* 127 (19 Nov. 2021), p. 190501. DOI: 10.1103/PhysRevLett.127.190501.

[15] T. Bédécarrats et al. « A new FDSOI spin qubit platform with 40nm effective control pitch ». In: *2021 IEEE International Electron Devices Meeting (IEDM)*. 2021, pp. 1–4. DOI: 10.1109/IEDM19574.2021.9720497.

[16] A. Corna. « Single Spin control and readout in silicon coupled quantum dots ». PhD thesis. Sept. 2017.

[17] B. Voisin et al. « Few-Electron Edge-State Quantum Dots in a Silicon Nanowire Field-Effect Transistor ». In: *Nano Letters* 14.4 (Apr. 2014), pp. 2094–2098. DOI: 10.1021/nl500299h.

[18] A. Crippa et al. « Level Spectrum and Charge Relaxation in a Silicon Double Quantum Dot Probed by Dual-Gate Reflectometry ». In: *Nano Letters* 17.2 (Feb. 2017), pp. 1001–1006. DOI: 10.1021/acs.nanolett.6b04354.

[19] A. Crippa et al. « Electrical Spin Driving by g-Matrix Modulation in Spin-Orbit Qubits ». In: *Physical Review Letters* 120.13 (Mar. 2018), p. 137702. DOI: 10.1103/physrevlett.120.137702.

[20] A. Crippa et al. « Gate-reflectometry dispersive readout and coherent control of a spin qubit in silicon ». In: *Nature Communications* 10.1 (2019), p. 2776. DOI: 10.1038/s41467-019-10848-z.

[21] R. Ezzouch et al. « Dispersively Probed Microwave Spectroscopy of a Silicon Hole Double Quantum Dot ». In: *Phys. Rev. Appl.* 16 (3 Sept. 2021), p. 034031. DOI: 10.1103/PhysRevApplied.16.034031.

[22] N. Piot et al. « A single hole spin with enhanced coherence in natural silicon ». In: *Nature Nanotechnology* 17.10 (Sept. 2022), pp. 1072–1077. DOI: 10.1038/s41565-022-01196-z.

[23] J. Duan et al. « Dispersive readout of reconfigurable ambipolar quantum dots in a silicon-on-insulator nanowire ». In: *Applied Physics Letters* 118.16 (Apr. 2021), p. 164002. DOI: 10.1063/5.0040259.

[24] C. P. Scheller et al. « Silver-epoxy microwave filters and thermalizers for millikelvin experiments ». In: *Applied Physics Letters* 104.21 (May 2014), p. 211106. DOI: 10.1063/1.4880099.

[25] R. J. Schoelkopf et al. « The Radio-Frequency Single-Electron Transistor (RF-SET): A Fast and Ultrasensitive Electrometer ». In: *Science* 280.5367 (1998), pp. 1238–1242. DOI: 10.1126/science.280.5367.1238.

[26] F. Vigneau et al. « Probing quantum devices with radio-frequency reflectometry ». In: *Applied Physics Reviews* 10.2 (Feb. 2023), p. 021305. DOI: 10.1063/5.0088229.

[27] J. M. Elzerman et al. « Few-electron quantum dot circuit with integrated charge read out ». In: *Phys. Rev. B* 67 (16 Apr. 2003), p. 161308. DOI: 10.1103/PhysRevB.67.161308.

[28] L. DiCarlo et al. « Differential Charge Sensing and Charge Delocalization in a Tunable Double Quantum Dot ». In: *Phys. Rev. Lett.* 92 (22 June 2004), p. 226801. DOI: 10.1103/PhysRevLett.92.226801.

[29] J. I. Colless et al. « Dispersive Readout of a Few-Electron Double Quantum Dot with Fast rf Gate Sensors ». In: *Phys. Rev. Lett.* 110 (4 Jan. 2013), p. 046805. DOI: 10.1103/PhysRevLett.110.046805.

[30] J. M. Elzerman et al. « Single-shot read-out of an individual electron spin in a quantum dot ». In: *Nature* 430.6998 (July 2004), pp. 431–435. DOI: 10.1038/nature02693.

[31] S. Amasha et al. *Measurements of the spin relaxation rate at low magnetic fields in a quantum dot.* 2006.

[32] A. West et al. « Gate-based single-shot readout of spins in silicon ». In: *Nature Nanotechnology* 14.5 (May 2019), pp. 437–441. DOI: 10.1038/s41565-019-0400-7.

[33] R. Mizuta et al. « Quantum and tunneling capacitance in charge and spin qubits ». In: *Phys. Rev. B* 95 (4 Jan. 2017), p. 045414. DOI: 10.1103/PhysRevB.95.045414.

[34] L. Hutin et al. « Gate reflectometry for probing charge and spin states in linear Si MOS split-gate arrays ». In: *2019 IEEE International Electron Devices Meeting (IEDM)*. 2019, pp. 37.7.1–37.7.4. DOI: 10.1109/IEDM19573.2019.8993580.

[35] T. Lundberg et al. « Spin Quintet in a Silicon Double Quantum Dot: Spin Blockade and Relaxation ». In: *Phys. Rev. X* 10 (4 Oct. 2020), p. 041010. DOI: 10.1103/PhysRevX.10.041010.

[36] A. Cottet, Christophe Mora, and Takis Kontos. « Mesoscopic admittance of a double quantum dot ». In: *Phys. Rev. B* 83 (12 Mar. 2011), p. 121311. DOI: 10.1103/PhysRevB.83.121311.

[37] S. Luryi. « Quantum capacitance devices ». In: *Applied Physics Letters* 52.6 (Feb. 1988), pp. 501–503. DOI: 10.1063/1.99649.

[38] M. G. House et al. « Radio frequency measurements of tunnel couplings and singlet–triplet spin states in Si:P quantum dots ». In: *Nature Communications* 6.1 (Nov. 2015), p. 8848. DOI: 10.1038/ncomms9848.

[39] M. Urdampilleta et al. « Charge Dynamics and Spin Blockade in a Hybrid Double Quantum Dot in Silicon ». In: *Phys. Rev. X* 5 (3 Aug. 2015), p. 031024. DOI: 10.1103/PhysRevX.5.031024.

[40] A. Megrant et al. « Planar superconducting resonators with internal quality factors above one million ». In: *Applied Physics Letters* 100.11 (Mar. 2012), p. 113510. DOI: 10.1063/1.3693409.

[41] C. X. Yu et al. « Strong coupling between a photon and a hole spin in silicon ». In: *Nature Nanotechnology* 18.7 (July 2023), pp. 741–746. DOI: 10.1038/s41565-023-01332-3.

[42] K. D. Petersson et al. « Circuit quantum electrodynamics with a spin qubit ». In: *Nature* 490.7420 (Oct. 2012), pp. 380–383. DOI: 10.1038/nature11559.

[43] G. Zheng et al. « Rapid gate-based spin read-out in silicon using an on-chip resonator ». In: *Nature Nanotechnology* 14.8 (Aug. 2019), pp. 742–746. DOI: 10.1038/s41565-019-0488-9.

CHAPTER 3

Operation of hole spin qubit and evidence of sweetlines for charge noise

In the context of identifying a mature platform for building quantum processors, hole spin systems emerge as a promising candidate with the recent operation of one [1, 2] and multiple qubits [3, 4, 5, 6]. They exhibit long coherence times, ranging from a few hundred microseconds in natural silicon to several milliseconds in Ge/SiGe heterostructures [7]. Additionally, they feature strong spin-orbit coupling, enabling low-power and all-electrical driving [1, 2, 8, 9, 10]. However, this same spin-orbit interaction also renders spin qubits highly vulnerable to electrical noise, such as charge noise, leading to phase randomization and decoherence. Charge noise is nowadays recognized as the primary source of decoherence for spin qubit systems [11, 12]. Significant efforts have been devoted to mitigate charge noise influence, revealing the existence of sweetspots in gate voltage [8, 13] or in magnetic field [10, 14, 15]. At this particular sweetspot, the coherence time of single-hole spin qubit has been extended up to 88 µs in Si-MOS architecture [10]. In this context, the following chapter aims at focusing on the experimental realization of a single-hole spin qubit to investigate the influence of charge noise with respect to magnetic field orientation. First, readout and spin manipulation techniques are described, followed by a discussion on g-matrix characterization. The latter provides crucial insights into the hole wavefunction and its response to charge noise and upon driving. Subsequently, attention is directed towards the first and second-order spin susceptibility to gate voltage fluctuations (emulating charge noise) as a function of magnetic field. Herein, we demonstrated the presence of sweetlines for charge noise rather than sweetspots. These one-dimensional features of zero-sensitivity to electrical noise pave the way for spin qubit operation with enhanced coherence time.

Contents

3

3.1 Hole spin readout

3.1.1 Objectives and roles of each gate

Before charge noise investigation, the accent is drawn on the specific tuning to operate a spin qubit within a semiconductor quantum dot. In this scope, figure 3.1 depicts the main wiring connections and QD formation further used in this manuscript.

The hole spin qubit studied in the following chapters 3 to 5 is enclosed in a QD underneath the gate T_3, also referred as QD_3 (underscored by the red arrow). Its spin orientation is readout by the means of a nearby charge sensor (red area) via spin-to-charge conversion and spin-dependent tunnelling similarly to references [10, 16, 17, 18, 19]. The charge sensor is made of a strongly accumulated QD merged below the gates T_1, B_1 and B_2 which is itself indirectly probed by radio-frequency reflectometry, as discussed in chapter 2. High-frequency signals on gates T_3 or T_4 allow for qubit manipulation [1]. Gates displayed in green (i.e. T_2 and B_3) are set to negative voltage before their accumulation threshold (no QD underneath) and are used to adjust tunnelling rates between QD_3 and the charge sensor (see section 3.1.2). Finally, a metal gate lying above the full device is set to $-10\,\mathrm{V}$ so as to lower the overall electrostatic barriers.

The next sections pinpoint the particular gate settings so that the charge occupancy of QD_3 -and thus its corresponding spin orientation- can be accurately

1. Unless explicitly specified, the microwave signals are preferentially sent through gate T_3.

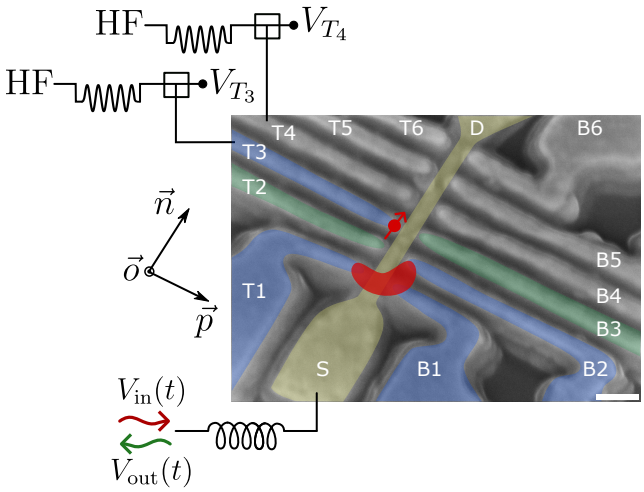

Figure 3.1 – **General description of gate settings and wiring for spin qubit definition:** False coloured SEM image of a nominally identical 6 split gates device. Yellow area defines the silicon nanowire in which QDs are hosted (under blue gates). The spin qubit lays under gate T_3 and is probed by a nearby charge sensor accumulated below gates T_1, B_1 and B_2. Estimated position of QDs are depicted by red areas. Gates displayed in gray remain at 0 bias voltage, whereas gates in green are set to negative voltage before their accumulation threshold. The latter are used to tune the transition rate between the qubit and the sensor for spin readout. Radio-frequency reflectometry setup is hooked on the Source contact. High-frequency (HF) signals can be sent through gates T_3 and T_4 for qubit manipulation. Finally, magnetic coordinate system is defined as $\vec{n}$ along the nanowire, $\vec{o}$ out-of-plane of the device and $\vec{p}$ as perpendicular to the silicon channel. Scale bar is 100 nm.

figured out. Primary focus is on the formation of a merged QD acting as the charge sensor. Then, the emphasis is laid in section 3.1.3 on the conditional charge state readout depending on the spin orientation.

3.1.2 Quantum dots settings for spin qubit definition

The need of a highly sensitive charge sensor

Forming a unique QD shared below multiple gates necessitates an important coupling between the dots underneath each single gate, see chapter 1, section 1.1.2 [20]. When the mutual coupling is strong enough, QDs will tend to merge. Despite the lack of dedicated barrier gates, coupling between dots can be increased by applying large negative voltage (compared to the respective threshold value) on each gate. This will, in turn, enlarge the dot charge occupancy, causing the holes wavefunction to spread beyond the gate dimension, and therefore merge.

Figure 3.2(a) shows the phase reflectometry signal versus T_1 and B_1 gate voltages, probed at a carrier tone $f_S = 361.5\,\text{MHz}$ (see chapter 2). In the meantime,

other gates remain at 0 V. Whenever a charge enters the dot, it modifies the quantum capacitance of the system, and thus results in a strong shift of the resonance frequency [21]. Consequently, each hole stepping in a QD is characterized by a peak in phase reflectometry, also known as "Coulomb peak". The spacing between two consecutive Coulomb peaks therefore corresponds to the energy to add a particle within the dot [22] and their height mainly depends on two phenomena. First, such tunnelling events can only be probed if the charge exchange rate is comparable or larger than the RF-resonant frequency [21]. Second, the electronic temperature strongly influences the peak height [23].

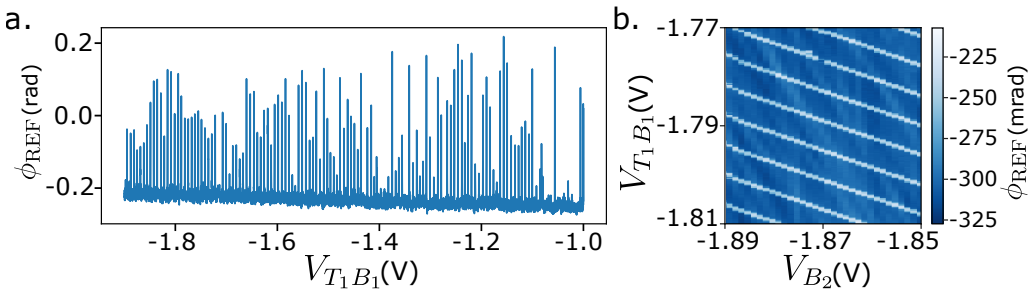

Figure 3.2 – **Characterization of merged quantum dot for charge sensing:** (a) Phase reflectometry signal, probed at $f_S = 361.5\,\text{MHz}$, as a function of simultaneously swept gates voltages of T_1 and B_1. Each peak corresponds to the transition of one charge within the QD formed under the two gates, also known as "Coulomb peaks". Gate voltages are swept well above their opening threshold to form a highly populated QD. (b) Charge stability diagram of QDs below gates T_1, B_1 and B_2. Diagonal lines indicate the complete merging of the quantum dots.

Hereafter, T_1 and B_1 gates are maintained in the strongly accumulated regime about $V_{T_1B_1} \in [-1.77, -1.81]\,\text{V}$, demonstrating constant charging energy and phase contrast about 100 mrad. Panel (b) of figure 3.2 depicts the charge stability diagram of the dots underneath gates T_1B_1 and B_2. When strongly accumulated, the two dots merge as theoretically schematized in chapter 1, section 1.1.2. In the present case, a unique large QD lies below the three gates. The role of this large QD is, in combination with the source contact, to form a charge sensor capable of probing the charge occupancy of the dot of interest QD_3.

When particle exchange occurs between the sensing dot and QD_3, the overall quantum capacitance is modified, causing a dispersive shift of the resonator frequency. This result in abrupt change in either phase or amplitude of the probed signal. Recording such characteristic breaks allows to indirectly determine QD_3 charge occupancy.

Setting the first hole regime for QD_3

Now that the sensing QD is formed, the attention of the reader is drawn on figure 3.3 which displays the charge stability diagram of the sensor dot (herein represented only by the gate B_2) and QD_3 (controlled by gate T_3). Light blue lines correspond to Coulomb peaks of the sensing dot partly affected by gate voltage of T_3 due to cross-talk coupling [20]. As aforementioned, charging events of QD_3 will cause a change in quantum capacitance of the sensing dot and therefore a break in the Coulomb peaks. Such charge exchange are highlighted by red dashed lines and permit an accurate evaluation of the dot charge occupancy denoted N. In this example, QD_3 is filled from $N = 0$ to $N = 3$ holes. In the following, the study will focus on the first interdot transition, highlighted by the white frame.

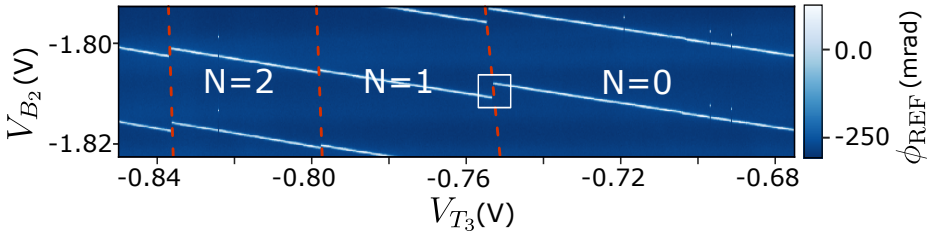

Figure 3.3 – **Charge occupancy of QD_3 probed by the means of nearby sensing dot:** Phase stability diagram between sensing dot (controlled by gate voltage B_2) and QD_3 (relates to T_3 voltage). Coulomb peaks discontinuities allow for an accurate estimation of QD_3 charge occupancy, characterized by the number of charges N, herein ranging from 0 to 3. Framed region highlights the interdot transition further studied for spin readout.

Charge transition rates

The last requirements before turning to spin readout is to ensure whether charging events are fully captured by reflectometry readout in the time domain. Indeed, probing the spin state will heavily rely on the ability of the sensing dot to resolve single-shot charging events [24, 25]. This results in a timescale competition between the transition rates for the charge to escape the dot Γ_{out} and either the qubit relaxation time T_1 or the integration time τ_{int}. If $\Gamma_{out} \ll \tau_{int}$, charging events are faster than probing, thus such charge exchange occurrence can be missed. On the contrary, if $\Gamma_{out} \gg {}^1/_{T_1}$, spin relaxation occurs before measurement, also causing false results. So far, spin qubit relaxation time in unknown [2] but is expected to range from few hundreds of microseconds to millisecond timescale [7]. Following the above criteria, charging events within $[50\,\mu s, 250\,\mu s]$ range are suitable for single-shot spin readout while setting the integration time to $5\,\mu s$. In other words, tunnelling rates targeted for this experiment are ranging from about $4\,ms^{-1}$ to

2. An example of spin relaxation time measurement can be found in appendix B.

$20\,\mathrm{ms}^{-1}$.

Experimentally, tunnel rates can be tuned by different manners. The most commonly used in semiconductor spin qubits relies on the use of dedicated "trench" or "barrier" gates, which intend to locally modify the electrostatic landscape, thus reducing/ increasing tunnel barriers between QDs [4, 5, 11]. In absence of such gates, tunnel rates can be adjusted by modification of the dot occupancy. In the present case, we perform an alternative approach by using both gates T_2 and B_3 as control knobs for charge transfer between the sensing dot and QD_3. Together, gates are modulating the electrostatic landscape between the two dots by pinching the wavefunctions, thus acting similarly to trench gates. Applying this procedure allows to tune tunnelling rates by several orders of magnitude [26] as long as the gate threshold is not overcome (otherwise a new QD is formed). In the following, those gates may be referred as "barrier gates".

Figure 3.4 is a time domain measurement of tunnel rates between the sensor and QD_3 when barrier gates are lowered to $V_{T_2} = V_{B_3} = -0.61\,\mathrm{V}$. At the interdot transition and in absence of magnetic field to lift the spin degeneracy, energy levels are lined up as sketched in panel (a). In this case, charge exchange happens at given rates called $\Gamma_{|0\rangle}$ ($\Gamma_{|1\rangle}$) when the charge escapes (enters) QD_3. The rates at which the charge transition occurs are mainly governed by gate voltages set on T_2 and B_3. Panel (b) is an example of phase reflectometry time-trace recorded when charging events occur for $\tau_{\mathrm{int}} = 5\,\mu\mathrm{s}$. A clear Random Telegraph Signal (RTS) is observed. To ensure this feature stems from charge transfer related to QD_3 (and not from nearby fluctuators), we verified that (i) the fraction of time spent by the hole within QD_3 relates to alignment of the energy level to the Fermi potential μ_S and (ii) tunnelling rates can be modified by the barrier gates [27]. Histogram in the right inset of panel (b) evidences two distinct states lower (higher) corresponding to QD_3 filled with one $|1\rangle$ (zero $|0\rangle$) hole. Such method is also known as "Full Counting Statistics" [28].

From time-traces, tunnelling rates can be calculated as the inverse of the average time duration spent inside or outside the QD [29]:

$$\boxed{\Gamma_{|0\rangle(|1\rangle)} = \frac{1}{\langle \Delta t_{|0\rangle(|1\rangle)} \rangle}} \tag{3.1}$$

In order to evaluate these durations denoted $\langle \Delta t_{|0\rangle(|1\rangle)} \rangle$, we define a threshold value as the mean between the center of each Gaussian envelopes in ϕ_{REF} histogram. For each data point from the recorded time-trace, the system is considered in filled (empty) state $|1\rangle$ ($|0\rangle$) whenever the signal is below (above) the threshold value. The post-treated sequence consequently comprises binary values depending on the charge state. From that, the averaged time spent in each charge state is estimated as the measurement integration time : $\tau_{\mathrm{int}} = 4.55\,\mu\mathrm{s}$ balanced

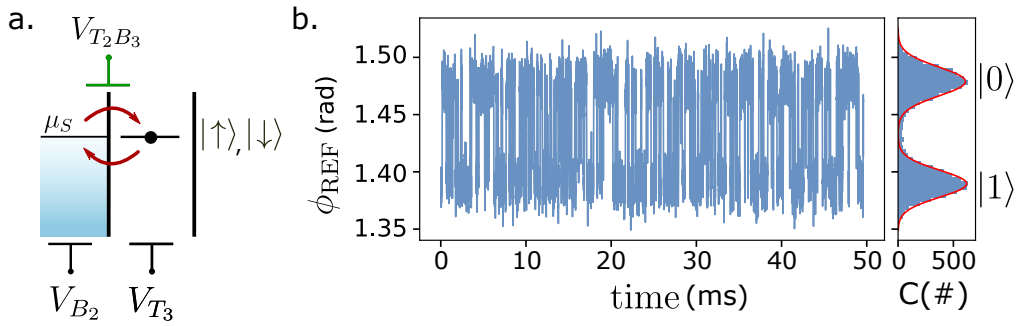

Figure 3.4 – **Resonant regime between charge sensor and QD_3:** (a) Schematic of sensing dot and QD_3 energy levels. So far, no external magnetic field is applied, hence the spin states $\{|\uparrow\rangle, |\downarrow\rangle\}$ are degenerate in energy for a fixed number of charge N. When the Fermi energy aligns with the QD level, charge transfer can occur at given rates $\Gamma_{|0\rangle}$ (resp. $\Gamma_{|1\rangle}$) to escape (resp. to enter) the dot. Such tunnelling events are tuned by the means of gates T_2 and B_3. (b) Time domain reflectometry measurement when the energy levels are resonant. Alternating phases of upper and lower states are clearly visible, revealing the passage of a charge within the QD_3. Right panel is an histogram of the recorded trace, illustrating the distinction between full $|1\rangle$ and empty $|0\rangle$ dot. From this time-trace, rates are inferred about $\Gamma_{|0\rangle} \sim 4.81\,\mathrm{ms}^{-1}$ and $\Gamma_{|1\rangle} \sim 4.61\,\mathrm{ms}^{-1}$ (see main text for details).

by the probability to be in the filled or empty states. More details about the fitting procedure and the tunnelling rates can be found in appendix B. Finally, in this instance:

$$\begin{cases} \langle \Delta t_{\mathrm{out}} \rangle \simeq 208\,\mu\mathrm{s} \\ \langle \Delta t_{\mathrm{in}} \rangle \simeq 217\,\mu\mathrm{s} \end{cases} \quad \Longrightarrow \quad \begin{cases} \Gamma_{\mathrm{out}} \simeq 4.81\,\mathrm{ms}^{-1} \\ \Gamma_{\mathrm{in}} \simeq 4.61\,\mathrm{ms}^{-1} \end{cases} \tag{3.2}$$

At these transition rates, the sensing dot accurately probes the charging events of QD_3, however so far no indication is provided concerning the hole spin state. Following section pinpoints methods for spin readout relying on spin-to-charge conversion and spin-dependent tunnelling techniques.

3.1.3 Single-shot spin readout by Elzerman method

Spin degeneracy is lifted in presence of external magnetic field and spin states are split by the Zeeman energy $E_Z = \mu_B \tilde{g} \mathbf{B}$. Nevertheless, direct probing of the spin orientation remains challenging due to the weak magnetic moment a spin conveys. First demonstration of single spin readout have been reported by Elzerman *et al.* [16] in a GaAs heterostructure, relying on conditional tunnelling events of the particle to a reservoir depending on its spin orientation. The hole spin state can be indirectly discriminated by filtering states of lowest energy $|\downarrow\rangle$(see details in next section). When "spin-dependent tunnelling" condition is fulfilled, a charge transfers from QD to the reservoir and causes an abrupt change (so-called "blip") in the charge sensor capacitance, consequently visible in the recorded signal. In other

words, the spin orientation information is translated into the conditional charge transfer: this is known as "spin-to-charge conversion". From the presence/absence of blips in the recorded signal, it is possible to deduce the initial spin orientation. Since then, single-shot spin readout using spin-to-charge conversion have been widely implemented in platforms such as semiconductor QDs [17, 30, 31], Si-MOS QDs [18], with a fidelity above the fault tolerant threshold [32, 33, 34].

However, it is worth mentioning that "Elzerman readout" method suffers from multiple moot points in the scope of large-scale implementation. First, spin states can only be distinguished provided a high-enough magnetic field to exceed the reservoir electron temperature ($E_Z \gg k_B T_e$). At the same time, a large magnetic field is detrimental to spin relaxation time, inducing undesired spin flips [35]. Second, in essence Elzerman readout necessitates the presence of a reservoir/sensing dot nearby the QD, which is hardly feasible in large QDs array. Finally, such readout is destructive as the $|\uparrow\rangle$-spin state tunnels out from the QD and is lost within the Fermi sea. The two last points can be circumvented using Pauli Spin Blockade (PSB) readout instead, also taking advantage of spin-to-charge conversion technique [36, 37].

Detailed principles of spin-to-charge conversion

Spin-to-charge conversion is performed when the Fermi energy of the sensing dot μ_S stands in between the spin energy levels (separated by E_Z) as sketched in left panels of figure 3.5. Two cases therefore arise depending on the spin orientation of the hole entering the QD:

- If the QD is initially filled with a $|\downarrow\rangle$-spin state, as shown in figure 3.5(a): the hole does not have sufficient energy to escape the dot and remains in the Coulomb blockade regime. The sensing dot does not experience any charge transfer, thus no signal is visible in phase reflectometry. Left panel of (a) illustrates the impossible tunnelling process, which in turn causes the absence of spin signature via spin-to-charge conversion in reflectometry signal (see right panel).
- On the contrary, if the QD is initially filled with an $|\uparrow\rangle$-spin state (figure 3.5(b)): its is energetically favourable for the hole to escape within the sensing dot. A tunnelling process occurs (depicted in left panel), causing a capacitive change in the sensing dot. This translates into a blip in phase reflectometry signal (see right panel). The charge is afterwards replaced by a $|\downarrow\rangle$-spin state, letting the system Coulomb blocked as in the previous point.

The combination of conditional charge exchange with a nearby reservoir (that depends on spin orientation) and dispersive readout allows for single-shot detection of spin state. Experimentally, energy levels can be tuned to align at convenience by the gate voltages V_{T_3} and V_{B_2}. Yet, as the hole g-factor is unknown (thus the spin splitting) further measurements are required to figure out the voltage range to set the Fermi energy level in between the spin ones.

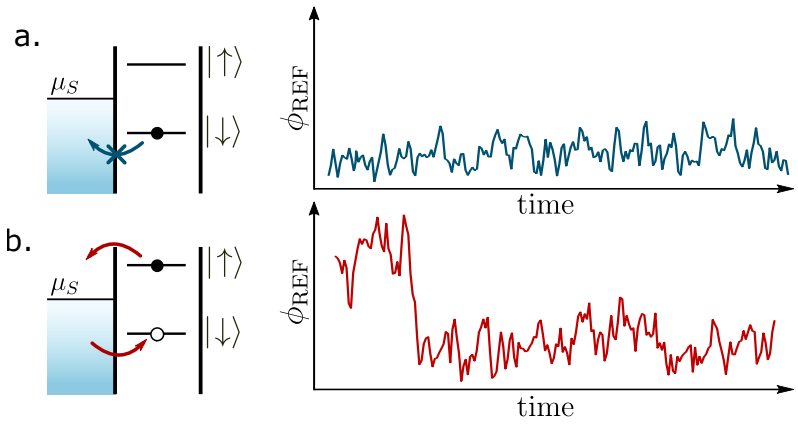

Figure 3.5 – **Elzerman readout principle:** (a) Illustration of measurement outcome when having initially a $|\downarrow\rangle$-state. Left panel illustrates the energy levels alignment and right panel displays an example of ϕ_{REF} measurement over time. The charge energy level is lower than that of the Fermi sea: $\mu_S > |\downarrow\rangle$, thus the charge remains in the Coulomb blockade regime. In this case, there is nothing to see in reflectometry signal. (b) Similar schematics when having initially an $|\uparrow\rangle$-state. As $\mu_S < |\uparrow\rangle$, the charge can escape the QD back to the sensing dot, causing an abrupt change in reflectometry phase signal. Such event is also called "blip". The charge is immediately replaced by one being $|\downarrow\rangle$-state. The latter is -as explained in (a)- in the Coulomb blockade regime, no more blips are visible.

Experimental evidence of spin signature: Elzerman tail

So as to evaluate the readout voltage range, a scan close by the interdot transition is performed using the AWG sequences displayed in figure 3.6(a). It consists in 3 distinct stages:

- (E)-stage to Empty the dot and remove the remaining $|\downarrow\rangle$-spin. The spin states are pulsed far above the Fermi energy level at $+V_{\mathrm{plunge}} = 2\,\mathrm{mV}$, such that it is energetically favourable for both spin states to escape QD_3. This stage is aimed to last for $t_{\mathrm{plunge}} = 20\,\mu\mathrm{s}$, much longer than the expected timescale to escape the dot. Importantly, voltage plunge values are expressed at the sample level and take into account the attenuation throughout the fridge (40 dB in this case).
- (L)-stage to Load the QD with an unknown spin orientation. The charge entering the dot randomly has an $|\uparrow\rangle$- or $|\downarrow\rangle$-spin state. To this aim, spin energy levels are deeply pulsed below the Fermi energy at $-V_{\mathrm{plunge}} = -2\,\mathrm{mV}$. This stage also lasts for t_{plunge} duration for similar reasons when comparing to tunnelling timescales.
- (R)-stage to Readout by the aforementioned method the spin orientation that has been loaded. The Fermi level is set in between the spin energy levels to allow for spin-to-charge conversion. At this stage, phase reflectometry signal is recorded, revealing the presence/absence of blip depending on the spin orientation (as in fig. 3.5). Time-traces are recorded for a duration of

$t_{\text{read}} = 500\,\mu\text{s}$.

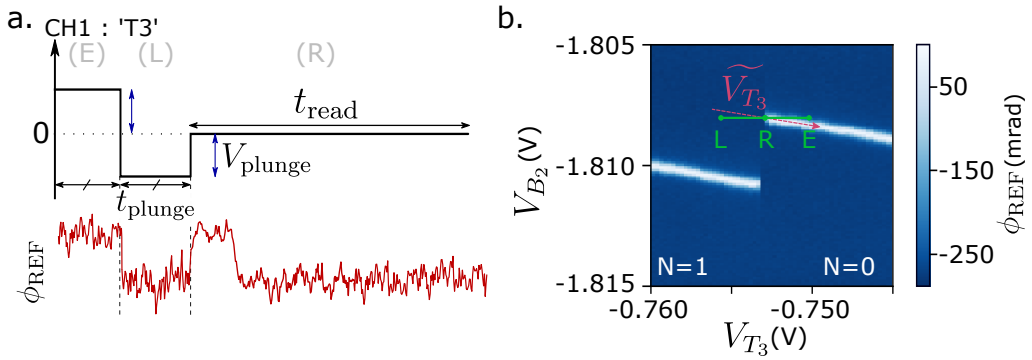

Figure 3.6 – **Interdot transition studied by Elzerman readout and AWG sequences:** (a) AWG waveform sequences applied on gate T_3, consisting of 3 stages: empty/load the QD (E)/(L) and read (R) by reflectometry. Lower panel is an example of phase reflectometry measurement in the case of an $|\uparrow\rangle$-spin state originally in the QD. Typical values of t_{plunge}, V_{plunge} and t_{read} are given in the main text. (b) First hole interdot transition visible in phase reflectometry. Detuning parameter $\widetilde{V_{T_3}}$ is defined as linear combination of voltages from gate T_3 and B_2 in order to scan across the interdot transition. Additionally, AWG sequences presented in panel (a) are added by the bias-tee. Their effect is sketched by the green line with the 3 distinct stages (E), (L) and (R).

AWG sequences are sent through RF lines and added at the sample level (bias-tees) to the DC gate voltage. We define a detuning axis parameter $\widetilde{V_{T_3}} = \gamma V_{T_3} + \eta V_{B_2}$ to scan through the interdot transition and compensate for the cross-talk between the two gates. Values of γ and η are experimentally measured so that $\gamma \simeq 1$ and $\eta \simeq -0.15$. Panel (b) of figure 3.6 illustrates the interdot transition with the detuning axis (red dashed line) added to the AWG sequences (green line) with the 3 stages.

As the signal induced by spin readout is faint, time-traces are averaged 2000 times for each DC bias voltage $\widetilde{V_{T_3}}$. Figure 3.7(a) shows a phase reflectometry measurement during (R)-stage, revealing different regimes delimited by the white dashed lines. On the left, spin states lay well below the Fermi energy, QD_3 is constantly filled, thus phase reflectometry signal is constant (dark blue). When decreasing $\widetilde{V_{T_3}}$ (or increasing the QD energy states), the higher energy spin level ($|\uparrow\rangle$) will align with the Fermi energy, allowing for charge exchange, as underscored by the dashed line with a red star. The corresponding energy levels are also sketched in upper panel of figure 3.7(b). In between the two dashed lines, voltage $\widetilde{V_{T_3}}$ is set such that the Fermi energy level stands within the spin splitting. In this case, spin signature is visible at the beginning of the readout stage as an increase of ϕ_{REF} signal (presence of blips) [3]. The second dashed line highlights the

3. Note that the spin signature is longer close by the red star compared to the pink one. This suggests that the tunnelling rates of the $|\uparrow\rangle$- and $|\downarrow\rangle$-spin state to the reservoir differ. So far, no

gate voltage on T_3 allowing for the $|\downarrow\rangle$-spin state to line up with the Fermi energy (see lower panel of figure 3.7(b)). This feature is also known as "Elzerman tail". Importantly, the distance between the two dashed lines is directly proportional to the spin splitting E_Z and the lever-arm α of T_3 on its quantum dot. Finally, when the two spin states are above the Fermi energy, QD_3 is empty, therefore the phase signal (light blue) is constant.

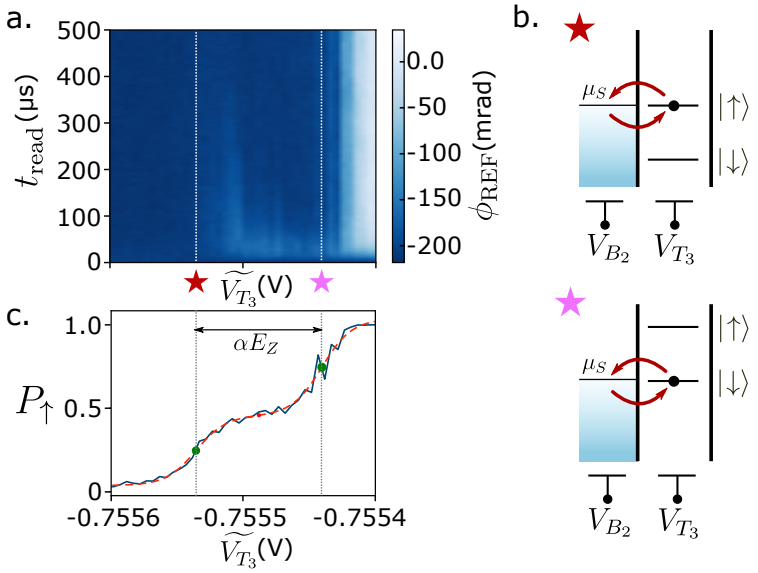

Figure 3.7 – **Spin selective readout by Elzerman readout:** (a) Phase reflectometry measurement for various gate voltage values on T_3 (only displayed during Read stage) and averaged over 2000 repetitions. Integration time is set at 5 µs and $\mathbf{B} = (0.95, 0.0, 0.0)$ T. White dashed lines highlight particular energy levels alignment sketched in panel (c). (b) Schematic of sensing dot and QD_3 energy levels. Left (right) panel corresponds to $|\uparrow\rangle(|\downarrow\rangle)$-spin state resonating with the sensor. (c) Averaged $|\uparrow\rangle$-state probability as a function of V_{T_3} corresponding to measurement in (a). Fit displayed in red dashed line allows to evaluate the gate voltage needed to align energy levels of the QD and that of the sensing dot. The distance between the two dashed lines is about $\delta V \simeq 95.3\,\mu\text{V}$ and directly relates to the Zeeman energy and the lever-arm α of the gate on QD_3.

The phase reflectometry signal $\phi_{\text{REF}}(t)$ recorded in panel (a) can be averaged in time and is compared to a threshold value to extract the probability of having an $|\uparrow\rangle$-spin state. This parameter is denoted $P_\uparrow$ and is plotted as a function of gate voltage $\widetilde{V_{T_3}}$ in figure 3.7(c). It manifests 3 major plateaus depending on the dot filling. When the dot is filled with one charge (left region), far in the Coulomb blockade regime the probability to have blip events is 0 as charge exchange is forbidden. In this case, the probability to overcome the defined threshold is 0. Within the Elzerman readout range (between the dashed lines), charge exchange

clear explanation is found.

is possible and a hole can enter the dot with an equal probability of being $|\downarrow\rangle$- or $|\uparrow\rangle$- state. As a consequence, $P_\uparrow$ should saturates around 0.5 value. Finally, when the dot is empty, the phase reflectometry signal is constantly above the threshold, thus $P_\uparrow$ equals 1. Note that by measuring a single time-trace and comparing to a threshold value enables to figure out charging events in a single-shot manner.

As mentioned previously, the distance between the two dashed lines directly relates to the lever-arm of the gate on its QD and the spin splitting. So far, two unknown quantities remain: the lever-arm α and the g-factor, responsible for the Zeeman splitting $E_Z \propto g$. Knowing one quantity [4] would thus allow for a rough, but efficient, estimation of the other. Due to the nature of holes, the energy level of the sensing dot follows, in reality, a Fermi distribution function, readily visible at the dashed line position. The $|\uparrow\rangle$-spin state probability can be fitted using the following formula:

$$P_\uparrow(V_{T_3}) = \frac{\alpha}{e^{\frac{-(V_{T_3}-V^0_{T_3})}{\delta V}}+1} + \frac{(1-\alpha)}{e^{\frac{-(V_{T_3}-V^1_{T_3})}{\delta V}}+1} + B \tag{3.3}$$

with,

α *the gate lever-arm on the dot* QD_3*,*

B *an offset value,*

$V^i_{T_3}$*, with* $i = \{0, 1\}$*, the gate voltage value at the inflexion point (i.e. at the dashed line position),*

δV *the Fermi distribution width at the inflexion point.*

The red dashed line is the fit using equation 3.1.3. Green points emphasize the inflexion point of gate voltage values (hence the dashed lines). In this example, Electrically Driven Spin Resonance measurement has been conducted at a same magnetic field orientation, revealing a Larmor frequency $f_L \simeq 11.92\,\mathrm{GHz}$. The resulting g-factor is $g_{\vec{n}} = 0.89$. Knowing both the g-factor and the Elzerman tail range δV permits to evaluate a gate lever-arm $\alpha \simeq 0.52\,\mathrm{eV\,V^{-1}}$. Despite the split gate geometry possibly having a weaker lever-arm than pump architecture, this rather large influence of T_3 on its QD permits an accurate control over the hole confinement.

Until now, the discussion focused on the experimental realization of a nearby charge sensor to probe the spin orientation of a hole particle inside a QD by Elzerman readout. This method permits to discriminate $|\uparrow\rangle$- and $|\downarrow\rangle$-states in a single-shot manner. Yet, the possibility to control the spin orientation remains to be implemented.

4. The g-factor value can readily be estimated by Electrically Driven Spin Resonance (EDSR) (see section 3.2.1).

3.2 Spin manipulation

One key feature of hole particles is that they exhibit an intrinsically strong Spin-Orbit Coupling (SOC). This enables spin manipulation using only electric fields [1, 38, 39] in contrary to electrons that often necessitate additional micromagnet to artificially increase the SOC or ESR line creating a slanting B-field responsible for spin control [40, 41]. Remarkably, on-demand electrical control of electron spin has been demonstrated in a Si-MOS structure with proper wavefunction hybridisation tuning between two QDs [5] [42]. Controlling such a spin state with electrical fields is known as "Electrically Driven Spin Resonance" (EDSR). In the following sections, EDSR measurements are performed in order to evaluate the spin Larmor frequency depending on external magnetic field orientation. In turn, this allows to infer the hole g-matrix, which constitutes a useful asset for modelling and give precious insights on physical phenomena at stake, among which charge noise contribution [10, 43, 44].

3.2.1 Electrically Driven Spin Resonance (EDSR)

In Elzerman readout procedure, the hole filling QD_3 at the end of (R)-stage is necessarily in the Coulomb blockage regime thus $|\downarrow\rangle$-stated. Indeed, either the loaded spin was already in $|\downarrow\rangle$-state or the initial $|\uparrow\rangle$-state has tunnelled out from the dot and has been replaced by a $|\downarrow\rangle$-spin. Owing to the (E)-stage, the hole stored within the QD is lost in the Fermi sea and another hole with unknown spin orientation ($|\uparrow\rangle$- or $|\downarrow\rangle$-) replaces it. As a consequence, removing the (E)-stage from Elzerman readout sequence is a way to initialize the hole spin orientation in the QD. Such AWG sequence is displayed in upper panel of figure 3.8(a), with a loading stage of $t_{\text{plunge}} = 20\,\mu\text{s}$ and $-V_{\text{plunge}} = -2\,\text{mV}$. The readout duration is $t_{\text{read}} = 500\,\mu\text{s}$.

In order to manipulate the hole spin state, sinusoidal MW signals are sent to the gate T_3 for a duration $t_{\text{burst}} = 5\,\mu\text{s}$ at a frequency denoted f_{MW} (see lower panel of figure 3.8(a)). If the MW frequency matches the spin Larmor frequency, the $|\downarrow\rangle$-spin state is stimulated to transition to its first excited state ($|\uparrow\rangle$). Consequently, the hole escapes the dot and triggers a detectable blip in reflectometry signal. Conversely, if the MW frequency significantly deviates from the Larmor frequency, the hole spin remains in its ground state ($|\downarrow\rangle$), and no change in reflectometry signal is recorded. This distinction in outcomes based on the frequency matching underscores the successful electrical spin manipulation [45]. In other words, the $|\uparrow\rangle$-state probability $P_\uparrow$ should evidence a peak as a function of MW frequency when matching the Larmor frequency. Figure 3.8(b) shows an example of such EDSR measurement when the MW tone is swept nearby the Larmor

5. Near the degeneracy point, the coupling of electron spins with their movement is enhanced by three orders of magnitude, opening the path towards EDSR operation for electron spins without on-chip micromagnet.

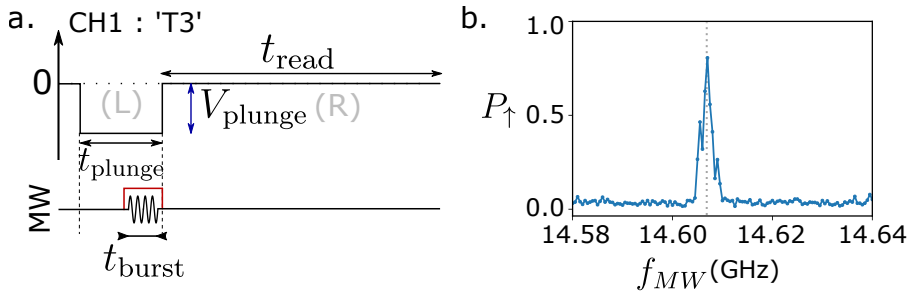

Figure 3.8 – **Electrically Driven Spin Resonance AWG sequences and measurement:** (a) AWG sequences used for EDSR measurements. A loading stage (L) of duration t_{plunge} permits to fill QD_3 with a hole particle. In the meantime, MW signals aiming to drive the spin state to an incoherent superposition of state is sent during t_{burst}. Pulse Modulation technique (displayed in red) is used to ensure no spurious leakage of MW signals. After manipulation, the spin state is readout by Elzerman method for a time t_{read}. Values of t_{plunge}, V_{plunge} and t_{read} are given in the main text. For each data points in panel (b), the measurements are repeated 2000 times and averaged. (b) Example of EDSR measurement. The $|\uparrow\rangle$-state probability is probed as a function of MW frequency f_{MW}. Whenever f_{MW} matches the Larmor frequency, the spin is driven to its excited state ($|\uparrow\rangle$) and can escape the dot, and is detected as a blip signature. When averaged over many iterations, the probability $P_\uparrow$ therefore increases, as readily highlighted by the dotted line.

frequency for an external magnetic field set at $\mathbf{B} = (0.865, 0.498, 0)$ T. A drastic increase in $|\uparrow\rangle$-spin state population is observed at $f_{\mathrm{MW}} = f_L \simeq 14.607$ GHz signalled by the dotted line. From such measurement, the g-factor can be inferred as : $g = {}^{h}f_L/\mu_B||B||$. Finally, we extract $g \simeq 1.046$ at this magnetic field orientation.

The strong SOC of hole particles, which allows for all-electrical driving, also favours HH-LH mixing in the case of strongly confined systems (e.g. QDs, see chapter 1 section 1.3.2). This phenomenon renders the hole g-matrix highly anisotropic with respect to magnetic field. The following section aims at evaluating such anisotropy as a function of field orientation using EDSR method.

3.2.2 g-matrix mapping

In numerous quantum systems utilizing hole spin particles, significant anisotropy in the g-factors has been reported. This observation provides valuable insights into the confinement of wavefunctions and their interaction with the surrounding environment [10, 14, 15, 46, 47].

Figure 3.9 gathers the inferred g-factors (blue dots) by EDSR measurement depending on the external magnetic field orientation. Each panel corresponds to a magnet plane accordingly to the coordinate system defined in fig. 3.1. The first hole confined within QD_3 exhibits a highly anisotropic g-matrix, ranging from

$g_{\min} \sim 0.89$ to $g_{\max} \sim 3.2$. The large g-factor values nearby the $\vec{p}$-axis suggests a strong hole wavefunction confinement in this direction. It can indeed be understood, as arising from the gate voltage difference between T_3 and B_3 that creates an important electric field perpendicularly to the Si-channel. A much weaker wavefunction confinement is deduced from the g-matrix along the nanowire direction $\vec{n}$. Furthermore, a clear tilt is found out of about 19° compared to the principal magnet axes in the center panel. Such mismatch between the spin basis and magnetic one is most likely attributed to the presence of strain [44, 48], and can marginally be due to the misalignment of the device to magnetic axes.

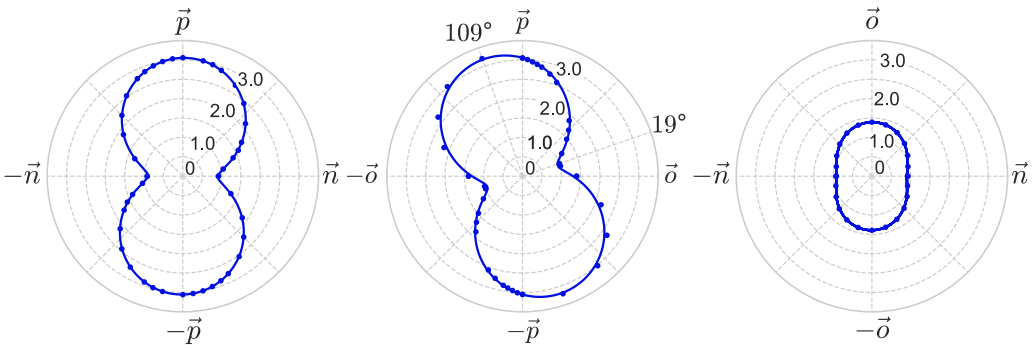

Figure 3.9 – **Spin resonance mapping with respect to magnetic field orientation:** Estimated g-factors as a function of magnetic field angle. Each panel corresponds to a principal magnet plane (from left to right: (NP), (OP), (NO) defined in figure 3.1). A strong anisotropy in magnetic field orientation is observed, ranging from $g_{\min} \sim 0.89$ to $g_{\max} \sim 3.2$. Solid line is a fit using formula 3.4.

The solid line is a fit of using the g-matrix formalism including measurements for all magnetic field orientations (see chapter 1 sec.1.4 for details). Equation 3.4 links the G-tensor and the measured Larmor frequency. Knowing at least six independent values of the Larmor frequency with respect to magnetic field orientation permits to evaluate the G-tensor element and consequently deduce the hole g-matrix:

$$\hbar f_L = \mu_B \sqrt{\mathbf{b}^T G \mathbf{b}} \qquad \text{and} \qquad G = g^T g = V g_d V^{\mathrm{T}}, \tag{3.4}$$

As a reminder, the above defined G-tensor accounts for the possible rotation with the principal directions of magnetic field (V) while conveying the square of hole g-matrix eigenvalues, denoted g_d^2. Subsequently, evaluating the G-tensor enables to figure out the hole spin Larmor response for any magnetic field orientations. We use least-square minimization fitting procedure to extract the elements:

$$G = \begin{bmatrix} 0.815 & 0.023 & 0.148 \\ 0.0228 & 1.943 & -2.824 \\ 0.148 & -2.824 & 9.320 \end{bmatrix}_{\{\vec{n},\vec{o},\vec{p}\}} \tag{3.5}$$

Finally, the principal g-factors values in the spin basis are estimated (up to a sign) after G-tensor diagonalization:

$$\boxed{\text{eigvals}(g) = \sqrt{\text{eigvals}(G)} = [1.005, 0.888, 3.206]_{\{\vec{n},\vec{o},\vec{p}\}}} \tag{3.6}$$

Experimental measurements of the G-tensor can be supported by theoretical calculations [6] while still relying on g-matrix formalism. This provides a useful asset for deep understanding of the first hole wavefunction confinement profile $|\psi(\mathbf{r})\rangle$ within QD_3 and its response upon electrical manipulation (i.e. Larmor and Rabi frequencies variations) [10, 49, 50].

To this aim, the device is meshed as a [110]-oriented Si-nanowire, topped by 40 nm wide gates, themselves separated by Si_3N_4 spacers. To reduce the simulation complexity, only 3-split gates are taken into consideration. The model includes strain, material specific properties (e.g. dielectric constants, disorder, surface roughness [51]) which defines the structural electrostatic potential $U_{\text{struc}}(\mathbf{r})$. The silicon band-structure is computed using 4-bands $\mathbf{k}\cdot\mathbf{p}$ model captured by the term $\mathcal{H}_{\mathbf{k}\cdot\mathbf{p}}$. Given the experimental gate voltages and meshing, the electrostatic landscape $U_{\text{elec}}(\mathbf{r})$ is calculated by finite volume Poisson equation solver. Finally, in presence of external magnetic field, an additional term $U_{\text{magn}}(\mathbf{r})$ enters into play [49]. The latter is calculated with first-order perturbation theory with respect to magnetic field as the Zeeman energy (thus the g-matrix) scales linearly with $\mathbf{B}$. As a result, the Hamiltonian to solve takes the form :

$$\mathcal{H}(V,\mathbf{B}) = \mathcal{H}_{\mathbf{k}\cdot\mathbf{p}} + U_{\text{struc}}(\mathbf{r}) + U_{\text{elec}}(\mathbf{r}) + U_{\text{magn}}(\mathbf{r}) \tag{3.7}$$

The hole wavefunction $|\psi(\mathbf{r})\rangle$, solution of $\mathcal{H}(V,\mathbf{B})\,|\psi(\mathbf{r})\rangle = E\,|\psi(\mathbf{r})\rangle$, is then computed by resolving the Schrödinger equation with finite difference method. Figure 3.10(a) and (b) displays the calculated hole wavefunction defining QD_3 within the device in top and transversal view. The g-matrix is finally obtained by identification of the diagonalized term $U_{\text{magn}}(\mathbf{r})$ compared to the system Hamiltonian in the heavy hole subspace: $\mathcal{H}(V,\mathbf{B}) = {}^1\!/_2\mu_B\boldsymbol{\sigma}\cdot g(V)\mathbf{B}$ (see ref.[49]).

The first hole accumulating in QD_3 actually locates under the spacer on the edge of gate T_3 in accordance with previous modellings done in the group, see ref.[52]. A strong confinement towards the nanowire facet is readily visible in panel (b), suggesting that a major electric field responsible for hole confinement comes perpendicularly to the Si-channel. Such conclusion stands in good agreement with the large g-factor values measured close by $\vec{p}$-axis.

3.2.3 Digression about coherent spin manipulation

A qubit is defined by the ability of a two-level system to be (i) initialized, (ii) coherently manipulated and (iii) readout. So far, we demonstrated that the spin

6. Modelling and computations are performed by E. A. Rodríguez-Mena with the help of L. Mauro and Y.-M. Niquet from CEA, IRIG-MEM-LSim group.

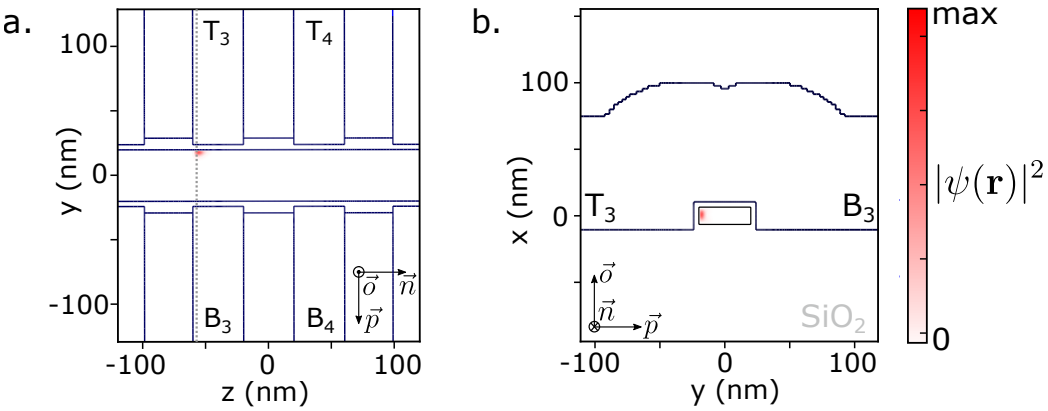

Figure 3.10 – **Simulation of the first hole wavefunction:** (a) Top view of the device with gate boundaries in black. The hole wavefunction (red area) is mostly located by the side of gate T_3 towards T_2. Note that these simulations emulate a simplified system with only 3-split gates and do not take into account the nearby strongly accumulated charge sensor. (b) View across the nanowire of first hole wavefunction confinement. Herein, the hole in highly squeezed onto the nanowire facet, suggesting that the main electrostatic potentials responsible for confinement profile acts perpendicularly to the Si-channel. Cut taken at $z = -57\,\text{nm}$ in panel (a).

orientation can be initialized, readout and flipped by the means of EDSR. However, the spin does not necessarily maintain its coherence for long driving duration. To this aim, AWG sequences presented in figure 3.8 remain the same, except that MW burst duration is decreased down to 1 µs or below. Following figure 3.11 illustrates the $|\uparrow\rangle$-state probability probed as a function of the MW tone (close by Larmor frequency) and the MW burst duration. It exhibits alternating phases of high and low $P_\uparrow$ values, revealing a so-called "Rabi chevron" pattern, signature of coherent control of hole spin qubit. For an external magnetic field $\mathbf{B} = (0, 0.95, 0)\,\text{T}$, the qubit Rabi frequency is about $f_R \sim 5\,\text{MHz}$ (extraction of the qubit Rabi frequency is detailed in chapter 4 sec.4.2.2).

3.3 Evaluation of the longitudinal contribution $\beta_\parallel$ of charge noise

Strong spin-orbit interaction is an ambivalent property for hole spins. On the one hand, it allows for fast and low-power electrical manipulation (EDSR), even performed at high temperature regime (few Kelvin) [9]. On the other hand, it exposes the qubit to electrical noise stemming from its nearby environment. Such charge noise contribution is known to be the main source of decoherence for spin qubit system [8, 11, 12]. Many experimental efforts have been made to cope with the charge noise contribution evidencing dephasing sweetspots in gate voltage [8, 13] or magnetic field orientations [10, 15]. At these sweetspots, the longitudinal contribution of charge noise vanishes, therefore the qubit coherence time is maxi-

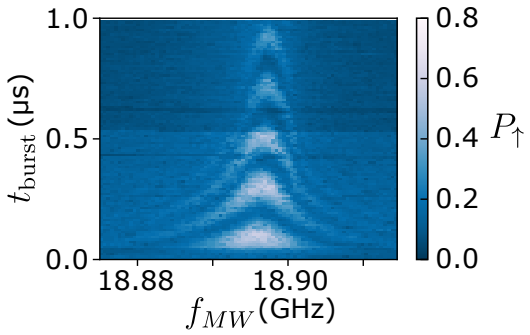

Figure 3.11 – **Coherent spin manipulation:** $|\uparrow\rangle$-spin state probability as a function of driving MW tone and burst duration. Alternating high and low values of $P_\uparrow$ reveal coherent manipulation of the spin state. This measurement is also referred as "Rabi chevron" and is recorded at $\mathbf{B} = (0, 0.95, 0)$ T.

mized reaching up to $T_2^E = 88\,\mu$s in Si-MOS device [10]. These studies have been corroborated by numerous theoretical simulations [44, 53, 54, 55].

As mentioned in the previous chapter in section 1.4.2, charge noise contribution can be casted into two distinct contributions : a longitudinal term $\beta_\parallel$ responsible for decoherence, and a transverse term $\beta_\perp$ which accounts as a spin driving contribution. In the following, the attention is primarily drawn onto the characterization of the longitudinal component of charge noise with respect to magnetic field orientation. Since the oxides separating the Si-nanowire (hence the qubit) from the gate are known to be significant source of charge noise, we assume that the primary source of charge noise affecting the qubit can be studied considering voltage fluctuations of the host gate T_3[7], as discussed in refs. [10, 44]. As the qubit behaviour is actually strongly constrained by the gate, it is worth defining the longitudinal spin electric susceptibility, herein denoted $\beta_\parallel$ by abuse of language, as the first derivative of Larmor frequency with respect to gate voltage V_{G_n}.

The first section emphasizes the experimental implementation of $\beta_\parallel$ measurement versus magnetic field. Subsequently, $\beta_\parallel$ anisotropy is examined, followed by a detailed evaluation of the G'-tensor.

3.3.1 First-order longitudinal contribution of charge noise

Probing the longitudinal component of charge noise $\beta_\parallel$ boils down to evaluate the Larmor frequency shift induced by an extra plunge pulse on T_3, whose amplitude is denoted δV_{T_3} so that $\beta_\parallel \propto \partial f_L / \partial \delta V_{T_3}$. In figure 3.12(a) are depicted the AWG sequences sent at the sample level to assess $\beta_\parallel$. In comparison to EDSR se-

7. In reality, the spacers around the gates are also a significant source of charge noise. Therefore, all gate voltage variations should be taken into account to fully capture the charge noise anisotropy.

quences (fig.3.8(a)), two stages are added after spin manipulation (L) and readout (R). First stage (C1) is a compensating step to ensure that the DC bias level of the overall sequence is 0 after being filtered and biased. As the amplitude of (C1) is $+\delta V_{T_3}$, the hole particle will escape the dot, acting similarly to an empty stage in Elzerman readout method. (C2) period, whose duration is $t_{\text{read}} = 500\,\mu\text{s}$, aims at loading the dot again with a $|\downarrow\rangle$-spin state.

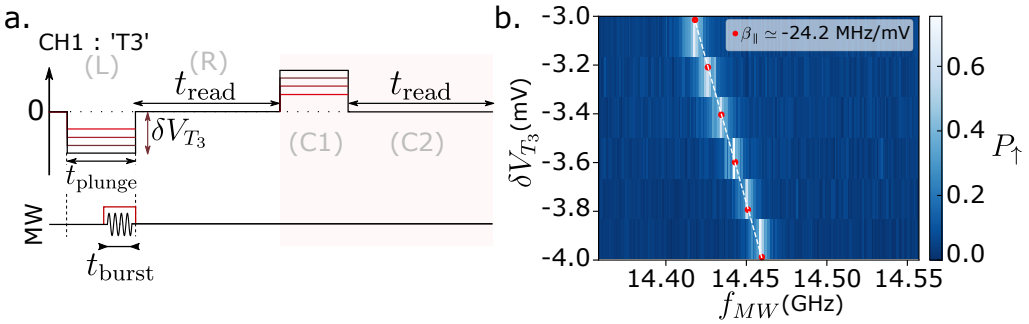

Figure 3.12 – **AWG sequences used for $\beta_{\parallel}$ evaluation:** (a) Adapted EDSR sequences for $\beta_{\parallel}$ estimation. During qubit control stage (L), the plunge amplitude δV_{T_3} is varied to evaluate how much the qubit Larmor frequency is shifted. Microwave tone is sent for a duration $t_{\text{burst}} = 5\,\mu\text{s}$. Readout stage lasts 500 µs. Two stages (C1) and (C2) are added to maintain the sequence DC value to 0 when passing through filters and bias-tees, illustrated by the red shaded area. (b) $|\uparrow\rangle$-state probability as a function of MW tone and plunge value on gate T_3. The sequence is repeated, thresholded and averaged 2000 times to evaluate $P_{\uparrow}$. For each value of δV_{T_3}, the frequency sweep is fitted with a Lorentzian function to extract the Larmor frequency value (red points). A linear regression of the evaluated Larmor values compared to the plunge amplitudes gives $\beta_{\parallel} = {}^{\partial f_L}/_{\partial \delta V_{T_3}} \simeq -24.2\,\text{MHz}\,\text{mV}^{-1}$ as highlighted by the white dashed line in this instance.

An example of $P_{\uparrow}$ measurement as a function of MW tone and plunge amplitude is shown in figure 3.12(b) for a magnetic field $\mathbf{B} = (0.704, 0.0, 0.256)\,\text{T}$. The Larmor frequency, showcased by the red points, is estimated for each value of plunge amplitude by fitting $P_{\uparrow} = \mathcal{L}(f_{\text{MW}})$ with a Lorentzian function $\mathcal{L}$. The value of spin susceptibility $\beta_{\parallel}$ is then obtained by a linear regression of f_L values versus δV_{T_3}, herein $\beta_{\parallel} \simeq -24.2\,\text{MHz}\,\text{mV}^{-1}$ (white dashed line). In this situation, the Larmor frequency experiences a shift as long as the plunge amplitude is varied due to the longitudinal charge noise contribution, i.e. $\beta_{\parallel} \neq 0$, so this is not a sweetspot.

Such experiment can be repeated with different magnetic field orientations as illustrated in figure 3.13(a). Each panel corresponds to a principle magnet plane and evidences a strong anisotropy of longitudinal spin susceptibility depending on field orientation, ranging from $\min(\beta_{\parallel}) \sim -80\,\text{MHz}\,\text{mV}^{-1}$ to $\max(\beta_{\parallel}) \sim 5\,\text{MHz}\,\text{mV}^{-1}$. Yet, 4 particular points exhibit a zero-sensitivity to charge noise induced by the gate T_3 as underscored by the red arrows: there are 4 sweetspots between (OP) and (NP) planes. Remarkably, the sweetspots appear in different magnet planes

than in ref.[10] which is imputed to gate layout differences (ref.[10] is using "pump" geometry, whereas herein this is "split" gate device). Gate geometry plays a key role in hole wavefunction confinement and therefore in charge noise response [44]. In the following, spin susceptibility values will be displayed in one map, depending on their magnetic spherical coordinates (ψ, θ) as defined in figure 3.13(b).

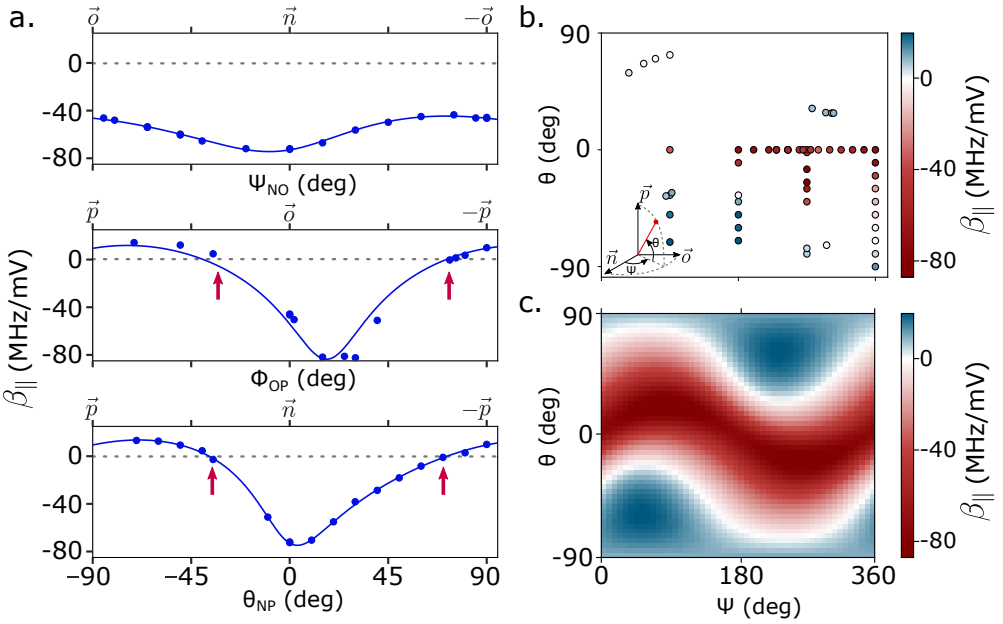

Figure 3.13 – **Longitudinal contribution of charge noise depending on magnetic field orientation:** (a) Measured values of first-order longitudinal contribution of charge noise $\beta_\parallel$ as a function of magnetic field angle. Both panel correspond to a principal magnet plane ((NO), (OP) and (NP)). Red arrows highlight four magnetic field orientations of zero-sensitivity to first-order charge noise contribution, i.e. sweetspots. Solid line is a fit (see main text for details). (b) All $\beta_\parallel$ measurements gathered versus magnetic field orientation defined by θ and ψ angles. System coordinate is displayed in the bottom left accordingly to $\vec{n}$, $\vec{o}$ and $\vec{p}$ magnet axes. (c) Fitted values of $\beta_\parallel$ depending on the field orientation. Zero-sensitivity to longitudinal charge noise forms a continuum highlighted by the white line: the sweetline. Moreover, a strong anisotropy in $\beta_\parallel$ depending on field orientation is visible.

With the $\partial f_L/\partial \delta V_{T_3}$ measurements and knowing the G-tensor from equation 3.5, it is possible to reconstruct the complete variation of $\beta_\parallel$ as a function of magnetic field orientation as in equation 3.8. Importantly, all measurements are rescaled at a chosen reference frequency $f_L = 17.99\,\mathrm{GHz}$.

$$\beta_\parallel(\mathbf{B}) = \left.\frac{\partial f_L}{\partial \delta V_{T_3}}\right|_{f_L=17.99\,\mathrm{GHz}} = \frac{\mu_B B}{h}\frac{\mathbf{b}^T \cdot G' \cdot \mathbf{b}}{2\sqrt{\mathbf{b}^T \cdot G \cdot \mathbf{b}}} \tag{3.8}$$

In this equation, only G'-tensor, defined as $\partial G/\partial \delta V_{T_3}$, remains unknown. At

least nine independent measurements of $\beta_{\parallel}$ would therefore allow to reconstruct G'-tensor using least-square fitting method as previously. We finally obtain:

$$G' = \begin{bmatrix} -9.410 & 1.004 & -4.736 \\ 1.004 & -9.235 & -7.340 \\ -4.736 & -7.340 & 4.110 \end{bmatrix}_{\{\vec{n},\vec{o},\vec{p}\}} \tag{3.9}$$

and the corresponding eigenvalues:

$$\boxed{\text{eigvals}(G') = [8.607, -10.241, -12.900]_{\{\vec{n},\vec{o},\vec{p}\}}} \tag{3.10}$$

Figure 3.13(c) shows the complete variations of $\beta_{\parallel}$ depending on magnetic field orientation when fitted with the extracted G'-tensor using equation 3.8. Alongside a strong anisotropy in field orientation, $\beta_{\parallel}$ values evidence two continuous lines of zero-sensitivity to charge noise induced by the above gate voltage fluctuations. These "sweetlines" for charge noise open the path to optimal operation points for silicon spin qubit with enhanced coherence times, while extending the dimension of already reported sweetspots [10, 44]. Note that the nature of the dephasing sweetspots coincides with the theoretical predictions in table 1.2 in chapter 1, forecasting the existence of two sweetlines regarding the sign of G'-matrix eigenvalues $(+,-,-)$[8]. Moreover, G'-matrix enables to figure out the sweetline equation in magnetic field, which obeys the condition: $\mathbf{b}^T G' \mathbf{b} = 0$.

Considering gate voltage fluctuations as the primary source of charge noise, we assessed the first-order longitudinal contribution $\beta_{\parallel}$ experienced by the hole spin qubit originating from its gate T_3. This investigation unveils the presence of a continuous line of Larmor insensitivity ($\partial f_L / \partial \delta V_{T_3} = 0$), also known as "sweetlines". This first experimental demonstration, consistent with theoretical forecasts [44], expands the dimension of sweetspots, facilitating qubit operation at these optimal dephasing points. Yet, strictly speaking, the resulting charge noise contribution experienced by the spin qubit is the sum of all fluctuations induced by the surrounding gates (refer to chapter 1). In order to validate the presence of sweetlines in the discussed system, we evaluate -in the following section- the second-order term of charge noise $\beta_{\parallel}^{(T_4)}$, relative to the first neighbouring gate T_4.

3.3.2 Assessing second-order of longitudinal charge noise

This section focuses on the evaluation of the spin sensitivity to voltage fluctuations of a nearby gate T_4, which stands few tens of nanometers apart from the dot. This quantity is denoted as:

$$\beta_{\parallel}^{(T_4)}(\mathbf{B}) = \frac{\partial f_L}{\partial \delta V_{T_4}}(\mathbf{B}) \tag{3.11}$$

8. G'-matrix originates from two distinct contributions: the modulation of both g-matrix and principal magnetic axes (see details in chapter 1). So far, no indications on such contributions are provided while knowing G'.

To evaluate how much the spin Larmor frequency is affected by changes in V_{T_4}, AWG sequences displayed in figure 3.14(a) are implemented. The sequences sent on channel related to gate T_3 and on microwave source remain the same than in EDSR measurement. A loading (L)-stage ensures that the dot is filled with a $|\downarrow\rangle$-spin state while being subject to a MW tone during $t_{\text{burst}} = 5\,\mu\text{s}$ at f_{MW}. In the meantime, high-frequency signals are sent to gate T_4 so as to modify its voltage value by δV_{T_4} for a period of t_{plunge}. Finally, the spin state is readout during (R)-stage for 500 µs. For sake of clarity, compensation stages (C1) and (C2), which are added to gate T_4, are not shown in the sequences but act for similar reasons than in previous section.

Longitudinal response of second-order gate fluctuations are shown in figure 3.14(b) in the principal magnet planes. Gate voltage variations of T_4 cause slight changes in the Larmor frequency, resulting in spin susceptibility ranging from $\min(\beta_{\parallel}^{(T_4)}) \sim -0.5\,\text{MHz}\,\text{mV}^{-1}$ to a maximum value of about $\sim 0.5\,\text{MHz}\,\text{mV}^{-1}$. In this case, the minor fluctuations of $\beta_{\parallel}^{(T_4)}$make it difficult to definitively conclude on the presence of sweetspots for T_4. Such lack of resolution in $\beta_{\parallel}^{(T_4)}$could have been circumvented by the use of Hahn-echo sequences as in ref. [10]. Nonetheless, it is worth mentioning that the absolute values of fluctuations caused by T_4 remain much weaker (by more than one order of magnitude) than the ones induced by gate T_3: $\beta_{\parallel}^{(T_4)} \ll \beta_{\parallel}$. As a consequence, charge noise contribution induced by gate voltage fluctuations will be, in the following chapters, mostly attributed to the gate hosting the hole spin qubit.

For sake of completeness, some assumptions in this section can be argued. Second-order contribution of charge noise has been evaluated using gate T_4, which demonstrates a readily inferior influence on the spin qubit than T_3. However, considering that the contribution of gate T_4 can equals the effect of gate T_2 (which is also first neighbouring gate to the qubit) is debatable. Indeed, the hole wavefunction, estimated in section 3.2.2, appears to be located closer to gate T_2 than T_4. Based on this reasoning, the dot location suggests a different influence of the two gates to the spin susceptibility, thus to charge noise. It is unfortunately impossible in this device to evaluate accurately the contribution of gate T_2 to the Larmor frequency shift owing to a limited number of high-frequency lines inside the fridge.

3.4 Conclusions

For the purpose of charge noise investigation, we conducted the experimental implementation of a single hole spin qubit inside a QD in Si-MOS architecture. Spin readout necessitates the presence of a nearby charge sensor, made of strongly accumulated QD, probed by dispersive sensing and Elzerman method. Leveraging the intrinsically strong spin-orbit interaction of hole particles, spin can be coher-

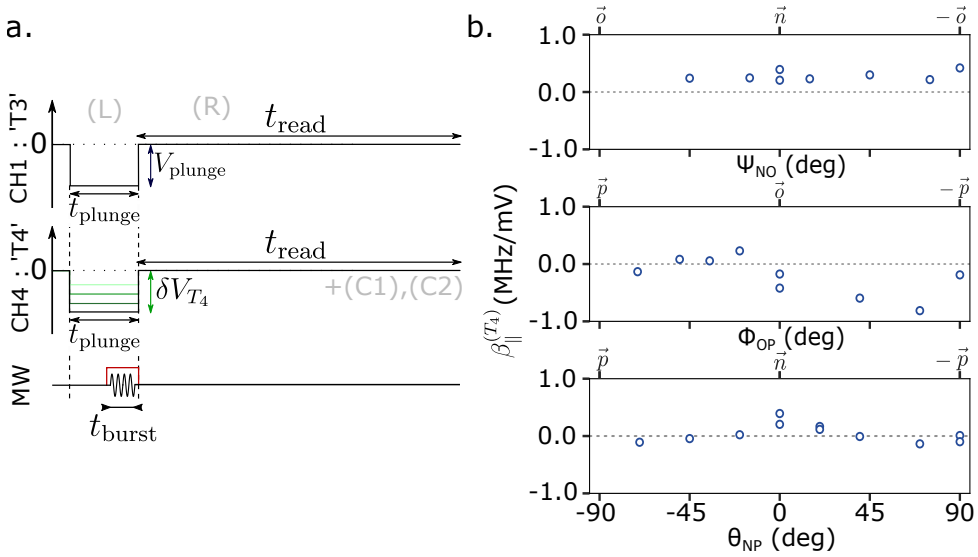

Figure 3.14 – **Second-order sensitivity to gate voltage fluctuations:** (a) AWG sequences to probe the spin susceptibility to gate voltage modifications T_4, denoted $\beta_{\parallel}^{(T_4)}$. In this case, gate voltage of T_3 alternates between a loading value $V_{\text{plunge}} = -2\,\text{mV}$ during $t_{\text{plunge}} = 20\,\mu\text{s}$ and a reading (R)-stage lasting for $500\,\mu\text{s}$. During spin manipulation, the voltage of the nearby gate T_4 is changed by δV_{T_4} amplitude value. The Larmor shift induced by δV_{T_4} is recorded as presented previously. Red signal represents the Pulse Modulation to avoid spurious leakages from MW tone. (b) Spin susceptibility to gate T_4, labelled $\beta_{\parallel}^{(T_4)}$, depending on magnetic field orientation. As previously displayed, each panel corresponds to a principal magnet plane (from top to bottom: (NO), (OP) or (NP)). The weak variations of $\beta_{\parallel}^{(T_4)}$renders any conclusions about the evidence of sweetspots for T_4 hard to draw.

ently manipulated by EDSR, enabling to map out the hole g-matrix with respect to magnetic field orientation. The latter provides pivotal keys to figure out the hole wavefunction location and its response to charge noise influence and upon driving (see next chapter). The first-order of charge noise experienced by the spin qubit, attributed to gate voltage fluctuations, manifests the presence of two sweetlines, i.e. zero-sensitivity, depending on magnetic field orientation. Moreover, we observed that the second-order of charge noise contribution (stemming from the nearby gate) is negligible in this case. Despite the lack of information on charge noise instigated by defects and fluctuators, this experimental realization paves the way towards spin qubit operation with enhanced coherence time [10] in specific magnetic field areas.

References

[1] R. Maurand et al. « A CMOS silicon spin qubit ». In: *Nature Communications* (May 2016). DOI: 10.1038/ncomms13575.

[2] N. W. Hendrickx et al. « A single-hole spin qubit ». In: *Nature Communications* 11.1 (July 2020), p. 3478. DOI: 10.1038/s41467-020-17211-7.

[3] M. Veldhorst et al. « A two-qubit logic gate in silicon ». In: *Nature* 526.7573 (Oct. 2015), pp. 410–414. DOI: 10.1038/nature15263.

[4] N. W. Hendrickx et al. « Fast two-qubit logic with holes in germanium ». In: *Nature* 577.7791 (2020), pp. 487–491. DOI: 10.1038/s41586-019-1919-3.

[5] N. W. Hendrickx et al. « A four-qubit germanium quantum processor ». In: *Nature* 591.7851 (Mar. 2021), pp. 580–585. DOI: 10.1038/s41586-021-03332-6.

[6] S. G. J. Philips et al. « Universal control of a six-qubit quantum processor in silicon ». In: *Nature* 609.7929 (Sept. 2022), pp. 919–924. DOI: 10.1038/s41586-022-05117-x.

[7] P. Stano and Daniel Loss. « Review of performance metrics of spin qubits in gated semiconducting nanostructures ». In: *Nature Reviews Physics* 4.10 (Oct. 2022), pp. 672–688. DOI: 10.1038/s42254-022-00484-w.

[8] Z. Wang et al. « Optimal operation points for ultrafast, highly coherent Ge hole spin-orbit qubits ». In: *npj Quantum Information* 7.1 (Apr. 2021), p. 54. DOI: 10.1038/s41534-021-00386-2.

[9] L. C. Camenzind et al. « A hole spin qubit in a fin field-effect transistor above 4 kelvin ». In: *Nature Electronics* 5.3 (Mar. 2022), pp. 178–183. DOI: 10.1038/s41928-022-00722-0.

[10] N. Piot et al. « A single hole spin with enhanced coherence in natural silicon ». In: *Nature Nanotechnology* 17.10 (Sept. 2022), pp. 1072–1077. DOI: 10.1038/s41565-022-01196-z.

[11] J. Yoneda et al. « A quantum-dot spin qubit with coherence limited by charge noise and fidelity higher than 99.9% ». In: *Nature Nanotechnology* 13.2 (2018), pp. 102–106. DOI: 10.1038/s41565-017-0014-x.

[12] F. N. M. Froning et al. « Ultrafast hole spin qubit with gate-tunable spin–orbit switch functionality ». In: *Nature Nanotechnology* 16.3 (Mar. 2021), pp. 308–312. DOI: 10.1038/s41565-020-00828-6.

[13] M. J. Carballido et al. *A Qubit with Simultaneously Maximized Speed and Coherence*. arXiv. 2024. DOI: 10.48550/arXiv.2402.07313.

[14] T. Tanttu et al. « Controlling Spin-Orbit Interactions in Silicon Quantum Dots Using Magnetic Field Direction ». In: *Physical Review X* 9 (2 May 2019), p. 021028. DOI: 10.1103/PhysRevX.9.021028.

[15] N. W. Hendrickx et al. *Sweet-spot operation of a germanium hole spin qubit with highly anisotropic noise sensitivity*. arXiv. 2023. DOI: 10.48550/arXiv.2305.13150.

[16] J. M. Elzerman et al. « Single-shot read-out of an individual electron spin in a quantum dot ». In: *Nature* 430.6998 (July 2004), pp. 431–435. DOI: 10.1038/nature02693.

[17] A. Morello et al. « Single-shot readout of an electron spin in silicon ». In: *Nature* 467.7316 (Oct. 2010), pp. 687–691. DOI: 10.1038/nature09392.

[18] M. Veldhorst et al. « An addressable quantum dot qubit with fault-tolerant control-fidelity ». In: *Nature Nanotechnology* 9.12 (Dec. 2014), pp. 981–985. DOI: 10.1038/nnano.2014.216.

[19] E. Chanrion et al. « Charge Detection in an Array of CMOS Quantum Dots ». In: *Phys. Rev. Appl.* 14 (2 Aug. 2020), p. 024066. DOI: 10.1103/PhysRevApplied.14.024066.

[20] R. Hanson et al. « Spins in few-electron quantum dots ». In: *Reviews of Modern Physics* 79 (4 Oct. 2007), pp. 1217–1265. DOI: 10.1103/RevModPhys.79.1217.

[21] R. Mizuta et al. « Quantum and tunneling capacitance in charge and spin qubits ». In: *Phys. Rev. B* 95 (4 Jan. 2017), p. 045414. DOI: 10.1103/PhysRevB.95.045414.

[22] L. P. Kouwenhoven et al. « Excitation Spectra of Circular, Few-Electron Quantum Dots ». In: *Science* 278.5344 (1997), pp. 1788–1792. DOI: 10.1126/science.278.5344.1788.

[23] E. B. Foxman et al. « Crossover from single-level to multilevel transport in artificial atoms ». In: *Phys. Rev. B* 50 (19 Nov. 1994), pp. 14193–14199. DOI: 10.1103/PhysRevB.50.14193.

[24] G. Burkard et al. « Semiconductor spin qubits ». In: *Rev. Mod. Phys.* 95 (2 June 2023), p. 025003. DOI: 10.1103/RevModPhys.95.025003.

[25] F. Vigneau et al. « Probing quantum devices with radio-frequency reflectometry ». In: *Applied Physics Reviews* 10.2 (Feb. 2023), p. 021305. DOI: 10.1063/5.0088229.

[26] V. Schmitt et al. *Tunable interdot coupling in SiMOS architectures over more than nine orders of magnitude*. March Meeting. Mar. 2022.

[27] L. M. K. Vandersypen et al. « Interfacing spin qubits in quantum dots and donors—hot, dense, and coherent ». In: *npj Quantum Information* 3.1 (Sept. 2017), p. 34. DOI: 10.1038/s41534-017-0038-y.

[28] R. Schleser et al. « Time-resolved detection of individual electrons in a quantum dot ». In: *Applied Physics Letters* 85.11 (Sept. 2004), pp. 2005–2007. DOI: 10.1063/1.1784875.

[29] S. Gustavsson et al. « Counting Statistics of Single Electron Transport in a Quantum Dot ». In: *Phys. Rev. Lett.* 96 (7 Feb. 2006), p. 076605. DOI: 10.1103/PhysRevLett.96.076605.

[30] C. B. Simmons et al. « Tunable Spin Loading and T1 of a Silicon Spin Qubit Measured by Single-Shot Readout ». In: *Phys. Rev. Lett.* 106 (15 Apr. 2011), p. 156804. DOI: 10.1103/PhysRevLett.106.156804.

[31] H. Büch et al. « Spin readout and addressability of phosphorus-donor clusters in silicon ». In: *Nature Communications* 4.1 (June 2013), p. 2017. DOI: 10.1038/ncomms3017.

[32] T. F. Watson et al. « High-Fidelity Rapid Initialization and Read-Out of an Electron Spin via the Single Donor D^- Charge State ». In: *Phys. Rev. Lett.* 115 (16 Oct. 2015), p. 166806. DOI: 10.1103/PhysRevLett.115.166806.

[33] A. R. Mills et al. « Two-qubit silicon quantum processor with operation fidelity exceeding 99% ». In: *Science Advances* 8.14 (2024/02/06 2021), eabn5130. DOI: 10.1126/sciadv.abn5130.

[34] D. Keith et al. « Benchmarking high fidelity single-shot readout of semiconductor qubits ». In: *New Journal of Physics* 21.6 (June 2019), p. 063011. DOI: 10.1088/1367-2630/ab242c.

[35] Y. Fang et al. « Recent advances in hole-spin qubits ». In: *Materials for Quantum Technology* 3.1 (Mar. 2023), p. 012003. DOI: 10.1088/2633-4356/acb87e.

[36] K. Ono et al. « Current Rectification by Pauli Exclusion in a Weakly Coupled Double Quantum Dot System ». In: *Science* 297.5585 (Aug. 2002), pp. 1313–1317. DOI: 10.1126/science.1070958.

[37] A. C. Johnson et al. « Triplet–singlet spin relaxation via nuclei in a double quantum dot ». In: *Nature* 435.7044 (June 2005), pp. 925–928. DOI: 10.1038/nature03815.

[38] V. S. Pribiag et al. « Electrical control of single hole spins in nanowire quantum dots ». In: *Nature Nanotechnology* 8.3 (Mar. 2013), pp. 170–174. DOI: 10.1038/nnano.2013.5.

[39] Y. Kato et al. « Gigahertz Electron Spin Manipulation Using Voltage-Controlled g-Tensor Modulation ». In: *Science* 299.5610 (2003), pp. 1201–1204. DOI: 10.1126/science.1080880.

[40] M. Pioro-Ladrière et al. « Electrically driven single-electron spin resonance in a slanting Zeeman field ». In: *Nature Physics* 4.10 (Oct. 2008), pp. 776–779. DOI: 10.1038/nphys1053.

[41] E. Kawakami et al. « Electrical control of a long-lived spin qubit in a Si/SiGe quantum dot ». In: *Nature Nanotechnology* 9.9 (Sept. 2014), pp. 666–670. DOI: 10.1038/nnano.2014.153.

[42] W. Gilbert et al. « On-demand electrical control of spin qubits ». In: *Nature Nanotechnology* 18.2 (Feb. 2023), pp. 131–136. DOI: 10.1038/s41565-022-01280-4.

[43] B. Venitucci. « Modélisation de la manipulation électrique des qubits de trou dans le silicium ». Theses. Université Grenoble Alpes (2020), Nov. 2020.

[44] Lorenzo Mauro et al. « Geometry of the dephasing sweet spots of spin-orbit qubits ». In: *Phys. Rev. B* 109 (15 Apr. 2024), p. 155406. DOI: 10.1103/PhysRevB.109.155406.

[45] K. C. Nowack et al. « Coherent Control of a Single Electron Spin with Electric Fields ». In: *Science* 318.5855 (2007), pp. 1430–1433. DOI: 10.1126/science.1148092.

[46] N. Ares et al. « Nature of Tunable Hole g Factors in Quantum Dots ». In: *Physical Review Letters* 110 (4 Jan. 2013), p. 046602. DOI: 10.1103/PhysRevLett.110.046602.

[47] S. D. Liles et al. « Electrical control of the g tensor of the first hole in a silicon MOS quantum dot ». In: *Phys. Rev. B* 104 (23 Dec. 2021), p. 235303. DOI: 10.1103/PhysRevB.104.235303.

[48] J. C. Abadillo-Uriel et al. « Hole-Spin Driving by Strain-Induced Spin-Orbit Interactions ». In: *Phys. Rev. Lett.* 131 (9 Sept. 2023), p. 097002. DOI: 10.1103/PhysRevLett.131.097002.

[49] B. Venitucci et al. « Electrical manipulation of semiconductor spin qubits within the g-matrix formalism ». In: *Phys. Rev. B* 98 (15 Oct. 2018), p. 155319. DOI: 10.1103/PhysRevB.98.155319.

[50] B. Martinez et al. « Hole spin manipulation in inhomogeneous and nonseparable electric fields ». In: *Phys. Rev. B* 106 (23 Dec. 2022), p. 235426. DOI: 10.1103/PhysRevB.106.235426.

[51] B. Martinez and Y.-M. Niquet. « Variability of Electron and Hole Spin Qubits Due to Interface Roughness and Charge Traps ». In: *Phys. Rev. Appl.* 17 (2 Feb. 2022), p. 024022. DOI: 10.1103/PhysRevApplied.17.024022.

[52] B. Voisin et al. « Few-Electron Edge-State Quantum Dots in a Silicon Nanowire Field-Effect Transistor ». In: *Nano Letters* 14.4 (Apr. 2014), pp. 2094–2098. DOI: 10.1021/nl500299h.

[53] S. Bosco and Daniel Loss. « Fully Tunable Hyperfine Interactions of Hole Spin Qubits in Si and Ge Quantum Dots ». In: *Phys. Rev. Lett.* 127 (19 Nov. 2021), p. 190501. DOI: 10.1103/PhysRevLett.127.190501.

[54] S. Bosco, Bence Hetényi, and Daniel Loss. « Hole Spin Qubits in Si FinFETs With Fully Tunable Spin-Orbit Coupling and Sweet Spots for Charge Noise ». In: *PRX Quantum* 2 (1 Mar. 2021), p. 010348. DOI: 10.1103/PRXQuantum.2.010348.

[55] V. P. Michal et al. « Tunable hole spin-photon interaction based on g-matrix modulation ». In: *Phys. Rev. B* 107 (4 Jan. 2023), p. L041303. DOI: 10.1103/PhysRevB.107.L041303.

CHAPTER 4

Gate-tunable sweetlines for charge noise

Charge noise hinders hole spin qubit operation by limiting its coherence times [1, 2, 3]. In the previous chapter, sweetlines for charge noise (rather than sweetspots) have been evidenced with respect to magnetic field orientation and expand the degree of freedom to manipulate hole spins with enhanced coherence times [4]. From this experimental demonstration, two main questions arise.

On the one hand, is this longitudinal spin susceptibility to electrical noise given by nature or can it be tuned ? By definition, this spin sensitivity $\beta_{\parallel}$ correlates with the hole g-matrix and its first derivative with respect to gate voltage. Besides, experimental realizations [5, 6] proved that hole g-matrices can be tuned in **B**-field by changing the particle wavefunction confinement. Putting these two concepts together means that modifying the hole wavefunction confinement (thus g) is expected to indirectly result in an alteration of spin susceptibility in magnetic field. By extension, sweetlines for charge noise are predicted to be tunable [7]. This characteristic will be tackled in the first section of this chapter.

On the other hand, a question about the relevance of such dephasing sweetspots is raised. Indeed, what is the gain in spin qubit operation if having an extended coherence time (i.e. mitigated coupling to electrical noise) comes along with an overall decoupling to the driving electrical fields (i.e. low manipulation speed)? To this aim, the emphasis is laid, in section 4.2, on the angular dependency in magnetic field of transverse component of charge noise $\beta_{\perp}$. The latter can be reconstructed using g-matrix formalism [8] and with experimental measurements of the Rabi frequency. Reciprocal sweetness relation [9] between $\beta_{\parallel}$ and $\beta_{\perp}$ is addressed. Moreover, a crucial metric for single qubit gate efficiency, Q-factor, is evaluated at a sweetspot.

Contents

4

4.1 Modifying the (w)hole g-matrix

The g-matrix is a key element to understand the interaction of the hole particle with its environment. In particular, the g-matrix governs the magnetic field response of the hole spin transition (as $E_Z \propto g$) [10, 11, 12], the hole spin susceptibility to longitudinal contribution of charge noise ($\beta_{\parallel} = f(G, G')$) [4, 5, 7, 9] and the hole behaviour upon driving[1] ($\beta_{\perp} = f(G, G')$) [13]. Additionally, knowing the hole g-matrix allows to infer the particle wavefunction confinement within the device [14].

The shape of the hole g-matrix inside a QD (especially in the case of the first hole) stems from the electrostatic landscape and the presence of strain in the device. Modifications of the electrostatic environment experienced by the hole particle will alter its g-matrix [6] and thus, its response to noise and driving contributions. Based on this reasoning, next sections focus on the electrical control of the first hole g-matrix and then on the impact on the longitudinal spin susceptibility to charge noise. In other words, gate voltages responsible for the electrostatic potential confining the hole is changed, so that the effects on spin susceptibility and on the sweetlines are assessed.

4.1.1 Changing confinement gate B_3

As detailed in the previous chapter, the first hole wavefunction is mainly squeezed towards the nanowire facet, suggesting that a $\vec{p}$-oriented electrostatic

1. Further explanations are given in section 4.2.2.

potential is mostly responsible for the particle confinement. The latter originates from the potential difference between the gates T_3 and B_3, which is about 0.305 V across the nanowire width of 40 nm. Decreasing gate voltage V_{B_3} would diminish the electric field amplitude, and is thus expected to pull the hole wavefunction more towards the center of the nanowire. Nevertheless, gate B_3 can only be set within a narrow voltage range as (i) B_3 acts as a barrier gate to set tunnelling rates for spin qubit readout, (ii) B_3 voltage must remain below the gate accumulation threshold to avoid the formation of a QD underneath. Indeed, a QD below gate B_3 could screen the electric field experienced by the hole within QD_3 underneath gate T_3. From dispersive charge sensing, the first hole accumulates below gate B_3 at a gate voltage $V_{B_3}^* \sim -0.640\,\mathrm{V}$. This $V_{B_3}^*$ sets the upper bound value for B_3 gate voltage.

About the influence of V_{B_3} on spin readout

So far, gate B_3 in combination with T_2 were used as barrier gates, i.e. control knobs for tunnelling rates permitting single-shot spin readout (see section 3.1.3). If the B_3 gate voltage is decreased (increased), tunnelling rates will undoubtedly increase (decrease), potentially exceeding the tunnelling range that can be probed [2]. In order to circumvent such readout limitations, the second barrier gate T_2 will be used to compensate for B_3 voltage change so that the tunnelling rates remain in the few kHz span. For sake of clarity, in the following, only V_{B_3} value is alluded, even though V_{T_2} is also modified. The complete gate settings can be found in appendix.

About the influence of V_{B_3} on the g-matrix

In this section, we evaluate the influence of gate B_3 on the wavefunction confinement by probing the hole g-matrix using EDSR method. Figure 5.3 illustrates the g-matrix fitted values (as in the previous chapter) in magnetic field orientation for three different values of B_3 gate voltage. From blue to red: $V_{B_3}^{(0)} \sim -0.445\,\mathrm{V}$, $V_{B_3}^{(2)} \sim -0.540\,\mathrm{V}$ and $V_{B_3}^{(1)} \sim -0.635\,\mathrm{V}$ [3]. A distinct alteration of the g-matrix profile is observed in principal planes of the magnet. This evidences the influence of gate B_3 onto the first hole wavefunction accumulated below T_3. Moreover, a tilt between each configuration witnesses the rotation of the spin basis (compared to the magnet one) depending on B_3 gate voltage value. This can be attributed to the spatial displacement of the hole wavefunction along the nanowire ($\pm\vec{n}$), which experiences strain. Further investigations would be needed to fully capture the strain contribution herein. For each gate configuration, the G-tensors are gathered in table 4.1 (fitting procedure remains the same as in the previous chapter).

2. In chapter 3, the desired tunnelling rates range was from 4 kHz to 20 kHz.

3. Note that configuration n°0 (displayed in blue) is the one detailed in the previous chapter. The exponant stands for the gate configuration labelling.

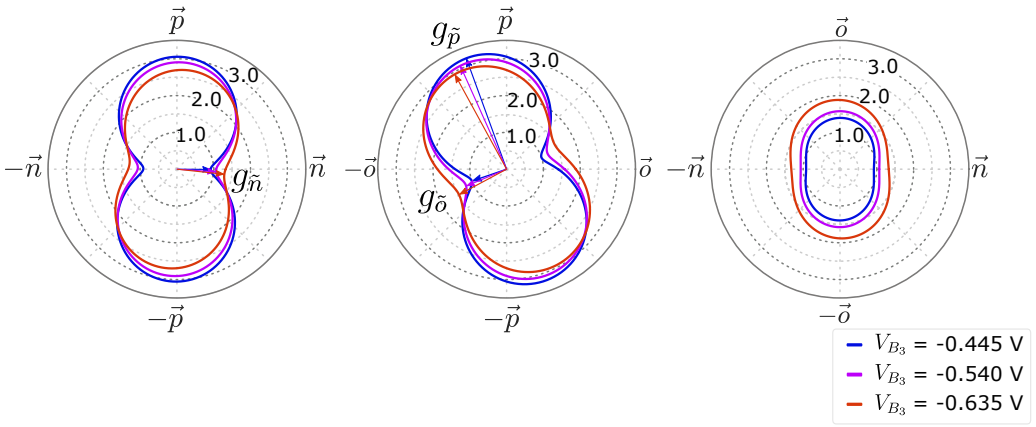

Figure 4.1 – **Comparison of the g-matrices when varying gate voltage V_{B_3}:** Fitted values of g-matrices as a function of magnetic field orientation for 3 different values of gate voltage V_{B_3}. Each panel corresponds to a principal magnet plane. The fitting procedure is the same as in the previous chapter. A clear modification of the absolute values of g is observed in each panel. This comes along with a tilt of the spin basis, suggesting the presence of strain within the device. Main g-factors projected in the spin basis are highlighted by the arrows, labelled $g_{\tilde{x}}$.

Config.	V_{B_3}(V)	$G_{\{n,o,p\}}$	$g_{\{\tilde{n},\tilde{o},\tilde{p}\}}$
n°0 (blue)	-0.445	$\begin{bmatrix} 0.815 & 0.023 & 0.148 \\ 0.0228 & 1.943 & -2.824 \\ 0.148 & -2.824 & 9.320 \end{bmatrix}$	(3.206, 0.888, 1.005)
n°2 (purple)	-0.540	$\begin{bmatrix} 1.139 & 0.007 & 0.271 \\ 0.007 & 2.485 & -2.734 \\ 0.271 & -2.734 & 8.423 \end{bmatrix}$	(3.082, 1.047, 1.205)
n°1 (red)	-0.635	$\begin{bmatrix} 1.793 & -0.203 & 0.722 \\ -0.203 & 3.564 & -2.472 \\ 0.722 & -2.472 & 6.984 \end{bmatrix}$	(2.948, 1.273, 1.485)

Table 4.1 – **Evaluated G-tensors for different values of V_{B_3}:** Results of the fitting procedure, giving G-matrices for three different values of gate voltage V_{B_3}. From the square-roots of G eigenvalues, are inferred the main g-factors denoted $g_{\{\tilde{n},\tilde{o},\tilde{p}\}}$ in the spin basis.

The main g-matrix values projected into the spin basis are deduced as the square-roots of the G eigenvalues, see fourth column of table 4.1. We denote $g_{\tilde{x}}$ with $\tilde{x} = \{\tilde{n}, \tilde{o}, \tilde{p}\}$ the main g-factor in the spin basis along the $\tilde{x}$-axis. The latter are also depicted by the arrows (with corresponding colours) in figure 4.1. The main g-factors $g_{\{\tilde{n},\tilde{o},\tilde{p}\}}$ exhibit a strong modulation up to 30% when varying B_3

gate voltage about 190 mV. Figure 4.2 illustrates the variations of $g_{\{\tilde{n},\tilde{o},\tilde{p}\}}$ as a function of the applied gate voltage. The overall diminution of $g_{\tilde{p}}$, highlighted by the dots, evidences a weaker confinement along $\tilde{p}$-axis. In other words, gate B_3 can be employed to pull the hole wavefunction within the nanowire, i.e. "deconfine" the hole from the NW facet. This $g_{\tilde{p}}$ decrease is accompanied with an increase in both $g_{\tilde{n}}$ and $g_{\tilde{o}}$ values. Noticeably, those variations seem to scale linearly within the gate voltage span, as underscored by the dashed lines (guide to the eyes).

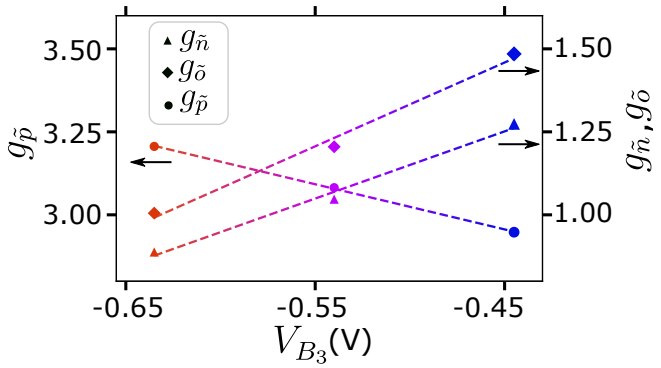

Figure 4.2 – **Principal g-factors depending on confinement potential:** Main g-factor values obtained by diagonalization of the G-tensor (see previous chapter for detailed explanation) when decreasing the gate voltage V_{B_3}. Gate B_3 is mostly responsible for the hole wavefunction confinement, thus changing its voltage value inherently modifies the hole g-matrix. In almost 200 mV voltage span, main g-factors are ranging about $[2.94, 3.2]$ ($[1.27, 0.89]$ and $[1.49, 1.0]$) for $g_{\tilde{p}}$ ($g_{\tilde{n}}$ and $g_{\tilde{o}}$). Noticeably, the main g-factor modulations in the spin basis are linear in gate voltage as indicated by the dashed lines.

Upon changing the electrostatic landscape of QD_3, which hosts the spin qubit, the hole g-matrix is heavily modified. As a consequence, changing gate voltage set on B_3 is expected to modify the hole spin susceptibilities to charge noise. In the following section, longitudinal contributions of charge noise are evaluated (similarly to the previous chapter) depending on magnetic field orientations, for different values of gate voltage V_{B_3}.

4.1.2 Influence of B_3 gate voltage on the spin susceptibility $\beta_{\parallel}$

As the hole g-matrix is affected by changes in V_{B_3}, its sensitivity to longitudinal charge noise stemming from gate T_3 is also altered. To unveil the contribution of V_{B_3} onto the sweetlines for charge noise, we reproduce the measurement procedure of $\beta_{\parallel}(\mathbf{B})$ as detailed in chapter 3. From the evaluation of G-tensor and the Larmor frequency shift measurements, it is possible to deduce the G'-tensor values for each gate configuration. Such matrices are gathered in table 4.2. A schematic of the hole wavefunction confinement across the nanowire is provided in figure 4.3(a) relatively to V_{B_3}. The decrease of B_3 voltage reduces the potential difference between gates T_3 and B_3, thus the electric field responsible for hole con-

finement along $\vec{p}$-axis. As a consequence, the anisotropy of the spin susceptibility $\beta_{\|}$ depending on **B**-field is highly altered, as shown in figure 4.3(b).

First, the absolute values of $\beta_{\|}$ change as underscored by the colour intensity in different panels. For sake of clarity, spin susceptibility values are plotted within $[-80, 80]\,\mathrm{MHz\,mV^{-1}}$ range. Second, the position of the sweetline (white region) is displaced in magnetic field, depending on B_3 voltage setting.

Config.	V_{B_3}(V)	$G'_{\{n,o,p\}}$
n°0 (blue)	-0.445	$\begin{bmatrix} -9.41 & 1.003 & -4.736 \\ 1.003 & -9.235 & -7.340 \\ -4.736 & -7.340 & 4.111 \end{bmatrix}$
n°2 (purple)	-0.540	$\begin{bmatrix} -6.011 & 4.194 & 6.510 \\ 4.194 & -7.114 & -6.980 \\ -6.510 & -6.980 & 16.726 \end{bmatrix}$
n°1 (red)	-0.635	$\begin{bmatrix} -10.386 & 0.927 & -5.756 \\ 0.927 & -11.388 & -6.699 \\ -5.756 & -6.699 & 7.429 \end{bmatrix}$

Table 4.2 – **Evaluated G'-tensors for different values of V_{B_3}:** Estimated G'-tensors depending on B_3 gate voltage. The three configurations are same than in section 4.1.1. Knowing both G and G'-tensors permits to reconstruct the spin qubit susceptibility to charge noise versus magnetic field orientation. G'-tensor eigenvalue signs are $(+,-,-)$ (same notations than in ref. [7]) for each configuration, suggesting the presence of sweetlines [7].

So as to quantify the effect of V_{B_3} onto the spin sensitivity to T_3 voltage fluctuations, the sweetspot positions in (NP) principal magnet plane, denoted $\theta_{\beta_{\|}=0}$, are collected as symbolized by the stars. White dashed lines in figure 4.3 are guide to the eyes to distinguish the principal magnet plane. Figure 4.4 gathers the sweetspot angular positions in magnetic field as a function of V_{B_3}. The variations of $\theta_{\beta_{\|}=0}$ witnesses a certain electric tunability of the sweetspot (and so as the sweetline) positions up to 26 ° for a gate span of 190 mV.

Sweetlines for charge noise are of crucial importance to operate spin qubit systems with enhanced coherence time. This experimental demonstration of gate-tunability property of the sweetlines allows for an additional degree of freedom for spin qubit manipulation. Indeed, in the scope of large-scale QD arrays, it is thus possible to tune and align sweetlines of each spin qubit to create an optimal operation point at given magnetic field orientations. Moreover, as gates may be tuned much faster than magnetic field orientation, electrical driving may help to

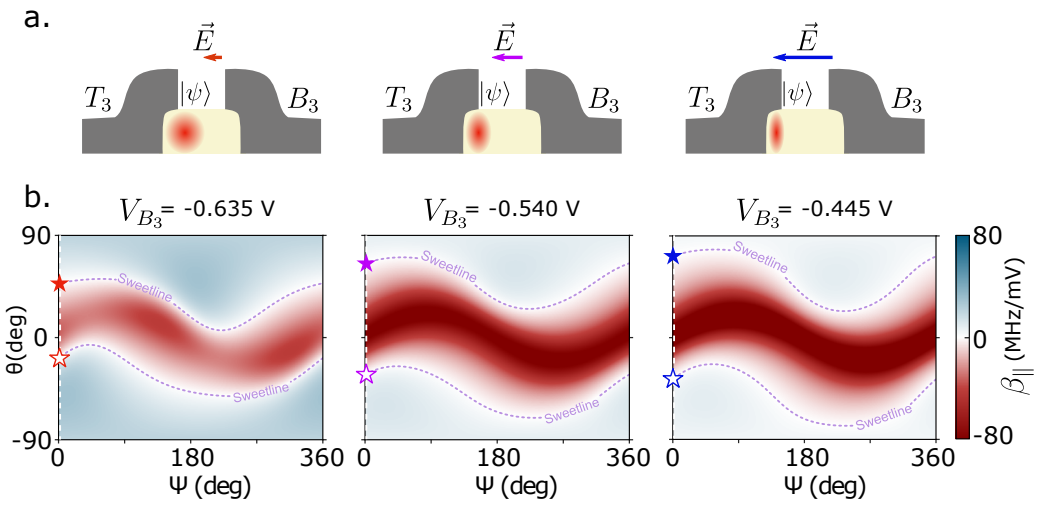

Figure 4.3 – **Spin susceptibility evolution depending on gate voltage V_{B_3}:** (a) Sketches of electric field experienced by the hole spin qubit, responsible for its wavefunction confinement $|\psi\rangle$. When the gate voltage of B_3 is decreased, the potential difference between gates T_3 and B_3 is reduced, so as the electric field. (b) Fitted $\beta_{\parallel}$ values as a function of magnetic field orientation for 3 different settings of gate on B_3. All data are rescaled at a fixed reference frequency $f_L = 17.99\,\mathrm{GHz}$. The discrepancies in confinement profile induce changes in $\beta_{\parallel}$ anisotropy. The sweetline position evolves alongside the absolute values of spin susceptibility depending on V_{B_3}. Star symbols highlight sweetspot positions ($\theta_{\beta_{\parallel}=0}$) in principle magnet plane (dashed lines). $\psi = 0\,\mathrm{deg}$ symbolizes the (NP) plane.

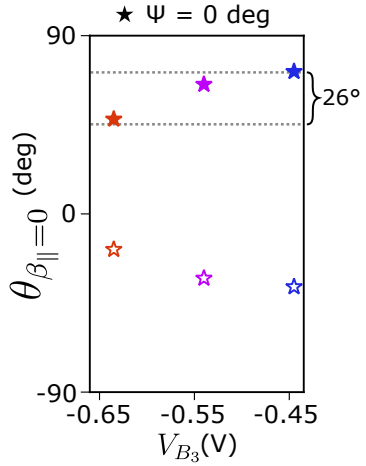

Figure 4.4 – **Sweetspot positions in principle magnet planes versus confinement potential:** Sweetspot positions (star symbols) measured in the (NP) magnetic plane as a function of gate voltage V_{B_3}. This reveals the gate-tunability of sweetlines in magnetic field within 190 mV range up to 26° as underscored by the grey dashed lines.

operate the qubit in and out from a sweetspot. As a consequence, gate-tunable sweetlines, which constitute a major result of this study, open a path towards the realization of highly coherent multiple-qubit systems.

4.1.3 Digression: comparison of spin susceptibilities to gates T_3 and B_3

By definition, the spin susceptibility to charge noise induced by gate X is - to within a constant factor- the Larmor frequency shift experienced by the qubit due to the same gate voltage fluctuations. With this reasoning, it is possible to estimate the contribution of gate B_3 when comparing the g-matrix differences (shown in fig. 4.2) with the voltage changes between two gate configurations. In other words, the spin susceptibility of a gate can be redefined as:

$$\beta_{\parallel}^{(X)}(n \to m) = \frac{\mu_B}{h} \frac{\Delta f_L(\mathbf{B})}{\Delta V_X}(n \to m) \tag{4.1}$$

with,

n, m *the gate configurations labelling: 0 (resp. 2 and 1) stands for* $V_{B_3} = -0.445\,\mathrm{V}$ *(resp.* $V_{B_3} = -0.540\,\mathrm{V}$ *and* $V_{B_3} = -0.635\,\mathrm{V}$*),*

$\Delta f_L(\boldsymbol{B})$ *the measured difference of Larmor frequencies between two gate configurations (*n *and* m*) at a given magnetic field orientation,*

ΔV_X *the gate voltage span of* X *between gate configurations* n *and* m*.*

From the G-tensors, presented in table 4.1, it is possible to evaluate the qubit Larmor frequency at any magnetic field orientation. We infer the Larmor frequency difference between two gate configurations (0 and 1), which is denoted $\beta_{\parallel}^{(B_3)}$ $(0 \to 1)$, as highlighted by the pink shaded area in figure 4.5(a). The spin sensitivity to a B_3 voltage change of 190 mV is calculated using equation 4.1 and is reported in solid pink line in panel (b) as a function of magnetic field angle. Similar estimations are conducted between the three gate configurations, leading to dashed ($\beta_{\parallel}^{(B_3)}$ $(1 \to 2)$) and dotted ($\beta_{\parallel}^{(B_3)}$ $(0 \to 2)$) curves. In order to compare the influence of gates T_3 and B_3, the spin susceptibility to T_3 fluctuations measured in chapter 3 is represented in blue (solid line is the fit). Remarkably, contributions of B_3 and T_3 gates have opposite behaviour depending on magnetic field angle and similar amplitude (meaning comparable influence on the spin). This suggests that the main electrical field affecting the spin qubit, acts perpendicularly to the nanowire (along $\vec{p}$-axis) and stems from the electrostatics set by B_3 and T_3 gate voltages.

Furthermore, the presence of sweetspots, i.e. field orientation at which the Larmor frequency remains unchanged regardless the variations in B_3 voltage, are revealed as underscored by the pink triangles. The poor coincidence between the sweetspots of gates B_3 and T_3 can be explained by different factors. First, it is

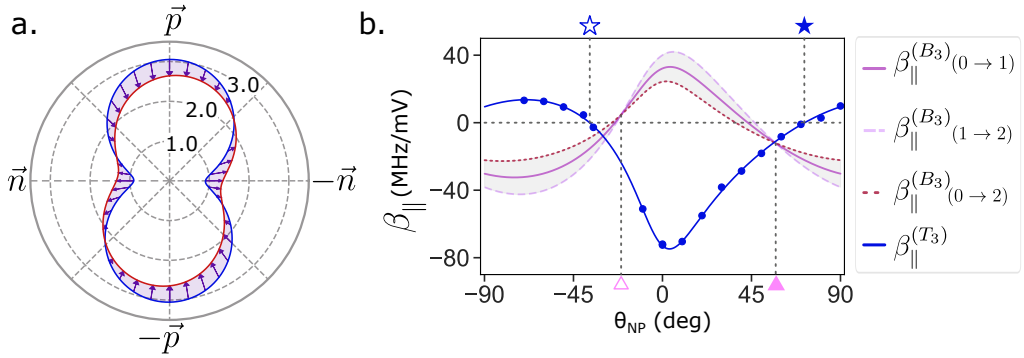

Figure 4.5 – **Estimation of the longitudinal charge noise induced by the gate B_3:** (a) Comparison between g-matrices in the (NP) plane for two different gate voltage configurations (blue: $V_{B_3} = -0.445\,\mathrm{V}$ and red: $V_{B_3} = -0.635\,\mathrm{V}$). The discrepancies in g-matrix as a function of magnetic field angle provides a direct insight on the contribution of B_3 to the Larmor frequency shift experienced by the spin qubit. The grey shaded area, rescaled with μ_B and the voltage difference $\delta V_{B_3} = -190\,\mathrm{mV}$, therefore gives the contribution of B_3 to spin susceptibility between configurations labelled 0 and 1. This quantity, denoted $\beta_{\parallel}^{(B_3)}$ $(0 \to 1)$, is plotted as the purple solid curve in panel (b). The same estimation can be done between configurations 1 and 2 ($\beta_{\parallel}^{(B_3)}$ $(1 \to 2)$) and 0 and 2 ($\beta_{\parallel}^{(B_3)}$ $(0 \to 2)$) having a gate voltage difference of $\delta V_{B_3} = -0.095\,\mathrm{mV}$, see panel (b). (b) Longitudinal charge noise contribution experienced by the hole spin qubit depending on magnetic field angle in the (NP) plane. In pink/purple are depicted the contributions stemming from B_3 gate, estimated from the g-matrix modifications. Additionally, points and fit (solid line) of spin susceptibility induced by gate T_3 are shown in blue.

important to bear in mind that changes in B_3 gate voltage also impose modifications of T_2 potential to perform spin readout (see section 4.1.1). As the lever-arm of T_2 gate on the QD is strong, the influence of T_2 on the spin susceptibility to charge noise may play a non-negligible role alongside gate B_3. Owing to these electrostatic changes, the hole wavefunction may be displaced within the nanowire and may experience additional phenomena stemming from disorder and strain in the device. Second, spin susceptibility of gate T_3 is measured within few millivolts span by pulsing whereas B_3 contribution to charge noise is estimated over 190 mV range. Due to the impossibility to send high-frequency signals on gate B_3, the extracted spin susceptibility $\beta_{\parallel}^{(B_3)}$ is in fact an averaged value over the gate voltage span, with reduced precision. Figure 4.6 displays the complete magnetic field dependency of $\beta_{\parallel}^{(B_3)}$ estimated from the difference in gate configurations 0 and 1. A similar anisotropy compared to $\beta_{\parallel}$ from gate T_3 is unveiled (to be compared with fig. 4.3). Finally, B_3 longitudinal noise also exhibits the presence of sweetlines (white regions) for the hole spin qubit enclosed in QD_3.

So far, the attention was drawn onto the deep understanding of the spin sensitivity anisotropy to charge noise with respect to magnetic field orientation. The

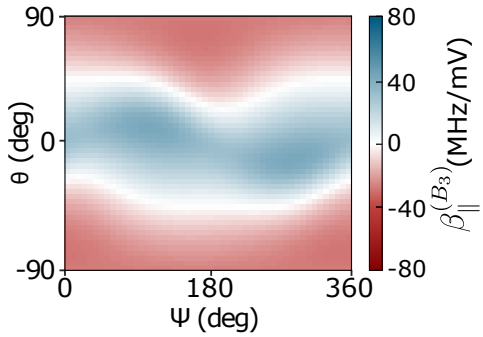

Figure 4.6 – **Longitudinal spin susceptibility of the confining gate B_3:** Evaluated spin susceptibility induced by gate B_3, denoted $\beta_{\parallel}^{(B_3)}$ $(0 \rightarrow 1)$ with respect to magnetic field orientation. Remarkably, the spin sensitivity is highly similar (up to a sign) to the one induced by gate T_3 (see fig. 4.3), suggesting that the main sources of charge noise are acting perpendicularly to the silicon channel. The presence of two sweetlines is also observed.

latter is assumed at first-order to stem from nearby gate voltage fluctuations. A clear relation between the G-tensor and its first derivative with gate voltage is established and allows for a full reconstruction of the spin susceptibility in magnetic field. Experimental measurements demonstrated the existence of sweetlines (1D feature of zero-sensitivity) in magnetic field, which can be all-electrically tuned upon changing the hole wavefunction confinement. The electrostatic engineering using gates opens a path towards switching functionality to operate a qubit in and out from the sweetlines [15]. Furthermore, the tunability of sweetline positions, thus their alignment in field, is an appealing property in the scope of large-scale QD arrays for spin qubit operation.

In the following, the focus is laid onto the evaluation of spin qubit performances at and far from sweetspots. The qubit coherence time is first tackled, introducing concepts such as Ramsey and Hahn-Echo measurements. Second, the transverse contribution of charge noise $\beta_{\perp}$ induced by the host gate T_3 is studied, through the Rabi frequency evolution in magnetic field.

4.2 Spin qubit performance metrics on the sweetline

Mitigating the longitudinal contribution of charge noise, responsible for degradation of the spin qubit coherence time, permits an enhancement of the latter by an order of magnitude in the case of holes in Si-MOS structure reaching up to $T_2^E = 88\,\mu s$ [4]. In addition, a reciprocal relation between longitudinal $\beta_{\parallel}$ and transverse $\beta_{\perp}$ contributions of charge noise is theoretically predicted [9], also known as "reciprocal sweetness". Following ref.[9], a maximum operation speed (i.e. Rabi frequency) is expected to coincide with sweetspots (thus longest coher-

ence times), which would constitute an optimal operation point for spin qubit systems. In the next sections, the aim is to evaluate at first, both the spin coherence times (T_2^* and T_2^E) and then the operation speed (f_R) so as to unveil charge noise influence (emulated by gate voltage fluctuations) onto the qubit performances.

4.2.1 Coherence time estimation

The limiting time until the spin qubit becomes a statistical mixture of state is a crucial metric to assess a qubit quality, known as coherence time. There are two principal ways to measure such coherence time, which differ by their cancellation to low-frequency noise: Ramsey (labelled hereafter T_2^*) [16] and Hahn-echo (denoted T_2^E) experiments [17, 18]. Such coherence times are expected to increase on the sweetline due to the longitudinal charge noise mitigations compared to any magnetic field orientation [4, 7, 9].

From now on, the gate configuration chosen for the following measurement is for $V_{B_3}^{(1)} = -0.635\,\mathrm{V}$ (corresponding to configuration n°1) [4]. The magnetic field angular dependence of both Ramsey and Hahn-Echo coherence times are performed to be compared with the longitudinal charge noise influence $\beta_{\parallel}$. Note that, in the next sections, the MW tone is sent through gate T_4, which mainly plays a role in Rabi frequency measurements (see section 4.2.2) and is not expected to affect coherence time measurements.

Ramsey experiment

T_2^* estimation is performed using the AWG sequences shown in figure 4.7. A first $\pi/2$-pulse, whose duration is denoted $t_{\pi/2}$, is sent at a MW frequency labelled f_{MW} to create a superposition of state [5]. During a time t_{wait}, the qubit freely evolves and precesses at its Larmor frequency, which rotates in the MW rotating frame at a frequency detuning: $\delta f = f_{\mathrm{MW}} - f_L$. A second $\pi/2$-pulse projects the system for spin readout. This last $\pi/2$-pulse can be seen as a projection onto the poles of the Bloch sphere defining $|\uparrow\rangle$- and $|\downarrow\rangle$-states.

Depending on the waiting time between the $\pi/2$-pulses, the $|\uparrow\rangle$-spin state probability experiences oscillations with a period proportional to δf with a decaying envelope corresponding to the coherence time. In left panel of figure 4.8(a), the $|\uparrow\rangle$-state probability is recorded for various waiting times as a function of MW frequency at a sweetspot $\mathbf{B} = (-0.887, -0.156, 0.216)\,\mathrm{T}$. Red dotted line indicates the qubit Larmor frequency (no oscillations are visible as $\delta f = 0$). Ramsey fringes are measured for 5 minutes at $\delta f = 4\,\mathrm{MHz}$ as shown in panel (b) of the same figure. When averaged, such oscillations can be fitted to extract the Ramsey coherence

4. Note that there is no particular reason for this gate configuration choice. Same measurements can be conducted for $V_{B_3} = -0.540\,\mathrm{V}$ and $V_{B_3} = -0.445\,\mathrm{V}$.

5. The calibration of $\pi/2$-pulse duration can be found in appendix.

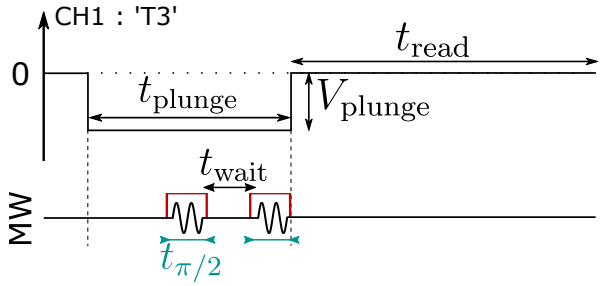

Figure 4.7 – **AWG sequences used to perform Ramsey coherence time measurements:** The spin is manipulated during plunge stage lasting $t_{\text{plunge}} = 20\,\mu\text{s}$ with $V_{\text{plunge}} = -2\,\text{mV}$. Two $\pi/2$-pulses, separated by a waiting time t_{wait}, aim at controlling the spin orientation. Pulse modulation, in red, prevents spurious leakages from the MW tone. Once manipulated, the spin orientation is readout during $t_{\text{read}} = 500\,\mu\text{s}$. In total, such sequence, whose duration is $520\,\mu\text{s}$, is repeated with 40 different values of t_{wait} to constitute one time-trace. The latter therefore lasts for $520 \times 10^{-6} \times 40 = 2.08\,\text{ms}$ and is averaged 2000 times. Finally, the measurement duration is $2000 \times 2.08 \times 10^{-3} = 4.16\,\text{s}$ plus communication time with the setup.

time as:

$$P_{\uparrow}(t) = A\cos(2\pi\delta f \times t + \phi_0)e^{-\left(\frac{t}{T_2^*}\right)^{\beta}} + B \tag{4.2}$$

with,

A and B adjustable parameters for the amplitude and offset of the signal,

ϕ_0 adjustable phase parameter (by default is 0),

β the envelope decay, related to the noise acting on the spin qubit and temperature [19]. Herein, β is 2 corresponding to a Gaussian envelope decay following ref. [20].

Figure 4.8(c) displays the averaged time-traces over 5 minutes and the corresponding fit (solid line). From this, the Ramsey coherence time is evaluated about $T_2^* = 1.03\,\mu\text{s}$ when considering a Gaussian envelope decay (i.e. a fixed parameter $\beta = 2$). At a sweetspot in Si/SiO_2 structure, the hole spin coherence time is larger by one order of magnitude than the ones reported in Ge/Si nanowires about $0.18\,\mu\text{s}$ [21, 22]. Yet, it is shorter -but approaching- coherence timescales evidenced in purified Si/SiO_2 heterostructures about tens of microseconds, which benefit from the absence of hyperfine interactions [23, 24].

Despite the fairly easy estimation of the sweetline equation, given by the solutions $\mathbf{b}^T G' \mathbf{b} = 0$, experimental probing of the performance onto the sweetline is challenging as the angular accuracy required in magnetic field is about a quarter of a degree. Even though measurements were conducted in various combination of (θ, ψ) magnetic angles, the data shown hereafter are only presented in the (NP) plane for sake of simplicity. In order to compare the contribution to charge noise

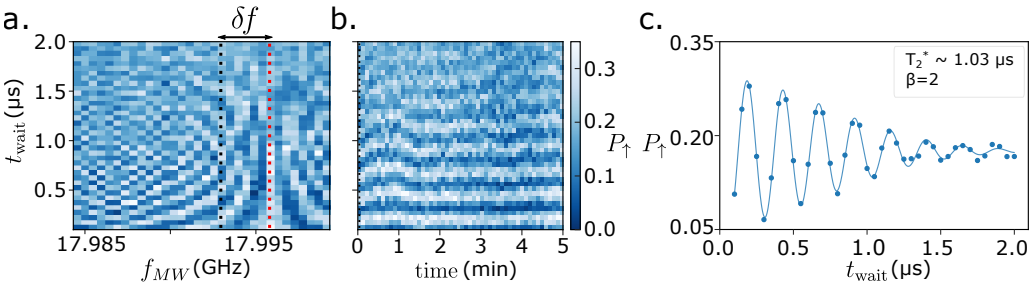

Figure 4.8 – **Evaluation of Ramsey coherence time at a sweetspot:** (a) $|\uparrow\rangle$-spin state probability when changing both the waiting time between the $\pi/2$-pulses and the MW frequency. At the Larmor frequency, highlighted by the red dotted line, the qubit does not experience oscillations, whereas at δf detuning, alternating values of $P_\uparrow$ are readily observed. (b) Repeated measurements of Ramsey fringes during 5 minutes at a MW frequency $\delta f = 4\,\text{MHz}$. (c) Averaged time-traces for 5 minutes, revealing oscillating $|\uparrow\rangle$-state probability as a function of waiting time. Fit using equation 4.2, illustrated as a solid line, estimates a Ramsey coherence time about $T_2^* \simeq 1.03\,\mu\text{s}$. Additional fitting parameters are: $\phi_0 \simeq 3/2\,\pi$, $A \simeq 0.116$ and $B \simeq 0.175$.

at and far from a sweetspot position, figure 4.9 shows the Ramsey coherence time as a function of magnetic angle, thus crossing two sweetspots, highlighted by the dashed lines (red and empty stars displayed at the top). We remember the reader that the Ramsey coherence time is expected to be inversely proportional to the spin susceptibility $\beta_\parallel$ to all gate fluctuations as mentioned in chapter 1. Considering a single gate contribution leads to the below equation 4.3. Ramsey coherence times range from 0.35 µs to almost 1.0 µs close by sweetspots. This factor 3 enhancement in Ramsey coherence time is weak but the signature of successful cancellation of first-order charge noise contribution stemming from the top gate.

$$\frac{1}{T_2^*} \propto \beta_\parallel \tag{4.3}$$

Nevertheless, during a time t_{wait}, the qubit state precesses at a given detuning frequency δf which fluctuates over time due to low-frequency noise. As a consequence, T_2^* quantity becomes a stochastic variable and its probability distribution can be evaluated by a skewed Gamma function [25]. For sake of clarity, as the evaluation of low-frequency noise does not constitute the main concern of this chapter, data illustrating the following discussion are in appendix C.2.2. At a sweetspot ($\theta = 35\,^\circ$ underscored by the solid red star), we measure Ramsey fringes for 7914 repetitions to evaluate the remaining low-frequency noise and perform a Fourier Transform. The frequency spectrum suggests, in addition to higher-orders of charge noise contribution, the existence of a source of noise at $f_{\text{noise}} \sim 0.3\,\text{Hz}$, which could be attributed to the presence of two-level fluctuators close by QD_3. This supplementary source of noise limits the Ramsey coherence time enhancement at a sweetspot. Performing Hahn-Echo experiment circumvents such fluctuators contribution by cancelling low-frequency noise.

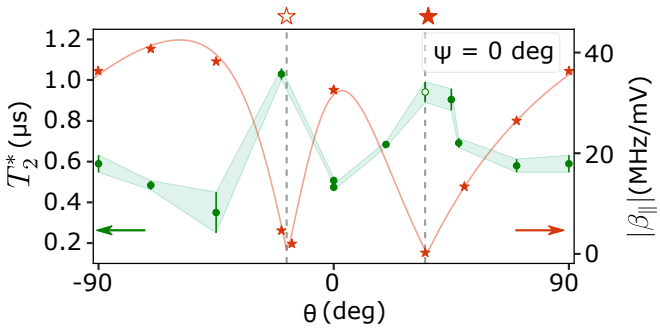

Figure 4.9 – **Comparison of Ramsey coherence time with longitudinal contribution of charge noise in (NP) plane:** Ramsey coherence time (green points) plotted as a function of magnetic field angle in (NP) plane. Values ranging from 0.35 µs to almost 1.0 µs demonstrates a weak, but non-negligible enhancement of the qubit coherence time close by the sweetspot angles. In red are depicted the absolute values of $\beta_\parallel$ in the (NP) plane and the corresponding fit (solid line) explained in left panel of figure 4.3. Dashed lines evidence the sweetspot positions where the coherence time is expected to increase.

4

Hahn-echo experiment

In comparison with Ramsey measurements, Hahn-Echo experiment [17] comprises an extra "refocusing" π-pulse set in between the driving $\pi/2$-pulses, see figure 4.10. It allows, during waiting time, to mitigate the low-frequency noise impacting the qubit precession frequency δf.

Herein, AWG sequences used for T_2^E estimation are working in pair: a first sequence $(+)$ is sent with a succession of $+\pi/2$,$+\pi$, $+\pi/2$ pulses followed by a second sequence $(-)$ comprising $+\pi/2$,$+\pi$, $-\pi/2$ gates. Only the sign of the last $\pi/2$-pulse differ between the two sequences. Experimentally, this sign is set by the output channel of MW source used (I or Q, see center panel). Considering an ideal case, the last $\pi/2$-pulse aims at projecting the spin state respectively onto its initial (excited) state $|\downarrow\rangle(|\uparrow\rangle)$ when having a positive (negative) sign. In order to evaluate the amplitude decay of the $|\uparrow\rangle$-spin probability due to decoherence, we evaluate the signal difference between $(+)$ and $(-)$ sequences. Note that the described implementation is a simplified case of two-axis control where the amplitude of the $\pi/2$-pulse is gradually shifted from I to Q MW port so that: $A_{\pi/2} = A_I(\phi) + A_Q(\phi)$, where A denotes the signal amplitude and $\tan\phi = {}^{A_I}/_{A_Q}$.

The amplitude decay of the $|\uparrow\rangle$-spin probability, calculated as $\langle P_\uparrow^{(+)}(t) - P_\uparrow^{(-)}(t)\rangle$, is shown in figure 4.11(a) depending on waiting time value and over 60 repetitions at a sweetspot with $\mathbf{B} = (0.489, -0.131, 0.318)$ T. The $|\uparrow\rangle$-state probability exhibits a clear decay over increasing waiting time duration, that can be fitted using

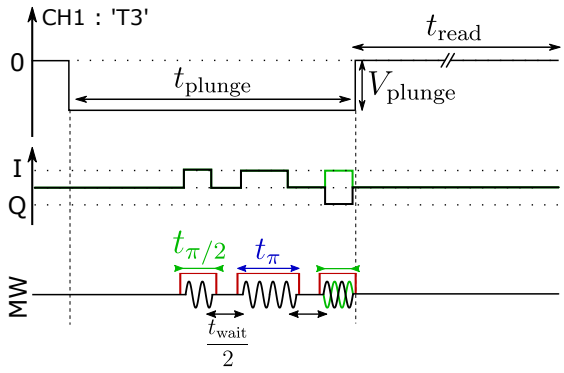

Figure 4.10 – **AWG sequences used to perform Hahn-Echo coherence time measurements:** Upper panel depicts the sequence sent on gate T_3 in order to manipulate the spin state (plunge) and read it out (read). In this case, $t_{\text{plunge}} = 200\,\mu\text{s}$, $V_{\text{plunge}} = -2\,\text{mV}$ and $t_{\text{read}} = 500\,\mu\text{s}$. During manipulation stage, the spin state experiences a first $\pi/2$-pulse to create a state superposition. After a free evolution duration $t_{\text{wait}}/2$, a π-pulse is sent to cancel low-frequency noise. Finally, the spin state is controlled by a $\pi/2$-pulse alternatively sent from I or Q port of the MW source. Each sequence lasts 700 µs and is repeated 160 times. A whole measurement, comprising 71 values of t_{wait}, therefore lasts 7.95 s.

the equation below with A, T_2^E and β as free parameters:

$$P_{\uparrow}(t) = Ae^{-\left(t_{\text{wait}}/T_2^E\right)^{\beta}} \tag{4.4}$$

The probability of recording an $|\uparrow\rangle$-spin state is averaged over several repetitions as presented in panel (b) of figure 4.11. Solid line is the fit from equation 4.4 revealing a Hahn-Echo coherence time of $T_2^E = 55.5\,\mu\text{s}$ and $\beta = 1.8$. Compared to the recent literature [20], the above estimated Hahn-Echo coherence time is in agreement with reported values in similar device structure when operated at a sweetspot $T_2^E = 88\,\mu\text{s}$ [4] with both first and second-order of gate noise minimized, and is much larger than T_2^E when no magnetic field calibration, i.e. the qubit is operated onto the sweetline, is done $T_2^E = 1.5\,\mu\text{s}$ [19, 26].

A comparison of coherence times at and far from a sweetspot is shown in figure 4.12 when recording T_2^E depending on magnetic field angle in (NP) plane. For comparison purposes, the inverse of T_2^E is plotted (green diamonds) alongside the absolute value of longitudinal spin susceptibility $\beta_{\parallel}$ to T_3 (red stars and fit as solid line). A high anisotropy of coherence timescales, ranging from 6.93 µs aside from a sweetspot (dashed blue line) to 40.23 µs at a sweetspot angle (grey dashed line), illustrates the successful mitigation of gate induced charge noise. Remarkably, this T_2^E anisotropy aligns closely with $\beta_{\parallel}$ variations, corroborating the hypothesis that coherence time is primarily limited by electrical noise. Operating the spin qubit at a sweetspot position enhances its Hahn-Echo coherence time by about a factor 6 in this instance and is in agreement with reported values in ref. [4].

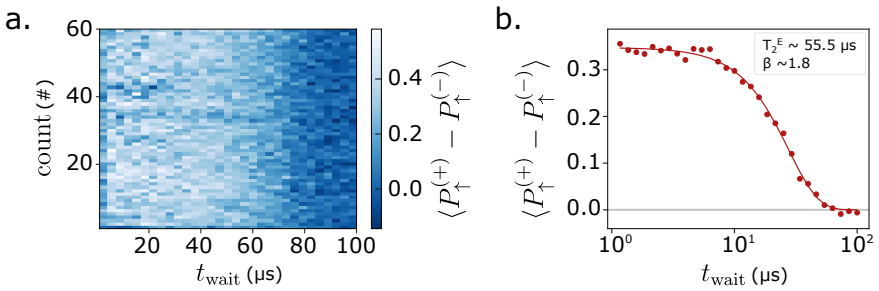

Figure 4.11 – **Example of Hahn-Echo coherence time measurement at a sweetspot:** (a) $|\uparrow\rangle$-spin state probability decay as a function of the waiting time and repeated. $|\uparrow\rangle$-state probability is calculated as the difference of signal amplitudes (not shown here). A clear amplitude decay is observed from short to long waiting times. Averaging $P_\uparrow$ time-traces gives the curve in panel (b). (b) Averaged $P_\uparrow$ time-traces as a function of the waiting time. The amplitude decay is fitted using equation 4.4, estimating $T_2^E = 55.5\,\mu s$ at $\mathbf{B} = (0.489, -0.131, 0.318)\,T$ with a free parameter exponent converging to $\beta = 1.8$.

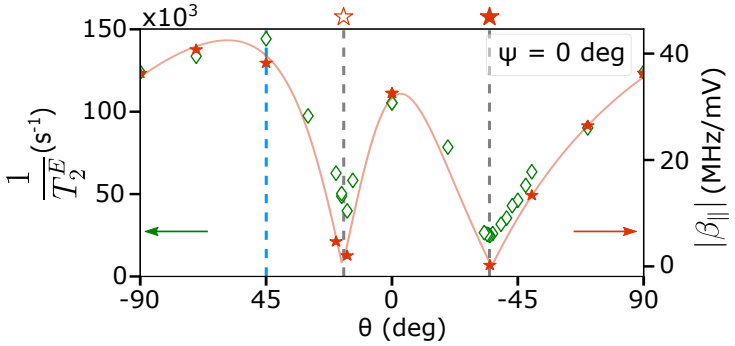

Figure 4.12 – **Hahn-Echo coherence time measured across (NP) magnet plane:** Inverse of Hahn-Echo coherence time plotted as a function of magnetic field direction defined by the angle θ in the (NP) plane. Values ranging from $T_2^E = 6.93\,\mu s$ (dashed blue line) to $T_2^E = 40.23\,\mu s$ (red star angle) evidence an enhancement about a factor 6 in coherence time. Red solid line and points indicate the absolute value of longitudinal contribution of T_3 charge noise as in the previous sections. Grey dashed lines underscore the sweetspot magnetic angles.

4.2.2 Rabi frequency evaluation

From the literature [4] and this above experimental demonstration, it is clear that the coherence time (either Ramsey or Hahn-Echo) is enhanced when electrical noise contribution is mitigated. However, decoupling the spin qubit from its (noisy) environment also comes along with a concomitant reduction of its manipulation speed. Such trade-off is a limiting factor that hampers the spin qubit implementation for quantum computation [7, 27, 28]. As briefly alluded in introduction of section 4.2, theoretical study [9] predicts a "reciprocal sweetness" relation between transverse $\beta_\perp$ and longitudinal $\beta_\parallel$ charge noise components tackling

the aforementioned limitation. This reciprocal sweetness relation can be experimentally translated as: the maxima of Rabi frequency lie nearby the dephasing sweetspots (i.e. longest coherence times), thus forming optimal qubit operation point. In the succeeding sections, we characterize the transverse contribution of charge noise by probing the angular dependence of Rabi frequency in magnetic field, knowing the relation below.

$$f_R = \frac{\mu_B}{2h} B V_{ac}\, \beta_\perp = \frac{\mu_B}{2hg^*} \mathbf{B} V_{ac} |(g\mathbf{b}) \times (g'\mathbf{b})| \tag{4.5}$$

From the previous measurements of $\beta_\parallel$, both G and G'-tensors are known. As a consequence, measuring at least 3 independent magnetic field orientations permits to fit the complete angular variations of the Rabi frequency in magnetic field.

Examination of the reciprocal sweetness relation

The qubit manipulation speed, characterized by the Rabi frequency, results from two driving mechanisms: the g-tensor modulation resonance (g-TMR) and the iso-Zeeman resonance (IZR). Both processes are directly related to the hole g-matrix, hence the Rabi frequency is modified with respect to magnetic field orientation [13, 14]. The question that consequently arises is: do these Rabi frequency variations coincide with the electrical noise in the magnetic field? To tackle the question, we measure the Rabi frequency for different magnetic field orientations, and reconstruct the transverse spin susceptibility by means of the g-matrix formalism.

The AWG sequence used to experimentally perform Rabi oscillation measurements is the same than EDSR one with a MW burst duration sub-microsecond timescale (see section 3.2.1). The microwave tone is sent via gate T_3 to allow for the comparison between the measured $\beta_\parallel$ and f_R. Figure 4.13(a) displays the Rabi oscillations recorded for a MW tone nearby the Larmor frequency (red dashed line). In this instance, measurements are conducted nearby a sweetspot (white star in (NP) plane) at $P_{\mathrm{MW}} = 18\,\mathrm{dBm}$ and $\mathbf{B} = (-0.867, 0.0, 0.316)\,\mathrm{T}$, corresponding to $\theta = -20°$. We evaluate the fridge attenuation, in addition to the intrinsic losses at room temperature for a MW tone at 18 GHz to be about 50 dB. The driving amplitude at the device level can be calculated as follow:

$$A_{\mathrm{MW}} = 10^{[P_{\mathrm{MW}} - (A_{\mathrm{fridge}} + A_{18\mathrm{GHz}}) - 30]/20} \times \sqrt{Z_0} \tag{4.6}$$

with $Z_0 = 50\,\Omega$ is the impedance of the transmission line. Hence, in this example, $A_{\mathrm{MW}} = 5.61\,\mathrm{mV}$ at the device level. From equation 4.7, underscored by the white points in the figure panel (a), we fit the Rabi chevron and estimate the Rabi frequency to be about $f_R = 7.87\,\mathrm{MHz}$.

$$P_\uparrow(\delta f, t) = A\, \frac{f_R^2}{f_R^2 + \delta f^2} \sin^2\left(2\pi \frac{t}{2} \sqrt{f_R^2 + \delta f^2}\right) + B \tag{4.7}$$

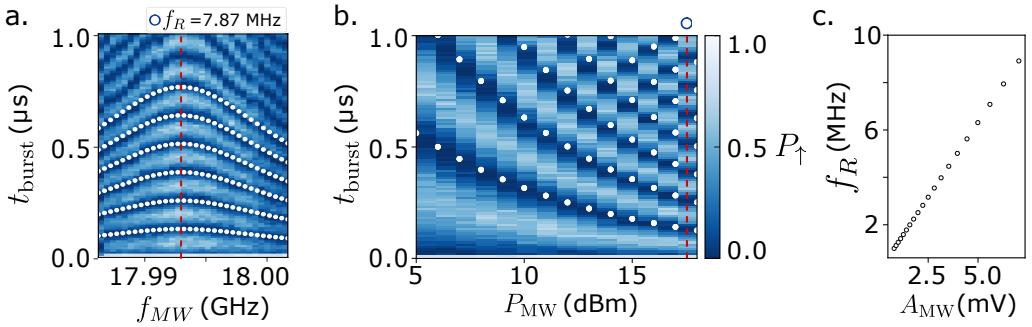

Figure 4.13 – **Example of coherent oscillations captured by Rabi chevrons:** (a) $|\uparrow\rangle$-spin state probability when driving the spin qubit for a duration t_{burst} up to microsecond at a MW tone close by the Larmor frequency. Measurement is taken at $P_{\mathrm{MW}} = 18\,\mathrm{dBm}$ nearby a sweetspot (empty red star in figure 4.12) for $\mathbf{B} = (-0.867, 0.0, 0.316)\,\mathrm{T}$. Each time-trace is averaged about 2000 times. White points display a fit of $P_\uparrow$ minima using the formula 4.7. This allows to estimate the qubit Rabi frequency $f_R = 7.87\,\mathrm{MHz}$. Such measurement is often referred as Rabi "chevron". The red dashed line indicates the qubit Larmor frequency $f_L = 17.993\,\mathrm{GHz}$. (b) Rabi oscillations recorded for different MW power values at the Larmor frequency. This measurement is hereafter labelled "power chevron". White points are a fit using equation 4.8 so that the Rabi frequency can be estimated at any MW power. (c) Estimated Rabi frequencies as a function of drive amplitude calculated from panel (b). The driving amplitude is evaluated using equation 4.6.

Comparing Rabi frequencies between experimental setup is little relevant as the MW power sent to the device cannot be accurately estimated. In panel (b) of figure 4.13 are shown Rabi oscillations measured at the Larmor frequency when increasing MW power. The higher amplitude of the driving signals, the faster the qubit is manipulated. In practice, the qubit Rabi frequency scales linearly with the microwave amplitude A_{MW}, as illustrated in panel (c), in which the drive amplitude is calculated with equation 4.6 from powers in panel (b). Some saturation at large MW power, not observed in the present case, have been evidenced and attributed to dot confinement anharmonicity [29, 30]. So as to know the Rabi frequency at any MW signal amplitude, the power chevron (panel (b)) is fitted using the formula 4.8, as emphasized by white points.

$$P_\uparrow(p,t) = A\sin^2\left(2\pi\frac{t}{2}\sqrt{10^{\frac{p}{10}}}f_R + \phi_0\right) + B \tag{4.8}$$

The anisotropy of Rabi frequency with respect to magnetic field direction in the (NP) plane is presented in figure 4.14. So as to rigorously compare the Rabi frequencies, a peculiar attention is drawn onto having the same measurement settings (Larmor frequency and MW power) at different field angles. In the (NP) plane, values are ranging from $f_R = 0.984\,\mathrm{MHz}$ to $f_R = 6.643\,\mathrm{MHz}$ witnessing a strong modulation of f_R values depending on $\mathbf{B}$-field. Nevertheless, no clear correspondence is evidenced when compared to the longitudinal charge noise (in red).

One sweetspot exhibits a rapid electrical control over the spin qubit orientation (empty red star) whereas the other sweetspot (red star) seems to have a much slower manipulation speed. The crucial information evidenced herein is that all sweetspots are not necessarily equivalent in terms of speed of operation (f_R).

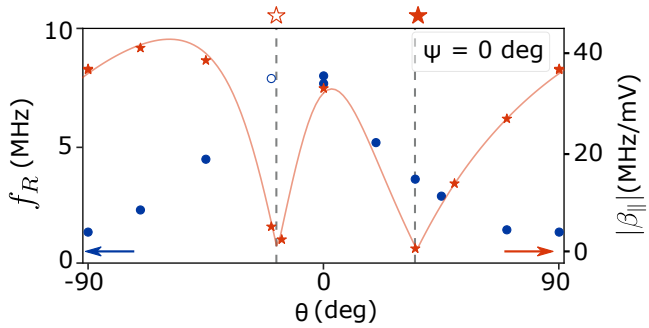

Figure 4.14 – **Angular dependence of Rabi frequencies in magnetic field:** Rabi frequency variations according to magnetic field direction in (NP) plane. A large anisotropy in Rabi frequencies ranging from 0.984 MHz to 6.643 MHz is readily evidenced. Red line and points represent the absolute value of the longitudinal electric noise induced by gate T_3. At the sweetspot orientations (grey dashed lines) two distinct cases are observed: one sweetspot with a fast electrical control ($\theta = -20°$ also presented in figure 4.13) whereas the other one ($\theta = 35°$) exhibits a much slower Rabi frequency.

Importantly, this measurement does not invalidate the reciprocal sweetness relation, as a maximum of Rabi frequency stands nearby a dephasing sweetspot. To ensure that maxima of Rabi frequency (i.e. minima of $\beta_\perp$) coincide with maxima of coherence time (i.e. minima of $\beta_\parallel$), it is relevant to evaluate the Rabi frequency variations for a complete magnetic angular dependence (θ, ψ). To this aim, $\beta_\perp$ contribution can be derived from its definition in equation 4.5 as [31]:

$$\beta_\perp(\theta,\psi) = \frac{1}{(g^*)^2}\left|\mathbf{t}\times\left[\frac{\partial g_d}{\partial V}\hat{V}^T\mathbf{b} + g_d\left(\frac{\partial \hat{V}}{\partial V}\right)^T\mathbf{b} - \hat{P}\mathbf{t}\right]\right| \tag{4.9}$$

with the notations

$$\boldsymbol{t} = g_d\hat{V}^T\boldsymbol{b} \text{ and } \hat{P} = \left(\frac{\partial \hat{U}}{\partial V}\right)^T\cdot\hat{U}$$

$$g^* = |g\boldsymbol{b}| \text{ and } g = \hat{U}g_d\hat{V}^T$$

In equation 4.9, all terms are explicit from the g-matrix decomposition except the anti-symmetric matrix $\hat{P}$. As a consequence, knowing G and G'-tensors with values of Rabi frequency for at least 3 independent orientations of magnetic field allows to evaluate the $\hat{P}$-matrix and thus to reconstruct the complete angular map of $\beta_\perp(\theta,\psi)$. From least-square minimization method, the evaluated $\hat{P}$-matrix is:

$$\hat{P} \cong \begin{bmatrix} 0 & 1.217 & 0.789 \\ -1.217 & 0 & 2.169 \\ -0.789 & -2.169 & 0 \end{bmatrix} \tag{4.10}$$

The following figure 4.15 illustrates the fitted angular map of $\beta_\perp(\theta, \psi)$ when $V_{B_3} = -0.635\,\mathrm{V}$ rescaled at a constant Larmor frequency of 18 GHz. The sweetline equation found from $\beta_\parallel$ fitting procedure is added as a purple dashed line, revealing that maxima of $\beta_\perp$ (hence that of the Rabi frequency) are always coinciding with particular sweetspots (minima of $\beta_\parallel$) [9]. In that sense, the reciprocal relation is, by definition, fulfilled. The subtlety resides in the fact that not all sweetspot manifest optimal operation speed but only part of them.

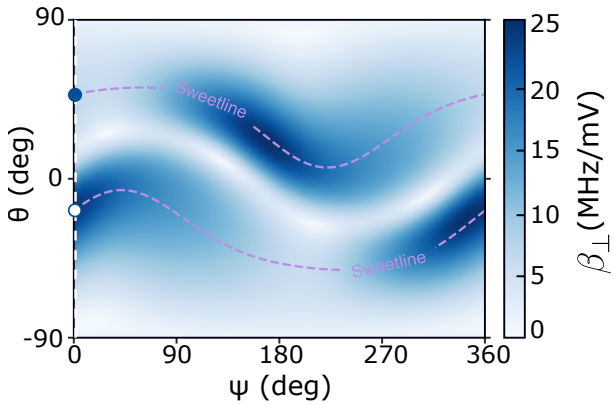

Figure 4.15 – **Evolution of $\beta_\perp$ depending on magnetic field orientation at constant Larmor frequency:** Anisotropy of $\beta_\perp$ with respect to magnetic field orientation. Maxima (dark blue regions) are observed onto the sweetlines highlighted by the purple dashed lines (taken from $\beta_\parallel$ fitting procedure so that $\mathbf{b}^T G' \mathbf{b} = 0$). White dashed line and circles at $\psi = 0°$ illustrate the (NP) plane shown in the previous figure. In (NP) plane, figure 4.14, one of the two sweetspots manifests a larger Rabi frequency, in agreement with the fitted angular map shown herein.

This first experimental demonstration of reciprocal sweetness relation must however be treated with caution. Indeed, fitting the anisotropy of transverse component of charge noise is challenging and many sources of error hinder the fit accuracy. First, despite the particular attention drawn onto measuring at a fixed Larmor frequency and fixed MW power, the fitting procedure does not account for possible fluctuations of MW amplitude (denoted V_{ac} in equation 4.5) perceived at the device level. In addition, cross-talk between gates prevent the isolation of a single gate contribution to the qubit manipulation. Measured Rabi frequencies thus stem from the driving via multiple gates whereas the longitudinal spin susceptibility relates to a single gate. In this sense, the comparison between measured $\beta_\parallel$ and $\beta_\perp$ must be viewed critically.

4.2.3 Q-factor measurements

Operating the spin qubit on the sweetline ensures an extended coherence time and can also, for some sweetspots, exhibit a faster Rabi frequency. A relevant metrics to characterize the efficiency of a single qubit gate is the quality factor defined as:

$$Q_{\mathrm{R}} = 2 f_R T_2^{\mathrm{R}} \tag{4.11}$$

The latter determines the number of π-rotations achievable within the decoherence time T_2^{R} upon driving. From now on, the focus is laid upon the estimation of the Q-factor at a sweetspot (solid red star, at $\theta = 35°$) chosen for its long coherence time $T_2^E \simeq 40\,\mu\mathrm{s}$ and a decent Rabi frequency about $f_R = 3.58\,\mathrm{MHz}$.

Influence of the driving gate on f_R

Remarkably, the Rabi frequency is experimentally strongly affected by the gate used to drive the qubit. The two panels of figure 4.16 are Rabi chevron measured with same experimental settings (same MW amplitude, magnetic field orientation and at similar Larmor frequencies[6]) when driving either on gate T_3 or T_4. On the left panel, MW tone is sent via gate T_3 and the resulting Rabi frequency is $f_R = 3.58\,\mathrm{MHz}$. On the right panel in which the MW tone is sent via gate T_4, the Rabi frequency reaches up to $f_R = 9.57\,\mathrm{MHz}$.

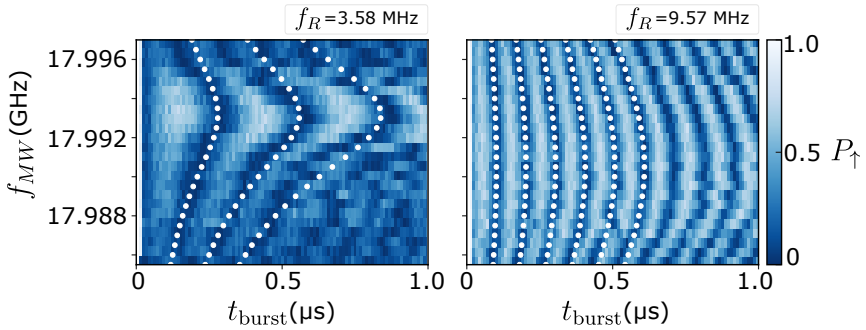

Figure 4.16 – **Rabi chevrons comparison for different driving gates:** Left (right) panel is a chevron measurement probed at $P_{\mathrm{MW}} = 18\,\mathrm{dBm}$ (at room temperature) for a sweetspot orientation $\mathbf{B} = (0.515, 0.0, 0.360)\,\mathrm{T}$ when driving by gate T_3 (T_4). A non-negligible difference in evaluated Rabi frequencies is observed, suggesting that the leading driving mechanism is Iso-Zeeman Resonance. The equivalent drive amplitude at the sample level is $A_{\mathrm{MW}} = 5.61\,\mathrm{mV}$.

Such a difference in Rabi frequency can be explained by the driving mechanisms involved for spin manipulation which differ depending on the gate used.

6. We verify that this Larmor frequency difference is negligible in term of driving amplitude modifications to compare the Rabi chevrons. Attenuations throughout the fridge are the same between the two gate lines.

Indeed, the driving tone can be seen as an electric field, whose orientation depends on the gate used to control the qubit: either mostly vertical when pulsing on T_3 or horizontal in the case of gate T_4. This is expected to rather favour g-TMR or iso-Zeeman driving mechanism. As a short term prospect, it may be relevant to compute the angular Rabi frequency map when pulsing on each gate and separate the contributions of both driving mechanisms, as in ref. [13]. This could provide additional insights on the cross-talk between the two gates upon manipulation, and some quantitative understanding on the ratio of the two driving mechanisms.

In the next section, Q-factor is evaluated while driving the spin state via gate T_4, demonstrating faster operation speed. Magnetic field is set to a sweetspot orientation $\mathbf{B} = (0.515, 0.0, 0.360)\,\mathrm{T}$.

Hole spin qubit Q-factor at a sweetspot

Measuring single qubit Q-factor boils down to probe Rabi oscillations damping for long burst duration. An example of damped Rabi oscillations depending on burst period is illustrated in figure 4.17(a) at $P_{\mathrm{MW}} = +18\,\mathrm{dBm}$. Solid line is a sinusoidal fitting function permitting to estimate the Rabi frequency and the oscillation amplitudes, denoted $\mathrm{A_{osc}}$. The latter are plotted in panel (b) of the same figure and fitted with an exponential decay ($\mathrm{A_{osc}} = e^{-t/T_2^{\mathrm{R}}}$) to estimate T_2^R similarly to ref. [1]. Knowing f_R and T_2^R finally gives $Q_R \sim 690$. The large value of Q_R herein demonstrated at a sweetspot competes with reported values for electrons in natural silicon ($Q \sim 140$) [30] and with state-of-the-art Q-factor in purified silicon ($Q \sim 888$) [1]. It is furthermore much larger than reported values for hole spin qubit in Germanium ($Q \sim 45$) [32], that justifies operating hole spin qubit at a dephasing sweetspot. This predicts a rough estimation of π-gate fidelity about $F_\pi = e^{-1/Q} \simeq 99.8(5)\%$ following calculations from ref. [32].

Moreover, as the Rabi frequency varies with MW power, same measurements are repeated with increasing the drive amplitude shown in panel (c) and (d). From room temperature measurements, we estimate the attenuation of the RF lines at $f_{\mathrm{probe}} = 18\,\mathrm{GHz}$ is $A_{18\mathrm{GHz}} \simeq 10\,\mathrm{dB}$. A clear increase of both Q_R and f_R is observed when enlarging the drive amplitude, reaching up to the aforementioned Q-factor value. The non-saturating behaviour of f_R with MW amplitude suggests that higher Q-factor values could have been achieved if larger drive amplitude could have been reached.

4.2.4 Discussion about inhomogeneities on the sweetline

Dephasing sweetspots offer a possibility to artificially extend the hole spin qubit coherence time while maintaining a fast manipulation speed, thus constituting optimal operation points. Yet, all sweetspots on the sweetline are not equiv-

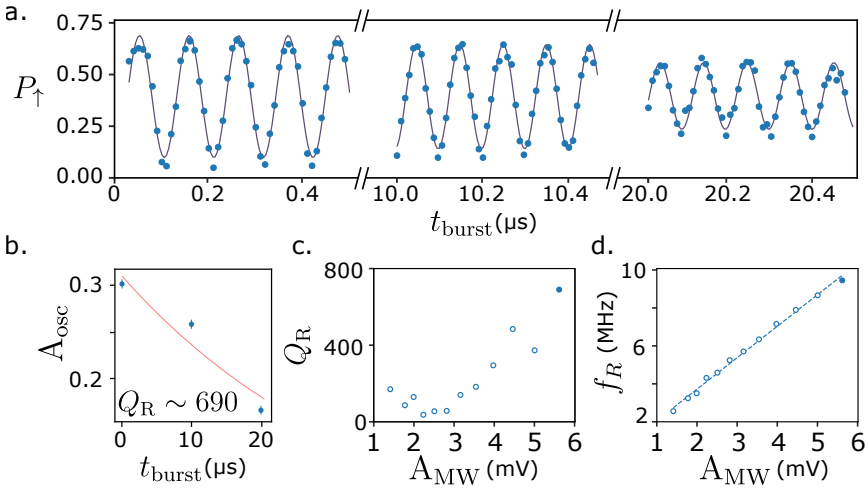

Figure 4.17 – **Q-factor evaluation at a sweetspot:** (a) Example of Rabi oscillations recorded for 500 ns in 3 distinct burst sections and averaged 10 times. Solid line is a sinusoidal fit with the same initial phase term for each burst duration segment. The evaluated amplitudes, labelled A_{osc}, are plotted in panel (b). The MW power used in this instance corresponds to a driving amplitude (taking into account the fridge attenuation and the power delivered at 18 GHz) about $A_{MW} \simeq 5.61$ mV. (b) Oscillation amplitudes for each segment are fitted (see solid red line) with an exponential decay. The calculated Q-factor value is about 690. (c) and (d) Evolution of Q-factor and Rabi frequency as a function of MW power used for spin manipulation. An overall increase for larger MW power values is observed. In panel (d), solid line is a linear regression.

alent. As aforementioned, probing qubit performance metrics along the sweetline is challenging as the required precision is about a quarter of an angular degree. To circumvent such difficulties, perpendicular cut across the sweetline have been performed.

On the one hand, coherence times along the sweetline change and are in average (when measured as closely as possible to sweetspot) about 20 µs. Some peculiar magnetic field orientations, which belong to the sweetline, can, as shown in figure 4.11(b), reach up to 55 µs coherence. Even though T_2 time remains better on the sweetline, such variability may be attributed to (i) the higher-orders of gate fluctuations that have their own angular symmetry, (ii) to the presence of nearby fluctuators strongly affecting qubit performances [7] (iii) to hyperfine interactions[7].

On the other hand, figure 4.14 readily demonstrates (for two sweetspots) high variability of Rabi frequencies along the sweetline. Despite the possible enhancement by changing the driving gate, Rabi frequencies remain in the few megahertz

7. Note that hyperfine interactions induce low-frequency noise which only affects the Ramsey coherence time, T_2^*, since it is cancelled in the case of Hahn-Echo measurements.

range, regardless the magnetic field orientation. Cancelling the longitudinal charge noise does not drastically reduce the spin control in that case, nor does it necessarily come along with an enhanced operation speed. In other words, along the sweetline, some sweetspots may exhibit a higher Rabi frequency, i.e. a reciprocal sweetness nature which is not necessarily accurate for all sweetspots. The latter characteristic can experimentally be challenging to elucidate owing to cross-talk between gates. Indeed, reciprocal sweetness relation compares longitudinal and transverse contributions of a single gate (e.g. $\beta_{\parallel}^{(T_3)}$ and $\beta_{\perp}^{(T_3)}$). Having some cross-talk between the lines causes all gates to contribute -to some extend- to spin manipulation. In that sense, the transverse component of electrical noise $\beta_{\perp}$ is hardly predictable for each gate separately and must be considered as a whole.

4.3 Conclusions

Dephasing sweetline constitutes an appealing property of hole spin in the context of qubit manipulation as it extends the coherence time (T_2^E and T_2^*) while maintaining fast and all-electrical driving possibility ($f_R \sim$ MHz). Some sweetspot even demonstrates operation quality factor Q about 690, competing with state-of-the-art values reported for electrons in ^{28}Si [1] and holes in Ge [32]. This corresponds to π-gate fidelity of 99.8(5) %. Alongside an overall increase of the qubit coherence time and decent Rabi frequencies, sweetlines for charge noise are highly tunable. Modifying the hole wavefunction confinement indirectly affects the g-matrix and its first derivative to gate voltage $\partial g/\partial V_{T_3}$ which in turn alters the longitudinal component of charge noise $\beta_{\parallel}$. The angular position of the sweetline can be tuned up to 26° in magnetic field (herein arbitrarily measured in the (NP) plane) and fully reconstruct using the g-matrix formalism. The fact that such optimal operation points can be set at will in magnetic field orientation opens promising prospects when scaling-up to multiple qubits system. In that sense, each qubit could be tuned to exhibit its dedicated sweetspot at a common magnetic field direction.

References

[1] J. Yoneda et al. « A quantum-dot spin qubit with coherence limited by charge noise and fidelity higher than 99.9% ». In: *Nature Nanotechnology* 13.2 (2018), pp. 102–106. DOI: 10.1038/s41565-017-0014-x.

[2] Y. Choi and R. Joynt. « Anisotropy with respect to the applied magnetic field of spin qubit decoherence times ». In: *npj Quantum Information* 8.1 (June 2022), p. 70. DOI: 10.1038/s41534-022-00576-6.

[3] O. Malkoc, P. Stano, and D. Loss. « Charge-Noise-Induced Dephasing in Silicon Hole-Spin Qubits ». In: *Phys. Rev. Lett.* 129 (24 Dec. 2022), p. 247701. DOI: 10.1103/PhysRevLett.129.247701.

[4] N. Piot et al. « A single hole spin with enhanced coherence in natural silicon ». In: *Nature Nanotechnology* 17.10 (Sept. 2022), pp. 1072–1077. DOI: 10.1038/s41565-022-01196-z.

[5] T. Tanttu et al. « Controlling Spin-Orbit Interactions in Silicon Quantum Dots Using Magnetic Field Direction ». In: *Physical Review X* 9 (2 May 2019), p. 021028. DOI: 10.1103/PhysRevX.9.021028.

[6] S. D. Liles et al. « Electrical control of the g tensor of the first hole in a silicon MOS quantum dot ». In: *Phys. Rev. B* 104 (23 Dec. 2021), p. 235303. DOI: 10.1103/PhysRevB.104.235303.

[7] Lorenzo Mauro et al. « Geometry of the dephasing sweet spots of spin-orbit qubits ». In: *Phys. Rev. B* 109 (15 Apr. 2024), p. 155406. DOI: 10.1103/PhysRevB.109.155406.

[8] B. Venitucci. « Modélisation de la manipulation électrique des qubits de trou dans le silicium ». Theses. Université Grenoble Alpes (2020), Nov. 2020.

[9] V. P. Michal et al. « Tunable hole spin-photon interaction based on g-matrix modulation ». In: *Phys. Rev. B* 107 (4 Jan. 2023), p. L041303. DOI: 10.1103/PhysRevB.107.L041303.

[10] R. Hanson et al. « Spins in few-electron quantum dots ». In: *Reviews of Modern Physics* 79 (4 Oct. 2007), pp. 1217–1265. DOI: 10.1103/RevModPhys.79.1217.

[11] N. Ares et al. « Nature of Tunable Hole g Factors in Quantum Dots ». In: *Physical Review Letters* 110 (4 Jan. 2013), p. 046602. DOI: 10.1103/PhysRevLett.110.046602.

[12] C. Gradl et al. « Asymmetric g Tensor in Low-Symmetry Two-Dimensional Hole Systems ». In: *Phys. Rev. X* 8 (2 June 2018), p. 021068. DOI: 10.1103/PhysRevX.8.021068.

[13] A. Crippa et al. « Electrical Spin Driving by g-Matrix Modulation in Spin-Orbit Qubits ». In: *Physical Review Letters* 120.13 (Mar. 2018), p. 137702. DOI: 10.1103/physrevlett.120.137702.

[14] B. Venitucci et al. « Electrical manipulation of semiconductor spin qubits within the g-matrix formalism ». In: *Phys. Rev. B* 98 (15 Oct. 2018), p. 155319. DOI: 10.1103/PhysRevB.98.155319.

[15] F. N. M. Froning et al. « Ultrafast hole spin qubit with gate-tunable spin–orbit switch functionality ». In: *Nature Nanotechnology* 16.3 (Mar. 2021), pp. 308–312. DOI: 10.1038/s41565-020-00828-6.

[16] D. Vion et al. « Manipulating the Quantum State of an Electrical Circuit ». In: *Science* 296.5569 (May 2002), pp. 886–889. DOI: 10.1126/science.1069372.

[17] F. H. L. Koppens, K. C. Nowack, and L. M. K. Vandersypen. « Spin Echo of a Single Electron Spin in a Quantum Dot ». In: *Phys. Rev. Lett.* 100 (23 June 2008), p. 236802. DOI: 10.1103/PhysRevLett.100.236802.

[18] G. Burkard et al. « Semiconductor spin qubits ». In: *Rev. Mod. Phys.* 95 (2 June 2023), p. 025003. DOI: 10.1103/RevModPhys.95.025003.

[19] L. C. Camenzind et al. « A hole spin qubit in a fin field-effect transistor above 4 kelvin ». In: *Nature Electronics* 5.3 (Mar. 2022), pp. 178–183. DOI: 10.1038/s41928-022-00722-0.

[20] P. Stano and Daniel Loss. « Review of performance metrics of spin qubits in gated semiconducting nanostructures ». In: *Nature Reviews Physics* 4.10 (Oct. 2022), pp. 672–688. DOI: 10.1038/s42254-022-00484-w.

[21] A. P. Higginbotham et al. « Hole Spin Coherence in a Ge/Si Heterostructure Nanowire ». In: *Nano Letters* 14.6 (June 2014), pp. 3582–3586. DOI: 10.1021/nl501242b.

[22] H. Watzinger et al. « A germanium hole spin qubit ». In: *Nature Communications* 9.1 (2018), p. 3902. DOI: 10.1038/s41467-018-06418-4.

[23] R. Zhao et al. « Single-spin qubits in isotopically enriched silicon at low magnetic field ». In: *Nature Communications* 10.1 (Dec. 2019), p. 5500. DOI: 10.1038/s41467-019-13416-7.

[24] P. Harvey-Collard et al. « Spin-orbit Interactions for Singlet-Triplet Qubits in Silicon ». In: *Phys. Rev. Lett.* 122 (21 May 2019), p. 217702. DOI: 10.1103/PhysRevLett.122.217702.

[25] M. R. Delbecq et al. « Quantum Dephasing in a Gated GaAs Triple Quantum Dot due to Nonergodic Noise ». In: *Phys. Rev. Lett.* 116 (4 Jan. 2016), p. 046802. DOI: 10.1103/PhysRevLett.116.046802.

[26] R. Maurand et al. « A CMOS silicon spin qubit ». In: *Nature Communications* (May 2016). DOI: 10.1038/ncomms13575.

[27] W. Gilbert et al. « On-demand electrical control of spin qubits ». In: *Nature Nanotechnology* 18.2 (Feb. 2023), pp. 131–136. DOI: 10.1038/s41565-022-01280-4.

[28] M. J. Carballido et al. *A Qubit with Simultaneously Maximized Speed and Coherence*. arXiv. 2024. DOI: 10.48550/arXiv.2402.07313.

[29] J. Yoneda et al. « Fast Electrical Control of Single Electron Spins in Quantum Dots with Vanishing Influence from Nuclear Spins ». In: *Phys. Rev. Lett.* 113 (26 Dec. 2014), p. 267601. DOI: 10.1103/PhysRevLett.113.267601.

[30] K. Takeda et al. « A fault-tolerant addressable spin qubit in a natural silicon quantum dot ». In: *Science Advances* 2.8 (2016), e1600694. DOI: 10.1126/sciadv.1600694.

[31] E. A. Rodríguez-Mena. « Some computations related to the g-matrix formalism ». Private communications. Jan. 2024.

[32] K. Wang et al. « Ultrafast coherent control of a hole spin qubit in a germanium quantum dot ». In: *Nature Communications* 13.1 (Jan. 2022), p. 206. DOI: 10.1038/s41467-021-27880-7.

CHAPTER 5

Extending sweetline concept to 2 qubits

When manipulated at a dephasing sweetspot, single hole spin qubit exhibits enhanced performances [1, 2, 3]. In the scope of scalability, one could imagine having sweetspots of multiple qubits system to shared orientations, therefore constituting common optimal operation points. However, it is known [4, 5] that a variability between quantum dots confinement, mostly attributed to fabrication imperfections, can cause the spin qubit to have highly unalike behaviour, among which, a different response to longitudinal charge noise. As a result, it is a priori improbable for two qubits on the same chip to share a common sweetspot at a magnetic field orientation. Since the angular position in magnetic field of these sweetlines is electrically tunable, a proper calibration could possibly extend multiple qubits system functioning, by creating shared sweetspots.

Herein is tackled the concept of sweetlines and optimal operation points when implementing two neighbouring hole spin qubits. First focus is laid on the realization of a second spin qubit underneath gate T_4 and the understanding of the longitudinal spin susceptibility to charge noise (similarly to chapter 3). Then, the emphasize is drawn onto the comparison of the two qubits and towards the experimental alignment of both sweetlines.

Contents

Disclaimer : The data provided in this chapter are extremely recent, and their interpretation should be approached with caution as they might be incomplete. Some further measurements are still ongoing.

5.1 Operation of a second qubit below gate T_4

5.1.1 Gate settings and readout

Thanks to the device geometry, a second qubit can be implemented underneath gate T_4 as shown in figure 6.1 without modifying the previously defined qubit confined in QD_3. A single hole is enclosed within a QD located under gate T_4, hereafter denoted QD_4. Its spin orientation is probed by Elzerman readout (as in chapter 3) via a strongly accumulated charge sensor below the gates B_5, B_6 and T_6 (red area). Charging events of the latter sensor are measured by radio-frequency reflectometry at a carrier tone $f_D = 292.2\,\mathrm{MHz}$ (see chapter 2) connected to the Drain (D) contact. As for QD_3, gates displayed in green, i.e. B_4 and T_5, are used to monitor the tunnelling rates between QD_4 and its dedicated charge sensor. In a similar manner than chapter 4, B_4 gate will also be used to tailor the electric field confining the hole wavefunction. The spin will be electrically manipulated thanks to MW tone sent through gate T_4.

5.1.2 Comparison between the two qubits g-matrices

In a similar fashion than in previous chapters, we first figure out the hole g-factor anisotropy in magnetic field orientation before investigating the longitudinal spin susceptibility and the presence of sweetlines. The hole g-factor accumulated in QD_4 is inferred by measuring the angular dependence of the Larmor frequency with respect to magnetic field by EDSR. Results are shown for $V_{B_4} = 0.2\,\mathrm{V}$ in figure 5.2 as the light green points and line (fit). In this case, the extrema of principal g-factors are $g_{\min} = 1.27$ and $g_{\max} = 2.90$. When comparing to the qubit in QD_3 (red

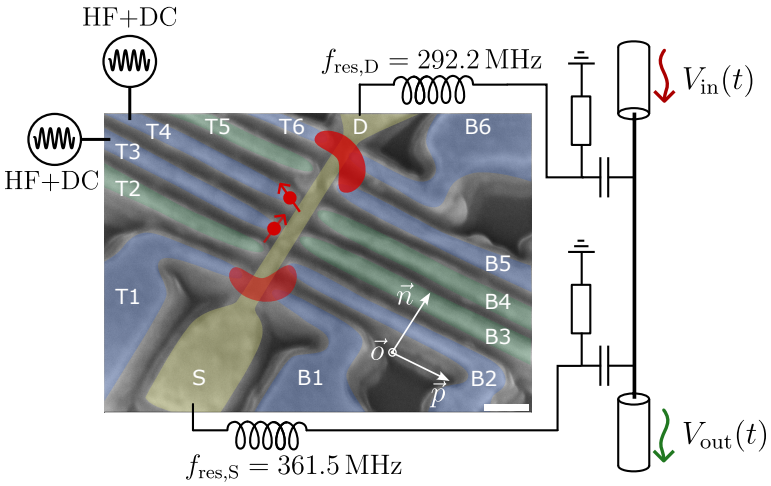

Figure 5.1 – **General description of gate role and wiring:** False coloured SEM image of the sample (as in chapter 3) showing the 6-split gate device. Red arrows illustrate the location of QDs of interest, each one hosting a single hole whose spin is used as a qubit. Concerning the qubit underneath gate T_4, its spin orientation is readout by Elzerman method with a charge sensor (red area) located below gates T_6, B_6 and T_5. Radio-frequency measurement are performed via the Drain (D) contact for QD_4 readout. Scale bar is 100 nm.

points and line), rather similar anisotropy amplitude is observed, despite a change in the spin basis (characterized by the angular tilt) that can be attributed to the presence of strain along the nanowire. Remarkably, the electric field stemming from gate voltages difference across the nanowire are highly different, but gives similar g-factor anisotropy (except the spin basis). Such discrepancies in gate regimes can be understood by a certain gate threshold variability (already seen in chapter 2) and the possible presence of strain and/or defects surrounding the qubits [6, 7, 8]. Nowadays, the lack of QD uniformity due to fabrication imperfections is a hold to advances for spin qubit in semiconductor materials [4, 5].

At this point, it is relevant to specify that the exchange between the two qubits is of negligible amplitude. Indeed, due to the large effective mass of particles confined in low dimensional silicon system and the possible presence of dopants/defects, the qubits underneath gates T_3 and T_4 are located far apart and the resulting exchange energy (function of the two wavefunctions overlap) thus tends to zero. In addition, no tunnelling, i.e. charge exchange, can happen between the two dots QD_3 and QD_4. Despite the rather small gate pitch compared to Germanium platforms [9], in the present case, each qubit behaves as an independent one. Consequently, the below investigation rather constitutes a proof of concept demonstrating the alignment of each qubit sweetline, opening the path towards enhanced operation points for multi-qubits systems.

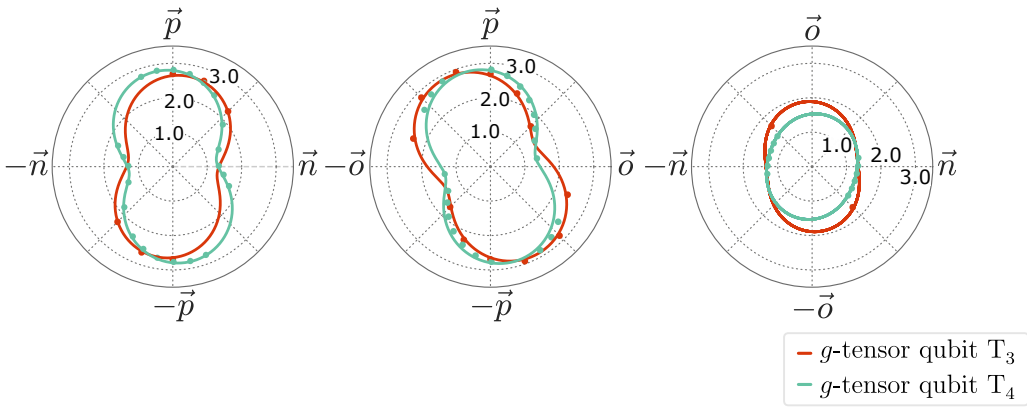

Figure 5.2 – **Hole g-matrix comparison between qubits located below gate T_3 and T_4:** Red (blue) points are g-factor values evaluated by EDSR relating to the qubit located underneath gate T_3 (T_4). Solid lines are the fitted g-matrices using g-matrix formalism as chapter 3. A certain variability in the g-matrix is observed between the two qubits, possibly due to disorder, strain and fabrication imperfections. The g-matrix configuration presented for the qubit below T_3 is for $V_{B_3} = -0.635\,\mathrm{V}$ and below T_4 gate is for $V_{B_4} = 0.2\,\mathrm{V}$.

5.1.3 Sweetline tuning of QD_4

Once again, the qubit g-matrix is measured depending on the gate voltage set on gate B_4 expected to be responsible for the hole wavefunction confinement, as for B_3 gate on QD_3 in chapter 4. From figure 5.3, a much weaker evolution of the g-matrices is observed over 450 mV voltage span than in the case of QD_3. Importantly, note that the voltage range used for V_{B_4} slightly differs from the one with V_{B_3}. This can be understood by the variability in gate voltage threshold (already observed in room temperature I-V characteristics in chapter 2). Furthermore, when setting V_{B_4} to more positive values and $V_{B_4} > 0.1\,\mathrm{V}$, i.e. presuming to confine more the hole wavefunction perpendicularly to the nanowire (towards $\vec{p}$-axis), the main g-factor along this axis surprisingly decreases. Main g-factors evolution for the ten gate configurations projected in the magnet basis can be found in appendix D. A possible reason explicating this g-factor evolution is that the potential difference induced between gates T_4 and B_4 is of weak influence on the dot shape, for instance if the resulting electric field is screened from the hole. This corroborates the idea that some defects might be present nearby the hole spin qubit in QD_4. Besides changes in B_4 potential, the reader should bear in mind that the voltage on gate T_5 is also modified, that may result in an overall deconfinement of the hole wavefunction along the $\vec{n}$-axis and extra strain contribution.

Despite a rather weak influence of the confining gate B_4 on the hole g-matrix, and thus on the corresponding G-tensor, the longitudinal spin susceptibility can still vary by way of the G'-tensor.

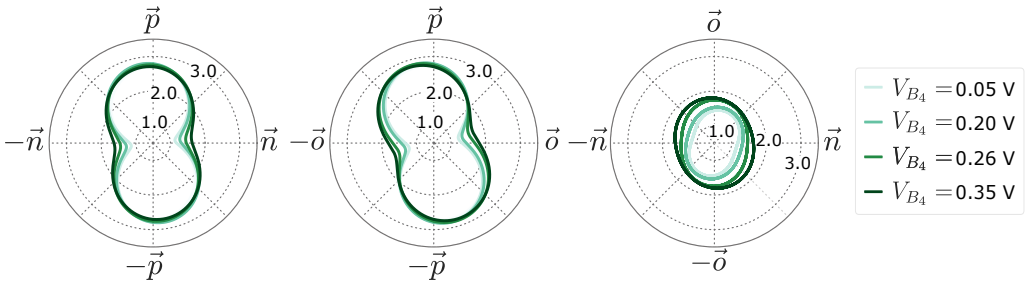

Figure 5.3 – **Comparison of the g-matrices for different values of V_{B_4}:** Angular dependence of the g-matrix to magnetic field for multiple gate voltage values on B_4 modifying the qubit confinement profile. For sake of clarity, only part of the fits from the measured gate configurations are displayed. Their obtention protocol is the same as before, relying on g-matrix formalism. A weak variation of the g-matrix is observed over 355 mV voltage span.

We evaluate, in a similar manner than in the previous chapter, the impact of V_{B_4} on the measured spin susceptibility $\beta_{\parallel}$ shown in figure 5.4. At first glance, most of the gate configurations lead to the presence of sweetlines as highlighted by the purple dashed lines, except at $V_{B_4} = -0.1\,\mathrm{V}$ for which the G'-tensor eigenvalues are all negative. Moreover, sweetlines are mostly swirling around or near the $\vec{p}$-axis ($\forall\,\psi, \theta = 90°$) but no clear pattern is observed when looking to the sweetline angular positions with respect to V_{B_4} values. Stars and circles in second panel underscore the sweetspot angular positions respectively in (NP) and (OP) planes (further discussed in section 5.5). Importantly, configurations such as $V_{B_4} = 0.0\,\mathrm{V}$ and $V_{B_4} = -0.02\,\mathrm{V}$ may appear to be strongly different in terms of longitudinal spin sensitivity anisotropy but actually only result in a slight change of the spin basis (hence a sweetline rotation), which is further emphasized by the 2D display. These two configurations are also presented in appendix D as 3D spheres in magnetic field.

If we now compare the longitudinal spin susceptibility anisotropy of each qubit (underneath T_3 and T_4) with its dedicated confining gate (B_3 and B_4), few important remarks are emerging. First, the absolute amplitude of both spin susceptibilities are similar and about few tens of MHz/mV. Yet, the sign of the spin susceptibility (in other words, the Larmor frequency shift) presented hereafter has opposite sign compared to the one measured in chapter 3 for the qubit hosted in QD_3. So far, no clear explanation of this sign opposition is found, but it suggests a different underlying physics between the two qubits. In addition, as the spin basis of each hole are quite similar, sweetlines are located nearby the $\vec{p}$-axis, meaning that some common sweetspots for the two qubits exist and may constitute resilient orientations for longitudinal charge noise. Unfortunately, as the spin basis is intrinsically given by the system symmetries, strain in the nanowire and dot non-uniformity, there is no straightforward manner to control and tune them so

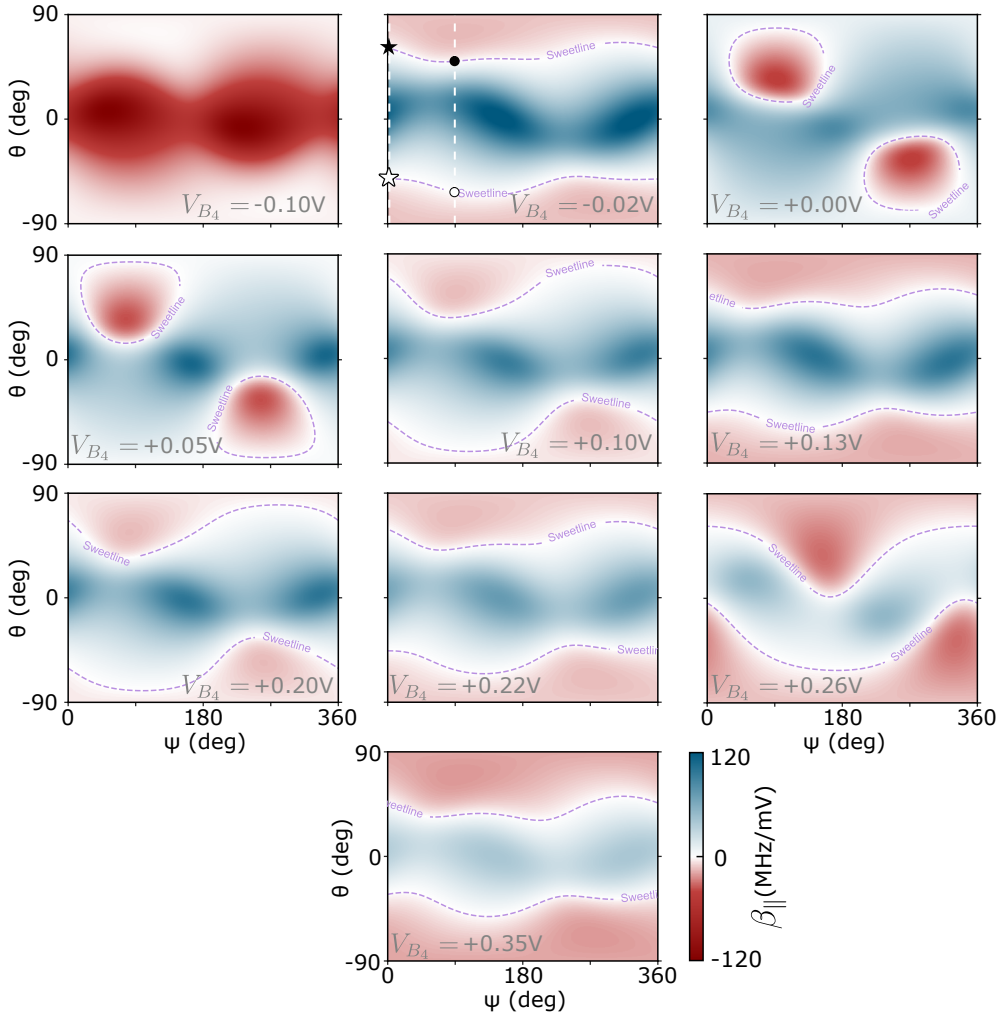

Figure 5.4 – **Longitudinal spin susceptibility of qubit located under T_4 versus confinement:** Angular dependence of the longitudinal spin susceptibility of the hole spin qubit in QD_4, denoted $\beta_{\parallel}$, in magnetic field and for different values of its confinement gate voltage V_{B_4}. Sweetlines with different angular positions are readily visible in all panels except at $V_{B_4} = -0.1\,\mathrm{V}$ for which no sign inversion is measured : $\beta_{\parallel} < 0, \forall(\theta, \psi)$. Dashed line in second panel emphasize the sweetspot angular positions in the principle magnet planes, further discussed in figure 5.5.

that the sweetlines of each qubit completely overlap.

5.2 Alignment of sweetspots

Owing to the experimental difficulties to completely overlap sweetline between different qubits, the attention is laid upon the alignment of sweetspots corresponding to each qubit at a common magnetic field orientation.

In figure 5.5(a) are gathered the fitted longitudinal spin susceptibility values evaluated for each B_4 gate voltage in (NP) (left panel) and (OP) (right panel) magnet planes. In both cases, the sweetspot angular positions are highlighted by stars (for the (NP) plane) and circles ((OP) plane). Again, no straightforward correspondence between the sweetspot angular positions and the confining gate voltage is observed, nevertheless sweetspots from qubit hosted below T_4 lay nearby that of qubit below T_3 presented in the previous chapter. For sake of comparison, sweetspot angular positions measured for the qubit underneath gate T_3 are shown with the same convention in panel (b) accordingly to the confining gate voltage V_{B_3}. Panel (c) focuses on the sweetspot positions, denoted $\theta_{\beta_{\parallel}=0}$, of both qubit in the (NP) magnet plane. The estimation of uncertainties stemming from by errors in the G'-tensor fitting procedure can be found in appendix. The red and pink shaded areas illustrate the range to tune the sweetspot angular location of the qubit within QD_3 and QD_4. Apart from cross-talk contribution, gates B_3 and B_4 can be tuned independently so that each qubit can be confined at will, in turn modifying their longitudinal spin susceptibility. It is clear from panel (c) that finding a common magnetic field for two sweetspots is possible, in particular for positive values of θ angle. For instance, setting $V_{B_3} = -0.540\,\mathrm{V}$ and $V_{B_4} \simeq 0.2\,\mathrm{V}$ would allow to have a common sweetspot located nearby ($\psi = 0°, \theta_{\beta_{\parallel}=0} \simeq 65°$), indicated by the dotted lines. Similar reasoning can be applied to (OP) plane, so as to form a common sweetspot field orientation.

Aligning sweetlines from one qubit to another is challenging because it is highly unlikely that the two systems have the same spin basis due to QD variability. Even in the case of two qubits, the tuning dimension is reduced down to finding a common sweetspot (1D) instead of a common sweetline (2D). Extending this reasoning to a n-qubits system seems therefore to drastically narrow the possibility of finding a common magnetic field orientation. However, the gate tunability property of sweetlines, gives a non-negligible range of angles to tune the sweetspot locations [1]. Despite the variability between the two aforementioned qubits, it is always possible to find a decent range within which a common sweetspot orientation can be found. As a consequence, the sweetline tunability can be seen as a alternative solution

1. Under right conditions, these additional spin susceptibility measurements compared to the confining gate voltage can take down to half a day for a single gate configuration.

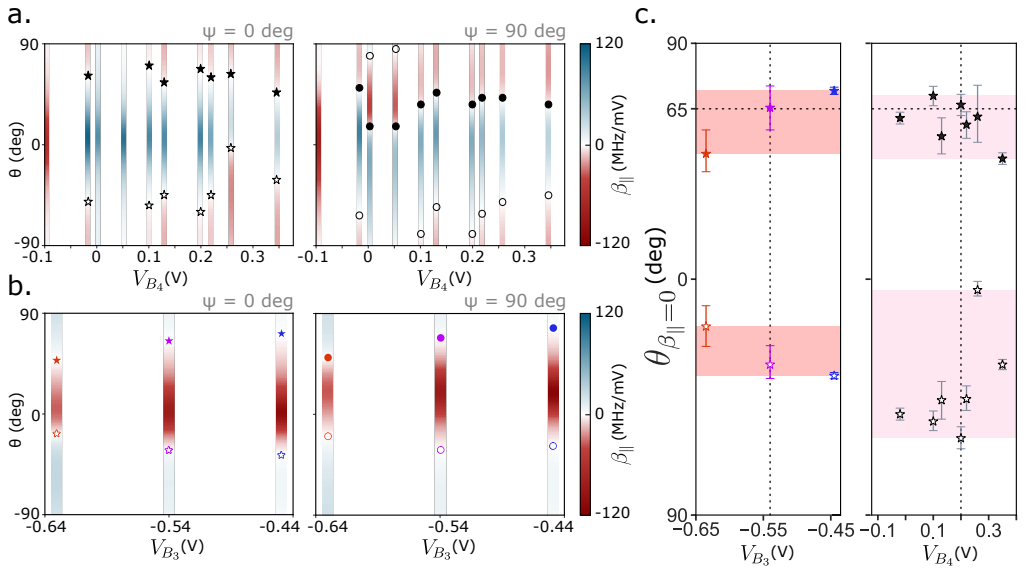

Figure 5.5 – **Spin susceptibility in particular magnet planes for different values of confinement gate:** (a) Left (resp. right) panel shows the estimated spin susceptibility values $\beta_\parallel$ in (NP) (resp. (OP)) plane, i.e. $\psi = 0°$ (resp. $\psi = 90°$), depending on the gate voltage value set on B_4 gate. Sweetspot angular positions are highlighted by the stars (resp. circles). Comparing the 10 gate configurations, no clear relation between the sweetspot positions in θ angle and the confinement gate voltage is observed. The distinction between plain and empty symbols is to identify the two sweetlines. (b) For comparison purposes, angular position of gate T_3 qubit are shown, in both (NP) and (OP) magnet planes. With the same convention, stars and circles illustrate the sweetspot positions with respect to the confining gate voltage V_{B_3}. (c) Comparison of sweetspot angular positions in the (NP) magnet plane between the two qubits, left (right) panel being data from qubit underneath gate T_3 (T_4). Coloured stars are sweetspot angular positions of qubit T_3 presented in the previous chapter, whereas black stars illustrate sweetspot of the qubit underneath gate T_4. The red and pink shaded areas emphasize the range of angles within which sweetspot positions can be adjusted.

to quantum dots variability as it allows to adjust sweetspot angular position to create multiple qubits resilient to first-order longitudinal spin susceptibility.

5.3 Conclusions and prospects

In order to draw some qualitative conclusions from the demonstration of a shared sweetspot between two qubits, we hope in the near future to be able to compare the performances of each qubit when operated at the shared sweetspot field orientation and when operated away from it. As a figure of merit, we chose both the Q-factor, introduced in the previous chapter, and randomized benchmarking fidelity. Importantly, we remind the reader that the two qubits are not interacting and that this demonstration is rather a proof of concept for coupled

multi-qubit systems.

As a side note, we would like to point out that here only the longitudinal component of charge noise is assessed, hence no information on the Rabi frequency is provided. It would be relevant to analyse how the transverse spin susceptibility is altered by modifications of the confining gate in order to align sweetspots which exhibit both a maximum of coherence and operation speed.

As a follow-up to chapters 3 and 4, the longitudinal spin sensitivity to gate fluctuations of a second qubit (under the T_4 gate) is characterised with respect to the magnetic field. In most cases, the presence of sweetlines is observed. The comparison of two qubits gives crucial insights into the QD variability, the presence of strain and defects within the same Si-nanowire. Despite the intrinsic differences between the two qubits, we demonstrate the feasibility of overlapping two sweetspots at a common magnetic field orientation by modifying the confining gate. Combined with the improved coherence time (and possibly maximised operating speed), the study of shared sweetspots is a promising path in the context of large QD arrays.

References

[1] N. Piot et al. « A single hole spin with enhanced coherence in natural silicon ». In: *Nature Nanotechnology* 17.10 (Sept. 2022), pp. 1072–1077. DOI: 10.1038/s41565-022-01196-z.

[2] N. W. Hendrickx et al. *Sweet-spot operation of a germanium hole spin qubit with highly anisotropic noise sensitivity*. arXiv. 2023. DOI: 10.48550/arXiv.2305.13150.

[3] Lorenzo Mauro et al. « Geometry of the dephasing sweet spots of spin-orbit qubits ». In: *Phys. Rev. B* 109 (15 Apr. 2024), p. 155406. DOI: 10.1103/PhysRevB.109.155406.

[4] Floris A. Zwanenburg et al. « Silicon quantum electronics ». In: *Rev. Mod. Phys.* 85 (3 July 2013), pp. 961–1019. DOI: 10.1103/RevModPhys.85.961.

[5] L. M. K. Vandersypen et al. « Interfacing spin qubits in quantum dots and donors—hot, dense, and coherent ». In: *npj Quantum Information* 3.1 (Sept. 2017), p. 34. DOI: 10.1038/s41534-017-0038-y.

[6] B. Martinez and Y.-M. Niquet. « Variability of Electron and Hole Spin Qubits Due to Interface Roughness and Charge Traps ». In: *Phys. Rev. Appl.* 17 (2 Feb. 2022), p. 024022. DOI: 10.1103/PhysRevApplied.17.024022.

[7] L. Cvitkovich et al. « Variability in Si/SiGe and Si/SiO2 Spin Qubits due to Interfacial Disorder ». In: *2023 International Conference on Simulation of Semiconductor Processes and Devices (SISPAD)*. 2023, pp. 341–344. DOI: 10.23919/SISPAD57422.2023.10319618.

[8] M. Cowie et al. *Spatially resolved random telegraph fluctuations of a single trap at the Si/SiO2 interface*. arXiv. 2024. DOI: 10.48550/arXiv.2403.07251.

[9] N. W. Hendrickx et al. « A four-qubit germanium quantum processor ». In: *Nature* 591.7851 (Mar. 2021), pp. 580–585. DOI: 10.1038/s41586-021-03332-6.

CHAPTER 6

Spectroscopy measurements on an isolated singlet-triplet system

Besides the experimental realization of dephasing sweetlines for charge noise, spin qubit performances could possibly be enhanced by isolating the system of interest from its nearby fluctuating environment, e.g. charge sensors. When decoupled from the electrical environment, the remaining dissipation channels, detrimental to qubit coherence, are only bosonic modes (phonons) [1] and magnetic noise (hyperfine interactions) [2]. In this chapter, a new paradigm is adopted and the aim is now to operate hole Singlet-Triplet (S-T) spin qubit within an isolated Double Quantum Dot (DQD) on a "pump"-geometry device. This constitutes a follow-up study to ref. [3]. From decades, S-T qubits have been investigated and successfully demonstrated single- and two-qubit gate operation in various materials [4, 5, 6], exhibiting a coherence time of $T_2^E = 1.8\,\mu s$ in Germanium [7], and the coupling between multiple S-T qubits [8]. In a vast majority, such systems are read out by Pauli-Spin Blockade (PSB) technique [9, 10, 11, 12, 13] allowing for high-fidelity and single-shot measurements. Leveraging on the absence of charge sensor for qubit readout, we employ gate-based dispersive sensing to figure out the hole spin orientation [14, 15]. The latter technique offers the advantages of being rapid, non-invasive and easily scalable to large QD array systems thanks to its small on-chip footprint [16, 17, 18, 19]. Primary focus is drawn onto the experimental realization of an isolated DQD in the few holes regime and on methods to figure out the dots charge occupancy. Spectroscopy response to increasing magnetic field amplitude is measured to infer the parity of DQD hole filling similarly to refs. [20, 21, 22]. Finally, we demonstrated successful spin manipulation for even parity filling in each dot and simultaneously in both, revealed by spectroscopy [23] and EDSR measurements.

Contents

6.1 Isolation of DQD system and readout by gate reflectometry

6.1.1 Device presentation

In this chapter, the device presented consists in a "pump" geometry (as presented in chapter 2) made of 5 independent gates, hereafter labelled G_i with $i \in \{1, 2, 3, 4, 5\}$. A false coloured SEM image of such device is presented in figure 6.1(a). A Double Quantum Dot (DQD) is formed below the gates G_2 and G_3 while hosting few holes. This same DQD is isolated from the nearby reservoirs (Source : S and Drain : D) by the means of gates G_1 and G_4 set with positive voltage, thus playing the role of "barriers" preventing charge transition. For initialisation purposes, detailed in section 6.1.3, G_5 is set to large negative voltage to extend the Drain reservoir close by the DQD. A metal gate standing on top of the sample is set at $-30\,\mathrm{V}$ so as to lower the overall electrostatic potentials. Owing to the absence of connected charge reservoir nearby the DQD, qubit readout cannot rely on the aforementioned spin-to-charge conversion [1].

In this chapter, readout is rather performed by in-situ dispersive sensing via radio-frequency reflectometry connected to gate G_3 that probes the hole spin transition, see section 6.1.2. The resonator is made of an on-chip resonant circuit made of a surface mount inductor $L = 220\,\mathrm{nH}$ and a parasitic capacitor, which finally exhibits a resonance at $f_{\mathrm{res}} = 503.3\,\mathrm{MHz}$. The evaluated quality factors are about $Q_{\mathrm{int}} = 197$ and $Q_c = 624$. Finally, MW tones can be send to gates G_2 (and G_4) for spin manipulation.

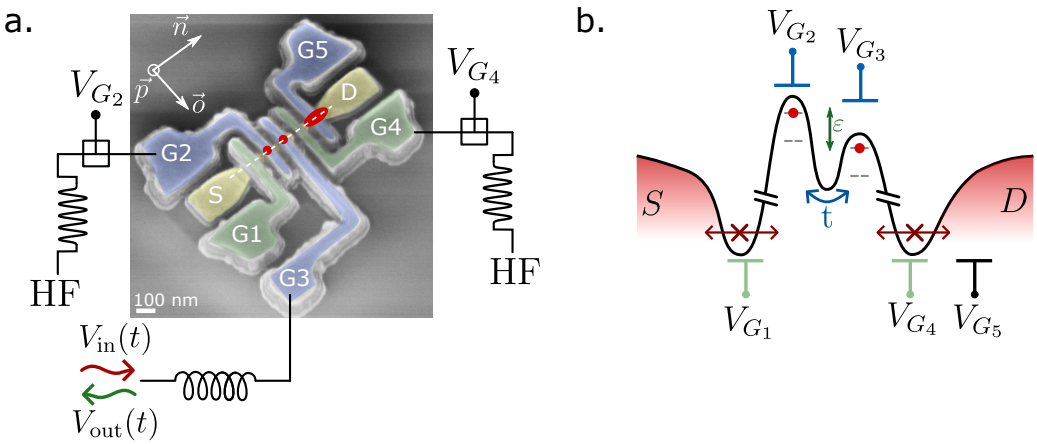

Figure 6.1 – **Device image and main wiring:** (a) False coloured SEM image of a 5 pump gates device presented hereafter and high-frequency lines wiring. Gates in blue have negative voltages, meaning that a QD is formed underneath. QDs below gates G_2 and G_3 will be operated in the few holes regime, forming the DQD of interest, whereas G_5 hosts a strongly accumulated QD. In green are highlighted gates which will be used as "barriers" to isolate the DQD system from the holes reservoirs with positive bias voltage. Red areas underscore the position of QDs (and their dimension quantitatively relates to the dot filling). MW tone can be send to gates G_2 and G_4. Readout is performed by radio-frequency reflectometry connected to gate G_3. Magnetic coordinate system is defined by axes $\{\vec{n}, \vec{o}, \vec{p}\}$. Scale bar is 100 nm. (b) Sketch of the desired electrostatic potential along the nanowire (dashed line in panel (a)) to operate a DQD that cannot exchange charges with nearby reservoirs. Red areas indicate the hole occupancy (i.e. a Fermi distribution function within the reservoirs and few particles in the DQD).

Figure 6.1(b) illustrates the desired electrostatic potential along the Si-nanowire, indicated by the dashed line in panel (a). Source and Drain connections, which constitute reservoirs of hole particles, cannot exchange charges with the DQD owing to electrostatic barriers controlled by gates G_1 and G_4. From the DQD formed underneath G_2 and G_3, two key parameters are defined:

- The detuning ε symbolizes the potential mismatch between the two dots. The latter is controlled by the difference in gate voltages of the dots to within a lever-arm parameter α.
- The interdot tunnel coupling t, which translates the ability of a hole particle to hop from one QD to the neighbouring one. Due to the absence of dedicated "trench" gates, tunnel coupling is hardly tunable in this experiment and will be mainly governed by the spatial distance separating the two dots and wavefunctions overlap.

The Hamiltonian governing such isolated DQD system is $\hat{\mathcal{H}} = -\varepsilon(t)/2\,\hat{\sigma}_Z - \Delta/2\,\hat{\sigma}_X$ with the corresponding eigenvalues denoted $E_\pm = \sqrt{\varepsilon^2 + \Delta^2}$ and $\Delta = 2t$. Changing the detuning parameter, i.e. the gate voltages, allows for the hole particle transfer between the dots, in turn recorded by radio-frequency reflectometry con-

nected to G_3.

6.1.2 Specifications due to gate-reflectometry readout

Over the years, the number of spin qubits to probe tends to skyrocket [24, 25], thus increasing the readout complexity with the need of nearby charge sensors. As an alternative approach, gate-based reflectometry copes with this overhead complexity by eliminating the need of a close by charge sensor. The latter technique has demonstrated a high-sensitivity (comparable to charge sensors) [26] and the possibility for spin state readout in single- and double- QD structures [18, 27, 28, 29, 30].

A DQD system acts as a variable capacitance, denoted δC_{sample}, which directly relates to the two dots charge state. When connected to a resonator, these capacitance modifications are readily captured by a reflectometry phase shift $\delta\phi_{\text{REF}}$ as expressed by equation 6.1 [19, 31].

$$\delta C_{\text{sample}} \propto -\delta\phi_{\text{REF}} \tag{6.1}$$

As mentioned in chapter 2, the sample capacitive variations can be expressed as the sum of 2 terms: $\delta C_{\text{sample}} = \delta C_Q + \delta C_{\text{tunnelling}}$. First contribution stems from the band curvatures of the energy states and the difference in each state population, whereas the second accounts for inelastic tunnelling processes. In this instance, inelastic processes cannot occur so that the capacitance variations are only due to quantum capacitive changes [28]. Considering that the ground and first excited states are denoted $|-\rangle$ and $|+\rangle$, the quantum capacitance reads:

$$\delta C_{\text{sample}} = \delta C_Q \propto -\frac{\partial^2 E_{\pm}}{\partial \varepsilon^2}(P_+ - P_-) \tag{6.2}$$

In other words, the phase shift experienced by the resonator is directly proportional to the energy curvature at a given detuning value as emphasized by equation 6.3. Note that the frequency shift can also be derived from the Jaynes-Cummings hamiltonian expressed as a function of the resonator frequency shift χ and its coupling quality factor Q_c [3].

$$\boxed{\delta\phi_{\text{REF}} \propto \frac{\partial^2 E_{\pm}}{\partial \varepsilon^2}(P_+ - P_-)} \tag{6.3}$$

In the following, phase reflectometry probed onto gate G_3 is used to indirectly sense the charge transfer between QDs underneath G_2 and G_3 as an interdot transition. As charge exchange between gate G_3 and G_4 is forbidden, only interdot signature from the DQD system are expected.

6.1.3 Initialisation process and stability diagram

Trapping charges within a DQD necessitates particular gate setting stages as expressed in table 6.1. To prevent charge transfer from the DQD and nearby reservoirs, which means to isolate the DQD from its environment, G_1 and G_4 play a crucial role as they first allow few charges to enter G_2 and G_3 QDs in step n°1, and are then set to positive voltage so that holes cannot escape the DQD anymore, in step n°7. Between first and last step of initialisation protocol, gate voltages of G_1 and G_4 are strongly modified by 1.2 V.

Step	$\widetilde{V_{G_1}}$	$\widetilde{V_{G_2}}$	$\widetilde{V_{G_3}}$	$\widetilde{V_{G_4}}$	V_{G_5}
1	-1.0	-0.7	-0.7	-1.0	-2.0
2	-1.0	$V_{G_2}^{\text{init}}$	-0.7	-1.0	-2.0
3	-1.0	$V_{G_2}^{\text{init}}$	$V_{G_3}^{\text{init}}$	-1.0	-2.0
4	0.0	$V_{G_2}^{\text{init}}$	$V_{G_3}^{\text{init}}$	-1.0	-2.0
5	0.0	$V_{G_2}^{\text{init}}$	$V_{G_3}^{\text{init}}$	0.0	-2.0
6	+0.2	$V_{G_2}^{\text{init}}$	$V_{G_3}^{\text{init}}$	0.0	-2.0
7	+0.2	$V_{G_2}^{\text{init}}$	$V_{G_3}^{\text{init}}$	+0.2	-2.0

Table 6.1 – **Initialisation protocol to isolate DQD below G_2 and G_3:** Gate voltage steps to form an isolated DQD below gates G_2 and G_3 while preventing charge exchange with the nearby reservoirs. Gate voltages are expressed in volt, and are swept during initialisation by steps of 10 mV to compensate with the neighbouring gates. $V_{G_i}^{\text{init}}$ is the initial value chosen to initialise the DQD. These values will strongly affect the DQD charge occupancy when isolated. Step n°7 gate configurations can be seen as figure 6.1(b).

Owing to cross-talk between gates, this large gate voltage span affects the electrostatic potential of gates G_2 and G_3, and thus alter the resulting DQD charge occupancy. This in turn strongly impair the initialisation protocol reproducibility. The latter issue can be circumvented by the use of virtual gates, compensating for the gate cross-talks [32]. We define M as a 4×4 compensation matrix and the virtual (i.e. independent) gates $\widetilde{V_{G_i}}, i \in [\![1, 4]\!]$ [1]:

$$\widetilde{V_{G_i}} = M \cdot V_{G_i} \tag{6.4}$$

The evaluation of the compensation matrix can be found in appendix.

Gate voltages are gradually changed by steps of 10 mV to allow for compensation of other nearby gate voltages. Up to stage n°7, barrier gates are set to 0.2 V acting as an electrostatic potential boundary preventing the hole flow. In

1. Note that, as gate G_5 is not used for initialisation protocol and its charge occupancy is not of crucial importance, this gate is not compensated.

the meantime, both virtual gates G_2 and G_3 are maintained to their initialisation value denoted $V_{G_i}^{\text{init}}$, which governs the final DQD charge occupancy. Gate G_5 hosts a strongly accumulated QD, as $V_{G_5} = -2.0\,\text{V}$, in order to replicate the behaviour of S and D reservoirs.

Once the initialisation is done, gate voltages of G_2 and G_3 can be modified (without the need of compensation), thus changing the detuning parameter ε. Lower panel of figure 6.2 shows a stability diagram probed by phase reflectometry for the above defined DQD. Unlike honeycomb-like stability diagrams [1], herein only the interdot transitions are observed as a shift in phase reflectometry (light blue lines) since the dot-lead charge transfer are forbidden (isolated regime). We define (N,M) as the charge occupancy of QD underneath (G_2, G_3). In this instance, 5 holes are transferring from one QD to the other, controlled by G_2 and G_3 gate voltages. Top panel is a cut at $V_{G_3} = -0.968\,\text{V}$, revealing the presence of 5 clear dips in phase reflectometry signal. Each dip, underscored by dashed lines, can be understood as a hole interdot transition from which the DQD charge occupancy is figured out. Over more than 0.6 V voltage span, holes remain trapped within the DQD and can reliably be moved as emphasized by the DQD charge occupancy going from $(5, 0)$ to $(0, 5)$ without missing a hole transition.

An efficient way to trap charges within QDs and read the charge transition via gate-reflectometry is presented in the above section. However, this initialisation protocol still presents some moot points and remains to be improved.

6.1.4 Digression about the reliability of initialisation protocol

We demonstrated that the aforementioned initialisation protocol permits to isolate few charges spread between two neighbouring QDs and that their transfer can be determined by reflectometry. Nevertheless, figuring out the exact number of charges, especially when trying to trap few holes (e.g. $N + M < 4$), remains challenging. Two main reasons that could be detrimental to the initialisation protocol are tackled in this section and offer some points of improvement.

First, the definition of the compensation matrix M is only valid for a narrow gate voltage range. Indeed, M-matrix stems from the experimental evaluation of the gate cross-talks on a given interdot transition (see appendix E). From few holes regime to large dot occupancy, cross-talks between gates can be highly modified. Setting initial values $V_{G_2}^{\text{init}}$, $V_{G_3}^{\text{init}}$ far from the cross-talk measurement point could result in a poor compensation. As a consequence, the expected number of charges trapped within the DQD before initialisation can strongly differ from the effective DQD charge occupancy once isolated. In the described experiment, compensation matrix is calculated from an interdot transition in the few holes regime.

Second, some interdot transitions may possibly not be captured by gate reflec-

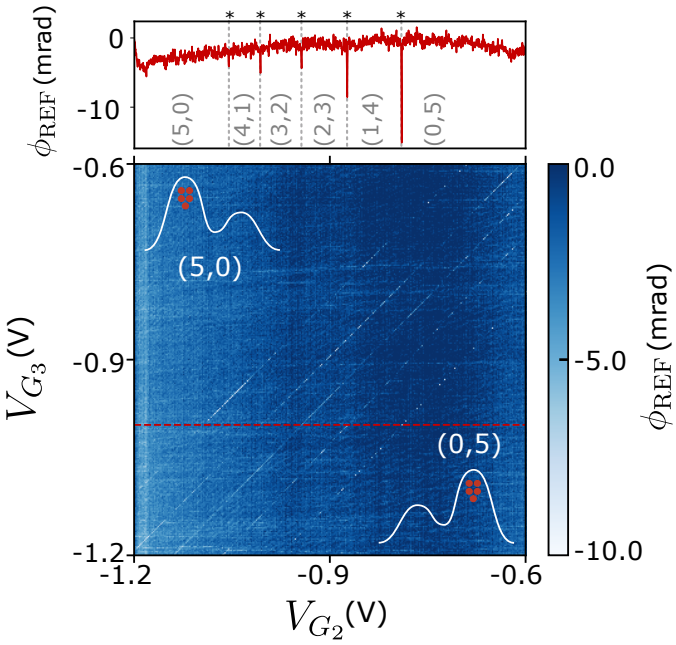

Figure 6.2 – **Stability diagram of DQD isolating five holes:** Stability diagram of the DQD underneath G_2 and G_3 when phase reflectometry is measured. Light blue lines are interdot transitions, i.e. when a hole particle transits from one dot to the other. Over 600 mV gate span, 5 interdot transitions are visible, proving that 5 holes are trapped inside the DQD. Insets in top left and bottom right corners are schematics of electrostatic potential of the DQD and charge occupancy (red circles embody a hole particle). Top panel is a phase reflectometry cut at $V_{G_3} = -0.968\,\mathrm{V}$, revealing the presence of 5 dips, underscored by dotted lines, synonym of a charge transition process. Numbers (N,M) indicate the charge occupancy of the dot underneath (G_2, G_3). In this instance, $V_{G_2}^{\mathrm{init}} = -0.41\,\mathrm{V}$ and $V_{G_3}^{\mathrm{init}} = -0.5\,\mathrm{V}$.

tometry. In a case where tunnelling rates are slower than the probing frequency ($f_{\mathrm{res}} \simeq 503\,\mathrm{MHz}$), some interdot transition events can be missed. In other words, only transition whose rates exceed the probing tone can be readily observed by gate-reflectometry [6, 22]. In absence of dedicated trench gates to tune such tunnelling rates, charge occupancy of the described DQD is hardly determined below 4 holes.

As an alternative approach, magnetospectroscopy technique probes the hole interdot transition response in magnetic field, that ascertains the charge occupancy parity [20], meaning either even ($N + M = 2n$) or odd configuration ($N + M = 2n+1$ with $n \in \mathbb{N}$). In combination with stability diagrams, magnetospectroscopy is a powerful tool to discriminate DQD filling and energy spectrum [21, 22, 33]. The latter technique is explained in section 6.2.2 when the DQD is occupied by 4 holes.

6.2 Even parity filling: spectroscopy measurements

The following sections focus on the magnetospectroscopy and spectroscopy measurements of an interdot transition while the DQD is filled with an even number of charges. The latter system is initialized for $(V_{G_2}^{\text{init}}, V_{G_3}^{\text{init}}) = (-0.60, -0.71)\text{V}$, giving 4 visible interdot transitions. The charge occupancy parity plays a major role in the energy diagrams and thus on the DQD response to spectroscopy. As above mentioned, figuring out the exact number of charges is arduous and can be corroborated by magnetospectroscopy measurements [20]. The emphasis is first laid onto the specificities of such energy diagram for an even number of holes occupying the DQD. This gives rise to peculiar magnetic field response then shown in section 6.2.2. Finally, spectroscopy and EDSR measurements performed on an interdot transition are tackled to evaluate each QD g-factor.

6.2.1 Energy diagram and definition of singlet-triplet states

When a DQD is filled with an even number of charges, each hole transfer can be seen as the transition of an excess particle as $(2,0) \leftrightarrow (1,1)$ states. Considering two holes occupy the same dot, they either form a singlet state ($S = 0$), often denoted $S(2,0)$ as the energy ground state, or constitute triplet states (S=1)[1]. In presence of external magnetic field, these latter triplet states will stand far above the considered energies herein, so will not be taken into account in the following discussion. In a similar fashion, in the $(1,1)$ charge state, the two holes also compose singlet and triplet (S-T) states while being in different QD. Such energy states form an eigenbasis $\mathcal{B}$:

$$\begin{cases} S(2,0) \\ T_-(1,1) = |\downarrow\downarrow\rangle \\ T_0(1,1) = \dfrac{1}{\sqrt{2}}(|\uparrow\downarrow\rangle + |\downarrow\uparrow\rangle) \\ T_+(1,1) = |\uparrow\uparrow\rangle \\ S(1,1) = \dfrac{1}{\sqrt{2}}(|\uparrow\downarrow\rangle - |\downarrow\uparrow\rangle) \end{cases} \tag{6.5}$$

Figure 6.3(a) illustrates the energy diagram of such DQD system in absence of magnetic field while considering no coupling between the two dots. In this case, triplet states of $(2,0)$ charge state lay at higher energies (not depicted herein), whereas triplets from the $(1,1)$ configuration are degenerate with the singlet state. When considering non-zero tunnel coupling t between the dots, singlet states hybridize and an avoided crossing of $\Delta = 2t$ emerges at zero detuning, see panel (b). When the sample experiences external magnetic field, spin degeneracy is lifted by the Zeeman energy relative to each QD g-factor. In the energy diagram of panel (c), triplet states separate by the E_{Z_i} corresponding to dot i Zeeman splitting.

This situation mainly depicts the case of an electron spin, when $E_{Z_1} = E_{Z_2}$. Owing to the nature of hole particles, spin-orbit interaction causes spin-flip tunnelling events when the particle travels over a spin-orbit length [2, 23, 34]. As a consequence, singlet and triplet states are mixed, and a spin-orbit gap Δ_{SO} emerges a shown in panel (d). The strength of spin-flip tunnelling amplitude is highly anisotropic in magnetic field orientation [23, 35].

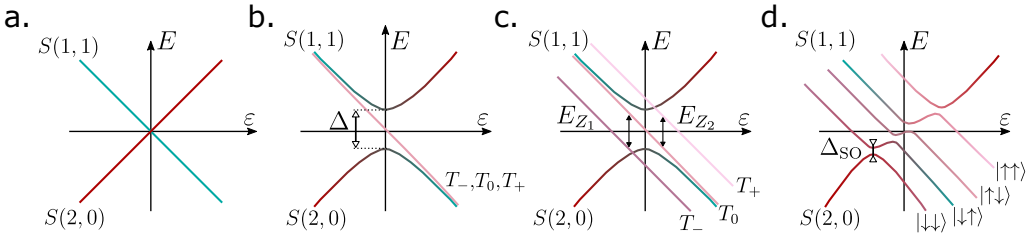

Figure 6.3 – **Energy diagrams of S-T system:** (a) Energy diagram considering the tunnel coupling between the dots and external magnetic field are 0. Triplets states of (1,1) charge occupancy are degenerate with the singlet state. (b) When a finite tunnel coupling exists between the dots, singlet states anti-cross at zero detuning by a value denoted $\Delta = 2t$. (c) Adding an external magnetic field lifts the triplet degeneracy by the Zeeman splitting relative to each QD, that differs due to the g-factors discrepancy. (d) In the case of hole particles, spin-orbit induces extra spin-flip tunnelling events, therefore hybridizing singlet and triplet states as transcribed by Δ_{SO} quantity.

At large magnetic field so that the Zeeman energy of dot 1 is larger than the tunnel coupling ($E_{Z_1} > t$), $S(1,1)$ and $T_0(1,1)$ are no longer eigenstates of the DQD system, therefore a new basis defined as: $\mathcal{B}' = \{|\downarrow\downarrow\rangle, |\downarrow\uparrow\rangle, |\uparrow\downarrow\rangle, |\uparrow\uparrow\rangle, S(2,0)\}$ is more suitable to capture the DQD physics. The corresponding Hamiltonian reads:

$$\mathcal{H} = \begin{bmatrix} -\frac{\varepsilon}{2} & t & t_{\mathrm{SO}} & t_{\mathrm{SO}} & t_{\mathrm{SO}} \\ t & \frac{\varepsilon}{2} & 0 & E_Z^- & 0 \\ t_{\mathrm{SO}} & 0 & \frac{\varepsilon}{2} - E_Z^+ & 0 & 0 \\ t_{\mathrm{SO}} & E_Z^- & 0 & \frac{\varepsilon}{2} & 0 \\ t_{\mathrm{SO}} & 0 & 0 & 0 & \frac{\varepsilon}{2} + E_Z^+ \end{bmatrix}_{\mathcal{B}'} \tag{6.6}$$

with,

t and t_{SO} the strength of tunnel and spin-orbit couplings. In this Hamiltonian, the coupling strength of SOC is assumed to be equivalent between triplets and singlet,

$E_Z^-(E_Z^+)$ the difference (sum) of the Zeeman energies : $\mu_B(g_1 - g_2)\boldsymbol{B}$ resp. $\mu_B(g_1 + g_2)\boldsymbol{B}$.

If the dot is filled with an odd number of charges, each hole transfer between dots can be derived as a $(1,0) \leftrightarrow (0,1)$ transition. In this situation, the resulting eigenstates exhibit different energy diagrams and response to external magnetic

field [2]. Subsequently, it is possible to infer the DQD charge occupancy parity (even or odd) from the dispersive response in magnetic field. This method is referred as magnetospectroscopy and is detailed in the next section.

6.2.2 Confirmation of dot filling parity by magnetospectroscopy

The DQD is filled in a reproducible manner with 4 trapped holes. In order to confirm the dots occupancy, spectroscopy response is probed on an interdot transition with increasing external magnetic field amplitude along $\vec{p}$-axis. Measurement is shown in figure 6.4(a) and readily manifests two distinct regimes.

As long as the magnetic field is below a critical value $\mathbf{B}_p^{\text{crit}}$ such that $E_{Z_1} < t$, underscored by the white dashed line, the hybridized singlet state remains the ground state and the dispersive phase shift is directly related to the tunnel coupling $\Delta/2$. Whenever $\mathbf{B}_p > \mathbf{B}_p^{\text{crit}}$, $|\downarrow\downarrow\rangle$-state becomes the lowest energy state and mixes with the singlet energy level mediated by spin-orbit coupling Δ_{SO}. Depending on the relative strength of Δ and Δ_{SO}, the phase shift either fade ($\Delta_{\text{SO}} \ll \Delta$) as in refs. [17, 21, 22] or increases as in the presented figure ($\Delta_{\text{SO}} < \Delta$) [22]. Since the energy of $|\downarrow\downarrow\rangle$-state is proportional to the magnetic field amplitude, the induced phase variation shifts towards more negative detuning values (i.e. more negative V_{G_3}). Figure 6.4(a) is a signature of an even number of charges occupying the DQD.

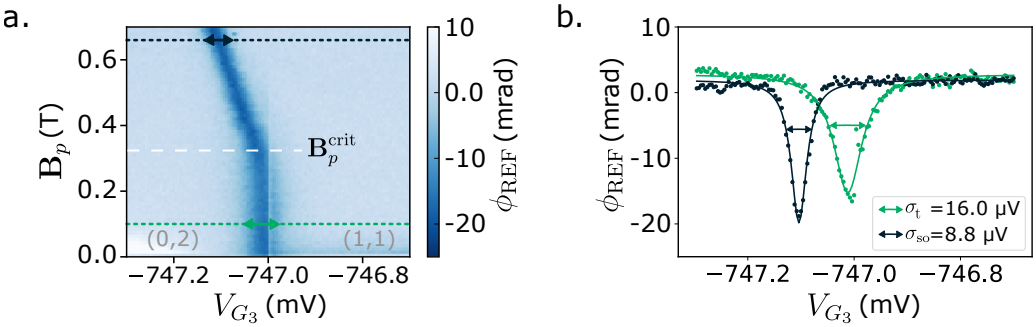

Figure 6.4 – **Example of magnetospectroscopy measurement for an even charge configuration:** (a) Phase reflectometry measured at an interdot transition (symbolized by the dark blue signal) while increasing external magnetic field. Phase alteration induced by the hole transition $(2,0) \leftrightarrow (1,1)$ is shifted from $\mathbf{B}_p \simeq 0.3\,\text{T}$, signature of an even charge occupancy parity. Dotted lines correspond to cut in panel (b). For sake of clarity, mean value along the ordinate axis is removed. The feature at $V_{G_3} = -0.747\,\text{V}$ is an artefact coming from the DAC. (b) Line cuts at low (green) and large (black) magnetic field amplitude revealing dispersive shift. From the FWHM fitted with a Lorentzian function, tunnel and spin-orbit coupling values are inferred.

2. The full derivation of the Hamiltonian in the case of an odd configuration stands beyond the scope of this chapter, but can be found in ref. [3].

Dotted lines indicates cuts at a constant magnetic field displayed in panel (b) in the two different regimes $\mathbf{B}_p > \mathbf{B}_p^{\text{crit}}$ (black) and $\mathbf{B}_p < \mathbf{B}_p^{\text{crit}}$ (green). Both are fitted with a Lorentzian function to extract the corresponding Full Width Half Maximum (FWHM) which are respectively $\sigma_{\text{SO}} = 8.8\,\mu\text{V}$ and $\sigma_{\text{t}} = 16.0\,\mu\text{V}$. The relation between FWHM and the coupling strength depends on an effective hole temperature. Following ref. [17], couplings can be evaluated without knowing this effective temperature value by considering σ_{t} ranging in $[3t, 4t] \times \alpha$, with α the gate lever-arm on the dot. From spectroscopy measurements (see section below), the gate lever-arm is estimated about $\alpha \sim 0.466\,\text{eV}\,\text{V}^{-1}$. Finally, the calculated tunnel and spin-orbit couplings are about:

$$\begin{cases} t \in [1.86, 2.49]\,\mu\text{eV} \\ t_{\text{SO}} \in [1.03, 1.37]\,\mu\text{eV} \end{cases} \tag{6.7}$$

Remarkably, the spin-orbit coupling is, in this instance, comparable with the tunnel coupling between the two dots and is much weaker than reported values in similar sample architecture [23]. This large spin-orbit coupling could be explained by the strong confinement of the hole wavefunction, e.g. due to the QD formation as corner dots [36].

From magnetospectroscopy measurement, the charge filling parity is deduced and confirms that 4 holes are currently trapped within the DQD. Next section aims at demonstrating the possibility to control each QD spin orientation by relying on spectroscopy technique combined with dispersive readout.

6.2.3 Spectroscopy and spins manipulation

When filled with an even number of charges, hole states form the aforementioned singlet and triplet states that can be used as a qubit. Equivalent states have been first reported using electron spin and demonstrated one and two qubit operation in GaAs [4, 37], in natural [5] and purified [11] silicon devices as well as high-fidelity readout by Pauli-Spin Blockade (PSB) [38, 39]. In a similar fashion, hole S-T qubits have been more recently reported in Germanium [7].

In this section, we aim at performing two-tone spectroscopy measurement as a readout technique and method to understand the underlying physics of such S-T system relying on hole spins as in ref. [23] on an isolated DQD system.

Spectroscopy measurements

Owing to their intrinsically strong spin-orbit interaction, S- and T- states of hole particles hybridize by Δ_{SO} at a detuning denoted $\varepsilon = \varepsilon_{\text{SO}}$. Nearby this particular detuning point, the DQD can be operated as a spin-flip charge qubit. Spin manipulation relies on Electrically Driven Spin Resonance (EDSR) technique, by exciting the qubit state with MW tone f_{MW} sent during the whole measurement.

Readout is performed by the above mentioned gate-based dispersive sensing at f_{res}. Importantly, as the MW signal amplitude strongly fluctuates depending on the MW tone, the room temperature level of MW signal is calibrated beforehand on few interdot transitions, as detailed in appendix E.

Figure 6.5(a) is an example of two-tone spectroscopy on an interdot transition in an even parity case ($N + M = 4$). At $\varepsilon = \varepsilon_{\text{SO}}$, corresponding to $V_{G_3} \simeq -746.11\,\text{mV}$ (grey dotted line), the phase reflectometry shift is visible but cancels out whenever a spin energy resonates with the MW frequency. At $f_{\text{MW}} = {}^{\Delta_{\text{SO}}}/_{h} \simeq 1.8\,\text{GHz}$, a hole spin is coherently driven into a statistical mixture of state. Both $|\downarrow\downarrow\rangle$- and $|\downarrow\uparrow\rangle$-states are thus equally populated and the resulting dispersive shift given by $\delta\phi_{\text{REF}} \propto {}^{\partial^2 E_{\pm}}/_{\partial\varepsilon^2}(P_+ - P_-) + {}^{\epsilon}/_{\Delta E}\,{}^{\partial(P_+ - P_-)}/_{\partial\epsilon}$ equals 0 as $P_+ \sim P_-$.

Aside from ε_{SO}, two branches are readily observed towards more positive V_{G_3} values. Each can be attributed to a successful spin transition to the excited state either in the left or right dot. Dispersive shift fades at larger detuning values due to the energy bands flattening but defines the Zeeman splitting required to rotate a spin in each dot, denoted $E_{|\downarrow\uparrow\rangle}$ and $E_{|\uparrow\downarrow\rangle}$. So as to evaluate the splitting energy of both dot (and thus infer the corresponding g-factors at a given B-field orientation), the Hamiltonian from equation 6.6 is solved with least-square minimization procedure. White circles are measured positions of each branch as a function of detuning used as inputs for the fit. The yellow dotted lines are the calculated position of the two branches from which are inferred the g-factors of left (g_L) and right (g_R) dots, the gate lever-arm, the tunnel and spin-orbit couplings:

$$\begin{cases} g_L = 1.42 \\ g_R = 2.75 \\ \alpha = 0.47\,\text{eV}\,\text{V}^{-1} \\ t = 11.47\,\mu\text{eV} \\ t_{\text{SO}} = 4.53\,\mu\text{eV} \end{cases} \tag{6.8}$$

Spectroscopy response of an isolated DQD probed by gate-based dispersive sensing in presence of external magnetic field is a compelling technique to unveil the physical phenomena (e.g. tunnel and SO couplings) responsible for spin manipulation. In the following, EDSR measurements are conducted on such interdot transition of hole particle when trapped inside a DQD system revealing addressability of spin state in each dot.

Manipulation of an isolated ST system

Thanks to spin-orbit coupling, spin manipulation is possible by electrical driving. Figure 3.8 is an EDSR measurement example performed at $\varepsilon = 0$. Dispersive

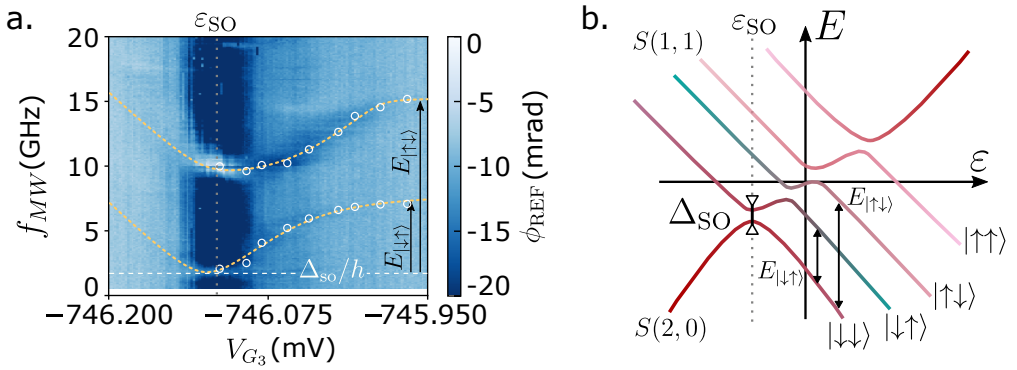

Figure 6.5 – **Spectroscopy measurement on an interdot transition for even parity filling:** (a) Dispersive shift probed onto an interdot transition while driving by MW tone (f_{MW}). Spin-orbit gap is observed about $\Delta_{\mathrm{so}}/h \simeq 1.8\,\mathrm{GHz}$ as illustrated by the white dashed line. A dispersive shift is also observed apart from the interdot transition. White points are the branch positions taken for the fit (see main text), whose result is shown by the yellow dotted lines. Measurement is performed for $\mathbf{B}_p = 0.4\,\mathrm{T}$. (b) Energy diagram highlighting the photon-induced spin transitions at stake with corresponding energies $E_{|\downarrow\uparrow\rangle}$ and $E_{|\uparrow\downarrow\rangle}$.

shift varies depending on MW frequency and magnetic field amplitude. As the triplet state energies (thus the spin transition) directly stem from B-field amplitude, the phase shift induced by spin rotation is expected to vary linearly for each excited state depending on the dot g-factor. On the figure, 3 lines of phase reflectometry shift are observed (dotted lines are guide to the eyes) and respectively attributed to $|\downarrow\downarrow\rangle \leftrightarrow |\downarrow\uparrow\rangle$, $|\downarrow\downarrow\rangle \leftrightarrow |\uparrow\downarrow\rangle$ and $|\downarrow\downarrow\rangle \leftrightarrow |\uparrow\uparrow\rangle$ state transitions. The width of each transition line highly depends on the energy curvature of each state at the measurement detuning value.

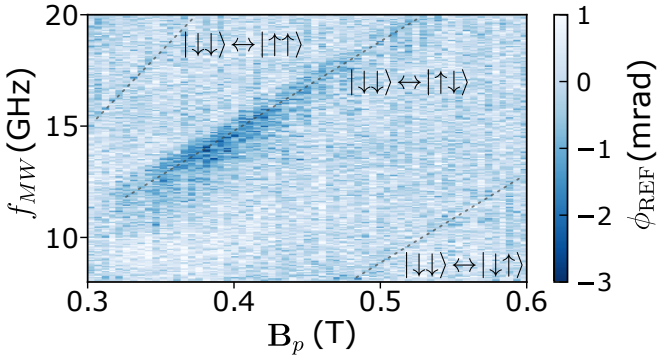

Figure 6.6 – **Electrically Driven Spin Resonance probed by dispersive sensing:** Phase shift recorded as a function of MW tone and external magnetic field amplitude along $\vec{p}$-axis. Herein, 3 types of transitions are observed and are attributed to the spin resonance from ground to excited states in each and both QDs. For sake of clarity, the average background is removed. The signal shift width directly stems from the detuning value set for measurement.

From the slope of the two first transitions, we estimate the dots g-factors about $g_R \simeq 1.33$ and $g_L \simeq 2.61$. In addition to the two spin transitions already observed in spectroscopy measurements, figure 6.6 unveils the presence of a third type of transition attributed to the successful spin manipulation in both dots. Such experimental realization is a first step towards the implementation of an isolated S-T qubit in natural silicon nanowire. So far, the demonstration remains incomplete as coherent oscillations have not been observed in this system.

6.3 Conclusions

Against a backdrop of enhancing spin qubit coherence time, we conducted preliminary measurements so as to unveil the possibility to operate a S-T hole spin qubit within an isolated DQD in natural silicon material. By compensating cross-talks between gates, successful isolation of few holes in a DQD was demonstrated using gate-based dispersive sensing. Nevertheless, owing to the absence of trench gates, and thus the impossibility to tune tunnel rates between the two dots, charge interdot transitions were hardly captured by gate reflectometry down to the first hole regime. In order to corroborate the estimated charge occupancy, magnetospectroscopy measurements were performed to discriminate the DQD parity filling. When an even number of charges lay in the DQD, holes form a S-T basis that can be used as a qubit. We demonstrated successful spin manipulation in both dots probed by EDSR measurements and unveiled DQD level spectrum using spectroscopy technique. Yet, no coherent oscillations have been observed in this system.

References

[1] R. Hanson et al. « Spins in few-electron quantum dots ». In: *Reviews of Modern Physics* 79 (4 Oct. 2007), pp. 1217–1265. DOI: 10.1103/RevModPhys.79.1217.

[2] Y. Fang et al. « Recent advances in hole-spin qubits ». In: *Materials for Quantum Technology* 3.1 (Mar. 2023), p. 012003. DOI: 10.1088/2633-4356/acb87e.

[3] R. Ezzouch. « Gate reflectometry as readout and spectroscopy tool for silicon spin qubits ». PhD thesis. June 2021.

[4] J. R. Petta et al. « Coherent Manipulation of Coupled Electron Spins in Semiconductor Quantum Dots ». In: *Science* 309.5744 (2005), pp. 2180–2184. DOI: 10.1126/science.1116955.

[5] B. M. Maune et al. « Coherent singlet-triplet oscillations in a silicon-based double quantum dot ». In: *Nature* 481.7381 (2012), pp. 344–347. DOI: 10.1038/nature10707.

[6] W. Gilbert et al. « Single-Electron Operation of a Silicon-CMOS 2 × 2 Quantum Dot Array with Integrated Charge Sensing ». In: *Nano Letters* 20.11 (2020). PMID: 33108202, pp. 7882–7888. DOI: 10.1021/acs.nanolett.0c02397.

[7] D. Jirovec et al. « A singlet-triplet hole spin qubit in planar Ge ». In: *Nature Materials* 20.8 (Aug. 2021), pp. 1106–1112. DOI: 10.1038/s41563-021-01022-2.

[8] S. Zhang, Yu He, and Peihao Huang. « Acceptor-based qubit in silicon with tunable strain ». In: *Phys. Rev. B* 107 (15 Apr. 2023), p. 155301. DOI: 10.1103/PhysRevB.107.155301.

[9] K. Ono et al. « Current Rectification by Pauli Exclusion in a Weakly Coupled Double Quantum Dot System ». In: *Science* 297.5585 (Aug. 2002), pp. 1313–1317. DOI: 10.1126/science.1070958.

[10] M. Brauns et al. « Electric-field dependent g-factor anisotropy in Ge-Si core-shell nanowire quantum dots ». In: *Phys. Rev. B* 93 (12 Mar. 2016), p. 121408. DOI: 10.1103/PhysRevB.93.121408.

[11] M. A. Fogarty et al. « Integrated silicon qubit platform with single-spin addressability, exchange control and single-shot singlet-triplet readout ». In: *Nature Communications* 9.1 (Oct. 2018), p. 4370. DOI: 10.1038/s41467-018-06039-x.

[12] G. Zheng et al. « Rapid gate-based spin read-out in silicon using an on-chip resonator ». In: *Nature Nanotechnology* 14.8 (Aug. 2019), pp. 742–746. DOI: 10.1038/s41565-019-0488-9.

[13] E. Vahapoglu et al. « Single-electron spin resonance in a nanoelectronic device using a global field ». In: *Science Advances* 7.33 (Aug. 2021), eabg9158. DOI: 10.1126/sciadv.abg9158.

[14] M. Urdampilleta et al. « Charge Dynamics and Spin Blockade in a Hybrid Double Quantum Dot in Silicon ». In: *Phys. Rev. X* 5 (3 Aug. 2015), p. 031024. DOI: 10.1103/PhysRevX.5.031024.

[15] L. Hutin et al. « Gate reflectometry for probing charge and spin states in linear Si MOS split-gate arrays ». In: *2019 IEEE International Electron Devices Meeting (IEDM)*. 2019, pp. 37.7.1–37.7.4. DOI: 10.1109/IEDM19573.2019.8993580.

[16] I. Ahmed et al. « Radio-Frequency Capacitive Gate-Based Sensing ». In: *Phys. Rev. Appl.* 10 (1 July 2018), p. 014018. DOI: 10.1103/PhysRevApplied.10.014018.

[17] A. Crippa et al. « Gate-reflectometry dispersive readout and coherent control of a spin qubit in silicon ». In: *Nature Communications* 10.1 (2019), p. 2776. DOI: 10.1038/s41467-019-10848-z.

[18] K. D. Petersson et al. « Charge and Spin State Readout of a Double Quantum Dot Coupled to a Resonator ». In: *Nano Letters* 10.8 (Aug. 2010), pp. 2789–2793. DOI: 10.1021/nl100663w.

[19] F. Vigneau et al. « Probing quantum devices with radio-frequency reflectometry ». In: *Applied Physics Reviews* 10.2 (Feb. 2023), p. 021305. DOI: 10.1063/5.0088229.

[20] M. D. Schroer et al. « Radio Frequency Charge Parity Meter ». In: *Phys. Rev. Lett.* 109 (16 Oct. 2012), p. 166804. DOI: 10.1103/PhysRevLett.109.166804.

[21] M. G. House et al. « Radio frequency measurements of tunnel couplings and singlet–triplet spin states in Si:P quantum dots ». In: *Nature Communications* 6.1 (Nov. 2015), p. 8848. DOI: 10.1038/ncomms9848.

[22] T. Lundberg et al. « Non-symmetric Pauli spin blockade in a silicon double quantum dot ». In: *npj Quantum Information* 10.1 (Mar. 2024), p. 28. DOI: 10.1038/s41534-024-00820-1.

[23] R. Ezzouch et al. « Dispersively Probed Microwave Spectroscopy of a Silicon Hole Double Quantum Dot ». In: *Phys. Rev. Appl.* 16 (3 Sept. 2021), p. 034031. DOI: 10.1103/PhysRevApplied.16.034031.

[24] N. W. Hendrickx et al. « A four-qubit germanium quantum processor ». In: *Nature* 591.7851 (Mar. 2021), pp. 580–585. DOI: 10.1038/s41586-021-03332-6.

[25] P.-A. Mortemousque et al. « Coherent control of individual electron spins in a two-dimensional quantum dot array ». In: *Nature Nanotechnology* 16.3 (Mar. 2021), pp. 296–301. DOI: 10.1038/s41565-020-00816-w.

[26] M. F. Gonzalez-Zalba et al. « Scaling silicon-based quantum computing using CMOS technology ». In: *Nature Electronics* 4.12 (Dec. 2021), pp. 872–884. DOI: 10.1038/s41928-021-00681-y.

[27] J. I. Colless et al. « Dispersive Readout of a Few-Electron Double Quantum Dot with Fast rf Gate Sensors ». In: *Phys. Rev. Lett.* 110 (4 Jan. 2013), p. 046805. DOI: 10.1103/PhysRevLett.110.046805.

[28] A. Crippa et al. « Level Spectrum and Charge Relaxation in a Silicon Double Quantum Dot Probed by Dual-Gate Reflectometry ». In: *Nano Letters* 17.2 (Feb. 2017), pp. 1001–1006. DOI: 10.1021/acs.nanolett.6b04354.

[29] M. Urdampilleta et al. « Gate-based high fidelity spin readout in a CMOS device ». In: *Nature Nanotechnology* 14.8 (Aug. 2019), pp. 737–741. DOI: 10.1038/s41565-019-0443-9.

[30] V. N. Ciriano-Tejel et al. « Spin Readout of a CMOS Quantum Dot by Gate Reflectometry and Spin-Dependent Tunneling ». In: *PRX Quantum* 2 (1 Mar. 2021), p. 010353. DOI: 10.1103/PRXQuantum.2.010353.

[31] R. Mizuta et al. « Quantum and tunneling capacitance in charge and spin qubits ». In: *Phys. Rev. B* 95 (4 Jan. 2017), p. 045414. DOI: 10.1103/PhysRevB.95.045414.

[32] T.-K. Hsiao et al. « Efficient Orthogonal Control of Tunnel Couplings in a Quantum Dot Array ». In: *Phys. Rev. Appl.* 13 (5 May 2020), p. 054018. DOI: 10.1103/PhysRevApplied.13.054018.

[33] T. Lundberg et al. « Spin Quintet in a Silicon Double Quantum Dot: Spin Blockade and Relaxation ». In: *Phys. Rev. X* 10 (4 Oct. 2020), p. 041010. DOI: 10.1103/PhysRevX.10.041010.

[34] C. X. Yu et al. « Strong coupling between a photon and a hole spin in silicon ». In: *Nature Nanotechnology* 18.7 (July 2023), pp. 741–746. DOI: 10.1038/s41565-023-01332-3.

[35] A. Russell et al. « Gate-Based Spin Readout of Hole Quantum Dots with Site-Dependent g-Factors ». In: *Phys. Rev. Appl.* 19 (4 Apr. 2023), p. 044039. DOI: 10.1103/PhysRevApplied.19.044039.

[36] B. Voisin et al. « Few-Electron Edge-State Quantum Dots in a Silicon Nanowire Field-Effect Transistor ». In: *Nano Letters* 14.4 (Apr. 2014), pp. 2094–2098. DOI: 10.1021/nl500299h.

[37] A. C. Johnson et al. « Triplet–singlet spin relaxation via nuclei in a double quantum dot ». In: *Nature* 435.7044 (June 2005), pp. 925–928. DOI: 10.1038/nature03815.

[38] K. Takeda et al. *Rapid single-shot parity spin readout in a silicon double quantum dot with fidelity exceeding 99 %*. 2023.

[39] G. Burkard et al. « Semiconductor spin qubits ». In: *Rev. Mod. Phys.* 95 (2 June 2023), p. 025003. DOI: 10.1103/RevModPhys.95.025003.

CHAPTER 7

Landau-Zener Adiabatic Inversion : Experimental Methods

Hole spin qubits in semiconductor quantum dots are highly susceptible to charge fluctuations in the surrounding environment, leading to a time-varying precession frequency (detailed in chapter 1). This poses significant challenges for qubit manipulation, necessitating a precise operation at the Larmor frequency. Following figure 7.1 is an example of an unsuccessful measurement using a standard method to evaluate the Rabi frequency, referred as "Rabi chevron" method (see details in section 4.2.2). In this case, the precession frequency -highlighted by a white dashed line- has shifted after a bit more than 100 ns by more than 10 MHz (half the frequency span). Qubit control is not possible any longer and the probability of having an up-spin state drops down to 0. The evaluation of the Rabi frequency necessitates a sufficiently stable Larmor precession for an accurate estimation.

To circumvent such limitations, various methods stemming from Nuclear Magnetic Resonance (NMR) field have been adapted to quantum operation [1, 2]. Over the past decades, coherent control of one [3, 4] (or multiple) quantum bit(s) [5, 6] have been realized. In the scope of Rabi frequency evaluation, Landau-Zener (LZ) adiabatic transition [7] appears as a favourable method for spin control as it does not require to probe at the precession frequency. Indeed, this approach relies on the system response to different dynamic regimes that could benefit to quantum systems susceptible to low-frequency noise or exhibiting a stochastic behaviour. Recently, LZ-transition with dressed states of spin qubit have been implemented [3, 8, 9], even demonstrating longer coherence time compared to undressed states [8].

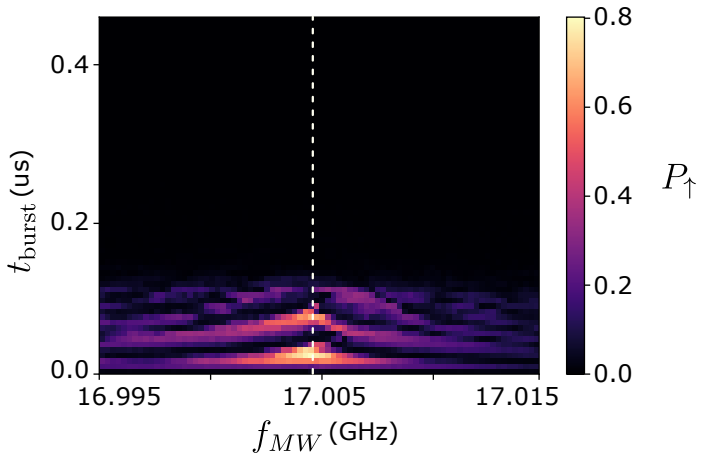

Figure 7.1 – **Example of a failed Rabi chevron measurement:** $|\uparrow\rangle$-spin state probability when varying the microwave burst duration t_{burst} close by the qubit Larmor frequency. The latter is highlighted by the white dashed line. This measurement is often referred as "chevron" pattern. The spin state alternates between up and down depending on the bursting time, demonstrating coherent oscillations. When $t_{\mathrm{burst}} > 100\,\mathrm{ns}$, the Larmor frequency has shifted outside the measurement window and the spin state cannot be rotated any longer. In this case, 0 probability is measured and the Rabi frequency (speed at which the qubit performs a π-rotation) cannot be accurately estimated.

This chapter aims at demonstrating whether LZ adiabatic inversion method can be used to reliably evaluate the Rabi frequency of a hole spin qubit dressed with an external electric field. The first section presents a theoretical introduction to dressed states and the basic knowledge for LZ-transition. Second and third sections focus on the experimental implementation of such adiabatic passage and a comparison to standard chevron measurements.

Contents

7.1 Theory and principles

7.1.1 Introduction to dressed states

In presence of microwave signals, the qubit spin states and the field modes interact and become a unique entangled system, forming so-called dressed states. These hybridized states are governed by the quantized Jaynes-Cummings hamiltonian [10], which includes the free Hamiltonian of each subsystem (the qubit denoted $\mathcal{H}_{qubit}$ and light field denoted $\mathcal{H}_{field}$) and an additional interaction term $\mathcal{H}_{int}$. Under the dipole approximation, the two-level system (TLS) can be described as a dipole moment $\mathbf{d}$ coupled to an electromagnetic field $\mathbf{E} \propto (a^\dagger + a)$, thus giving an interaction term:

$$\mathcal{H}_{int} = -\mathbf{d} \cdot \mathbf{E} = \hbar\chi(\hat{\sigma}^+ + \hat{\sigma}^-)(a^\dagger + a) \tag{7.1}$$

The total Hamiltonian therefore reads as:

$$\begin{aligned} \mathcal{H} &= \mathcal{H}_{qubit} + \mathcal{H}_{field} + \mathcal{H}_{int} \\ &= \frac{\hbar\omega_{\uparrow\downarrow}}{2}\hat{\sigma}_Z + \hbar\omega\left(\hat{n} + \frac{1}{2}\right) + \hbar\chi(\hat{\sigma}^+ + \hat{\sigma}^-)(a^\dagger + a) \end{aligned} \tag{7.2}$$

with

$\omega_{\uparrow\downarrow}$ *the Larmor angular frequency,*

ω *the field mode frequency,*

χ *the coupling strength between the qubit and the field states* [1]*,*

$\hat{N} = a^\dagger a$ *and* a, $a^\dagger$ *being the field mode photon annihilation and creation operators,*

$\hat{\sigma}^+ = \hat{\sigma}_X + i\hat{\sigma}_Y$, $\hat{\sigma}^- = \hat{\sigma}_X - i\hat{\sigma}_Y$ *the raising and lowering spin state operators.*

$\hat{\sigma}_X, \hat{\sigma}_Y, \hat{\sigma}_Z$ *the Pauli matrices.*

As the coupling strength is supposed to be much smaller than the main frequencies of the system ($\chi \ll \omega_{\uparrow\downarrow}, \omega$), the interaction Hamiltonian can be derived as a perturbation added to the uncoupled case : $\mathcal{H} = \mathcal{H}_0 + \mathcal{H}_{int}$. We first solve the hamiltonian in case of no interaction.

1. In this case, we consider the coupling from the ground state to the excited state to be the same than the coupling from the excited state to the ground state $\chi = \chi_{\downarrow\uparrow} = \chi_{\uparrow\downarrow}$.

Uncoupled system

Without any coupling between the qubit and light field, the system states can be separated as: $|\uparrow, n\rangle \equiv |\uparrow\rangle \otimes |n\rangle$ and $|\downarrow, n+1\rangle \equiv |\downarrow\rangle \otimes |n+1\rangle$, with n the number of photons. The qubit Hamiltonian will therefore independently apply to the spin states ($|\uparrow\rangle$ or $|\downarrow\rangle$ with the respective eigenvalues $\hbar\omega_{\uparrow\downarrow}/2$ or $-\hbar\omega_{\uparrow\downarrow}/2$) and so as the field Hamiltonian to the overall number of photons. We now restrict the derivation to the n^{th}-photon Hilbert subspace, which eigenbasis is $\mathcal{B} = \{|\uparrow, n\rangle, |\downarrow, n+1\rangle\}$. We consider $\mathcal{H}_0 = \mathcal{H}_{qubit} + \mathcal{H}_{field}$. The eigenstates of uncoupled hamiltonian are:

$$\begin{cases} \mathcal{H}_0 |\uparrow, n\rangle = E_{\uparrow,n} |\uparrow, n\rangle = \hbar \left[n\omega + \frac{\omega_{\uparrow\downarrow}}{2} \right] |\uparrow, n\rangle \\ \mathcal{H}_0 |\downarrow, n+1\rangle = E_{\downarrow,n+1} |\downarrow, n+1\rangle = \hbar \left[(n+1)\omega - \frac{\omega_{\uparrow\downarrow}}{2} \right] |\downarrow, n+1\rangle \end{cases} \tag{7.3}$$

In the resonant regime, meaning that $\omega_{\uparrow\downarrow} \sim \omega$, we define the frequency detuning as $\Delta = \omega_{\uparrow\downarrow} - \omega$ in such a way that:

$$\begin{cases} E_{\uparrow,n} = \hbar \left[(n + \frac{1}{2})\omega + \frac{\Delta}{2} \right] \\ E_{\downarrow,n+1} = \hbar \left[(n + \frac{1}{2})\omega - \frac{\Delta}{2} \right] \end{cases} \tag{7.4}$$

The only exception is for the lowest energy state $|\downarrow, 0\rangle$ which has a corresponding eigenvalue of 0.

Coupled system

We now introduce an interaction term between light and the two level system. We consider the interaction to be in the form of a cosine excitation : $\mathcal{H}_{int} = \hbar\,\Omega_R \cos(\omega_{\uparrow\downarrow} t)\hat{\sigma}_X$, with Ω_R the qubit Rabi angular frequency. In the interaction picture, we define:

$$|\psi(t)\rangle_{int} = \hat{U}_t\, \mathcal{H}_{int}\, \hat{U}_t^{\dagger}, \hat{U}_t = e^{\frac{i}{\hbar}\mathcal{H}_{qubit} t} \tag{7.5}$$

with

$|\psi(t)\rangle_{int}$ *a solution of the Schrödinger equation,*

$\hat{U}_t$ *the qubit time-evolution operator.*

Thus :

$$\begin{aligned} |\psi(t)\rangle_{int} &= \begin{bmatrix} e^{i\frac{\omega_{\uparrow\downarrow}}{2}t} & 0 \\ 0 & e^{-i\frac{\omega_{\uparrow\downarrow}}{2}t} \end{bmatrix} \begin{bmatrix} 0 & \hbar\,\Omega_R \cos(\omega_{\uparrow\downarrow} t) \\ \hbar\,\Omega_R \cos(\omega_{\uparrow\downarrow} t) & 0 \end{bmatrix} \begin{bmatrix} e^{-i\frac{\omega_{\uparrow\downarrow}}{2}t} & 0 \\ 0 & e^{i\frac{\omega_{\uparrow\downarrow}}{2}t} \end{bmatrix} |\psi(t=0)\rangle \\ &= \hbar\Omega_R \begin{bmatrix} 0 & e^{i\omega_{\uparrow\downarrow}t}\cos(\omega_{\uparrow\downarrow}t) \\ e^{-i\omega_{\uparrow\downarrow}t}\cos(\omega_{\uparrow\downarrow}t) & 0 \end{bmatrix} |\psi(t=0)\rangle \\ &= \hbar\Omega_R \begin{bmatrix} 0 & \frac{e^{2i\omega_{\uparrow\downarrow}t}}{2} + \frac{1}{2} \\ \frac{e^{-2i\omega_{\uparrow\downarrow}t}}{2} + \frac{1}{2} & 0 \end{bmatrix} |\psi(t=0)\rangle \end{aligned} \tag{7.6}$$

As the coupling strength χ is small compared to the single frequencies ω and $\omega_{\uparrow\downarrow}$, the Rotating Wave Approximation (RWA) can be employed to describe the coherent interaction of the two-level system with light field. The counter-rotating terms $e^{-2i\omega_{\uparrow\downarrow}t}$ are neglected as these are fast rotating terms. The approximate interaction Hamiltonian reads as:

$$\mathcal{H}_{int} \simeq \hbar\Omega_R \begin{bmatrix} 0 & \frac{1}{2} \\ \frac{1}{2} & 0 \end{bmatrix} = \hbar \frac{\Omega_R}{2} \hat{\sigma}_X \tag{7.7}$$

In the eigenbasis $\{|\uparrow, n\rangle, |\downarrow, n+1\rangle\}$ with $n = (0, 1, 2, ...)$, the system Hamiltonian finally boils down to a detuning and a coupling term, combination of uncoupled solution (7.4) and the interaction derivation from equation 7.7:

$$\boxed{\mathcal{H} = \hbar\omega \left(\hat{n} + \frac{1}{2}\right) + \hbar\frac{\Delta}{2}\hat{\sigma}_Z + \hbar\frac{\Omega_R}{2}\hat{\sigma}_X} \tag{7.8}$$

with

Ω_R *the Rabi frequency,*

n *the number of photons.*

The corresponding eigenvalues and eigenvectors of the system are:

$$E_\pm = \hbar\left[\omega\left(\hat{n} + \frac{1}{2}\right) \pm \frac{R_n}{2}\right], \text{and} \begin{cases} |\uparrow(n)\rangle = \frac{1}{\sqrt{2}}\left(|\uparrow, n\rangle + |\downarrow, n+1\rangle\right) \\ |\downarrow(n)\rangle = \frac{1}{\sqrt{2}}\left(|\uparrow, n\rangle - |\downarrow, n+1\rangle\right) \end{cases} \tag{7.9}$$

with

$R_n = \sqrt{\Omega_R^2 + \Delta^2}$ *the generalized Rabi frequency,*

The two coupled states $\{|\uparrow(n)\rangle, |\downarrow(n)\rangle\}$ exhibit an avoided crossing at resonance (i.e. at $\Delta = 0$) and remain similar to uncoupled states at large frequency detuning.
Each independent system has an energy splitting represented in figure 7.2(a). When the system is considered as uncoupled ($\chi = 0$), the qubit does not interact with the light field. On the contrary, for $\chi \neq 0$, the qubit and light interact and form dressed states, displayed in one Hilbert subspace in right panel of (a). The figure 7.2(b) displays the energy spectrum of such dressed states as a function of the frequency mismatch between the qubit and field modes. At resonance, the states are split by a factor directly proportional to the Rabi frequency.

Dressed states now form a new eigenbasis for spin qubit operation hereafter denoted $\mathcal{B} = \{|\uparrow(n)\rangle, |\downarrow(n)\rangle\}$. Changing from one quantum state to the other implies to operate the system dynamically. This physical phenomenon is described by Landau-Zener transition theory.

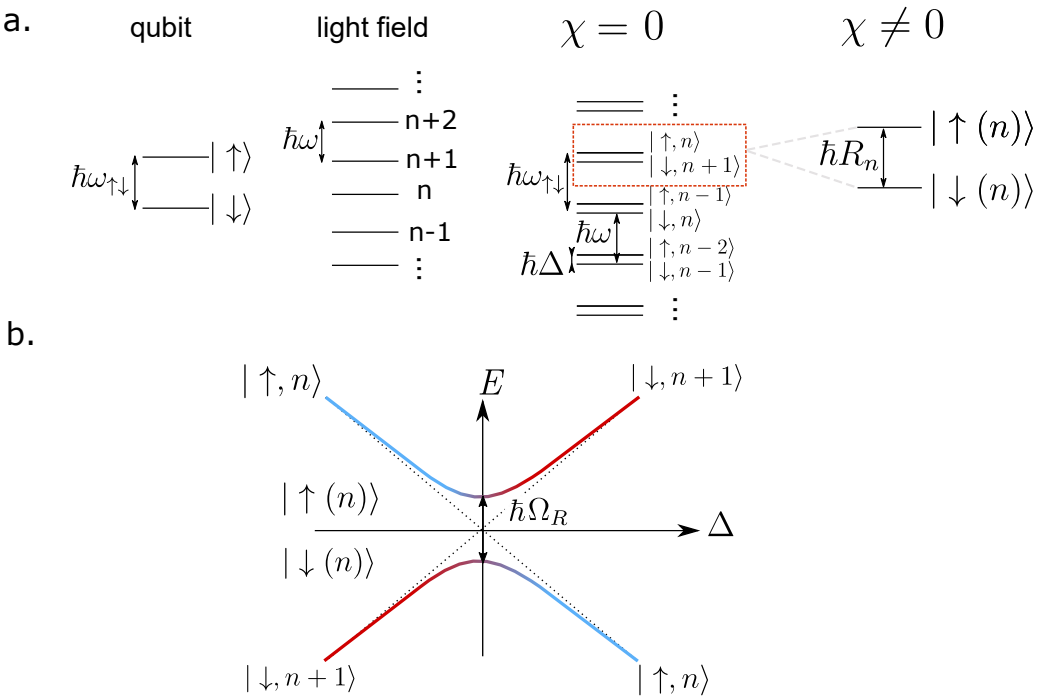

Figure 7.2 – **Energy spectrum when light and a two-level system interact:** (a) From left to right: energy levels of independent spin qubit and light field. Energy ladder description when the two subsystems are considered uncoupled ($\chi = 0$) defining the detuning parameter $\Delta = \omega_{\uparrow\downarrow} - \omega$ as the frequency mismatch. Right panel is the energy levels with non-zero interaction term ($\chi \neq 0$) revealing so-called dressed states $|\uparrow(n)\rangle$ and $|\downarrow(n)\rangle$ separated by the energy $\hbar R_n$. For sake of clarity, only the subspace $\{|\uparrow, n\rangle, |\downarrow, n+1\rangle\}$ is considered in this figure. (b) Dressed states energy spectrum as a function of frequency detuning Δ. At resonance, meaning $\omega_{\uparrow\downarrow} = \omega$, the two dressed states are split by the energy $\hbar\Omega_R$. For large frequency detuning, the dressed states almost behave as the uncoupled case.

7.1.2 Landau-Zener (LZ)-transition

Linear transition at an avoided crossing of a two-level system was first described in 1932 by Landau and Zener theory [7, 11, 12]. The probability of a non-adiabatic passage from ground to excited state is given by the Landau-Zener probability in equation 7.10, which is mainly governed by the transition dynamics with regard to the qubit Rabi frequency.

$$\boxed{P_{LZ} = e^{-2\pi\gamma}, \quad \text{with} \quad \gamma = \frac{\Omega_R^2}{\hbar v}} \tag{7.10}$$

with

P_{LZ} *the Landau-Zener probability,*

$v = \frac{\partial\Delta}{\partial t}$ *the Landau-Zener level velocity.*

Two different scenarii therefore arise depending on the transition dynamics. When the system initially lays in its ground state, an infinitely slow variation of the detuning parameter -with respect to the Rabi frequency- would cause an adiabatic transition. Thus, the system remains in its ground state. On the contrary, a fast detuning variation allows the avoided crossing passage and in turn promotes the quantum state into its excited state.

Considering the aforementioned dressed states as the two-level system of interest, an adiabatic transition would result in an spin inversion population. Indeed, as the dressed states almost behave as uncoupled ones for large detuning, the system undergoes a transition from $|\downarrow(n)\rangle_{\Delta\ll 0} \sim |\downarrow, n+1\rangle$ to $|\downarrow(n)\rangle_{\Delta\gg 0} \sim |\uparrow, n\rangle$. A fast passage will whereas be characterized by no spin rotation as the non-adiabatic transition transfers the state from $|\downarrow(n)\rangle_{\Delta\ll 0} \sim |\downarrow, n+1\rangle$ to $|\uparrow(n)\rangle_{\Delta\gg 0} \sim |\downarrow, n+1\rangle$. The following equation 7.11 summarizes the dynamic regimes governing the LZ-transition and the consequences on the spin state:

$$\begin{cases} \Omega_R^2 \gg \dfrac{\partial\Delta}{\partial t} & \Longrightarrow \text{Landau-Zener adiabatic inversion of the spin state.} \\ \Omega_R^2 \ll \dfrac{\partial\Delta}{\partial t} & \Longrightarrow \text{Non-adiabatic transition, the spin remains down.} \end{cases} \tag{7.11}$$

In other words, as the main interest is the spin orientation -regardless to the number of photons-, dressed states allow to control the spin rotation by changing the transition dynamics. The probability to rotate the spin from down to up-state directly relates to the probability of an adiabatic transition and thus reads as per equation 7.12. Figure 7.3 displays the $|\uparrow\rangle$-state probability dependency to the frequency detuning dynamics and reveals the distinction between adiabatic and non-adiabatic regimes.

$$P_\uparrow = 1 - P_{LZ} \tag{7.12}$$

When the detuning parameter is periodically swept: $\Delta(t) = A\cos(\omega t)$, the system encounters several avoided crossing transitions back and forth, also known as Landau-Zener-Stückelberg-Majorana interferometry. In this particular case, the quantum state acquires a phase due to the avoided crossing passages, so-called Stokes phase [13]. Herein, the transition boils down to a single passage with a linear velocity, thus no phase shift is taken into account.

Now that the relation between the system transition dynamics and the Rabi frequency is elucidated, the attention of the reader is drawn onto the experimental realization of such adiabatic and non-adiabatic regimes for a single hole particle within a QD.

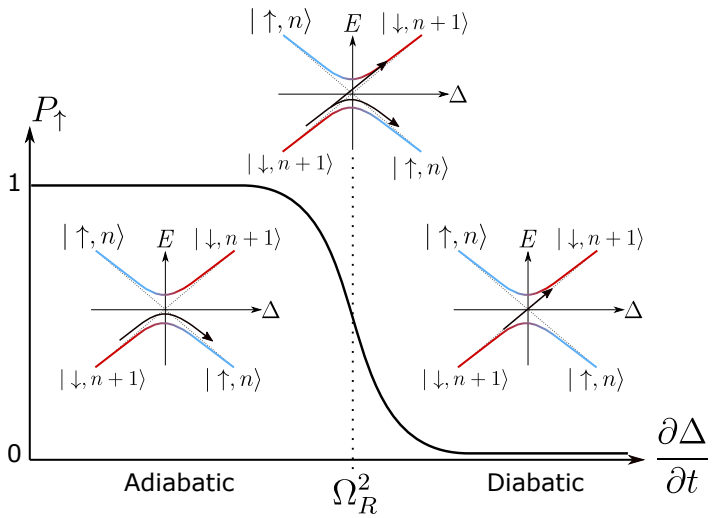

Figure 7.3 – **Landau-Zener probability: from adiabatic to non-adiabatic (chirp) passage:** Landau-Zener probability $P_\uparrow$ evolution as a function of the transition speed $\partial\Delta/\partial t$. The left inset represents an infinitely slow transition compared to the qubit Rabi frequency (adiabatic case). Here, the system remains in the ground state denoted $|\downarrow(n)\rangle$ and the spin orientation is flipped. The opposite case -i.e. non-adiabatic transition- is shown in the right inset and reveals the state transition from ground $|\downarrow(n)\rangle$ to excited dressed-state $|\uparrow(n)\rangle$. The qubit spin orientation is therefore preserved. When the transition velocity matches the Rabi frequency squared, the system undergoes both adiabatic and non-adiabatic passage with a probability of 50% each so that $P_\uparrow$ should equal 0.5.

7.1.3 LZ-transition as a method to probe Rabi frequency

Coupling a spin qubit to an electrical field creates an entangled system with two distinct dressed states $|\uparrow(n)\rangle$ and $|\downarrow(n)\rangle$, degenerate at resonance by a factor directly related to the Rabi frequency (see eq. 7.10). The latter can be evaluated using LZ-transition in different dynamical regimes, regardless to the number of photons. Indeed, the variation of $|\uparrow\rangle$-state probability with respect to the speed transition finally relates to the qubit Rabi frequency as expressed in equation 7.10. The system initially lays in its ground state $|\downarrow(n)\rangle$ and is repeatedly transferred to large positive frequency detuning at different speed while the spin-up probability is recorded (by Elzerman readout). Following section focuses on the implementation of such LZ-transition experiment to extract the qubit Rabi frequency.

7.2 Landau-Zener transition: experimental details

7.2.1 Experimental setup

A complete version of wiring schematics can be found in chapter 2. Room temperature wiring presented in section 2.2 is replaced by the wiring schematic in figure 7.4 to perform chirp experiment. The main differences from standard qubit setup stem from the frequency and pulse modulation techniques, hereafter detailed.

7.2.2 Methods: Waveform implementation

The detuning parameter Δ is defined as the mismatch of the qubit frequency and the field modes. Experimentally, this parameter embodies the difference between the Larmor frequency (qubit) and the microwave (MW) one used to excite the qubit: $\Delta/2\pi = f_{Larmor} - f_{MW}$. Consequently, Landau-Zener level velocity $v = \partial\Delta/\partial t$ is regulated by two parameters: the frequency detuning and the transition duration. On the one hand, frequency detuning Δ is swept by changing the MW tone f_{MW} using Frequency Modulation (FM) technique (detailed in section 7.2.2). On the other hand, the duration ∂t to go through the anti-crossing can be changed (detailed in section 7.2.2). The ratio between these two quantities finally giving the Landau-Zener velocity as follow:

$$\frac{\partial\Delta}{\partial t} = 2\pi\,\frac{f_{Larmor} - f_{MW}}{\partial t} = 2\pi\,\frac{\partial\delta f}{\partial t} \tag{7.13}$$

with

f_{Larmor} *the Larmor qubit frequency,*

f_{MW} *the MW tone frequency,*

δf *the frequency mismatch* $f_{Larmor} - f_{MW}$.

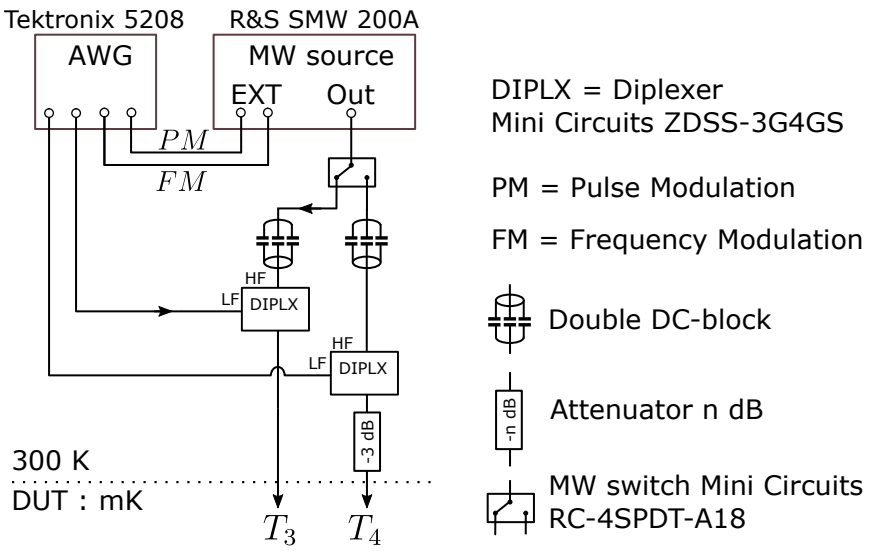

Figure 7.4 – **Room-temperature wiring schematic for Landau-Zener transition experiment:** High-frequency wiring schematic of room-temperature setup for LZ-transition experiment. Microwave signal, modulated in amplitude and in frequency, is sent via a diplexer to the gate hosting the qubit QD. Unless explicitly specified, the microwave tone is connected to gate T_3, but can at convenience be set on gate T_4. AWG stands for Arbitrary Waveform Generator and DUT for Device Under Test.

In practice, LZ-transition could be achieved by changing only one of the two parameters (either ∂t or Δ). However, it is necessary to scan the transition velocity over several orders of magnitude to accurately evaluate the Rabi frequency. In that sense, varying one parameter may not be sufficient due to restricted experimental settings. Hence, the two parameters will be swept in the following.

Microwave Frequency Modulation (FM)

In order to perform Landau-Zener adiabatic transition, the microwave frequency should be on the same order of magnitude as the Larmor frequency. Frequency modulation technique allows to change the MW tone as a function of an applied voltage as expressed in equation 7.14.

$$f_{MW} = f_{Larmor} + \alpha \times \partial V \tag{7.14}$$

with

α being the deviation parameter, setting the correspondence between frequency and voltage, expressed in $[MHz/V]$.

At a given passage duration ∂t, the transition velocity is therefore governed by the deviation parameter: $v \propto \alpha\, ^{\partial V}/_{\partial t}$. The latter typically ranges from 0 MHz/V

to +100 MHz/V and is set by the MW source. Figure 7.5(a) depicts the voltage waveforms used with frequency modulation to modify the frequency mismatch between dressed states, keeping the same transition duration.

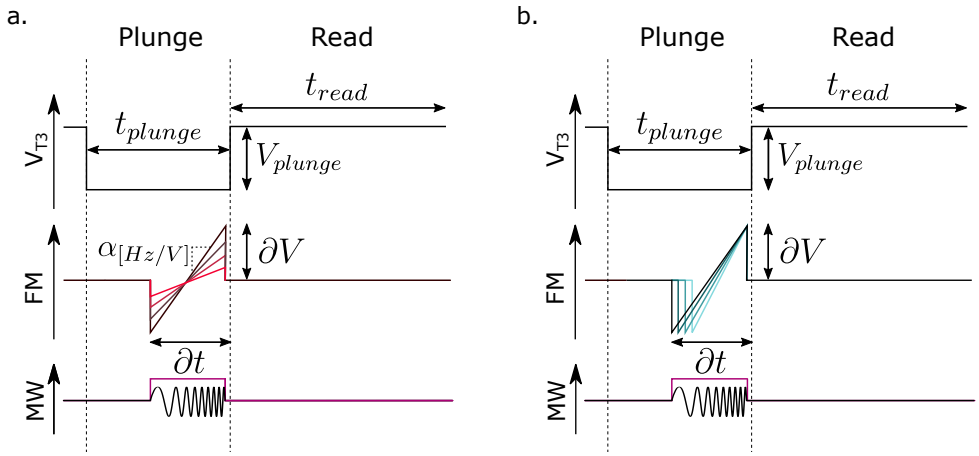

Figure 7.5 – **Waveforms to perform Landau-Zener passage:** (a) AWG and MW sequences used with Frequency Modulation (FM) to monitor frequency detuning at constant chirp duration. The upper panel is the qubit manipulation waveform during "Plunge"-stage and spin readout within the "Read"-stage. Below, the frequency modulation ramp to change frequency detuning. The base signal is set to match the Larmor frequency (hence $\Delta = 0$). As $\Delta \propto \partial V$, any modulation by ∂V shifts the MW tone from the Larmor frequency. The slope of this modulation is given by the deviation parameter α. Lower panel depicts the MW switching, controlled by Pulse Modulation (PM) technique, symbolized in pink. (b) AWG sequences used to vary the transition duration ∂t at a fixed deviation parameter. Qubit control sequence and MW switching remain the same than in (a).

About the consequences on Electrically Driven Spin Resonance (EDSR) measurement:

When frequency modulation is ON, the frequency range to excite the spin qubit is artificially widened by the deviation parameter value. This method can be very handy when searching for the qubit Larmor frequency. Indeed, at low microwave power, the intrinsic width of Larmor frequency directly relates to decoherence time as $\sigma_{\mathrm{FWHM}} \propto \frac{1}{T_2^*}$ [14] and can be a sharp feature of few kHz. Broadening the Larmor frequency width allows a rougher (thus faster) scan. The following figure compares the EDSR response without (left panel) and using LZ-method (right panel). When using frequency modulation, the Larmor frequency finally lays in the centre of the modulated signal, as highlighted by the black dashed line in right panel of figure 7.6 [2].

2. Unfortunately no example with and without Frequency modulation can be shown for the

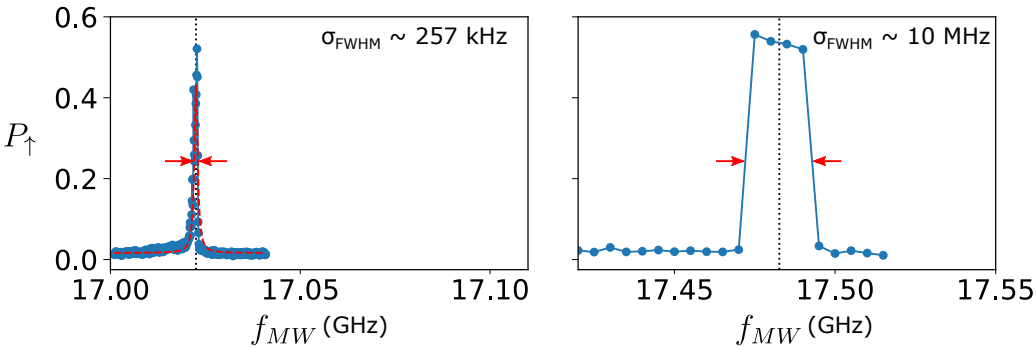

Figure 7.6 – **Comparison of EDSR measurements with and without frequency modulation:** Left panel : $|\uparrow\rangle$-state probability with respect to microwave frequency without using LZ-transition method. When the MW frequency matches the Larmor frequency, the qubit spin state rotates from ground ($|\downarrow\rangle$) to its excited ($|\uparrow\rangle$) state. The intrinsic width of the Larmor frequency inversely scales as the qubit decoherence time, thus giving a Full Width Half Maximum (FWHM) about $\sigma_{\mathrm{FWHM}} \sim 257\,\mathrm{kHz}$. The red dashed line is a Lorentzian fit used to extract the EDSR width. Right panel : EDSR measurement with LZ-transition method and frequency modulation. In this case, the Larmor frequency is artificially broadened by Frequency Modulation whose width is set by the deviation parameter value $\sigma_{\mathrm{FWHM}} \sim 10\,\mathrm{MHz}$. Black dashed lines symbolize the Larmor frequency in both case.

Changing transition duration

The second key parameter to perform adiabatic transition is the duration ∂t. Given a fixed frequency detuning, the system velocity to go through the avoided crossing is inversely proportional to the passage duration: $v \propto {}^{1}/_{\partial t}$. The figure 7.5(b) gathers the AWG pulse sequences used to perform LZ-transition at a given frequency detuning.

Pulse modulation (PM)

High-frequency signals are only applied during LZ-transition to avoid undesired driving of the qubit spin state. Microwave switching is controlled by Pulse Modulation (PM) technique, which consists in a binary sequence sent from the AWG to the MW source via an External (EXT) port (see details in figure 7.4). The signal is therefore modulated in amplitude between 0 (signal OFF) and 1 (signal ON) and is only effective during ∂t. When modulation is OFF, the microwave signal is attenuated by about 20 dB.

LZ-passage occurs during the spin manipulation stage (referred as "Plunge"). Then the spin orientation is measured via energy selective readout in the "Read"-stage. Plunge stage typically lasts for 20 µs while spin readout is performed in

same EDSR measurement. Still, it is important to stress here that the attenuation of the line between the two panels shown is highly similar, and that the EDSR peak broadening is mostly induced by the frequency modulation.

500 µs. Detailed explanations on the qubit control and readout stages are given in chapter 3.

7.3 Rabi frequency extraction using LZ-transition

7.3.1 Rabi frequency measurements and fitting

As explained in previous sections, the up-state probability is undoubtedly affected by the transition dynamics. The following figure 7.7(a) represents a typical chirp measurement while varying both the transition duration and the deviation parameter. Herein, the up-state probability is measured with respect to the deviation and transition duration. Each point therefore corresponds to a certain transition velocity : $P_\uparrow = f\left(\alpha\partial V/\partial t\right)$.

Even at first glance, different dynamic regimes arise depending on ∂t and α values. A small deviation and/or a long transition duration will favor spin with up-state (adiabatic transition), visible in the lower right corner of figure 7.7(a), whereas a fast transition, and/or a large frequency detuning causes no spin rotation (upper left corner of figure 7.7(a)). Finally, it is relevant to notice that multiple combination of $(\alpha, \partial t)$ gives a same transition velocity, thus forming a "iso-speed" line, represented by the white dotted line.

From panel (a), the up-state probability can therefore be reconstructed as a function of the LZ-velocity, combination of deviation and ∂t parameters, given by equation 7.13. This dependency to the transition velocity is depicted in figure 7.7(b) and can be fitted to extract the Rabi frequency. From equation 7.12, the exponent can be rewritten as function of frequencies, giving [8]:

$$\begin{aligned} -2\pi\gamma &= -2\pi\frac{\Omega_R^2}{\hbar\frac{\partial\Delta}{\partial t}} \\ &= -2\pi\frac{(2\pi f_R)^2}{\hbar\frac{\partial(2\pi\delta f)}{\partial t}} \\ &= -4\pi^2\frac{f_R^2}{\hbar\frac{\partial\delta f}{\partial t}} \end{aligned} \tag{7.15}$$

As a consequence, the up-state probability is given by:

$$\boxed{P_\uparrow = 1 - e^{-4\pi^2\frac{f_R^2}{\hbar\frac{\partial\delta f}{\partial t}}}} \tag{7.16}$$

In the presented example, the estimated Rabi frequency is about $f_R \simeq 127\,\mathrm{kHz}$ for a given microwave power of $P_{\mathrm{MW}} = -5.0\,\mathrm{dBm}$ at room temperature (corresponding to a drive amplitude about $A_{\mathrm{MW}} \simeq 561.6\,\mu\mathrm{V}$ at the sample level).

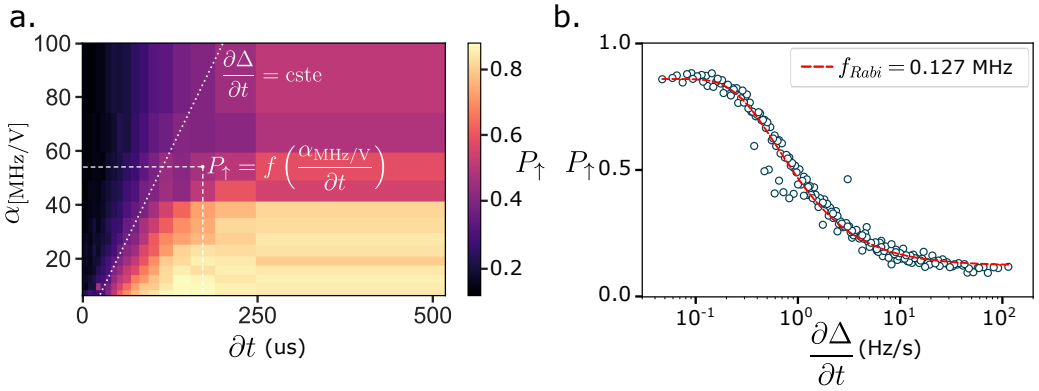

Figure 7.7 – **Example of chirp measurement:** (a) LZ up-state probability when varying both the transition duration and the deviation parameter measured at $P_{\mathrm{MW}} = -5.0\,\mathrm{dBm}$ (equivalent to $A_{\mathrm{MW}} \simeq 561.6\,\mu\mathrm{V}$). Each point is a unique combination of transition duration ∂t and frequency mismatch $\Delta \propto \alpha$, and thus corresponds to a probability of adiabatic transition $P_\uparrow$. Though, a same transition velocity can be achieved by different combination of deviation and chirp duration forming an "iso-speed" line, highlighted by the white dotted line. Note that, in order to drastically change the LZ-velocity, both parameters α and ∂t are in logarithmic scale. (b) Spin-up probability as a function of the transition velocity $\partial\Delta/\partial t$ in logscale. The velocity is reconstructed as the ratio between the deviation parameter and the duration of LZ-transition from panel (a). Red line is the fit using the formula 7.16, giving a Rabi frequency of 127 kHz.

In addition to the Rabi frequency, two free parameters (A, B) account for an up-state probability rescaling, such that : $P_\uparrow = A \times \left(1 - e^{-4\pi^2 \frac{f_R^2}{h\frac{\partial\delta f}{\partial t}}}\right) + B$.

7.3.2 Comparison between LZ-transition and Rabi chevron methods

Qubit Rabi frequency can be measured in several manners. The standard procedure usually consists in measuring coherent oscillations nearby the Larmor frequency and extract the time needed for the spin to perform a $2\pi-$rotation. This method is known as "Chevron measurement" and is presented in more details in chapter 4. It is also possible to measure coherent oscillations at the Larmor frequency for various driving power, later referred as power chevron.

In order to validate LZ-transition on dressed states as a way to evaluate Rabi frequency, we compare the results of Rabi frequencies measured with the chevron method at various driving amplitude and a chevron with power dependence. The experimental conditions, e.g. magnetic field orientation, qubit electrostatic environment, are kept the same.

Yet, as aforementioned, the setup wiring slightly differs between the two meth-

ods (see detailed setup in the corresponding sections) and a particular rescaling is needed to compare the two methods. Indeed, we used Frequency Modulation for LZ-transition whereas the chevron measurement uses I/Q modulation technique [3]. The delivered MW power for a same instruction is therefore different. This rescaling needs to be taken into account in the Rabi frequency probing as the latter scales linearly with the square root of MW power. We compare output levels of the MW source Rohde&Schwarz SMW200A measured with a Power Spectral Analyzer (PSA) Rohde&Schwarz FSL(9-18), at a given frequency ($f = 17.99\,\mathrm{GHz}$) for different values of instruction power P_{MW}. We ensure that the measurement bandwidth of the PSA is much larger than the FM applied ($BW \gg \alpha$). Following table 7.1 gathers the measured powers expressed in dBm with I/Q and FM modulations alternatively ON and OFF. The averaged level difference between I/Q and FM modulations is $\sim 3.025\,\mathrm{dBm}$. Consequently, a measurement at $P_{\mathrm{MW}} = +15\,\mathrm{dBm}$ using the chevron method would correspond to chirp measurement at about $P_{\mathrm{MW}} = +12\,\mathrm{dBm}$.

P_{MW}	I/Q	FM	P_{meas}
18	ON	OFF	7.6
	OFF	ON	5
15	ON	OFF	5.1
	OFF	ON	2
12	ON	OFF	2.2
	OFF	ON	-1
0	ON	OFF	-10
	OFF	ON	-13.2

Table 7.1 – **Comparison of MW output level depending on modulation modes used:** Output microwave level measured with PSA when using I/Q and FM modes. I/Q modulation is used for Chevron measurement whilst FM is used for LZ-transition. Values are measured at $f = 17.99\,\mathrm{GHz}$.

All Rabi frequency measurements are gathered in figure 7.8, where the blue (resp. green, red) points represent values using LZ-transition (resp. chevron, power chevron) method. Details on the fitting procedures of chevron measurements can be found in section 4.2.2. The overall LZ-transition measurements reasonably agree with estimated values from chevron methods, and scale linearly as the square root of MW level as theoretically expected. This confirms that LZ-transition can be used to perform spin rotation and accurately assess the Rabi frequency.

3. Note that LZ-transition can also be performed with I/Q modulation technique using single

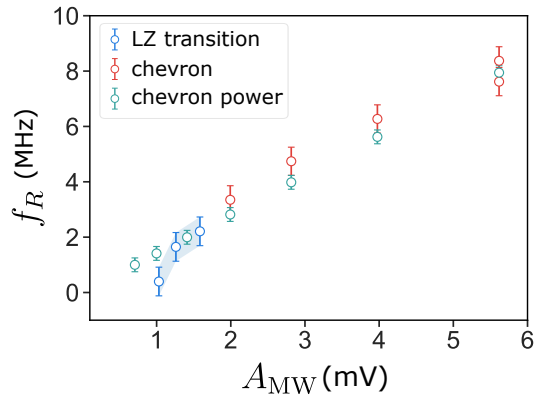

Figure 7.8 – **Comparison between Rabi frequencies measured with LZ-transition and chevron methods:** Rabi frequency as a function of the drive amplitude calculated at the sample level (see methods in chapter 4), measured with LZ-transition (blue), standard chevron (red) and chevron in power (green) method. The Rabi frequency scales linearly with the drive amplitude as expected.

7.4 Conclusions & limitations

Landau-Zener adiabatic passage appears as a powerful method for spin qubit control but also as a way to investigate the qubit properties. On the one hand, broadening the Larmor frequency width via Frequency Modulation technique allows for faster EDSR measurements. On the other hand, as the transition dynamics indirectly governs the spin orientation, it is an alternate way to estimate the Rabi frequency for instance in the case of a qubit experiencing low-frequency noise.

Importantly enough, one main limitation may arise when having too-fast Rabi frequency. Indeed, in order to fit Landau-Zener transition probability, the dressed states need to encounter both dynamical regimes (adiabatic and non-adiabatic, as shown in figure 7.3). It is always easy to slow-down the transition velocity (by decreasing the deviation parameter or extend the transition duration) to achieve adiabatic regime. However, non-adiabatic transition may be hard to reach due to restricted experimental settings (the maximum deviation parameter in R&S SMW200A is 160 MHz/V and the minimal pulse duration in the AWG Tektronix 5208 is about few nanoseconds). Therefore, non-adiabatic regime is no longer valid as soon as $\Omega_R^2 \sim 10\,\partial\Delta/\partial t$. Considering a FM-pulse of 1 V, meaning that the maximum frequency detuning is $\delta f = 160$ MHz and a pulse duration $\partial t = 10$ ns, the maximum frequency that LZ-transition could evaluate is about 500 MHz. Eventhough the MW power and the FM-pulse amplitude marginally play a role in this frequency limit, LZ-transition method can still be used on the majority of spin qubit in semiconductor structure with Rabi frequencies nowadays ranging from tens to hundreds of megahertz [15, 16, 17].

sideband cancelation.

References

[1] L. M. K. Vandersypen and I. L. Chuang. « NMR techniques for quantum control and computation ». In: *Reviews of Modern Physics* 76 (4 Jan. 2005), pp. 1037–1069. DOI: 10.1103/RevModPhys.76.1037.

[2] L. A. O'Dell. « The WURST kind of pulses in solid-state NMR ». In: *Solid State Nuclear Magnetic Resonance* 55-56 (2013), pp. 28–41. DOI: 10.1016/j.ssnmr.2013.10.003.

[3] J. R. Petta, H. Lu, and A. C. Gossard. « A Coherent Beam Splitter for Electronic Spin States ». In: *Science* 327.5966 (2010), pp. 669–672. DOI: 10.1126/science.1183628.

[4] J. Zhou et al. « Observation of Time-Domain Rabi Oscillations in the Landau-Zener Regime with a Single Electronic Spin ». In: *Phys. Rev. Lett.* 112 (1 Jan. 2014), p. 010503. DOI: 10.1103/PhysRevLett.112.010503.

[5] C. M. Quintana et al. « Cavity-Mediated Entanglement Generation Via Landau-Zener Interferometry ». In: *Phys. Rev. Lett.* 110 (17 Apr. 2013), p. 173603. DOI: 10.1103/PhysRevLett.110.173603.

[6] G. M. Leskowitz et al. « Three-qubit nuclear magnetic resonance quantum information processing with a single-crystal solid ». In: *The Journal of Chemical Physics* 119.3 (July 2003), pp. 1643–1649. DOI: 10.1063/1.1582171.

[7] Landau L. D. « On the Theory of Transfer of Energy at Collisions II. » In: *Physikalische Zeitschrift der Sowjetunion* 2.46 (1932).

[8] A. Laucht et al. « A dressed spin qubit in silicon ». In: *Nature Nanotechnology* 12.1 (Jan. 2017), pp. 61–66. DOI: 10.1038/nnano.2016.178.

[9] A. Laucht et al. « High-fidelity adiabatic inversion of a 31P electron spin qubit in natural silicon ». In: *Applied Physics Letters* 104.9 (Mar. 2014), p. 092115. DOI: 10.1063/1.4867905.

[10] E.T. Jaynes and F.W. Cummings. « Comparison of quantum and semiclassical radiation theories with application to the beam maser ». In: *Proceedings of the IEEE* 51.1 (1963), pp. 89–109. DOI: 10.1109/PROC.1963.1664.

[11] C. Zener and R. H. Fowler. « Non-adiabatic crossing of energy levels ». In: *Proceedings of the Royal Society of London. Series A, Containing Papers of a Mathematical and Physical Character* 137.833 (1932), pp. 696–702. DOI: 10.1098/rspa.1932.0165.

[12] S.N. Shevchenko, S. Ashhab, and F. Nori. « Landau–Zener–Stückelberg interferometry ». In: *Physics Reports* 492.1 (2010), pp. 1–30. DOI: 10.1016/j.physrep.2010.03.002.

[13] O. V. Ivakhnenko, S. N. Shevchenko, and F. Nori. « Nonadiabatic Landau–Zener–Stückelberg–Majorana transitions, dynamics, and interference ». In: *Physics Reports* 995 (2023), pp. 1–89. DOI: 10.1016/j.physrep.2022.10.002.

[14] E. Kawakami et al. « Electrical control of a long-lived spin qubit in a Si/SiGe quantum dot ». In: *Nature Nanotechnology* 9.9 (Sept. 2014), pp. 666–670. DOI: 10.1038/nnano.2014.153.

[15] N. W. Hendrickx et al. « A single-hole spin qubit ». In: *Nature Communications* 11.1 (July 2020), p. 3478. DOI: 10.1038/s41467-020-17211-7.

[16] F. N. M. Froning et al. « Ultrafast hole spin qubit with gate-tunable spin–orbit switch functionality ». In: *Nature Nanotechnology* 16.3 (Mar. 2021), pp. 308–312. DOI: 10.1038/s41565-020-00828-6.

[17] K. Takeda et al. « A fault-tolerant addressable spin qubit in a natural silicon quantum dot ». In: *Science Advances* 2.8 (2016), e1600694. DOI: 10.1126/sciadv.1600694.

Conclusions & outlook

Outstanding progresses have been made on hole spin qubits over the last three years, namely with the experimental scaling-up of on-chip spin qubits from one to more than six [1, 2, 3, 4]. In the meantime the electrical noise influence impairing with spin coherence time have been tackled [5, 6, 7], revealing enhanced coherence time about 88 µs corroborated with the presence of dephasing sweetspots [5, 8]. The swift evolution of quantum dot (QD) spin-based qubits is a reflection of their high-potential regarding to large-scale implementation, taking advantages of fabrication facilities. Up to now, challenges on the qubit error (due to decoherence and relaxation processes) caused by electrical and magnetic noises remain a hurdle for hole spin to outweigh on their electron counterpart. By isotopic purification or in the case of an ideal heavy hole system [9], magnetic noise stemming from hyperfine interaction can be greatly suppressed, and hence magnetic noise did not constitute the main focus of this experimental investigation.

In this thesis, we explored the electrical noise anisotropy with respect to magnetic field by investigating the dependency of dephasing sweetspots in single hole spin inside a QD defined within a natural Si-MOS nanowire (chapter 3 to 4). The spin readout is made by spin-to-charge conversion technique, probed with radio-frequency reflectometry (chapter 2). So as to mitigate the electrical noise hampering the qubit coherence time, we probed the spin susceptibility to gate fluctuations proving that sweetspots may be extended into continuous lines, named "sweetlines" (chapter 3). Importantly, the electrical noise evaluated herein boils down to the gate fluctuations, which does not capture the contribution from nearby two-level fluctuators. Due to the substantial relation between spin susceptibility to electrical noise and the particle wavefunction confinement, we unveiled the tunability of such sweetlines over more than 26° in magnetic field orientation (chapter 4). In addition to extended coherence time, sweetline operation appears to be compatible with fast and all-electrical driving with cutting-edge hole qubit quality factor, partly revealing a reciprocal sweetness relation behaviour (chapter 4). This experimental investigation opens the path towards optimal operation points for spin qubits in magnetic field direction, exhibiting long coherence time and fast manip-

ulation speed.

To go even further, we focused on the tuning of two sweetlines at a common magnetic field direction of uncoupled hole spin qubits as a proof of concept for large-scale QD arrays (chapter 5). Despite the mature fabrication processes inherited from microelectronics industry, the presence of defects and structural disorder underneath the gates combined with the large effective mass of holes in silicon, entails uncontrolled dot shape variability and thus render the sweetlines tuning challenging [10, 11]. As a possible solution, it would be relevant to reproduce a similar investigation having multiple and odd number of holes filling the QD. In this situation, the dot dimension will increase and is expected to be less prone to the defects location and disorder inside the nanowire. This could in turn result in standardizing the sweetline angular location and ease their alignment from qubit to qubit. Undoubtedly, the assessment of two qubit gate fidelity operated at a shared sweetspot would constitute a meaningful route for hole spin-based qubits.

Besides coherence times, electrical noise also influences the qubit relaxation times through phonon interactions. Despite the rather long relaxation times of confined spins, the correlation with longitudinal response to charge noise remains yet to be understood. Moreover, the effect of nuclear spin bath in natural materials also impairs qubit relaxation and coherence times via magnetic noise. So far, hyperfine interactions stand beyond the scope of this study, but deserve to be further investigated and corroborated with respect to magnetic field orientation and spin susceptibility [7]. Such resilience tunability of the hole spin with respect to electrical noise provides routes into the design of improved qubits, but requires a large number of control knobs, which are somewhat mismatched with scalability prospects.

To a greater extend, the large-scale implementation of spin qubit in QDs will raise many challenges with the endless increase in the number of pulsing line to control each qubit and the presence of nearby charge sensors to read the qubit state by spin-to-charge technique. As an alternative paradigm, we investigated the gate-based readout of a singlet-triplet qubit confined in an isolated double quantum dot (DQD) structure. Spectroscopy [12] and magnetospectroscopy [13, 14] techniques can be used to probe the spin orientation with reduced device wiring and the absence of a nearby charge sensor (chapter 6).

Hole spins confined in Silicon quantum dots proved beyond doubt a rapid evolution in the scope of quantum processors and with indubitable advantages. Despite remaining challenges that hinder their large-scale implementation, such qubits exhibit reasonable relaxation and coherence times combined with a fast operating speed. Today, the number of physical on-chip qubits is far too small to create an efficient quantum processor, and it is at an early stage of development that is likely to evolve rapidly in the near future.

In a nutshell:

- A single-hole spin qubit was operated in a natural Si-MOS architecture device (from LETI), spatially confined in a quantum dot defined by electrostatic potentials set by gate voltages.
- Hole spins exhibit a strong spin-orbit coupling that allows for all-electrical manipulation and, as a counterpart, an extra interaction to the environment, detrimental to qubit coherence.
- The high anisotropy of holes g-matrix and the influence of longitudinal charge noise contribution depending on magnetic field orientation are readily captured by the g-matrix formalism.
- Sweetlines are continuous lines in magnetic field orientation of spin zero-sensitivity to longitudinal charge noise term at which the spin qubit coherence time (T_2^E) is enhanced while maintaining a decent qubit control speed (f_R).
- Modification of the electrostatic potentials responsible for hole wavefunction confinement permits an ample tunability of the sweetline angular position in B-field, that is particularly appealing for large-scale implementation.
- Gate-based dispersive sensing and spectroscopy measurements provide a path for Singlet-Triplet qubit operation and readout in an isolated Double Quantum Dot structure.
- Probing Landau-Zener adiabatic transitions is a powerful method to experimentally figure out the Larmor spin resonance and to assess Rabi frequency in the case of a qubit experiencing low-frequency noise.

References

[1] N. W. Hendrickx et al. « A single-hole spin qubit ». In: *Nature Communications* 11.1 (July 2020), p. 3478. DOI: 10.1038/s41467-020-17211-7.

[2] N. W. Hendrickx et al. « A four-qubit germanium quantum processor ». In: *Nature* 591.7851 (Mar. 2021), pp. 580–585. DOI: 10.1038/s41586-021-03332-6.

[3] S. G. J. Philips et al. « Universal control of a six-qubit quantum processor in silicon ». In: *Nature* 609.7929 (Sept. 2022), pp. 919–924. DOI: 10.1038/s41586-022-05117-x.

[4] F. Borsoi et al. « Shared control of a 16 semiconductor quantum dot crossbar array ». In: *Nature Nanotechnology* 19.1 (Jan. 2024), pp. 21–27. DOI: 10.1038/s41565-023-01491-3.

[5] N. Piot et al. « A single hole spin with enhanced coherence in natural silicon ». In: *Nature Nanotechnology* 17.10 (Sept. 2022), pp. 1072–1077. DOI: 10.1038/s41565-022-01196-z.

[6] M. J. Carballido et al. *A Qubit with Simultaneously Maximized Speed and Coherence*. arXiv. 2024. DOI: 10.48550/arXiv.2402.07313.

[7] N. W. Hendrickx et al. *Sweet-spot operation of a germanium hole spin qubit with highly anisotropic noise sensitivity*. arXiv. 2023. DOI: 10.48550/arXiv.2305.13150.

[8] Lorenzo Mauro et al. « Geometry of the dephasing sweet spots of spin-orbit qubits ». In: *Phys. Rev. B* 109 (15 Apr. 2024), p. 155406. DOI: 10.1103/PhysRevB.109.155406.

[9] Jan Fischer et al. « Spin decoherence of a heavy hole coupled to nuclear spins in a quantum dot ». In: *Phys. Rev. B* 78 (15 Oct. 2008), p. 155329. DOI: 10.1103/PhysRevB.78.155329.

[10] Floris A. Zwanenburg et al. « Silicon quantum electronics ». In: *Rev. Mod. Phys.* 85 (3 July 2013), pp. 961–1019. DOI: 10.1103/RevModPhys.85.961.

[11] L. M. K. Vandersypen et al. « Interfacing spin qubits in quantum dots and donors—hot, dense, and coherent ». In: *npj Quantum Information* 3.1 (Sept. 2017), p. 34. DOI: 10.1038/s41534-017-0038-y.

[12] R. Ezzouch et al. « Dispersively Probed Microwave Spectroscopy of a Silicon Hole Double Quantum Dot ». In: *Phys. Rev. Appl.* 16 (3 Sept. 2021), p. 034031. DOI: 10.1103/PhysRevApplied.16.034031.

[13] M. G. House et al. « Radio frequency measurements of tunnel couplings and singlet–triplet spin states in Si:P quantum dots ». In: *Nature Communications* 6.1 (Nov. 2015), p. 8848. DOI: 10.1038/ncomms9848.

[14] T. Lundberg et al. « Non-symmetric Pauli spin blockade in a silicon double quantum dot ». In: *npj Quantum Information* 10.1 (Mar. 2024), p. 28. DOI: 10.1038/s41534-024-00820-1.

APPENDIX A

The following tables present the electronics and instruments used for experiments described throughout the manuscript. The magnet power supply is made of 3 Mercury iPS modules from Oxford Instruments.

A.1 RT Instruments

Label	Function	Company	Reference
AWG	Arbitrary Waveform Generator	Tektronix	5208
MW	Microwave Source	Rohde&Schwarz	SMW200A
Lock-in	Lock-in	Zurich Instruments	UHF-Li
DAC	Digital-Analog-Converter	Delft	IVVI
DAC (2)	Digital-Analog-Converter	Bilt	BE2142
DMM	Digital MultiMeter	Agilent	34410A

A.2 Electronics

In this section, all room temperature amplifiers, diplexers and filters are from Mini Circuits company. Low-noise amplifier is from LNA industry and the DC block comes from PicoSecond PulseLab.

A.3 PCB electronic components

All electronic components are soldered onto a home-made Printed Circuit Board (PCB). In the setup, two PCBs are stacked via an interposer. The bottom one is named Mother Board (MB) and the topmost is the Daughter Board (DB).

Label	Function	Reference	specs
LNA	Low Noise Amplifier	LNF-LNC0.2-3GHz	+30dB gain
A1	RT Amplifier	ZX60-P33-ULN	+22dB gain
A2	RT Amplifier	ZX60-P103-LN+	+20dB gain
DIPLX	Diplexer	ZDSS-3G4GS+	
LP	Low-pass filter	VLFX-650+	
HP1	High-pass filter	SHP-250+	
HP2	High-pass filter	SHP-300+	
DC block	LT DC block	5509-222-224	

Label	Function	Specs
L_S	Surface mount inductor	330 nH
L_D	Surface mount inductor	470 nH
C_{REF}	Bias-T for reflectometry (on DB)	10 nF
R_{REF}	Bias-T for reflectometry (on DB)	1 MΩ
$R_{T_{3,4}}$	Resistor bias-tee (on DB)	1 MΩ
C_{T_3}	Capacitor bias-tee (on DB)	10 nF
C_{T_4}	Capacitor bias-tee (on DB)	0 nF
R	Resistor filters (on MB)	2 kΩ
C	Capacitor filters (on MB)	10 nF

APPENDIX B

B.1 Lever-arm estimation of the nearby gates on QD_3

The lever-arm of a gate on a QD is a crucial quantity to understand what governs the hole wavefunction confinement and its position within the device [1]. In figure B.1 are shown lever-arms measured for all first-neighbouring gates of QD_3. Lever-arm value, denoted α, is estimated by a linear regression assessing the displacement in V_{T_3} of the first interdot transition. Indeed, due to mutual capacitance between gates, the potential needed for the first hole to enter QD_3 is modified by the near environment electrostatic potential. The influence of gates T_3 and B_2 cannot be evaluated with this method, as these gates are necessarily changed for readout [1].

A large disparity is observed between lever-arm values of different gates. Indeed, T_2 gate exhibits a strong influence of the dot whereas T_4 only affects by $\sim 2\,\%$ the dot potential. This may indicate that QD_3 is actually located closer to gate T_2 than T_4. Additionally, gate B_3 standing on the other side of the nanowire affects QD_3 by almost $20\,\%$. The influence of B_4 is negligible as expected from its spatial distance to the dot.

B.2 Resolving tunnelling events for spin readout

As mentioned in the core of this manuscript, the resolution of single-shot charging events is of pivotal importance for spin readout. Herein, some additional details about the tunnelling rates estimations are given. Figure B.2(a) shows a zoom on the recorded time-trace presented in figure 3.4 with the corresponding fit (dashed blue line). A threshold value is defined as the mean value between the two dot states (see right panel of figure 3.4). In this example, the threshold value is about 1.43 rad. Then, we define a binary sequence probing whether the phase reflectometry signal stands above or below the threshold value. Such sequence, used to extract the time spent in each filling state ($|0\rangle$ or $|1\rangle$), is underscored by the dashed blue line in panel (a). From the histogram presented in fig. 3.4, we evaluate a

1. Further in the main text, the lever-arm of gate T_3 on QD_3 is estimated about 50%.

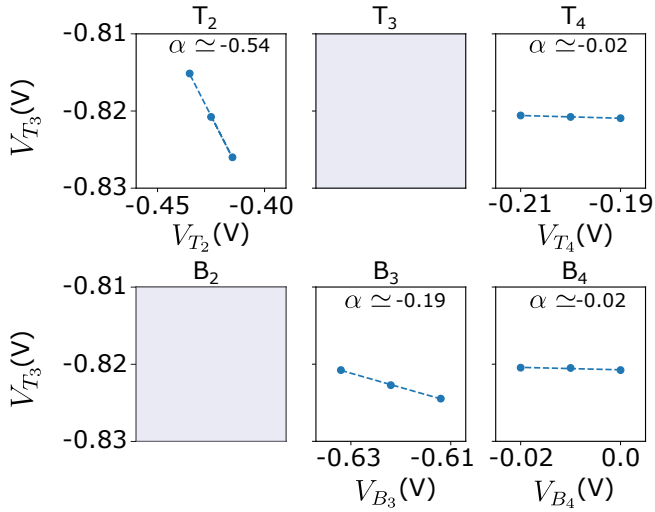

Figure B.1 – **Lever-arm estimation of gates surrounding QD$_3$:** Influence of gates nearby the QD hosting the spin qubit. Gates (either T_2, T_4, B_3 or B_4) are swept one at a time close by their working point and the position of the interdot transition is collected for $V_{B_2} = -1.79\,\mathrm{V}$. Due to mutual capacitance, first charge transition is affected by electrostatic landscape change. From the lever-arm α of each gate, it is possible to approximate the hole wavefunction position within the device.

signal-to-noise ratio (SNR) as in equation B.1 similarly to ref.[2]. At $\tau_{\mathrm{int}} = 5\,\mu\mathrm{s}$, SNR is estimated about 53.4.

$$\mathrm{SNR} = \frac{d^2}{\frac{1}{2}\left(\sigma^2_{|1\rangle} + \sigma^2_{|0\rangle}\right)} \tag{B.1}$$

with,

$d = |\phi_{|1\rangle} - \phi_{|0\rangle}|$ *the distance between centers of the Gaussian distribution of state* $|i\rangle$ *with* $i \in \{0, 1\}$,

$\sigma_{|i\rangle}$ *the full width half maximum of the corresponding Gaussian distribution of state* $|i\rangle$.

We repeat such fitting procedure across the interdot transition, defined by the detuning axis $\widetilde{V_{T_3}}$. Figure B.2(b) presents tunnelling rates $\Gamma_{|1\rangle}$ ($\Gamma_{|0\rangle}$) to enter (escape) the QD depending on the detuning parameter value. Saturations of the Fermi distribution functions remain hardly visible as the tunnelling events (especially in the case of $\Gamma_{|0\rangle}$) become too fast. Nevertheless, charging events are accurately captured close by (with a detuning offset of $k_B T \ln(2)$) the interdot transition (blue encircled point) with an integration time of 5 µs. Moreover, despite a lack of precision in rates estimation, it seems that $\Gamma_{|1\rangle}(\widetilde{V_{T_3}} \to -\infty) = 2\,\Gamma_{|0\rangle}(\widetilde{V_{T_3}} \to +\infty)$ as expected for a twofold degenerate system [3].

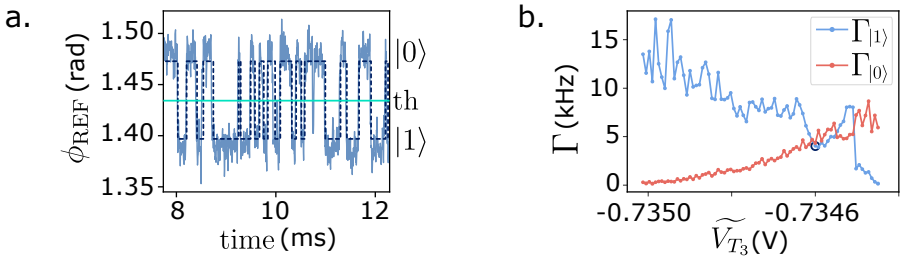

Figure B.2 – **Tunnelling rates of hole particle within QD$_3$:** (a) Zoom on reflectometry time-trace presented in fig. 3.4 to highlight fitting procedure used for tunnelling rates estimation. Green line is the threshold used to discriminate between $|0\rangle$ and $|1\rangle$ states. Dashed blue line is a binary sequence recording whether the measured phase signal is above or below the threshold. From this sequence, time spent in filled (empty) state are inferred, knowing that the integration time is set to 5 µs. (b) Evaluated tunnelling rates $\Gamma_{|0\rangle}$ ($\Gamma_{|1\rangle}$) as a function of detuning parameter $\widetilde{V_{T_3}}$. Encircled data point is presented in panel (a). Both tunnelling rates should follow a Fermi distribution function due to the nature of hole particles. See main text in chapter 3 for details on the estimation of the rates.

B.3 Relaxation time T_1

In order to evaluate spin relaxation time for a given magnetic field orientation, AWG sequence displayed in figure B.3 are implemented, similarly to refs. [4, 5]. It consists in three stages, same as for Elzerman readout method, except that the plunge duration is changed within [1 µs, 1 ms] range. As explained in the main text, for $t_{\text{plunge}} < T_1$, the probability to load the QD with an $|\uparrow\rangle$-spin state is 50%. On the contrary, for $t_{\text{plunge}} > T_1$, the initially loaded $|\uparrow\rangle$-spin state will have the time to relax as a $|\downarrow\rangle$-spin state. The probability of measuring an $|\uparrow\rangle$-spin state during (R)-stage should therefore drop down when increasing the plunge duration. This method benefits from the absence of MW tone needed to excite the qubit. Indeed, given a large g-factor, the MW frequency necessary to provoke spin transition may stand beyond the MW source range (limited to 40 GHz). Moreover, as the plunge amplitude is fixed, the influence of longitudinal spin susceptibility to charge noise is mitigated.

Phase reflectometry time-traces are recorded 8000 times and averaged, allowing to define a probability of having an $|\uparrow\rangle$-state that is later on denoted $P_\uparrow$. We measure the probability $P_\uparrow$ when increasing the plunge duration, as shown in figure B.4(a). A clear decrease of $P_\uparrow$ is observed and can be fitted using equation B.2 to extract a relaxation time of $T_1 = 393.6$ µs.

$$P_\uparrow = Ae^{-\frac{t}{T_1}} + B \tag{B.2}$$

with,

A, B the amplitude and offset of $P_\uparrow$ as free parameters.

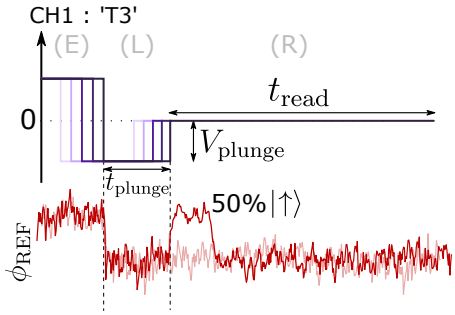

Figure B.3 – **AWG sequences used for relaxation time measurements:** AWG sequences sent on gate T_3 (upper panel) and example of the resulting phase reflectometry signal recorded (lower panel). These sequences are similar to the ones for Elzerman readout, except that the plunge duration is swept from few microseconds to millisecond timescales. The probability to load an $|\uparrow\rangle$-spin state is at maximum 50%. Increasing t_{plunge} duration will let time for the spin state to relax. Typical values are $V_{\text{plunge}} = 2\,\text{mV}$ and $t_{\text{read}} = 500\,\mu\text{s}$.

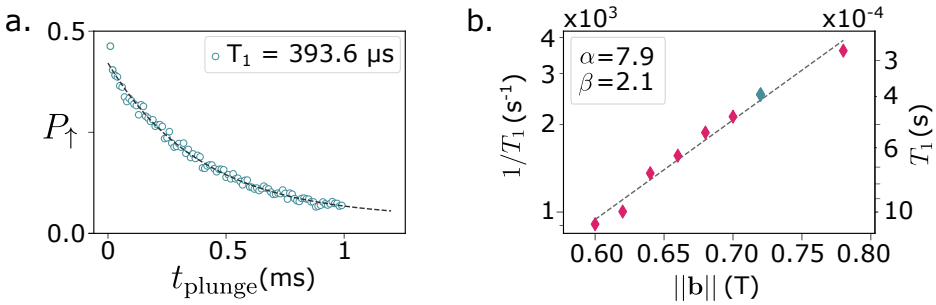

Figure B.4 – **Measured relaxation time of a hole spin qubit:** (a) Example of relaxation time measurement: $P_\uparrow$ value recorded as a function of plunge duration at $\mathbf{B} = (0, 0, 0.72)$ T. Data are fitted with an exponential decay, thus giving $T_1 \simeq 393.6\,\mu\text{s}$. Measurements are only recorded during (R)-stage. (b) Inverse of relaxation time (in log-scale) as a function of magnetic field module $||\mathbf{b}||$. A linear trend, stemming from the noise contribution, is readily observed. We extracte the slope coefficient to be 7.9. The blue point represents data displayed in panel (a).

Same measurement procedure is applied to extract T_1 values for different magnetic field amplitudes $||\mathbf{b}||$. Relaxation time dependency to b-field amplitude provides a direct insight on noise contribution influencing the qubit. In the particular case of hole spin system, relaxation time induced by phonon mechanisms should scale as B^{-5} (B^{-9}) for Dresselhaus (Rashba) dominated spin-orbit interactions. Dresselhaus term is vanished for zinc-blend structures (e.g. Si and Ge), therefore T_1 is expected to mostly scale as B^{-9} [6, 7, 8]. Figure B.4(b) represents the inverse of relaxation time (in log-scale) versus magnetic field amplitude. A linear regression of $\log(1/T_1) = \alpha||\mathbf{b}|| + \beta$ demonstrates a relation to magnetic field scaling as $T_1 \propto B^{-7.9}$. Note that, at this magnetic field orientation, spin relaxation time ranges from millisecond to few hundreds of microseconds timescale. These results

are in good agreement with already reported values for similar hole spin qubits [9].

Further investigations are required to conclude on the noise mechanisms acting on the hole spin qubit. It is worth mentioning that the magnetic field range herein is experimentally limited. On the one hand, small magnetic field values hinder spin readout (due to restricted spin splitting). On the other hand, a maximum of 1 T can be applied in total on the sample, thus limiting the upper bound for magnetic field amplitude.

References

[1] R. Hanson et al. « Spins in few-electron quantum dots ». In: *Reviews of Modern Physics* 79 (4 Oct. 2007), pp. 1217–1265. DOI: 10.1103/RevModPhys.79.1217.

[2] D. Keith et al. « Single-Shot Spin Readout in Semiconductors Near the Shot-Noise Sensitivity Limit ». In: *Phys. Rev. X* 9 (4 Oct. 2019), p. 041003. DOI: 10.1103/PhysRevX.9.041003.

[3] A. Hoffmann. « Thermodynamics and Spin-Orbit Interaction at the Level of Single Electrons ». PhD thesis. ETH Zürich, 2017.

[4] S. Amasha et al. *Measurements of the spin relaxation rate at low magnetic fields in a quantum dot*. 2006.

[5] A. Morello et al. « Single-shot readout of an electron spin in silicon ». In: *Nature* 467.7316 (Oct. 2010), pp. 687–691. DOI: 10.1038/nature09392.

[6] D. V. Bulaev and D. Loss. « Spin Relaxation and Decoherence of Holes in Quantum Dots ». In: *Phys. Rev. Lett.* 95 (7 Aug. 2005), p. 076805. DOI: 10.1103/PhysRevLett.95.076805.

[7] Y. Fang et al. « Recent advances in hole-spin qubits ». In: *Materials for Quantum Technology* 3.1 (Mar. 2023), p. 012003. DOI: 10.1088/2633-4356/acb87e.

[8] Z. Wang et al. « Optimal operation points for ultrafast, highly coherent Ge hole spin-orbit qubits ». In: *npj Quantum Information* 7.1 (Apr. 2021), p. 54. DOI: 10.1038/s41534-021-00386-2.

[9] P. Stano and Daniel Loss. « Review of performance metrics of spin qubits in gated semiconducting nanostructures ». In: *Nature Reviews Physics* 4.10 (Oct. 2022), pp. 672–688. DOI: 10.1038/s42254-022-00484-w.

APPENDIX C

C.1 Gate voltage settings

Gate voltages used to experimentally operate a hole spin qubit are shown in table C.1. Gate voltage V_{B_3} is used to modify the hole wavefunction confinement. In the meantime, V_{T_2} is changed to maintain tunnelling rates within a measurable range for single-shot spin readout [1].

Gate	Config. n°0	Config. n°2	Config. n°1
T_1	-1.840	-1.880	-1.880
T_2	-0.445	-0.485	-0.425
T_3*	-0.758	-0.806	-0.823
T_4	-0.200	-0.200	-0.200
T_5	0	0	0
T_6	0	0	0
B_1	-1.840	-1.880	-1.880
B_2*	-1.740	-1.782	-1.804
B_3	-0.445	-0.540	-0.635
B_4	0	0	0
B_5	0	0	0
B_6	0	0	0
Metal Line	-10	-10	-10

Table C.1 – **Experimental gate voltage settings:** Gate voltages expressed in volt depending on the configuration denoted n°0, n°2 and n°1 (displayed in the main text respectively in blue, violet, red). Importantly, V_{B_2} and V_{T_3} settings are constantly swept across the first hole interdot transition for spin readout, thus their gate voltage settings is herein indicated for order of magnitude purposes.

C.2 Ramsey experimental details

C.2.1 $\pi/2-$pulse calibration

Ramsey experiment necessitates to perform a $\pi/2$-rotation of the spin state to evaluate the coherence time (see main text). The burst duration is a priori unknown and needs for calibration. To this aim, the waiting time between two consecutive $\pi/2$-pulses is minimized to $t_{\text{wait}} = 10\,\text{ns}$. Figure C.1 illustrates the measurement for $\pi/2$-pulse duration calibration when recording $|\uparrow\rangle$-state probability. A maximum of $P_\uparrow$ corresponds to a π-rotation of the spin state for two consecutive $\pi/2$-pulses. The red dashed line highlights the maximum $P_\uparrow$ amplitude when averaged 5 times, thus corresponding to the duration needed for a single pulse to perform $\pi/2$-rotation. In this example, the duration needed to perform a $\pi/2$-rotation is about 60 ns.

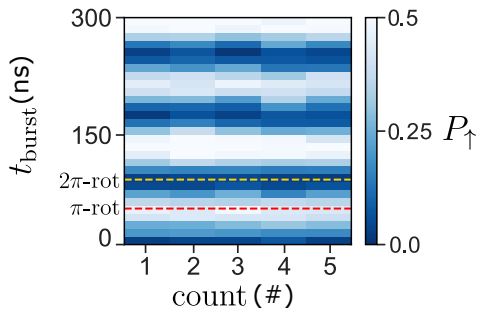

Figure C.1 – $\pi/2-$**pulse calibration for Ramsey experiment:** Repeated $P_\uparrow$ oscillations depending on the burst duration t_{burst} of a single pulse. In order to calibrate the MW duration to match a $\pi/2$ rotation of the spin state, the waiting time between two consecutive $\pi/2$ pulses is set to 10 ns. Oscillations are repeated 5 times and averaged to figure out the burst duration corresponding to a maximum of $|\uparrow\rangle$-state. Red (yellow) dashed line highlights the MW duration needed to perform a π (2π) rotation when performing two consecutive pulses.

C.2.2 Noise investigation at a sweetspot

Despite the mitigation of electrical noise stemming from gate voltage fluctuations $\beta_\parallel$, some low-frequency noise may persist. The absence of refocusing pulse in Ramsey experiment renders the evaluated coherence time subject to noise. As a consequence, Ramsey experiment can be used as a powerful tool to evaluate the Power Spectral Density (PSD) of such low-frequency noise. At a sweetspot with $\mathbf{B} = (0.516, 0.0, 0.360)\,\text{T}$, Ramsey oscillations are measured detuned by $\delta f = 4\,\text{MHz}$ to the Larmor frequency ($f_L = 17.992\,\text{GHz}$) for 7914 repetitions (measurement time $\sim 14\,\text{hours}$). Due to low-frequency noise, Ramsey coherence time T_2^* becomes a stochastic variable which can be fitted with a skewed Gaussian

distribution [2], as in equation C.1. The averaged coherence time is denoted $\overline{T_2^*}$.

$$f(T_2^*, \overline{T_2^*}, \sigma, \gamma) = \frac{A}{\sigma\sqrt{2\pi}} e^{-\frac{(T_2^* - \overline{T_2^*})}{2\sigma^2}} \left[1 + \mathrm{erf}\left(\frac{\gamma(T_2^* - \overline{T_2^*})}{\sigma\sqrt{2}}\right)\right] \tag{C.1}$$

with,

A *an amplitude parameter for the Gaussian distribution,*

γ *quantifies how skewed is the distribution function,*

$\overline{T_2^*}$ *the averaged coherence time,*

σ *relates to the variance of estimated coherence values,*

erf the error function.

Figure C.2(a) illustrates the histogram distribution of the coherence times extracted for each single repetition of time-trace measurement (lasting few seconds). Solid red line is a fit using equation C.1, that allows to evaluate an averaged Ramsey coherence time $\overline{T_2^*} = 0.942\,\mu s$ (emphasized by red dashed line).

Panel (b) of the same figure displays a Power Spectral Density (PSD) spectrum when evaluating $P_\uparrow$ in a single-shot manner. Such Single-Shot Ramsey (SSR) measurement boils down to recording $P_\uparrow$ over time when $t_{\mathrm{wait}} = 0.5\,\mu s$ is fixed onto a flank of a Ramsey oscillation [3]. We probe $P_\uparrow$ evolution for 16000 repetitions and perform a Fourier Transform. Each coloured trace corresponds to a peculiar sampling frequency: $f_{\mathrm{sampling}} = {}^1/_{(n+1)\delta t}$, with n the hold-off count between each time-trace ranging from 0 to 64, and $\delta t = 520\,\mu s$ the duration of a single-shot measurement. The sampling frequencies are therefore ranging from black to blue colours as $f_{\mathrm{sampling}} = [1923.1, 641.0, 384.6, 213.7, 113.1, 58.3, 29.6]\mathrm{Hz}$. Two dashed lines accentuate a global increase in the noise level centered at $f_{\mathrm{noise}} \simeq 0.3\,\mathrm{Hz}$ (i.e. $t_{\mathrm{noise}} \sim 3\,s$). This additional source of electrical noise can be imputed to the presence of nearby two-level fluctuator(s) affecting the spin qubit performances.

C.3 Variability in sweetspot performances

As mentioned in section 4.2.3, the Rabi frequencies are highly dependent on the driving gate responsible for spin manipulation. In figure C.3 are compared the Rabi frequencies measured as a function of magnetic field angle in (NP) plane when sending MW signals through gate T_3 (green) and T_4 (blue points). All measurements are conducted at a fixed MW power $P_{\mathrm{MW}} = +18\,\mathrm{dBm}$ (having same attenuation inside the dilution fridge) and at a constant Larmor frequency $f_L \simeq 17.992\,\mathrm{GHz}$, equivalent to a drive amplitude of $A_{\mathrm{MW}} = 5.61\,\mathrm{mV}$ at the device level. The operation speed (or Rabi frequency) witnesses a strong modulation depending on the driving gate, up to a factor 2 at $\theta = 0°$. Despite the possible cross-talk between the two gates, manipulating the spin orientation seems more efficient when using gate T_4. This may directly stem from the different contributions of

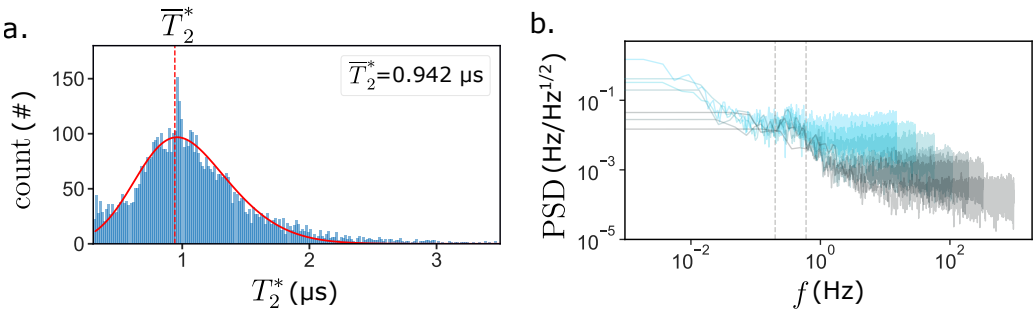

Figure C.2 – **Noise evaluation with Ramsey experiment:** (a) Fitted T_2^* values (see main text for details) over 7914 repetitions. Due to low-frequency noise, Ramsey coherence time becomes a stochastic variable centered at $\overline{T_2^*}$. Red solid line is a fit, permitting to extract the averaged Ramsey coherence time $\overline{T_2^*} = 0.942\,\mu s$ (underscored by red dashed line). (b) Power spectral density for different sampling frequencies (from black to blue, hold-off count between each single time-trace is $[0, 2, 4, 8, 16, 32, 64]$). Such frequency spectrum highlights that, about $f \simeq 0.3\,\text{Hz}$, an additional noise enters into play, suggesting the presence of nearby fluctuator(s) not cancelled at a sweetspot field orientation.

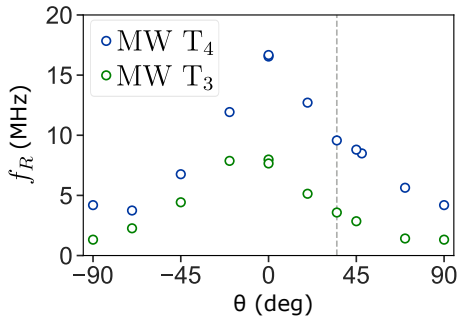

Figure C.3 – **Rabi frequency differences in (NP) magnet plane upon changing driving gate:** Measured Rabi frequencies as a function of magnetic field angle in the (NP) plane. Blue (green) points are Rabi frequency values measured upon driving by gate T_4 (T_3). A clear enhancement in manipulation speed is observed when driving on gate T_4. Grey dashed line underscores the magnetic field angle $\theta = 35°$ shown in figure 4.13.

the driving mechanisms g-TMR and iso-Zeeman [4, 5]. Finally, the grey dashed line emphasized the magnetic angle shown in figure 4.13.

C

References

[1] V. Schmitt et al. *Tunable interdot coupling in SiMOS architectures over more than nine orders of magnitude*. March Meeting. Mar. 2022.

[2] M. R. Delbecq et al. « Quantum Dephasing in a Gated GaAs Triple Quantum Dot due to Nonergodic Noise ». In: *Phys. Rev. Lett.* 116 (4 Jan. 2016), p. 046802. DOI: 10.1103/PhysRevLett.116.046802.

[3] N. Piot et al. « A single hole spin with enhanced coherence in natural silicon ». In: *Nature Nanotechnology* 17.10 (Sept. 2022), pp. 1072–1077. DOI: 10.1038/s41565-022-01196-z.

[4] B. Venitucci. « Modélisation de la manipulation électrique des qubits de trou dans le silicium ». Theses. Université Grenoble Alpes (2020), Nov. 2020.

[5] B. Martinez et al. « Hole spin manipulation in inhomogeneous and nonseparable electric fields ». In: *Phys. Rev. B* 106 (23 Dec. 2022), p. 235426. DOI: 10.1103/PhysRevB.106.235426.

APPENDIX D

D.1 Principle g-factor evolution with confining gate

Figure D.1 illustrates the evolution of the main g-factors projected onto the magnet basis, denoted g_x, $x = \{n, o, p\}$. The latter is rather used in this case than the spin one because it is hardly possible to discriminate the main g-factors, denoted $g_{\tilde{x}}$ in the spin basis, in particular between $\tilde{n}$ and $\tilde{o}$ axes when the spin basis drastically changes. It is clear from the lower panel, emphasizing the g_p dependency to confinement gate, that a maxima of g_p is reached for V_{B_4} about 0.15 V. Beyond this gate voltage, the hole wavefunction does not squeeze more toward the Si-nanowire facet. Still, it is relevant to notice that, despite this decrease, g_p remains the strong confinement axis, with $g_p \gg g_n, g_o$. This unexpected evolution reveals the variability in quantum dot confinement, possibly attributed to fabrication imperfections, the presence of defects/dopants and strain.

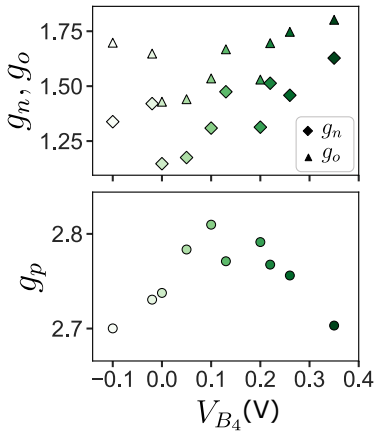

Figure D.1 – **Main g-factor values in the magnet basis depending on confinement:** Deduced principal g-factors in the magnet basis, denoted g_x with $x = \{\vec{n}, \vec{o}, \vec{p}\}$, depending on the confinement gate B_4. Principal g-factor along the $\vec{p}$-axis seems to reach a maximum value for $V_{B_4} = 0.1$ V before decreasing. Noticeably, g_n and g_o factors have similar dependency to gate voltage.

D.2 Spherical representation of longitudinal spin susceptibility

From main text in figure 5.4, changing B_4 gate voltage seems to readily affect the sweetline angular position, by modifying the G-tensor and undoubtedly the spin basis. When shown in 3D, as in the below figure D.2, the longitudinal spin susceptibility anisotropy is rather similar, except a slight tilt in the sweetline location. For $V_{B_4} = 0.0\,\mathrm{V}$, the sweetline does not swirl around $\vec{p}$ axis any longer, which results in 2D plot as a different profile at the poles (i.e. $\theta = \pm 90°$).

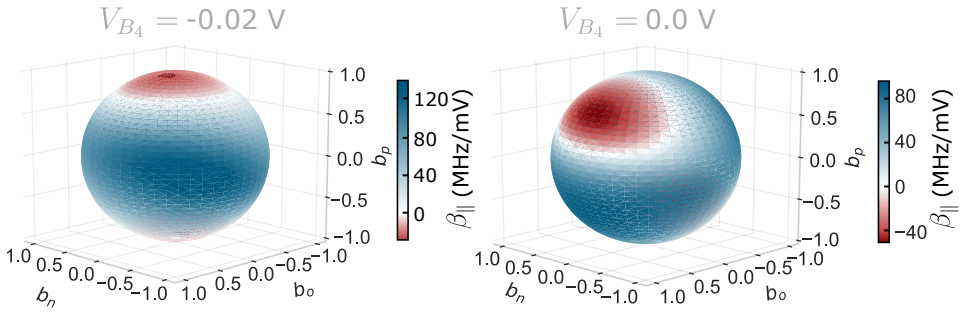

Figure D.2 – **Spherical representation of longitudinal spin susceptibility:** Anisotropy of QD_4 longitudinal spin susceptibility measured for two confining gate voltages $V_{B_4} = -0.02\,\mathrm{V}$ (left panel) and $V_{B_4} = 0.0\,\mathrm{V}$ (right panel) represented as a sphere in magnetic field basis. Between the two configurations, the spin basis changes and thus the sweetline position.

D.3 Fit quality and uncertainties about the sweetline position

Aligning sweetlines at a given magnetic field orientation heavily rely on the accuracy of the fitting procedures of both G and G'-tensors. Figure D.3 illustrates the accordance between experimental measurements and estimation of Larmor frequency and longitudinal spin susceptibility $\beta_\parallel$ for $V_{B_4} = 0.2\,\mathrm{V}$. A reasonable concordance of datasets with the fitted values is visible.

Any error induced by the fit in G'-tensor will result in non-negligible inaccuracy in the sweetline angular position. As the width of the sweetline can be less than a degree, it is crucial to assess the resulting uncertainties. We estimate the error as the standard deviation stemming from the G'-tensor. Zeros of longitudinal spin susceptibility fulfil the equation $\mathbf{b}^T G' \mathbf{b} = 0$, which can be derived in the (NP) plane as:

$$\begin{bmatrix}\sin\theta & \cos\theta\end{bmatrix} \begin{bmatrix}G'_{nn} & G'_{np} \\ G'_{np} & G'_{pp}\end{bmatrix} \begin{bmatrix}\sin\theta \\ \cos\theta\end{bmatrix} = 0 \tag{D.1}$$

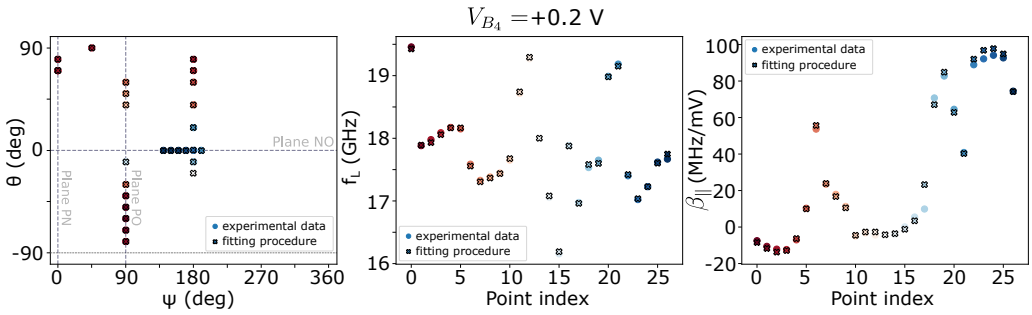

Figure D.3 – **Comparison between experimental and theoretical spin susceptibilities for $V_{B_4} = 0.2\,\mathrm{V}$:** Left panel illustrates all measurements of spin susceptibility depending on magnetic field angles (ψ, θ). Dashed lines emphasize the principal magnet planes. Central (right) panel shows the accordance between experimental and theoretical dataset with respect to the Larmor frequency (the longitudinal spin susceptibility). A decent agreement is found out after fitting procedure of G (for Larmor) and G'tensors (for $\beta_\parallel$). In all panels, circles are experimental data whereas crosses are estimations after fitting procedure.

which is equivalent to the equation system:

$$\sin^2\theta G'_{nn} + \sin 2\theta G'_{np} + \cos^2\theta G'_{pp} = 0 \tag{D.2}$$

We define t as $\tan\theta$ so that the previous equation reads:

$$t^2 G'_{nn} + 2t G'_{np} + G'_{pp} = 0 \tag{D.3}$$

with the corresponding solutions

$$\theta = \arctan\left[\frac{G'_{np} \pm \sqrt{(G'_{np})^2 - G'_{nn}G'_{pp}}}{G'_{nn}}\right]. \tag{D.4}$$

The equation D.4 is solved when considering the G'-tensor elements with the corresponding uncertainty : $G'_{ij} \mapsto G'_{ij} \pm \delta G'_{ij}$.

APPENDIX E

E.1 Preliminary characterization of the sample

Beforehand investigating the possibility to isolate a DQD system, few preliminary characterizations may be worth mentioning. Figure E.1(a) is an image of the board used herein. At the center, the sample is glued to the board and micro-bonded to DC and high-frequency lines. In order to ensure that the sample behaves as a transistor at room temperature, we measure the I-V characteristic of each gate whose results are shown in panel (b). A bias of 10 mV is applied between Source and Drain contacts. An excellent reproducibility of the gate opening threshold is observed from G_1 to G_5.

Finally, panel (c) presents the resonator frequency spectrum in amplitude (dark blue) and phase (light blue) at low temperature. To do so, a signal is sent at f_{REF} through the resonator connected to the sample, and is collected back to be demodulated. Apart from standing waves, a clear resonance is readily visible at $f_{\mathrm{res}} = 503.3\,\mathrm{MHz}$, as underscored by the dashed line. In the following, the probing frequency for reflectometry readout is set at f_{res}. Fitting the latter resonance enables to evaluate the resonator quality factors Q_{int} and Q_c mentioned in the main text.

E.2 Compensation matrix

Trapping hole charges within a DQD in a reproducible manner may be challenging in such sample geometry due to gate cross-talk. So as to dodge such limitations, we define a compensation matrix M aiming at counterbalancing cross-talks on the four gates needed to initialise the system in an isolated regime. Virtual gates are hereafter labelled $\widetilde{V_{G_i}}$ and defined as per equation E.1 [1].

$$\begin{bmatrix} \widetilde{V_{G_1}} \\ \widetilde{V_{G_2}} \\ \widetilde{V_{G_3}} \\ \widetilde{V_{G_4}} \end{bmatrix} = \begin{bmatrix} 1 & -\alpha_{n\to n+1} & -\alpha_{n\to n+2} & -\alpha_{n\to n+3} \\ -\alpha_{n\to n+1} & 1 & -\alpha_{\mathrm{DQD}} & -\alpha_{n\to n+2} \\ -\alpha_{n\to n+2} & -\alpha_{\mathrm{DQD}} & 1 & -\alpha_{n\to n+1} \\ -\alpha_{n\to n+3} & -\alpha_{n\to n+2} & -\alpha_{n\to n+1} & 1 \end{bmatrix} \cdot \begin{bmatrix} V_{G_1} \\ V_{G_2} \\ V_{G_3} \\ V_{G_4} \end{bmatrix} \tag{E.1}$$

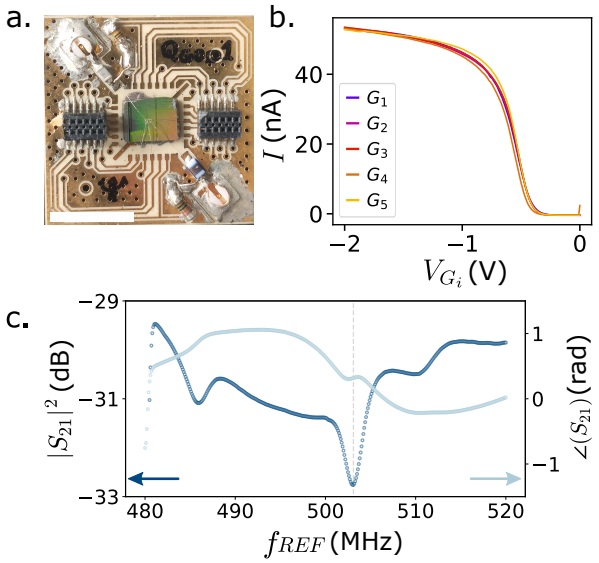

Figure E.1 – **Primary measurements of the sample:** (a) Picture of the board and the micro-bonded sample. Top left and bottom right connectors are for high-frequency signals either for reflectometry or for qubit manipulation (MW). The surface-mount inductor used in this experiment is $L = 220\,\mathrm{nH}$. Scale bar is 1 cm. (b) Room temperature I(V) characteristic of each gates. Similarly to chapter 2, while sweeping one gate, the others are maintained at $-2\,\mathrm{V}$. A bias of $V_{SD} = 10\,\mathrm{mV}$ is applied between source and drain contacts. (c) Resonator frequency spectrum at low temperature (4K). Dark (light) blue curve embodies the amplitude (phase) of the demodulated signal denoted S_{21} ($\arg(S_{21})$). For sake of clarity, we removed the electronic delay in the phase signal. Apart from standing waves, a resonance at frequency $f_{\mathrm{res}} = 503.3\,\mathrm{MHz}$ is observed, as indicated by the dashed line, corresponding to the resonator.

Two assumptions are herein drawn: first, cross-talks between first and second neighbouring gates is considered equal for all gates and second, the contribution to third neighbouring gate is neglected, thus $\alpha_{n\to n+3} = 0$. In order to evaluate the lever-arm between adjacent gates, we measure the displacement of an interdot position when varying first or second neighbouring gate voltage. Figure E.2 illustrates the cross-talk estimation of both $\alpha_{n\to n+1}$ and $\alpha_{n\to n+2}$. α_{DQD} is measured as the slope of the interdot transition and is about $-0.541\,\mathrm{eV\,V^{-1}}$ (not shown herein).

The final compensation matrix used in the main text is therefore:

$$M = \begin{bmatrix} 1 & 0.0277 & 0.0066 & 0 \\ 0.0277 & 1 & 0.5405 & 0.0066 \\ 0.0066 & 0.5405 & 1 & 0.0277 \\ 0 & 0.0066 & 0.0277 & 1 \end{bmatrix} \tag{E.2}$$

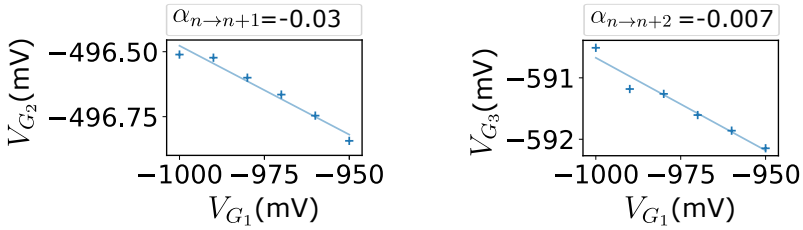

Figure E.2 – **Lever-arm measurements between first and second neighbour:** Left panel is the evaluation of cross-talk denoted $\alpha_{n\to n+1}$ of a gate on its first nearest neighbour. A linear regression of the interdot positions depending on V_{G_1} values estimates $\alpha_{n\to n+1} = -0.03$. Right panel is the same measurement process to evaluate second order cross-talk between gates, denoted $\alpha_{n\to n+2}$. In this case, the interdot position in gate G_3 is probed as a function of V_{G_1}. Finally, cross-talk is assessed as: $\alpha_{n\to n+2} = -0.007$.

E.3 Power calibration for spectroscopy

High-frequency lines in the fridge are attenuated by 37 dB up to the sample. However, when performing spectroscopy, the attenuation is altered depending on the MW frequency. In order to ensure a constant MW power experienced by the sample, we perform a power calibration on different interdot transitions to render it independent to hole spin physics [2].

An example of such calibration map is shown in lower panel of figure E.3. Phase reflectometry signal is recorded on an interdot transition while sweeping the MW frequency and level with $P_{\text{sample}} = P_{\text{MW}} - 37$. A clear increase of the MW power experienced by the hole particle is visible between the two white dotted lines for $f_{\text{MW}} \in [3.6, 8.0]$GHz. Dark blue line underscores an iso-power that ensures the interdot signal is decreased at maximum by 10% in amplitude. This curve could have been taken as calibration, setting the signal amplitude relatively to its frequency, but this requires too fast changes of MW source attenuation during measurement. Instead, the upper panel curve depicts the calibration chosen for spectroscopy experiments in the main text, taking into account the weaker attenuation between 4 and 8 GHz.

References

[1] T.-K. Hsiao et al. « Efficient Orthogonal Control of Tunnel Couplings in a Quantum Dot Array ». In: *Phys. Rev. Appl.* 13 (5 May 2020), p. 054018. DOI: 10.1103/PhysRevApplied.13.054018.

[2] R. Ezzouch. « Gate reflectometry as readout and spectroscopy tool for silicon spin qubits ». PhD thesis. June 2021.

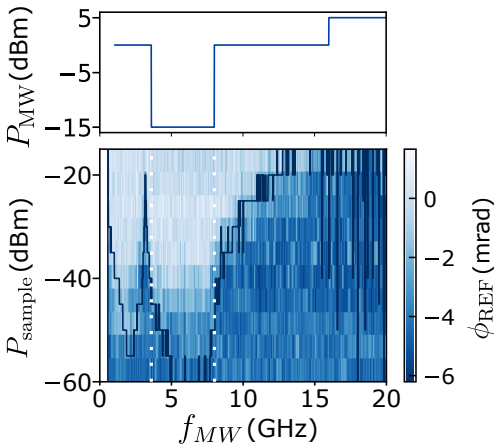

Figure E.3 – **Microwave power calibration depending on frequency:** Phase reflectometry signal recorded on an interdot transition dip when changing the MW frequency and amplitude. Dark blue line illustrates the constant power to send so that the interdot transition is decreased at maximum by 10% in amplitude. Dotted lines highlight the frequency span in which MW level experienced by the qubit is high.